C 55.13/2:ERL WPL-87

NOAA Technical Memorandum ERL WPL-87

COMPLETED
299

RADAR APPLICATIONS IN CLOUD AND CLEAR-AIR STUDIES

Earl E. Gossard
Richard G. Strauch

Wave Propagation Laboratory
Boulder, Colorado
November 1981

noaa NATIONAL OCEANIC AND ATMOSPHERIC ADMINISTRATION / Environmental Research Laboratories

NOAA TM ERL WPL-87

NOAA Technical Memorandum ERL WPL-87

RADAR APPLICATIONS IN CLOUD AND CLEAR-AIR STUDIES

Earl E. Gossard
Richard G. Strauch

Wave Propagation Laboratory
Boulder, Colorado
November 1981

UNITED STATES
DEPARTMENT OF COMMERCE
Malcolm Baldrige,
Secretary

NATIONAL OCEANIC AND
ATMOSPHERIC ADMINISTRATION
John V Byrne,
Administrator

Environmental Research
Laboratories
George H Ludwig
Director

NOTICE

Mention of a commercial company or product does not constitute an endorsement by NOAA Environmental Research Laboratories. Use for publicity or advertising purposes of information from this publication concerning proprietary products or the tests of such products is not authorized.

ACKNOWLEDGMENTS

The authors wish to express their sincere appreciation to Ms. Mildred Birchfield for her expert technical typing, her careful editorial layout and her editorial review and consultation on the text. We also appreciate valuable consultation with Drs. C. Gordon Little and Vernon Derr on special applications of radar and optical systems.

CONTENTS

		Page
CHAPTER 1 - INTRODUCTION		1
1.1	Radar Returns from Hydrometeors	1
	Review	1
	Relationships between cloud types and weather systems	3
	Cloud classifications - general and drop-size distributions	3
	Clouds and storm system morphology	6
	A little cloud physics - some definitions and nomenclature	18
1.2	Clear-Air Radar Returns	23
	Review	23
	Refractive index of the clear atmosphere	27
	Air Masses	31
	Source and formation	31
	Air mass modification - the surface layers	36
	Elevated layers	42
	Layers capping the convective boundary layer	42
	Sub-tropical subsidence layers	46
	Frontal discontinuities	53
	The stratosphere and middle atmosphere	59
CHAPTER 2 - PHYSICAL EFFECTS OF THE ATMOSPHERE ON RADAR WAVES		65
2.1	Introduction	65
2.2	Reflection and Refraction	65
2.3	Absorption	66
2.4	Scattering - General	66
	Scatter from clouds and precipitation	72
	Scatter from the clear air	74
	Scattering and the refractive index structure parameter	76
	Refractive index variance of clear air	77
	Effect of temperature-humidity covariance	78
2.5	Bragg Scatter from the Air Compared with Bragg Scatter from a Droplet Medium	79
	Temperature-Humidity Covariance in Clouds	80
2.6	Forward-Scatter Observation of Bragg-Coherence in Clouds	81
2.7	Conclusions	94
CHAPTER 3 - VARIOUS RADARS AND THEIR POTENTIAL FOR CLOUD AND CLEAR AIR DETECTION		95

CHAPTER 4 - RADAR REFLECTIVITY AND CLOUD CHARACTERISTICS 98

4.1 Introduction 98
4.2 Drop-Size Distribution - Some Special Cases 98
4.3 A General Drop-Size Distribution Function 99
4.4 Methods for Measuring Drop-Size In-Situ 104
4.5 Observations of Drop-Size Distribution in Natural Clouds 105
4.6 Observations of Drop-Size Distribution in Man-made Clouds 112
4.7 Observations of Cloud Reflectivity 113
Conclusions 116

CHAPTER 5 - RADAR ATTENUATION AND CLOUD OBSERVATION 117

5.1 Introduction 117
5.2 Attenuation of Radar Waves by Small Water Spheres 117
5.3 Optical Extinction by Small Water Drops 119
5.4 Cloud and Rain Parameter Diagrams 120
5.5 Measuring Z and k 122
5.6 Analysis of Errors 123
5.7 Conclusions 125

CHAPTER 6 - POLARIZATION AND SCATTERER CHARACTERIZATION 126

6.1 Introduction 126
6.2 Backscatter by Non-Spherical Particles 128
Discussion 128
Theory 128
Geometry of Scattering 131
Perfect Sphere 134
Random Orientation 135
Oriented Oblate Spheroids 135
Oriented Prolate Spheroids 136
6.3 Differential Reflectivity from Non-Spherical Particles 137
6.4 Attenuation by Non-Spherical Particles 141
6.5 Scattering in an Arbitrary Direction 143
6.6 Conclusions and Possible Observational Applications 144

CHAPTER 7 - DOPPLER RADAR OBSERVATION OF CLOUDS AND CLEAR-AIR 150

7.1 Doppler-Measured Radial Velocity - Range and Velocity Folding 150
7.2 Atmospheric Turbulence and Doppler Velocity Spectral Width 153
7.3 Multi-Radar Doppler Systems 159
Three-Dimensional Wind Fields in Storms Observed by Doppler Radar 161

Particle Fall Velocity 163
Boundary Conditions 165
7.4 Choice of Wavelength in Cloud-Sensing Doppler Radar Systems 166
7.5 Doppler Radar Studies of Clear-Air Structure 170
The Use of Chaff in Studies of the Clear-Air 170
7.6 Dual Doppler Radar Measurements in the Clear Air Without Chaff 175
7.7 Frequency-Modulated, Continuous-Wave (FM-CW) Radar 176
7.8 Doppler Radar Winds in the Stratosphere and Middle Atmosphere 185

CHAPTER 8 - BIOLOGICAL TARGETS AND THEIR ROLE IN RADAR BACKSCATTER 188

CHAPTER 9 - BOUNDARY LAYER STRUCTURE AND RADAR REFRACTION, DUCTING AND SCATTERING 196
9.1 Introduction 196
9.2 Refractive Index Structure of the Boundary Layer 200
9.3 Structure Parameter of Refractive Index in the Boundary Layer 207

CHAPTER 10 - BOUNDARY LAYERS UNDERGOING MODIFICATION 212
10.1 Introduction 212
10.2 Spatial Transition at the Lower Boundary 213
Traditional Diffusion Equation Approach 213
Flux Integral Method 216
Logarithmic Profiles 219
10.3 Boundary Layer Modification Due to Radiational Cooling at the Ground 223
Constant Flux Assumption at Lower Boundary 223
Quasi-Sinusoidal Variation of Surface Temperature 227

REFERENCES 234

APPENDIX A - SOME FUNDAMENTAL RADAR RELATIONSHIPS 247
The Radar Equation 247
Radar Reflectivity and Backscatter 248
Backscatter from Spherical Drops 250
Doppler Radars 251
Pulse Radars 251
FM-CW Radars 252

APPENDIX B - RELATIONSHIPS BETWEEN N AND ϕ 254

APPENDIX C - TABLES OF THE INCOMPLETE GAMMA FUNCTION 256

APPENDIX D - RELATIONSHIP BETWEEN DOPPLER SPECTRAL WIDTH AND TURBULENCE 257

APPENDIX E - VARIOUS SPECTRAL FORMS AND CONSTANTS 261

Some Spectral Relationships 261

The Balance Equations for Kinetic Energy and Temperature 263

The Spectral Forms and Constants 264

Velocity Field 264

Refractive Index Field 264

RADAR APPLICATIONS IN CLOUD AND CLEAR-AIR STUDIES

Earl E. Gossard and Richard G. Strauch
NOAA/ERL/Wave Propagation Laboratory
Boulder, Colorado 80303

CHAPTER 1 - INTRODUCTION

1.1 Radar Returns from Hydrometeors

Review

Since the advent of radar in World War II, it has been the most valuable man-made remote sensor for atmospheric observation, both in the ionosphere and in the troposphere. Wavelengths from many kilometers to a few millimeters have found useful applications. Weather radars have been used mainly for the observation of precipitation-size hydrometeors because the reflectivity of radar waves from small particles is very size dependent, and rain, snow, and hail are relatively large compared with non-precipitating hydrometeors such as clouds. There is a vast literature on the use of radars to observe precipitating systems and this subject will be touched on only lightly here. The reader is referred to readily available texts such as Atlas (1964), Battan (1973), Sal'man (1973, English translation available).

In the late 1950's and 1960's there were relatively large efforts at several laboratories to use radars for studies of clouds. Some of this work, in fact, led to the deployment of the U.S. Air Force TPQ-11 radar ceilometer used operationally around the globe (Petrocchi and Paulsen, 1966, see Fig. 1-1a,b,c). However, the success of cloud sensing radars was generally marginal (e.g., see Plank et al., 1954; Harper, 1964). There are several reasons why radars have, so far, been unimpressive in cloud studies: 1) except for the TPQ-11, the radars used have usually been designed for other purposes. For example, the wavelengths used have been in the centimeter range or longer. 2) The radar-observed bases and tops of clouds often did not agree well with the visible bases and tops. 3) No simple relationship was found between the radar observations and the cloud classification system of the meteorological services. According to Plank et al. (1954), of 89 periods during which echoes were received, slightly less than 50% could be classed as echoes from internationally defined cloud types. 4) For reasons never well understood, only about 50% of the clouds visually observed were detected by radar, and the presence of ice crystals seemed to be important. Harper (1964) reported

BEST DOCUMENT AVAILABLE

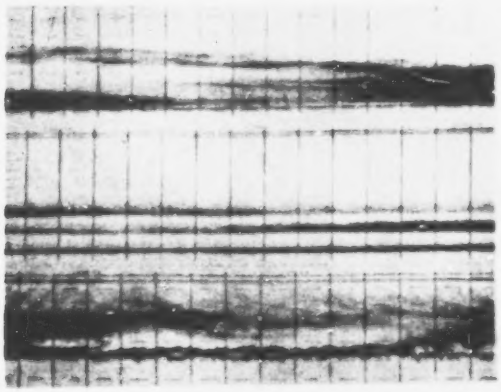

1 - 1A

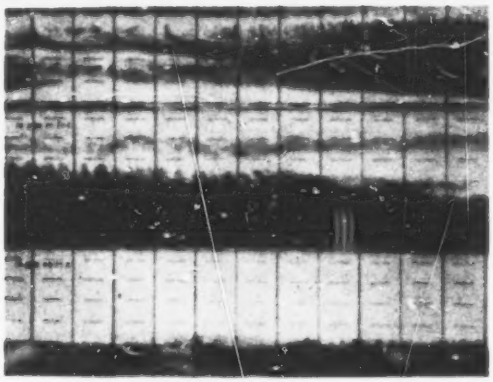

1 - 1B

1 - 1C

Figure 1-1a, 1-1b, 1-1c.--Radar cloud observations obtained with a TPQ-11, 8.6 mm, vertically pointing radar. Figure illustrates temporal changes within cloud structure and the influence of wind shear. Range mark, 5000', time mark, 5 minutes. (Petrocci and Paulsen, 1972).

that only about 50% of high clouds and 75% of medium clouds were detectable with a 0.86 cm wavelength radar in southern England.

For the reasons given above, radar cloud-sensing has generally not been vigorously pursued in the 1970's. However, in the last decade there have

been several developments in radar technology that suggest that radar cloud-studies should be resumed. These include the ready availability of low-noise components which can significantly improve the sensitivity of radar receivers. Furthermore, the technology of satellite communications has produced, and made commercially available, microwave components at wavelengths of a few millimeters that would have been expensive and inefficient a decade ago. Finally, new radars have been designed and built specifically for atmospheric investigations. Some of them, such as the FM-CW Doppler radar (Richter, 1969; Strauch et al., 1976; Chadwick et al., 1976), have great flexibility in spatial and temporal resolution, and have the ability to sense the clear air in addition to hydrometeors. The incorporation of computers into the new radar systems provides many options in the processing of data. It now seems clear that operational wind-sensing radars will eventually be deployed as part of the routine observational system of the weather services, and it is important to determine early what cloud-sensing capabilities may be anticipated from such radars. Lending further urgency to the development of cloud-sensing systems, is the increasing realization that detailed short-term prediction of storm development requires observation at a much earlier stage in storm evolution than is provided by conventional weather radars, and cloud seeding techniques may require injection of seed material at an early phase of cloud development.

Relationships Between Cloud Types and Weather Systems

Cloud Classification

The human eye-brain combination remains the most effective remote sensor of local weather, and the international classification of clouds is based on visual observations. Although the details in form adopted by cloud systems are limitless, the number of cloud types is rather restricted. This suggests that a limited number of dynamical and microphysical processes are decisive. The international cloud classification system recognizes low, medium, and high clouds whose major classes (called genera) are given in Table 1-1.

Cloud genera are mutually exclusive and are based on; a) the cloud's degree of vertical development, i.e., cumulus or stratus depending on whether vertical development is large or small and, b) whether the cloud is precipitating, i.e., the "nimbus" qualification. Thus, in addition to altitude, the genera define; 1) a major dynamical characteristic of the cloud (or at least of its environment) because vertical development indicates the degree of environmental stability, and 2) a major microphysical characteristic because

BEST DOCUMENT AVAILABLE

Table 1-1

Cloud genera	Altitude
Cirrus Cirro-stratus Cirro-cumulus	High
Alto-stratus Alto-cumulus	Medium
Strato-cumulus Nimbo-stratus Cumulus Cumulo-nimbus Stratus	Low

precipitation indicates degree of microphysical stability, i.e., precipitation requires colloidally unstable growth of droplets in the cloud environment.

The genera are further classified into species and varieties according to shape and the special characteristics they may display. For example, the genera classification may be qualified by the term "lenticular" if the cloud has the characteristic lens shape often seen over, or in the lee of, mountains.

No further details in cloud classification will be given here. The interested reader is referred to the International Cloud Atlas published by the World Meteorological Organization (WMO), Geneva, Switzerland and the many excellent texts on clouds and precipitation. Characteristics of cloud droplet populations found by different observers have been collected and summarized by Mason (1971). They are reproduced here in Table 1-2. In Table 1-2, r_d, r_{50}, and r_m are the mode, number density median, and mean of drop radii as defined by the different referenced observers and depending somewhat on the form of size distribution to which the data are to be fitted. n is drop number density and w is liquid water. Commonly assumed distributions used in radar meteorology literature are

<u>exponential</u>

$$N_D = N_o \exp[-3.67\ D/D_o] \qquad (1\text{-}1)$$

Table 1-2 (as summarized by Mason, 1971)

Characteristics of cloud-droplet populations

Cloud type	Author	r_{min} (μm)	r_{50} (μm)	r_d (μm)	r_m (μm)	r_{max} (μm)	$n(cm^{-3})$	$w(g\ m^{-3})$
Small continental cumulus								
(<7000 ft) Australia	Squires	2.5	6	--	--	10	420	0.4
U S.A.	Weickmann & aufm Kampe	3		6	9	33	300	1.0
England	Durbin			4	6	30	210	0.45
Russia	Kazas			4.3	4.7		310	0.15
U.S.A.	Draginis		6	7			300	0.40
Small maritime cummulus								
Hawaii	Squires	2.5	12	11	15	20	75	0.50
Caribbean	Draginis		9	11			45	0.4
Cumulus congestus								
U.S.A.	Weickmann & aufm Kampe	3		6	24	83	64	2.0
(600 m above base)								
Russia	Zaitsev	2		5.5		40	95	0.45
Cumulonimbus								
U.S.A.	Weickmann & aufm Kampe	2		5	20	100	72	2.5
Altostratus								
Germany	Diem	1		4.5	5	13	450	
Russia	Kazas			4.6	6.6		220	0.6
Nimbostratus								
Germany	Diem	1		4	6	20	330	
Stratus								
Germany	Diem	1		4	6	22	260	
Hawaii	Squires	2.5	13			45	24	0.35
Stratocumulus								
Germany	Diem	1		3.5	4	12	350	
England	Frith	3				25	500	
Orographic cloud								
Hawaii	Squires	5	13			34	45	0.30

BEST DOCUMENT AVAILABLE

BEST DOCUMENT AVAILABLE

where D_o is the volumetric mean diameter, N_o is a scaling factor characterizing drop number density, and N_D is the number of drops of diameter D per unit volume,

Best, 1951

$$1 - F = \exp[-(D/D_o)^b] \tag{1-2}$$

where F is the fraction of liquid water in drops of size less than diameter D, and b is a numerical factor.

In the cloud physics literature, commonly assumed distributions are:

log normal

$$N_r = \frac{N_T}{\sqrt{2\pi}\log\sigma} \exp - \frac{(\log r - \log r_g)^2}{2\log^2\sigma} \tag{1-3}$$

where r_g is the geometric mean radius, σ the standard deviation, N_r is number density of drops of radius r, and N_T is total number of drops per unit volume;

gamma distribution

$$N_r = \frac{N_T(\gamma\alpha)^{\gamma\alpha+1}}{\alpha\Gamma(\gamma\alpha+1)\exp\gamma\alpha}[\{1-(r-r_d)/\alpha\}^{\gamma\alpha}]\exp[-\gamma(r-r_d)] \tag{1-4}$$

where $\gamma = 1/(r_m - r_d)$ and $\alpha = r_d - r_{min}$;

modified gamma distribution (Deirmendjian, 1974; Sal'man, 1973);

$$N_r = a(r)^{\alpha}\exp[-br^{\gamma}] \tag{1-5}$$

where a, α and γ are empirically determined.

The two parameter distributions are of special interest to the radar meteorologist because it is relatively simple to design and build radar systems that can measure two independent quantities that depend on drop size distribution; these include reflectivity and attenuation or alternatively, reflectivity and differential reflectivity on orthogonal polarization channels.

Clouds and Storm System Morphology

The distribution of various cloud types in a classical frontal system is shown in Fig. 1-2 as given by Bergeron (1935). It should be compared with

BEST DOCUMENT AVAILABLE

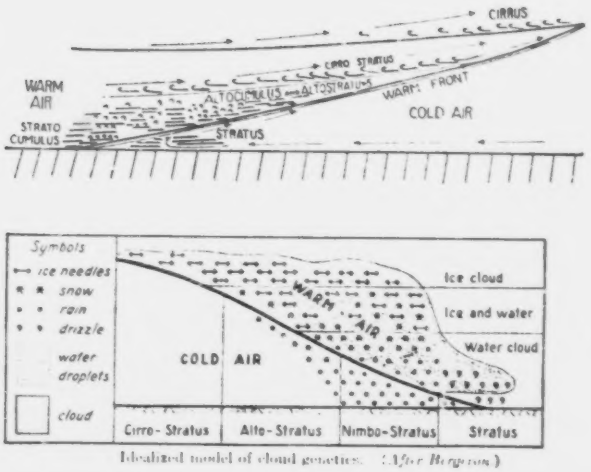

Idealized model of cloud genetics. (After Bergeron.)

Figure 1.2.--Idealized model of cloud distribution about typical frontal systems. Top frame: cloud types; Bottom frame: liquid-ice phase within cloud systems.

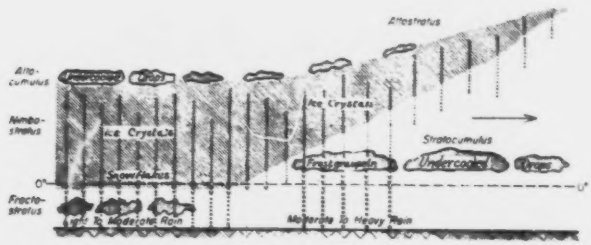

PRECIPITATION FROM NIMBOSTRATUS CLOUD SYSTEM

Showing distribution of ice and water clouds and areas of light, moderate, and heavy rain in a nimbostratus cloud system. The term "frostgraupeln" is apparently equivalent to the U. S. "sleet particles." (After Findeisen.)

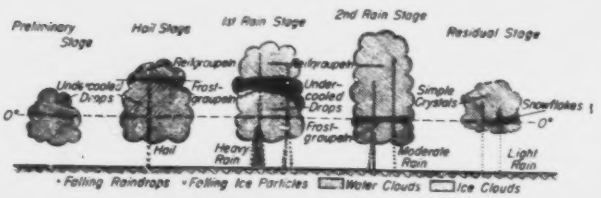

PRECIPITATION FROM CUMULONIMBUS CLOUDS

Showing growth and decay of cumulonimbus cloud with various types of precipitation. After Findeisen.)

Figure 1.3.--Distribution of liquid-ice phase particles around typical nimbo stratus and cumulonimbus cloud systems.

the cloud classification system given above. Figure 1-3 from Findeisen (1938) shows a vertical cross-section through a system of stratiform clouds. It is fairly typical of some kinds of warm frontal or moderately occluded situations. The main cloud mass is nimbo-stratus composed of ice crystals.

To the right are strato-cumulus clouds composed of supercooled water droplets. Below the 0° isotherm are fracto-stratus. Moderate rain is found where ice crystals fall into water clouds causing rapid drop growth; light rain is found where the falling ice crystals melt, and light drizzle may be found below water clouds unseeded by ice crystals from above if the clouds are low enough. The alto-cumulus water clouds at the top of the nimbo-stratus lie in a region where insufficient nuclei are present to transform them into ice crystals. They are secondary to the main nimbo-stratus but occur frequently nevertheless. Typically they are 200-300 m thick but may be much thicker.

A plan view of the distribution of cloud forms in the neighborhood of a classical frontal system is shown in Fig. 1-4a constructed from aircraft observations reported by Cunningham (1952). Figure 1-4b shows the corresponding radar PPI display. A vertical cross-section along the path DD is shown in Fig. 1-5.

For comparison, a plan view of cloud and precipitation distribution around an open wave situation observed by Browning and Harrold (1969) is shown in Fig. 1-6. They analyzed the large scale character of the storm from the synoptic radiosonde network. They used the wet-bulb potential temperature, which is conserved even if motions are non-isentropic as when evaporation/condensation is occurring. Browning and Harrold also made extensive use of Doppler radar in the analysis of the detailed kinematic structure of vertical sections through the storm and some fields in the vicinity of the frontal surface are shown in Fig. 1-7. The method is worth some detailed discussion as it introduces the subject of Doppler radar, a powerful and relatively new technique. They used the radar in the so-called "velocity-azimuth display" (VAD) mode, in which the radar executes a conical scan about the vertical axis. The radar thus senses the radial velocity component of the target particles (precipitation) over all azimuthal angles and all heights through the storm system. Thus, in the presence of a mean horizontal wind, the temporal record in radial velocity would simply appear as sinusoids at the various ranges (see Fig. 1-8 for a schematic illustration). A more physically suggestive display is the "plan shear indicator" (PSI), which is essentially a Doppler PPI (plan position indicator). In this display both position and velocity are indicated by the radial displacement of the echo from the origin. Range is radial distance from the center and the range "bins" contain the atmospheric echo at the various range increments which are determined by the range resolution of the particular radar (very nearly half the pulse length). The displacement of the echo (indicated by the dashed circles in Fig. 1-8) in each range bin from the center of the bin (indicated

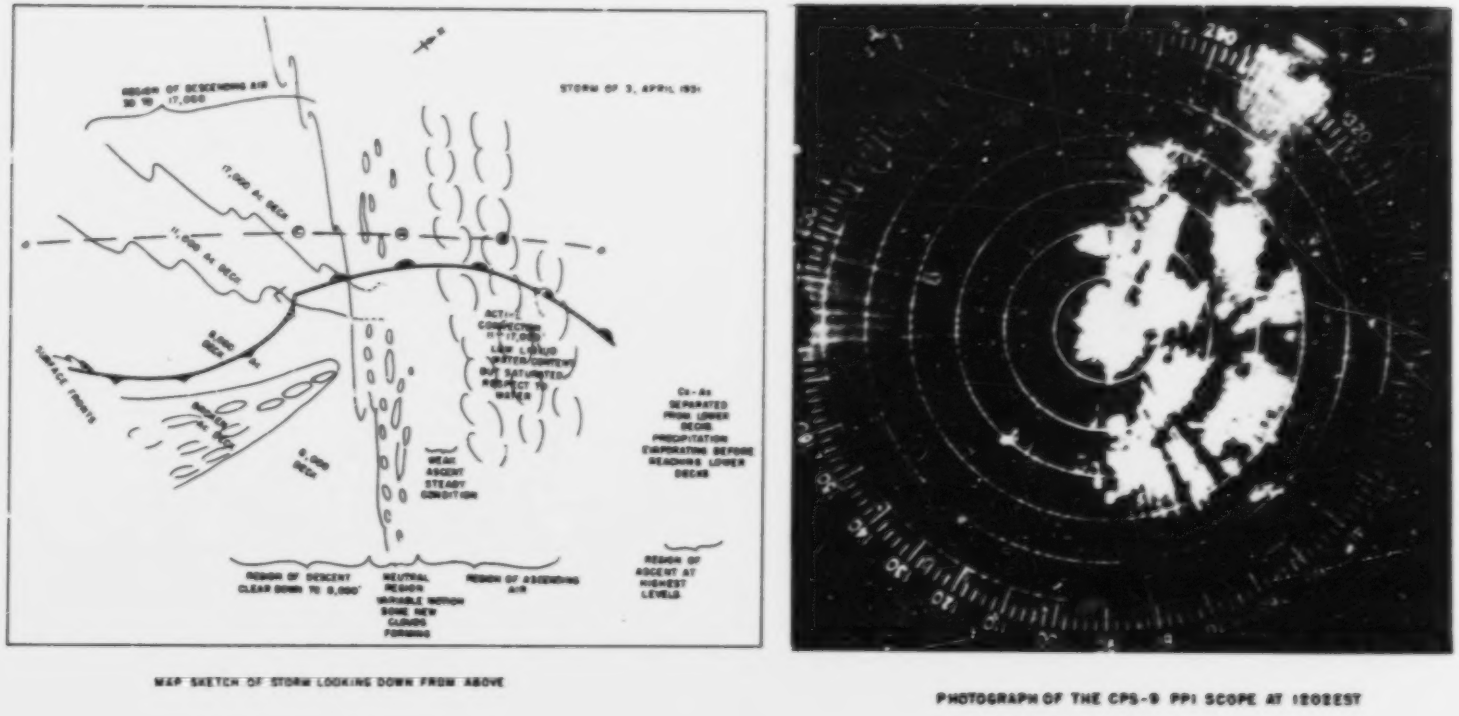
STORM OF 3, APRIL 1951
REGION OF DESCENDING AIR
TO 17,000
11,000 Ac DECK
11,000 Ac DECK
8,000 DECK
SURFACE FRONTS
ACTIVE CONVECTION TO 17,000
LOW LIQUID WATER CONTENT BUT SATURATED WITH RESPECT TO WATER
WEAK ASCENT STEADY CONDITION
Cu-As SEPARATED FROM LOWER DECKS
PRECIPITATION EVAPORATION BEFORE REACHING LOWER DECKS
REGION OF DESCENT CLEAR DOWN TO 8,000'
NEUTRAL REGION VARIABLE WITH SOME NEW CLOUDS FORMING
REGION OF ASCENDING AIR
REGION OF ASCENT AT HIGHEST LEVELS
MAP SKETCH OF STORM LOOKING DOWN FROM ABOVE
PHOTOGRAPH OF THE CPS-9 PPI SCOPE AT 1202EST

Figure 1.4.--Distribution of cloud types about a frontal system observed by Cunningham (1952) compared with corresponding displays on a radar scope at about the same time.

BEST DOCUMENT AVAILABLE

BEST DOCUMENT AVAILABLE

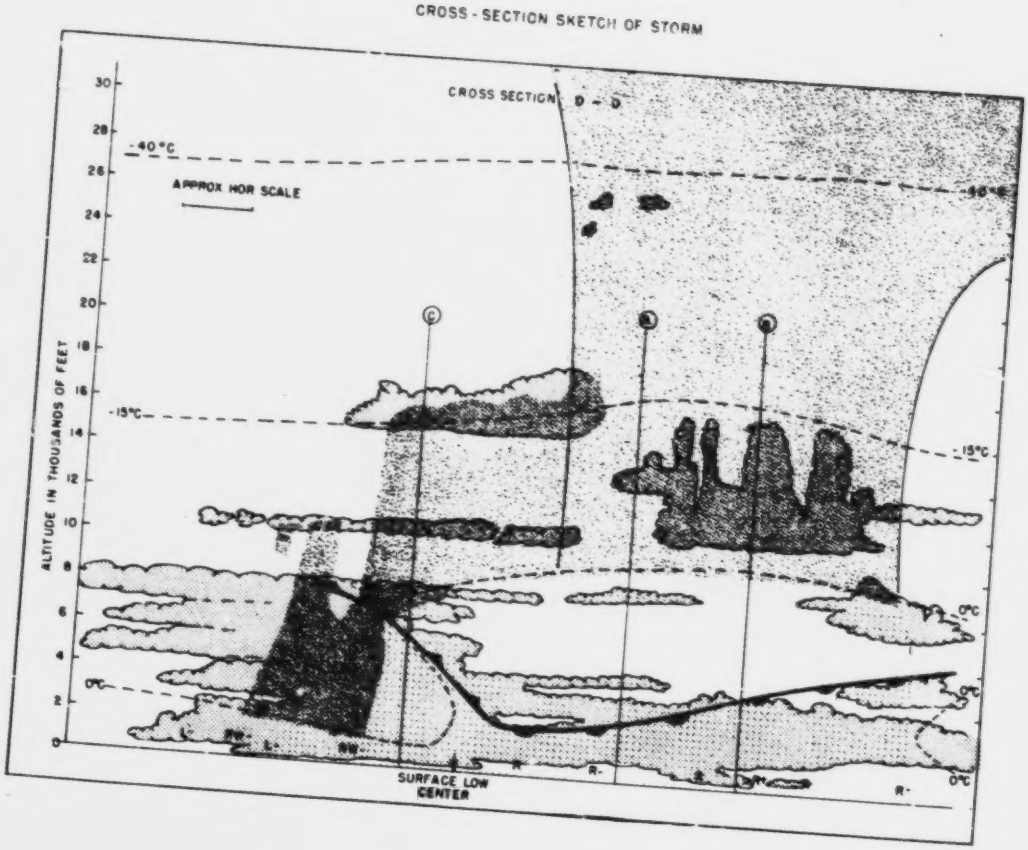

Figure 1.5.--Cross-section along the path DD of Fig. 1.4. The coarse stippling represents ice crystals or snow, the dense stippling represents liquid water cloud, the widely-spaced fine dotting represents rain, the dark areas represent regions where both liquid water and snow exist. In Region B the cirrus stratus is seeding the tall cumulus clouds which have relatively low liquid water content. Particles grow fairly rapidly under these conditions, and it is a region of moderate and heavy steady rain. In Region A there is no longer any strong vertical motion at intermediate levels. A balance is reached between the rate of cooling of an individual ascending air parcel and the rate at which water is being removed by the growing particles. Therefore, the humidity lies between ice saturation and water saturation. In Region C, near the southern edge of cirro stratus cloud, alto cumulus clouds are seen moving into the snow cloud at 17,000 and 11,000 feet. These clouds are apparently being rapidly depleted, perhaps contributing to some of the final heavy rain showers of the system.

BEST DOCUMENT AVAILABLE

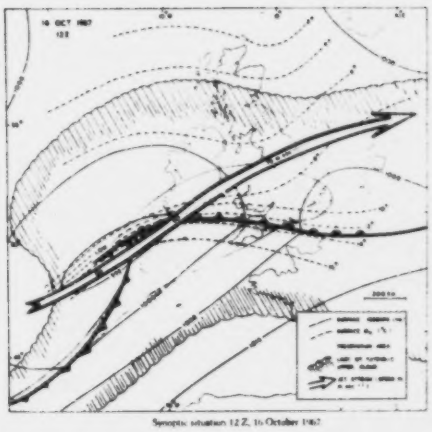

Figure 1.6.--A frontal wave system over the British Isles resembling that shown in Fig. 1.4. This system was analyzed by Browning and Harrold (1969) using a Doppler radar, located at Pershore (labeled P) as an important element in their observational program.

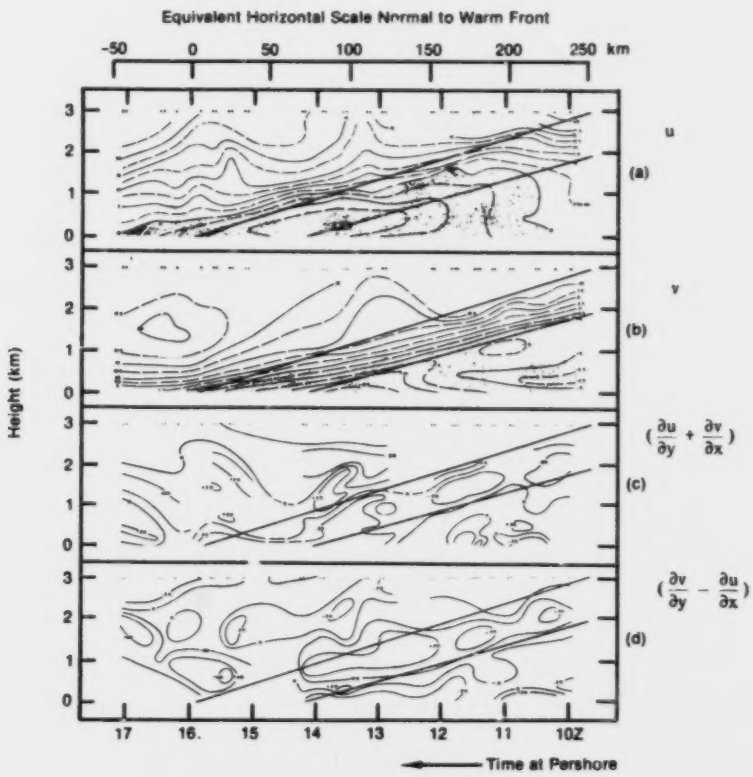

Figure 1.7.--Time-height cross-sections of basic wind field data in the vicinity of the front shown in Fig. 1.6. Data were obtained using a Doppler radar. Frames (a) and (b) show the u and v components of horizontal wind where u is parallel to the warm front and v is the wind component perpendicular to the front. Frames (c) and (d) show the fields of divergence and stretching deformation calculated from the radar data. The two solid lines indicate the warm frontal zone.

BEST DOCUMENT AVAILABLE

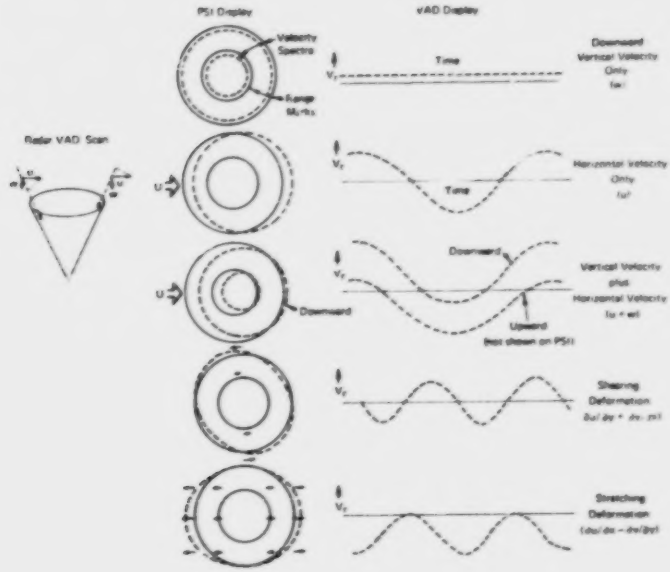

Figure 1.8.--Schematic illustration of how a Doppler radar is able to measure the various quantities indicated on the right-hand side of the figure. The radar uses a conical scan called velocity-azimuth-display (VAD). Such a scan also can be used for a plan-shear-indicator display (PSI) shown to the left of the VAD and described further in the text. The scan used in this kind of operation is shown schematically at the far left; the radar points more-or-less vertically and its scan describes a conical surface.

by the solid circles) is a measure of the component of target velocity toward, or away from the radar. Not only can harmonic analysis of the time series produced by VAD scans provide mean velocity, but spatial gradients of velocity over the diameter of the cone scanned by the radar can be deduced (Browning and Wexler, 1966). Furthermore, this information is produced continuously in time. If the targets are precipitation particles, the quiet-air fall-velocity creates difficulties in interpretation because it cannot be unambiguously separated from the clear air vertical velocity component. For clouds this is not a major problem. To see how the technique is implemented, write the x, y, z components of velocity as

$$u = u_o + x\frac{\partial u}{\partial x} + y\frac{\partial u}{\partial y} \quad \ldots$$

$$v = v_o + x\frac{\partial v}{\partial x} + y\frac{\partial v}{\partial y} \quad \ldots \qquad (1\text{-}6)$$

$$w = w_o + x\frac{\partial w}{\partial x} + y\frac{\partial w}{\partial y} \quad \ldots$$

BEST DOCUMENT AVAILABLE

where $r = (x^2 + y^2 + z^2)^{1/2}$ is range. In spherical coordinates $x = r\cos\theta\sin\phi$, $y = r\cos\theta\cos\phi$, $z = r\sin\theta$ so the radial velocity in spherical coordinates is

$$v_r = u\cos\theta\sin\phi + v\cos\theta\cos\phi + w\sin\theta \tag{1-7}$$

Using the identify $\sin^2\phi = (1/2)(1-\cos 2\phi)$, one readily finds

$$v_r(\phi) = u_o\cos\theta\sin\phi + v_o\cos\theta\cos\phi + (w_o + x\frac{\partial w}{\partial x} + y\frac{\partial w}{\partial y})\sin\theta$$

$$+ (1/2)r\underbrace{(\frac{\partial u}{\partial x} + \frac{\partial v}{\partial y})}_{\text{div}}\cos^2\theta + (1/2)r\underbrace{(\frac{\partial u}{\partial y} + \frac{\partial v}{\partial x})}_{\text{stretch. def.}}\sin 2\phi + (1/2)r\underbrace{(\frac{\partial v}{\partial y} - \frac{\partial u}{\partial x})}_{\text{shear def.}}\cos 2\phi$$

so the measured v_r has been expressed in terms of the divergence, stretching deformation and shearing deformation, and the mean velocity over the area scanned. If a harmonic analysis of the record of $v_r(\phi)$ is carried out, the coefficients are evaluated as

$$A_o = \frac{1}{2\pi}\int_{-\pi}^{\pi} v_r(\phi)d\phi,$$

$$A_n = \frac{1}{2\pi}\int_{-\pi}^{\pi} v_r(\phi)\cos n\phi\, d\phi,$$

$$B_n = \frac{1}{2\pi}\int_{-\pi}^{\pi} v_r(\phi)\sin n\phi\, d\phi$$

and it is found that

<u>mean wind</u>

$$u_o = A_1/\cos\theta,\ v_o = B_1/\cos\theta \tag{1-9a}$$

<u>horizontal divergence</u>

$$\frac{\partial u}{\partial x} + \frac{\partial v}{\partial y} = \frac{2}{r\cos^2\theta}[A_o - (w_o + x\frac{\partial w}{\partial x} + y\frac{\partial w}{\partial y})\sin\theta] \tag{1-9b}$$

<u>stretching deformation</u>

$$\frac{\partial u}{\partial x} - \frac{\partial v}{\partial y} = 2A_2/r\cos^2\theta \tag{1-9c}$$

<u>shearing deformation</u>

$$\frac{\partial u}{\partial y} + \frac{\partial v}{\partial x} = 2B_2/r\cos^2\theta\ . \tag{1-9d}$$

BEST DOCUMENT AVAILABLE

Equation (1-9b) demonstrates the fact that divergence and vertical motion are not independent. In fact, if the target fall velocity is zero, so that w consists only of air motion, the mass conservation relationship (the anelastic approximation) $\mathrm{div}(\rho \underset{\sim}{v}) \cong 0$ so that $\partial \rho w/\partial z = -\mathrm{div}_H(\rho \underset{\sim}{v})$, where div_H is horizontal divergence. Therefore, a good approximation to w_o can be found by integrating the product of $\mathrm{div}_H \underset{\sim}{v}$ and background density upward from a lower boundary at which w_o will be zero if the boundary is a horizontal plane. Also, the horizontal gradients of w can usually be neglected. Furthermore, the scan mode of the radar can include a vertically pointing position so that an independent measure of w_o can be obtained. Then (1-9b) gives

$$\frac{\partial \rho w}{\partial z} - \frac{2\tan^2\theta}{z}\rho w + \frac{2A_o\rho(z)}{z\sin\theta}\tan^2\theta = 0. \qquad (1\text{-}10)$$

Let $\rho w = W$ and $Z = \ln z$, then the differential equation to be solved is just

$$\frac{dW}{dZ} - \underbrace{(2\tan^2\theta)}_{a}W + \underbrace{\frac{2\tan^2\theta}{\sin\theta}}_{b}\underbrace{A_o(z)\rho(z)}_{f(z)} = 0$$

which is an ordinary, linear, but inhomogeneous, differential equation. It follows that the solution is:

$$W = be^{aZ_2}\int_{Z_1}^{Z_2} e^{-aZ}f(z)dZ.$$

Suppose f(z) is chosen to be its average value $\bar{f}$ in the interval Z_2 to Z_1. Then

$$W(Z_2) - W(Z_1) = -be^{aZ_2}\bar{f}[e^{-aZ_2} - e^{-aZ_1}].$$

Transforming back to w and z, the solution of Eq. (1-10) gives

$$\frac{2\Delta\rho}{\bar{\rho}} = \frac{w_2-w_1}{w_2+w_1} + \frac{2\bar{A}_o\tan^2\theta[(z_2/z_1)^{2\tan^2\theta}-1]}{w_2+w_1}.$$

From the equation of state,

$$p = \rho RT$$

where R is the gas constant of air and p is pressure. Taking the logarithmic derivative,

$$\frac{dp}{p} = \frac{d\rho}{\rho} + \frac{dT}{T}$$

BEST DOCUMENT AVAILABLE

and, from the hydrostatic equation $dp = -\rho g dz$, so

$$-\frac{g}{R\bar{T}}\,dz \cong \frac{d\rho}{\rho} + \frac{dT}{\bar{T}}\,.$$

Therefore

$$-\frac{T_2-T_1}{\bar{T}} = +\frac{g}{R\bar{T}}\,\Delta z + \frac{w_2-w_1}{2\bar{w}} + \frac{2\bar{A}_o}{2\bar{w}}\,\tan^2\theta[(z_2/z_1)^{2\tan^2\theta}-1]. \qquad (1\text{-}11)$$

The radar can measure w, $\bar{A}_o$, and Δz; in principle it therefore senses $\Delta T/\bar{T}$ to some extent.

Figure 1-7 shows the results of a divergence analysis and deformation analysis in a frontal zone using a single Doppler radar, but there is some uncertainty because the precipitation targets were falling. However, a cloud sensing radar could have provided unambiguous results in the non-precipitating cloud field. Figure 1-9 shows the time-height distribution of the precipitation echo in the frontal zone where the heavy solid curve delineates the depth of the radar echo and the thin solid curves are the reflectivity-weighted particle fall velocity (V_f) estimated from the Doppler radar. The figure shows a pronounced oscillatory character apparently well correlated with the surface rainfall and also correlated with the hatched areas which represent regions where clusters of precipitation-generating ice streamers were located suggesting that the slanting virga were seeding the underlying clouds. The areas of streamers were about 50 km across; the period of the storm oscillation was about 1 hour.

In recent years combinations of several Doppler radars have been particularly useful in providing a new insight into the spatial structures of the smaller storm cells (e.g., Lhermitte and Miller, 1970; Miller and Strauch, 1974; Doviak, 1977). In multiple radar configurations radars provide the best known method of observing the three dimensional wind fields within storms and they thus reveal the kinematic structure to complement the microphysical structure of cloud and storm systems. Figure 1-10 combines the dual-Doppler radar observations of the reflectivity and kinematic structure of a storm in northeastern Colorado with a classical reflectivity pattern observed in a storm near Wokingham in the U.K. taken from Browning and Ludlum, 1962. Some terms introduced by radar meteorologists into the literature on severe storms are identified in the upper frame and can be compared with the kinematic features in the lower frame. These features include the wall, the forward overhang, the echo-free vault, and the echo top. The reflectivity

BEST DOCUMENT AVAILABLE

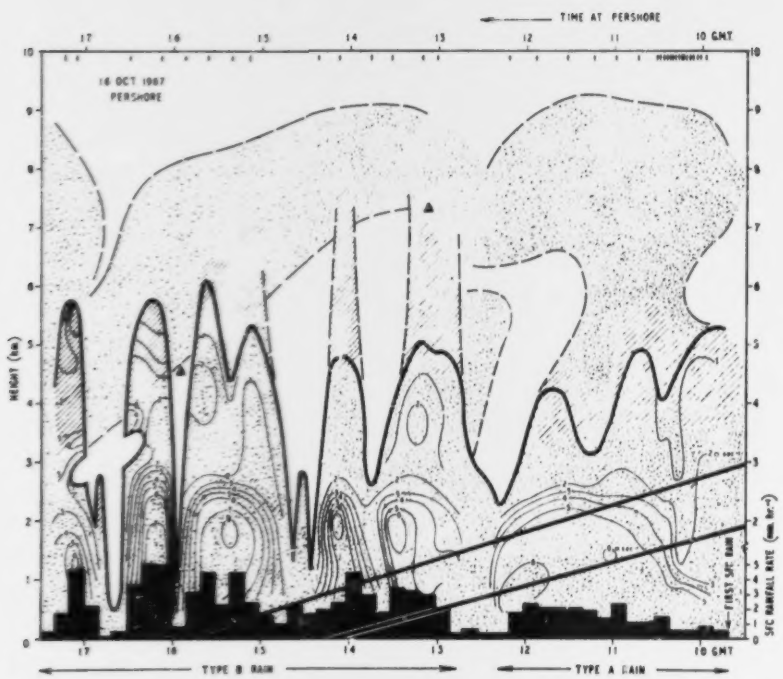

Figure 1.9.--Time-height section showing the vertical distribution of precipitation echo in the vicinity of the warm front shown in Fig. 1.6. The warm frontal zone is indicated by the two straight lines. The heavy solid contours represent the extent of echo detected by the Doppler radar when its antenna was pointed vertically. The thin solid isopleths at intervals of 1 m s^{-1} represent the reflectivity-weighted mean particle fall speed measured by the radar. The melting level is located at the height where the fall speed changes sharply from 2 to 5 m/s. The heavy dashed contours represent the upper extent of relatively weak echoes at higher levels. Areas where clusters of precipitation generators were observed are shown hatched. Surface rainfall rate is plotted as a block histogram at the bottom of the figure.

BEST DOCUMENT AVAILABLE

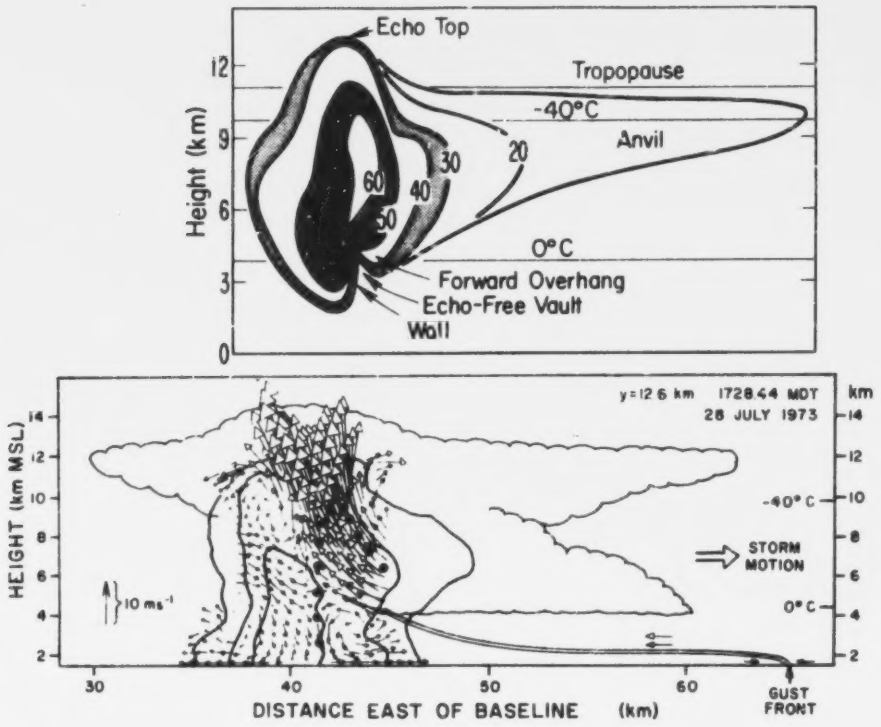

Figure 1.10.--Top frame - Pattern of radar reflectivity observed by Browning and Ludlum (1962) contours are in decibels of reflectivity factor dBZ. Some terms introduced into severe storm studies by the use of radar are shown on the drawing. Lower frame - Doppler radar-observed velocity fields in the plane parallel to the motion of a storm. Solid dots show calculated hail trajectories. Double-lined curve is schematic picture of probable gust front. The y coordinate is perpendicular to the direction of storm motion. The wind fields have been obtained using a pair of radars separated by a known baseline (see Chapter 7). Each radar scans the storm volume during the same time interval. Vertical velocity is obtained by requiring that mass continuity be satisfied. The wind fields, from Kropfli and Miller (1976), are the residuals after removal of the mean echo motion.

contours (solid curves, top and bottom) are in decibels of reflectivity factor (dBZ). Radar reflectivity is closely related to particle size and therefore to fall velocity, rain rate, and particle type, and the literature has many relationships between Z and R, Z and V_f, and Z and D, where R is rain rate, V_f is particle fall velocity and D is particle size. The reflectivity factor

$$Z = \sum N_i D_i^6$$

is the sum of the contribution to radar backscatter of all the particles per unit volume, where N_i is the number of particles of diameter D_i; it is usually

given in units of mm^6/m^3. In Fig. 1-10 it is expressed in decibel units called dBZ where 1 mm^6/m^3 = 0 dBZ. Reflectivity factors greater than 50 dBZ usually imply that hail is present. The solid circles in the top frame show the calculated hail trajectory. The myriad reflectivity relationships have been mainly developed for precipitating systems which are not the direct concern here where clouds are of primary interest. Figure 1-11, from Kropfli and Miller (1976) shows the trajectories of parcels moving through the same storm as shown in Fig. 1-10, assuming the storm to be essentially in steady state at that stage. The picture revealed by Doppler radar allows many important quantities to be calculated that were previously only available from sparse aircraft penetrations. These quantities are shown in Table 1-3 taken from Kropfli and Miller (1975). The radar observations suggest details of recirculation capable of producing the various classes of hydrometeors found in clouds, including hail.

A Little Cloud Physics - Some Definitions and Nomenclature

A cloud is typically made up of drops about 10 μm in diameter and with a number density of 50-1000 cm^{-3}. Their structure is generally colloidally stable, and individual droplets show little inclination to grow. However, when instability of the drop population does occur, some drops grow at the expense of others and precipitation takes place.

Probably the most important challenge in cloud physics is the understanding and prediction of the processes that cause a cloud to become unstable and precipitate. Processes that have been proposed and studied are:

1) electrical charge differences between particles,
2) aerodynamic attraction between particles falling at nearly the same speed,
3) capillary forces between particles of different sizes,
4) temperature differences between particles of different origin,
5) collisions due to differing fall velocities and to turbulence, and
6) growth of ice particles in a medium supersaturated with respect to ice, i.e., for water drops at saturation, the supersaturation with respect to ice is about 10% at -10°C and about 20% at -20°C.

They are listed in approximate reverse order of their importance according to current opinion, and they will be considered in that order.

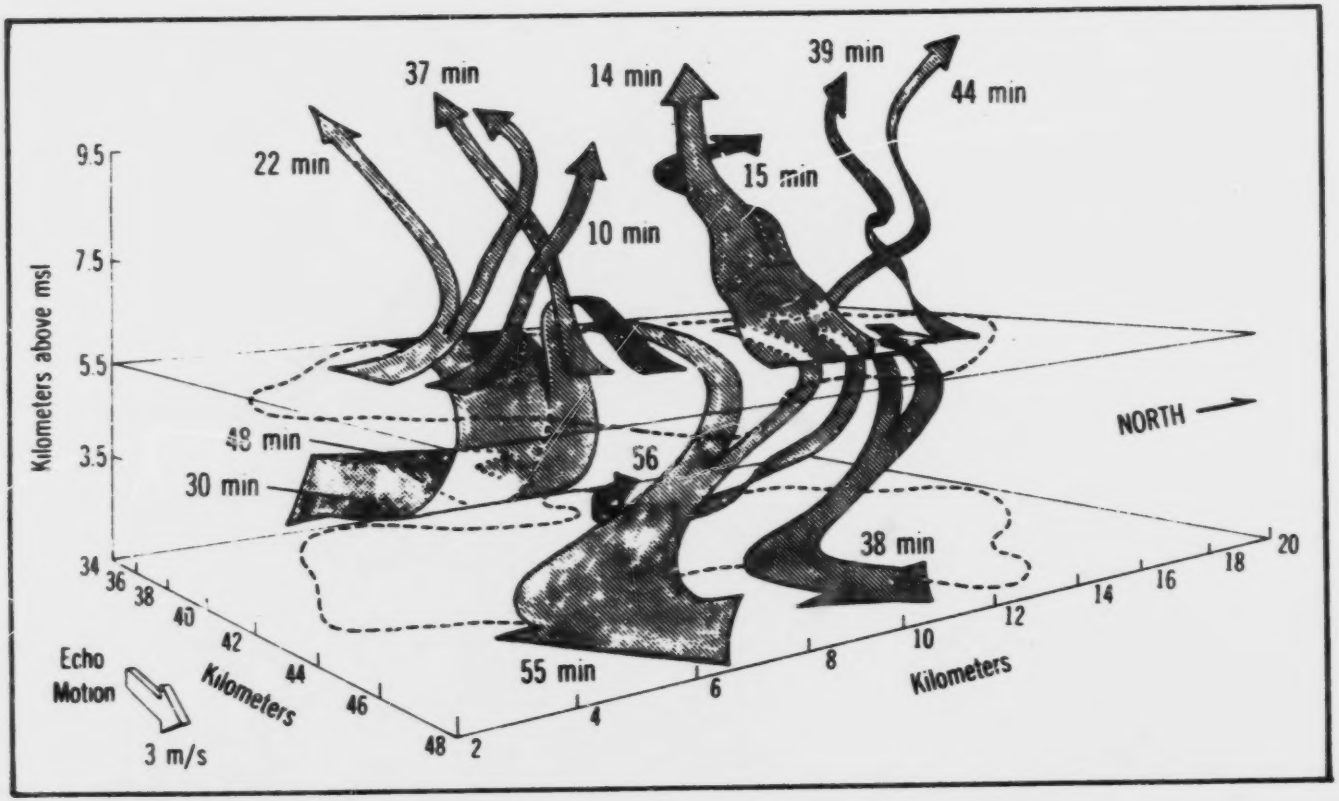

Figure 1.11.--Trajectories of parcels entering the storm shown in Fig. 1.10 at a level of 4 km. The time spent by the parcel within the storm system is indicated by the time in minutes shown for each arrow. (Kropfli and Miller, 1976.)

BEST DOCUMENT AVAILABLE

BEST DOCUMENT AVAILABLE

TABLE 1-3

Quantity	Doppler Radar Result	Published Value	Source*
Updraft mass flux at 8.5 km (F_m)	190×10^9 g/s	335×10^9 g/s	1
Downdraft mass flux at 3 km	-220×10^9 g/s		
Updraft energy flux	1.9×10^{11} cal/s		
Updraft vapor flux	1.4×10^9 g/s	3.4×10^9 g/s	1
Updraft area	75 km^2	85 km^2	1
Downdraft area	87 km^2		
Precipitating volume (>20 dBZ)	2.4×10^3 km^3		
$\overline{\zeta w}$ (vorticity flux)	1.8×10^{-3} m/s^2		
Storm kinetic energy	6.2×10^{13} cal	6.2×10^{14} cal	2
Environment kinetic energy	2.6×10^{12} cal		
Mean updraft speed	3.8 m/s	4.4 m/s	1
Mean downdraft speed	-1.2 m/s		
Flux of eastward momentum ($\overline{\rho uw}$)	-6.2 Newton/m^2		
Flux of northward momentum ($\overline{\rho vw}$)	1.3 Newton/m^2		
Updraft entrainment rate $\frac{1}{F_m}\frac{dF_m}{dz}$	2.6% km	4.1% km	3

* 1. Auer and Marwitz (1968) - 8 northeast Colorado storms.
2. Sellers (1972) - average summer storm.
3. Squires and Turner (1962) - updraft jet model.

It has been known for many decades that water droplets do not form in a clean laboratory environment until high supersaturation is reached. On the other hand clouds are known to form in the atmosphere at about saturation. The answer to this enigma is that the atmosphere is not a clean environment but contains tiny particles called cloud condensation nuclei (CCN) which serve as centers for condensation. This process is called heterogeneous nucleation. The process by which water droplets form directly in a clean environment is called homogeneous nucleation and is not important in nature. All processes involving a change of phase are called nucleation processes.

There are a wide variety of CCN of all sizes in the atmosphere at all times. They range in size from very large particles (>10 μm) which tend to form the nuclei of clouds to sizes of only a fraction of a micrometer. The typical size-number density distribution of the various classes of nuclei are summarized in Fig. 1-12 adopted from a classical study by Junge (1952). When a parcel of air is lifted it is cooled adiabatically. As it approaches saturation the more hygroscopic nuclei become centers of condensation, and visibility may become noticeably reduced at relative humidities much below saturation. If the relative humidity is greater than 100%, the atmosphere is said to be supersaturated and the percent excess above 100% is the degree of super-saturation. Because of the large number of CCN in the real atmosphere, condensation occurs before the supersaturation becomes excessive in the bulk atmosphere. However, on the micro-scale the thermodynamic relaxation time is large enough so that significant overshoot can produce relatively large supersaturation locally.

When an air parcel rises above the 0° isotherm the water droplets become supercooled. Once again laboratory experiments show that pure water droplets do not freeze above a temperature of -40°C. This is called homogeneous freezing. However, in the presence of nuclei, freezing temperatures may not be much below 0°C. Unlike the CCN, the ice nuclei are relatively rare. It is this fact that makes artificial seeding of the environment feasible — it is possible to alter the natural environment to a significant degree as far as the population of ice nuclei is concerned.

It was first pointed out by Bergeron (1933) that the all-important cause of colloidal instability is the co-existence of water droplets and ice within the cloud because there is considerable difference in saturation vapor pressure over ice and over water at the same temperature. Thus the water evaporates from the water drops and sublimes onto the ice particles. This process is most efficient at about -15°C. The individual drops then continue to grow

BEST DOCUMENT AVAILABLE

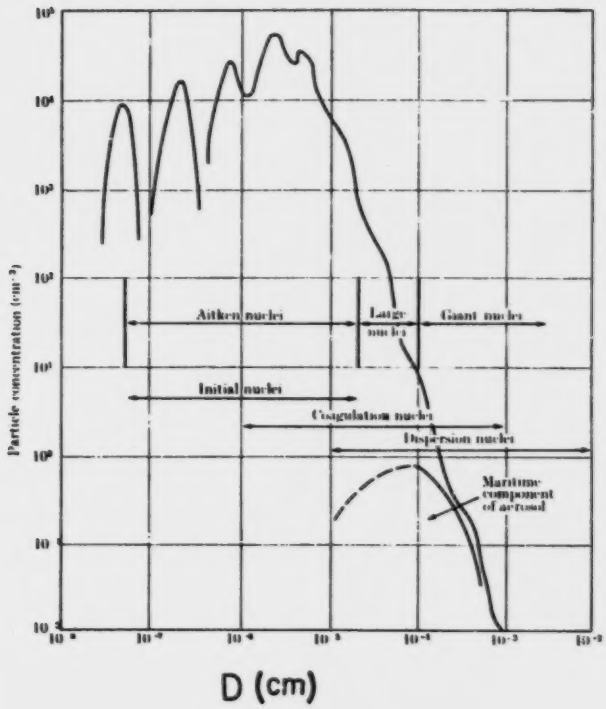

Figure 1.12.--The size distribution of naturally occurring aerosols in heavily populated air over land. (Junge, 1952.)

until they fall from the cloud or are broken up by collisions. Graphic evidence supporting this mechanism is the suddeness with which cumuli can be transformed into cumulo nimbi when glaciation occurs in the upper regions of the cloud. The final proof of the importance of the Bergeron mechanism came with the success achieved in artificially seeding natural clouds with dry ice and producing precipitation.

The other important process causing precipitation is drop collision and coalescence. This process can occur at any temperature and is therefore of dominant interest in warm clouds in which the Bergeron process is ineffective. A droplet falling through a population of smaller drops will have a very low probability of colliding with other drops unless its radius is larger than about 20 μm. Therefore, for a cloud to be unstable by this process it must contain some larger droplets. The critical size for continued growth is determined by the balance between growth processes and decay processes. The equilibrium vapor pressure over a water drop depends not only on its temperature but on its curvature (or radius) as well. That is, the saturation vapor pressure over a drop of radius r and temperature T is

BEST DOCUMENT AVAILABLE

$$e_s(r)/e_s(\infty) = \exp(2\sigma/rR_v\rho_L T) \qquad (1\text{-}12)$$

where σ is surface tension, R_v is the gas constant for water vapor, ρ_L is density of liquid water and $e_s(\infty)$ is the saturation vapor pressure above a plane water surface. Therefore, if a given supersaturation is inserted as the left-hand side of the equation, a critical value of r is defined such that drops of larger size will continue to grow by condensation from the environment, while smaller droplets will evaporate. The power backscattered from incident radar waves is very sensitive to drop size so that radars with appropriate wavelengths can be very sensitive monitors of the drop growth stability conditions that exist within a cloud.

The population of hydrometeors found in the atmosphere and the complicated processes of interaction that lead to their formation have been summarized by Braham and Squires (1974) in the diagram shown in Fig. 1-13. The balance between the many processes of growth and decay is very complicated, involving many nonlinear and irreversible interactions. Therefore, cloud physicists have recently achieved most progress by resorting to computer simulations. The process of entrainment and the proper introduction of the stochastic character of drop size growth and mixing into cloud models has perhaps been the most challenging task of the cloud physicist in the last decade.

1.2 Clear-Air Radar Returns

Review

There has been a recent upsurge of interest in the use of radar for clear-air studies. It is remarkable that such an old technique would find such a new area of application. The scientific community was slow to recognize and exploit the potential of radar for sensing the non-ionized clear atmosphere. Only in the last decade has significant attention been devoted to radar sensing of lower and middle atmospheric structures.

Since the early 1950's, the observational data and theoretical background were already available to predict the feasibility of ground-based radar systems capable of wind-sounding through the troposphere. The observational data base was provided by the tropospheric and stratospheric forward scatter measurements made over paths extending far beyond the optical horizon such as those reported by Ames et al. (1955) and reproduced on the left-hand

BEST DOCUMENT AVAILABLE

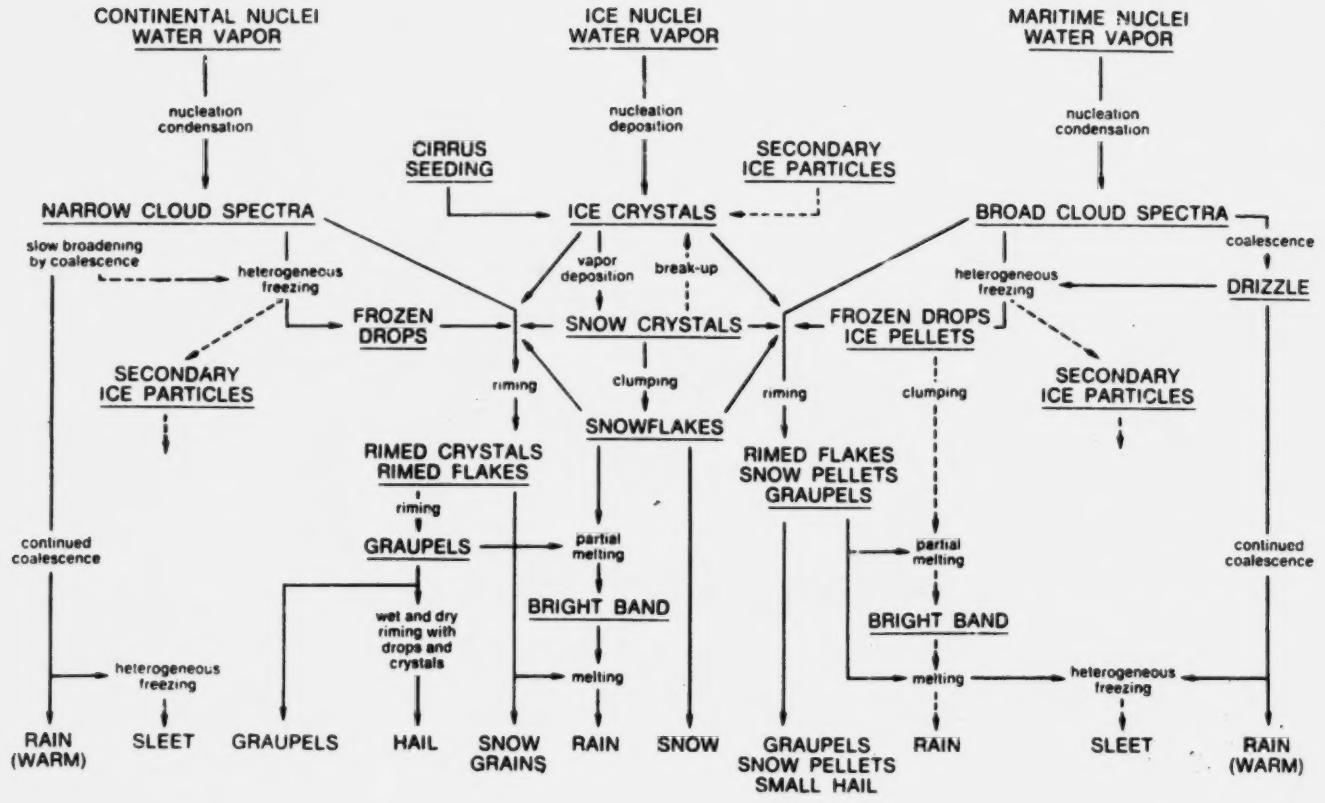

Figure 1.13.--The major types of precipitation elements and the physical processes through which they originate and grow. (Braham and Squires, 1974.)

frame of Figure 1-14. From such observations the height distribution of the reflectivity resulting from the turbulent fluctuations of refractive index can be deduced using the theory developed earlier by Booker and Gordon (1950). Expressed in terms of the parameters of modern turbulence theory, the result is shown in the right-hand frame of Figure 1-14, where C_n^2 is the structure constant for turbulent fluctuations of radio refractive index. From such information about atmospheric structure it would have been entirely possible to conclude in the 1950's that atmospheric sounding through the troposphere and into the stratosphere was practical and to design the radar system (power-aperture product) needed to carry out the experiments. (Actually, the troposcatter path data seem to lead to somewhat excessive values of C_n^2 aloft. This is probably a result of layering due to the normal stable stratification of the atmosphere.) However, no such program was undertaken, probably because the attention of a large percentage of the radar-oriented geophysicists of the day was directed toward the structure of the ionosphere. There appear to be two principal reasons for this: 1) Ionospheric structure was very important to prediction of the performance of HF radio systems. 2) Sounding of the lower atmosphere could be accomplished by balloon and therefore did not require the development of radar systems to do the job.

In the last decade or two, this situation has changed. Satellite communication has replaced HF communication in many areas of need, and research in ionospheric structure has therefore been significantly reduced. Thus, the attention of many radio-oriented geophysicists has been re-directed toward the lower atmosphere. In fact, somewhat to the embarrassment of radar meteorologists, the first radar wind-soundings of the clear stratosphere were made (at the suggestion of C. G. Little in 1967) by ionospheric physicists using an ionospheric research radar at Jicamarca, Peru (e.g., Woodman and Guillen, 1974).

However, the subject of radar returns from the clear air was not new to radar meteorologists (Hardy et al., 1966; Hardy and Katz, 1969). Since the advent of radar in the 2nd World War, mysterious returns from regions where there were apparently no targets had been noted, and a large literature exists on the subject of "angels," "ghosts" and "pixies." The controversy usually centered on the question of whether they resulted from refractive index fluctuations or from birds and insects. The situation at the time was well summarized by Plank (1956). In some cases layer structures in the troposphere had apparently been detected (Lane and Meadows (1963), and the tropopause was sometimes seen (Atlas et al., 1966). Insects and birds were sometimes identified (Glover and Hardy, 1966). However, it wasn't until the

BEST DOCUMENT AVAILABLE

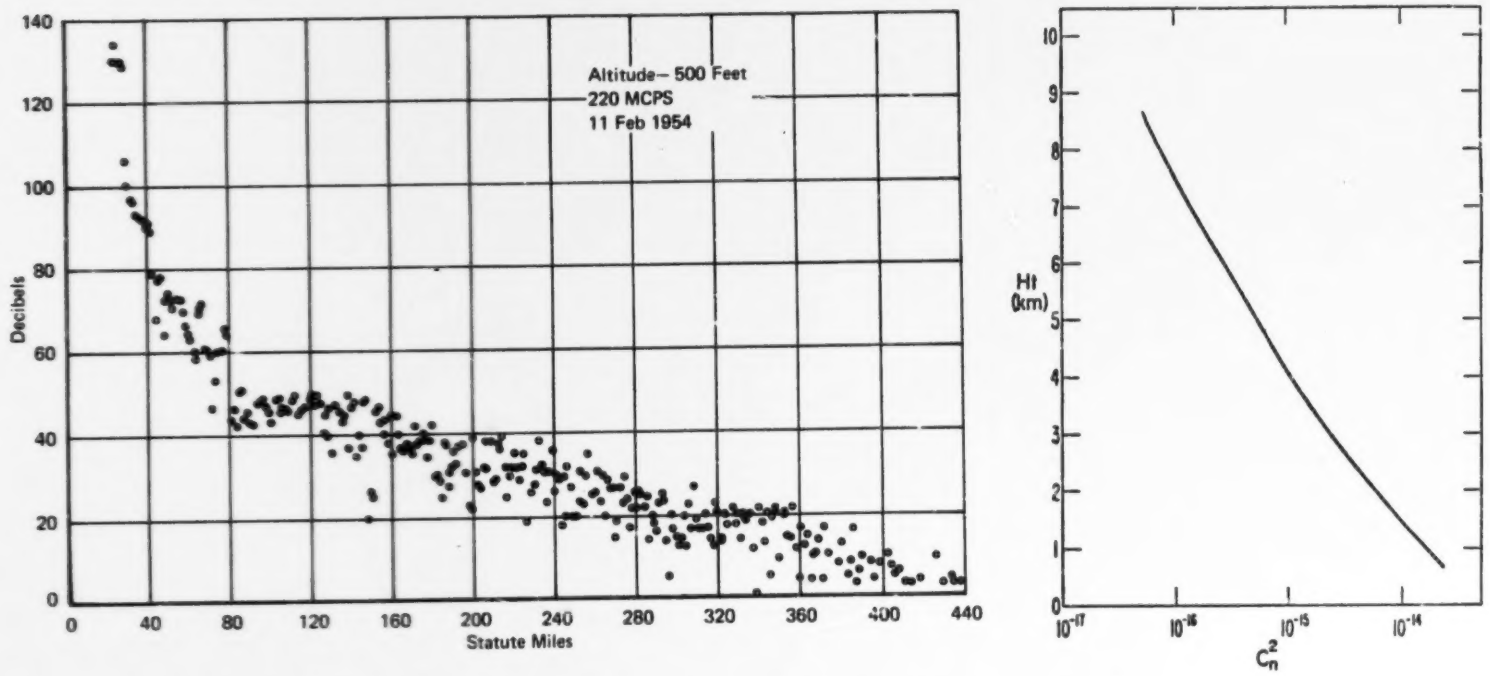

Figure 1.14.--Left: Decibels of power in relative units received from a coastal transmitter by an aircraft flying at 500 ft altitude away from the coastline. The purely scattered field begins about 80 miles from the transmitter where the rate of decrease of signal with distance becomes much less than the diffracted field found between 30 and 50 miles. Right: The height distribution of refractive index structure parameter deduced from the rate of decrease of scattered power in the left frame if the field results from Bragg scatter from the clear air.

development of an atmospheric radar capable of observing targets at very short ranges with very high resolution (the FM-CW radar, Richter, 1969), that the situation was really clarified. It was then revealed that both clear-air and insect radar returns are very important (see Fig. 1-15); their relative importance depends on season, altitude, time-of-day and climatological regime. In the early 1970's special sensitive radar systems were developed and exploited for clear-air observation (Dobson, 1970, Browning et al., 1972, Richter et al., 1972).

A final reason for the increased interest in the use of radar in the clear lower atmosphere is the dawning realization that present weather prediction methods and models have gone about as far as they can go without new observational quantities and techniques, and without greater spatial and temporal density in sounding data. Ground-based radars offer the possibility of immediate improvement in temporal density of wind sounding data. They also provide new observables to the meteorologist such as profiles of horizontal mass-divergence and turbulent dissipation rate. They can provide a crucial observational link between troposphere, stratosphere, mesosphere and ionosphere by observing the wind field across the various domains and establishing the degree of coupling from the solar-dominated ionosphere down to the dynamically, meteorologically important lower atmosphere.

Refractive Index of the Clear Atmosphere

The main cause of radar returns from the clear-air has now been well established to be the inhomogeneities in refractive index that result from turbulence. The radio refractive index at commonly used radar wavelengths is nondispersive and depends on the atmospheric temperature, humidity and pressure.

The various quantities used by the radio propagation community to represent refractive index in the atmosphere have been discussed by Bean and Dutton (1966). By definition, $N = (n-1) \times 10^6$ where n is radio refractive index. For microwave wavelengths that are not near gaseous absorption lines it is found that

$$N = \frac{77.6}{T} \left(P + \frac{4810\ e}{T}\right) . \qquad (1\text{-}12)$$

However, we will usually be more concerned with a closely related quantity called potential refractive index defined as

BEST DOCUMENT AVAILABLE

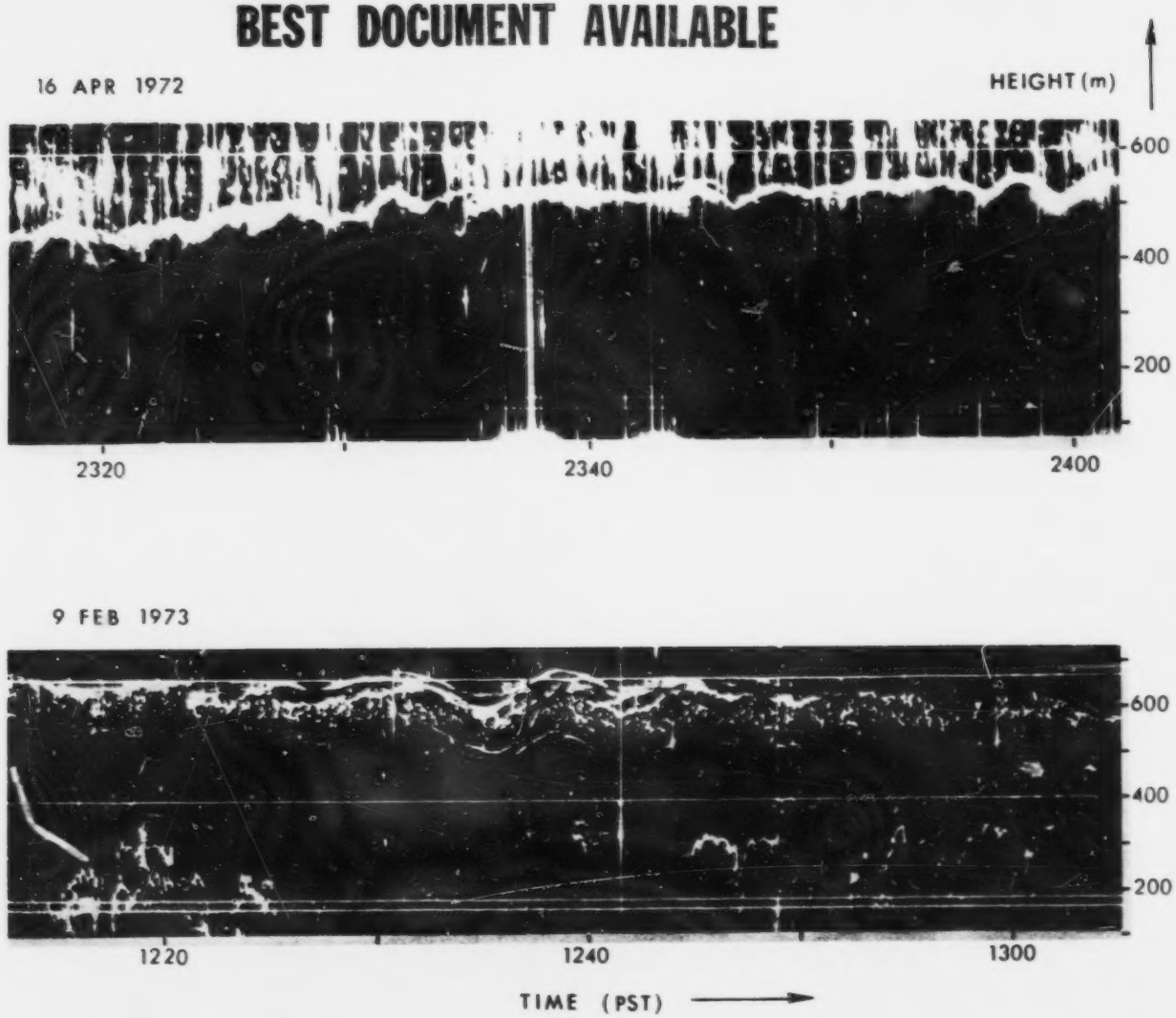

Figure 1.15.--Clear-air backscatter observed with a vertically pointing FM-CW radar at San Diego. Bragg backscatter from convective features in the boundary layer and from an elevated inversion is illustrated by the diffuse laminar type of return. The dots and vertical streaks result from particulate targets such as insects and birds. The horizontal straight lines are range markers.

$$\phi = \frac{77.6}{\theta} \left(1000 + \frac{4810\ e_p}{\theta}\right), \qquad (1\text{-}13)$$

where T is temperature (K), p is pressure (mb), e is vapor pressure (mb), θ is potential temperature and e_p is potential vapor pressure. Clearly the distribution of temperature and humidity largely determines the refractive index distribution; thus the exchange of heat between the lower atmosphere and the land or sea boundary, and the evaporation/condensation of moisture at the boundary, are the important processes. Various relationships between N and ϕ are derived in Appendix 3.

Because the radio refractive index varies with height, radio waves propagate on curved paths and methods of describing this effect by artificially modifying the refractive index have been developed. Therefore another quantity used to represent radio refractive index is the modified refractive index, M, whose effect is essentially to give an artificial upward curvature just equal to the curvature of the earth to horizontally propagating rays. Thus ray patterns of radio energy propagation can be plotted on diagrams in which the earth is a flat lower boundary. This greatly simplifies the mechanics of plotting and the interpretation of the diagrams in terms of ducting. More will be said of M in Chapter 9 when the formation of radio ducts is discussed. Here we just point out that it is related to N as

$$M = N + 0.157\ z \qquad (1\text{-}14)$$

where z is height in meters.

A parameter B is defined such that radio rays propagating in a "standard" atmosphere are straight lines. Thus, in this kind of plot, the earth is curved, but the rays are straight if the atmosphere is "standard." In this definition of B, "standard" means an atmosphere in which horizontally launched rays are bent downward with a radius of curvature 4/3 that of the earth's surface. In other words, the earth's radius is increased by a factor of 4/3 and the curvature of the rays of radio propagation is decreased by that amount thus straightening them out in this "standard" atmosphere. It is related to N as

$$B = N + 0.037\ z \qquad (1\text{-}15)$$

where z is height in meters.

BEST DOCUMENT AVAILABLE

The relationships between the various refractive index quantities are given in Fig. 1-16 along with a schematic picture of each profile through a surface refractive layer in an otherwise standard atmosphere. It is the height gradient of these quantities that must be considered when refraction and ducting of radar waves is considered. (Ducting occurs below the height at which dM/dz = 0 in Fig. 1-16.) The time-rate-of-change of the refractive index layer structure and layer undulations are the important classes of perturbation in these cases; the formation and fluctuation of holes and antiholes in ray patterns is the subject of a large body of literature and will not be considered here. A summary of ray tracing methods may be found in Bean and Dutton, (1966).

The backscatter, or radar reflectivity, is directly proportional to the turbulent structure constant of refractive index (C_n^2) which, in the inertial subrange of isotropic turbulence, is defined by the structure function given by

$$D(\ell) = \overline{[n'(r) - n'(r-\ell)]^2} = C_n^2 \, \ell^{2/3} \qquad (1\text{-}16)$$

where n is refractive index, primes indicate perturbation, r is position, and ℓ is the separation of two points at which n is being measured. The overbar

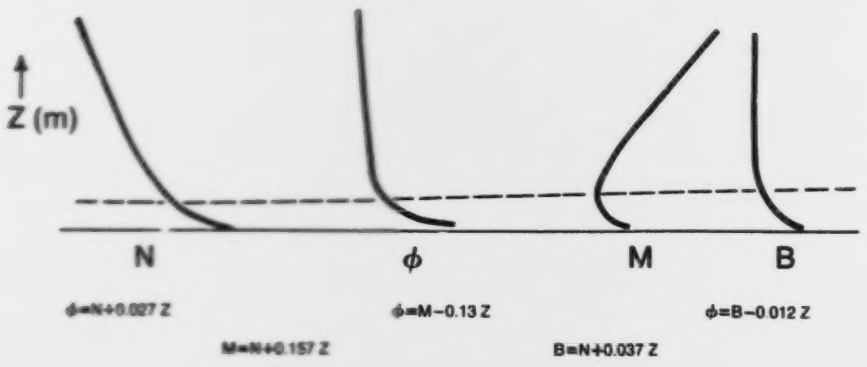

Figure 1.16.--Height distribution of some commonly used refractive index quantities shown schematically. By definition N = (n-1) x 10^6 where n is true radio refractive index. A horizontally-launched ray would exactly follow the earth's curvature at the height of the dashed line where dM/dZ = 0. This height is often called the duct height or duct thickness. The ducting of radar waves in the atmospheric boundary layer is discussed in detail in Chapter 10.

indicates time average. The relationship between radar reflectivity and C_n^2 was unambiguously established by Kropfli et al. (1968) in an experiment in which an aircraft carrying a microwave refractometer was tracked on one channel of a radar at Wallop's Island while the reflectivity immediately ahead of the aircraft was measured on another channel. The high correlation of backscatter with C_n^2 was further supported by measurements reported by Bean et al. (1972). The physics of this type of scatter resembles that of the X-ray scattering observed in crystals by Bragg and, is therefore, sometimes called Bragg scatter. A descriptive explanation of this type of scatter is shown in Fig. 17 for the general case of arbitrary incident and scattered waves. The formal theoretical development is given in Chapter 2. In contrast with incoherent backscatter from particulates described in Section 1.1, where the wavelength dependence is λ^{-4}, the wavelength dependence in Bragg scatter is $\lambda^{-1/3}$ for the turbulent perturbations obeying Eq. (1-16). The relative magnitudes of incoherent and Bragg scatter (solid and dashed lines respectively) are shown in Fig. 1-18. In backscatter the important scale of perturbation in the scattering medium is 1/2 the wavelength. For most radars this scale is smaller than is measurable by in-situ sensors. Therefore most in-situ measurements have sensed the longer scales, and the power in the $\lambda/2$ scale has been deduced by extrapolating the spectrum to the high wavenumbers (small scales). Observations of C_n^2 deduced from radar backscatter are reported by Gage and Balsley (1978), and by Chadwick and Moran (1980). A sample of the Chadwick/Moran observations is shown in Fig. 1-19. It illustrates the diurnal trend of C_n^2 and its large variability. The data are number of minutes in each hour that the backscattered power implied a C_n^2 in the indicated (logarithmically spaced) interval. FM-CW radar observations show that C_n^2 can get as large as 10^{-11} within thin layers as shown by Fig. 1-20 which we have adapted from Metcalf (1975) by converting his values of backscattered power to C_n^2. The various biological targets and C_n^2 lead to backscatter from a variety of meteorological features including the boundary layer, elevated layers and airmass discontinuities. Bean and Dutton (1966) have discussed the way the average refractive index varies with height, and Bean, Cahoon, Samson and Thayer (1966) have published a global climatology of the surface value and the scale height of an exponential fit to the height variation.

Air Masses

Source and formation

The convenient point to begin a discussion of atmospheric layering is with the concept of air masses — how they are formed and how they are modified with time and with spatial movement. An air mass is an extensive portion

BEST DOCUMENT AVAILABLE

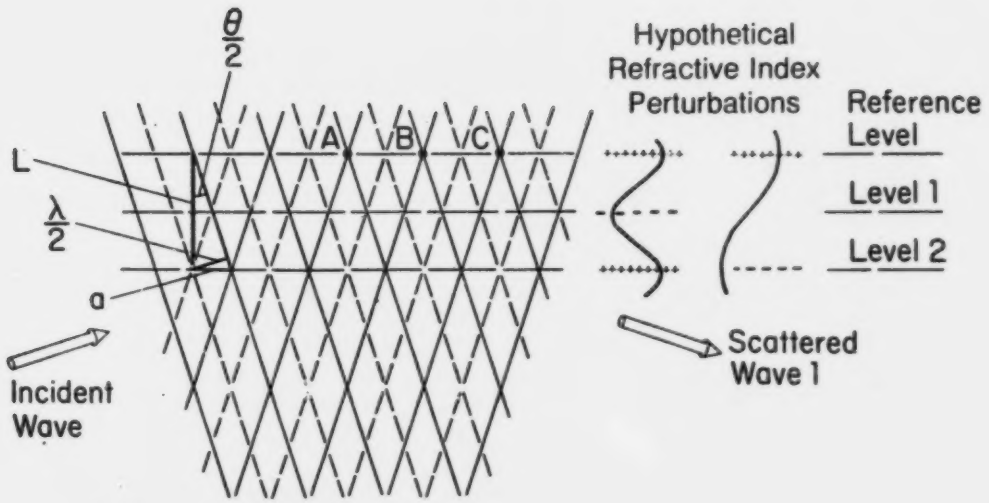

$$a = \frac{\lambda/2}{\cos\theta/2} = L\frac{\sin\theta/2}{\cos\theta/2}$$

$$L = \frac{\lambda}{2}\,\frac{1}{\sin\theta/2}$$

Figure 1.17.--Suppose an e.m. wave is incident on the Reference Level producing scattering at sample points A, B and C. Suppose the "crests" of the waves are represented by the solid lines and the "troughs" by dashed lines. Upgoing and downgoing waves are normal to the incident and scattered wave arrows respectively. Then for the upgoing and downgoing waves it is seen that crests coincide with crests and troughs with troughs at the Reference Level and at Level 2. However, crests coincide with troughs (that is they are out of phase) at Level 1. Therefore scattered waves from Level 2 will reinforce those from the reference level assuming that they have the same phase change on reflection at both levels. This will be the case if the refractive index perturbation is of vertical scale L, (left-hand set of ± symbols) because this means that the refractive index will be in its positive perturbation phase at Level 2 when the perturbation is positive at the Reference Level. If the scale of R.I. perturbation had been 2L, it would have been in its negative phase at Level 2 (right-hand set of ± symbols) and the reflection would therefore be phase shifted by 180° from the wave scattered by the positive perturbation at the Reference Level. Similarly, perturbations of L/4 will lead to waves out of phase in the scattering direction.

BEST DOCUMENT AVAILABLE

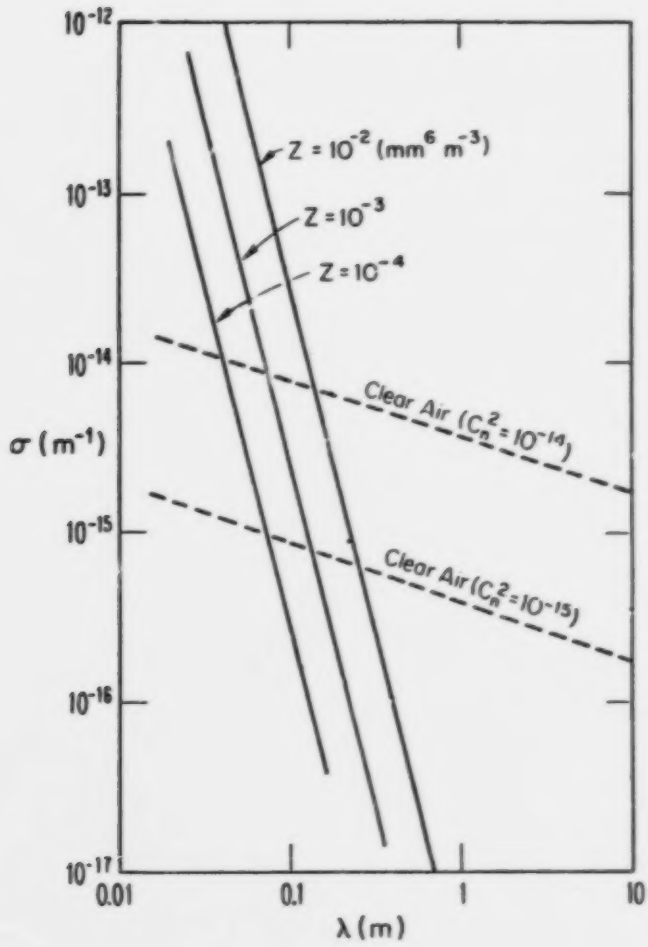

Figure 1.18.--Backscattering cross-section vs. wavelength for particulate scatterers (solid lines) and for Bragg backscatter (dashed curves). The radar reflectivity factor $Z = \sum_{i=1}^{i=\infty} N_i D_i^6$ where N_i is the number of drops of diameter D_i in a unit volume. The refractive index structure parameter C_n^2 is a measure of the turbulent fluctuations in n if the important scale ($\lambda/2$) lies within the inertial subrange of homogeneous isotropic turbulence.

BEST_DOCUMENT AVAILABLE

Figure 1.19--Histograms of number of minutes C_n^2 values lay within the indicated logarithmically spaced intervals (top scale) at a height of 805 m for a two day period as calculated from backscatter measured by a vertically pointing FM-CW radar reported by Chadwick et al. (1980).

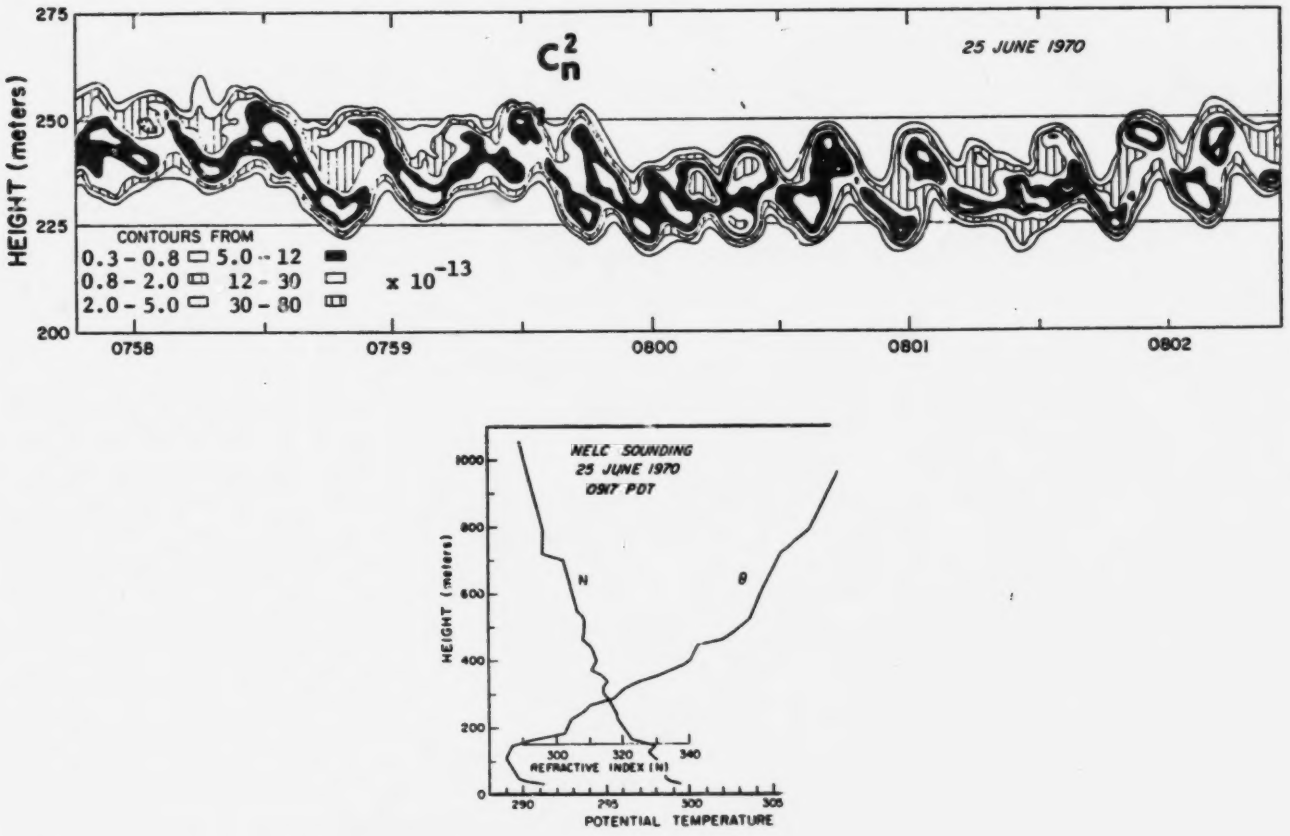

Figure 1.20.--Top frame: Fine structure of C_n^2 distribution in an elevated temperature inversion layer over San Diego as deduced from a vertically pointing FM-CW radar. Breaking wave structure suggests shear-induced dynamic instability in the layer. Bottom frame: Radiosonde soundings of radio refractive index and potential temperature. (Modified from Metcalf, 1975.)

BEST DOCUMENT AVAILABLE

of the earth's atmosphere with (approximate) horizontally homogeneous meteorological properties. Thus, the refractive index within an air mass can be considered to be approximately horizontally homogeneous and to have a vertical structure characteristic of its mode of formation, its movement and its relation to other adjacent or overlying masses of air. Air masses are characteristic of their various source regions. Such source regions are usually classified as primary or secondary. A primary source region is an extensive area favorable to air stagnation for appreciable periods of time. A secondary source region is one in which stagnation does not occur, but over which trajectories are so long that the air mass takes on the characteristics of the region through modification processes.

Figure 1-21 shows average height profiles of N in various Asian and North American air masses, and Fig. 1-22 shows similar profiles at specific locations in North America calculated by Gossard (1977) from averaged radiosonde temperature and humidity data published by Showalter (1939). It should be recognized that profiles such as these are not typical; the important layer structure has been largely erased by the averaging process. They should be treated as an ambient refractive index background on which appropriate layer structure should be superimposed according to the modification processes taking place locally.

Figure 1-23, adapted from Plank (1952), shows an example of the way the refractive index profile of an air mass is modified in its source region by outward radiation from the earth boundary and the compensating transfer of heat downward by conduction from the lower atmosphere. The surface boundary layer is therefore an important region through which transfer processes act to modify the overlying air masses. In Chapters 9 and 10 the transfer processes and the way they act to modify the refractive index structure of the overlying air, are considered in detail.

Air mass modification -- the surface layers

Air mass modification is primarily a result of two classes of processes:

1) Transfer of heat, moisture and momentum in response to changes in the underlying boundary.

2) Dynamical processes that cause convergence and divergence within the air mass.

BEST DOCUMENT AVAILABLE

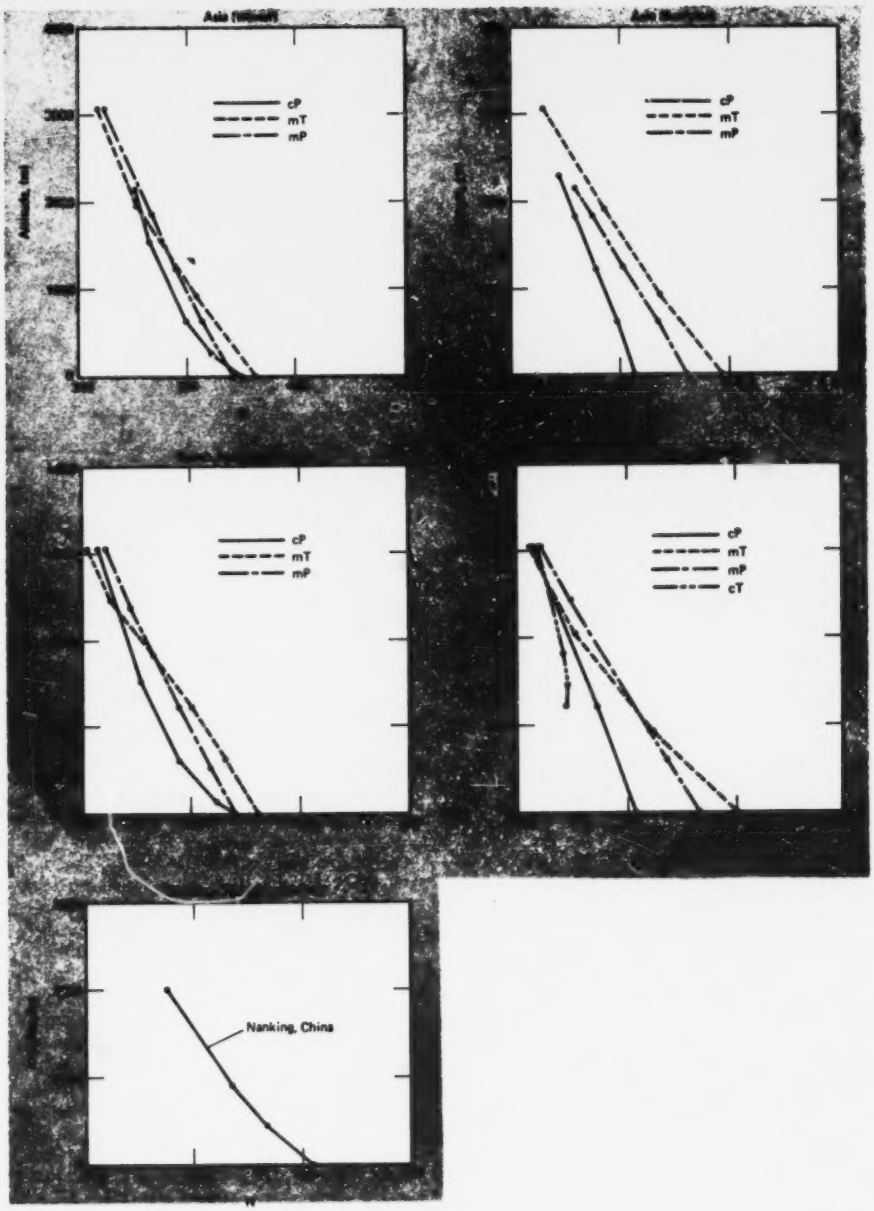

Figure 1.21.--Average refractive index distribution in some common airmasses in Asia and North America.

BEST DOCUMENT AVAILABLE

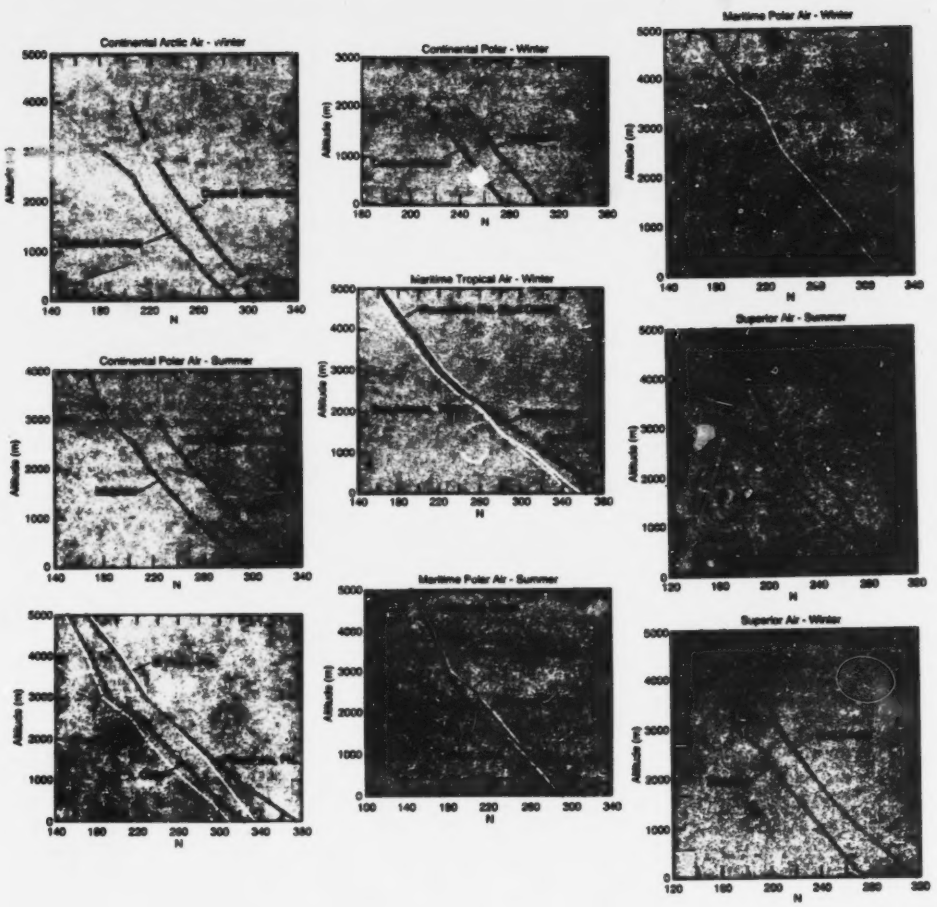
Continental Arctic Air - Winter
Continental Polar - Winter
Maritime Polar Air - Winter
Maritime Tropical Air - Winter
Continental Polar Air - Summer
Superior Air - Summer
Maritime Polar Air - Summer
Superior Air - Winter
Altitude (m)
N

Figure 1.22.--Average refractive index distribution in airmasses at various locations in North America.

BEST DOCUMENT AVAILABLE

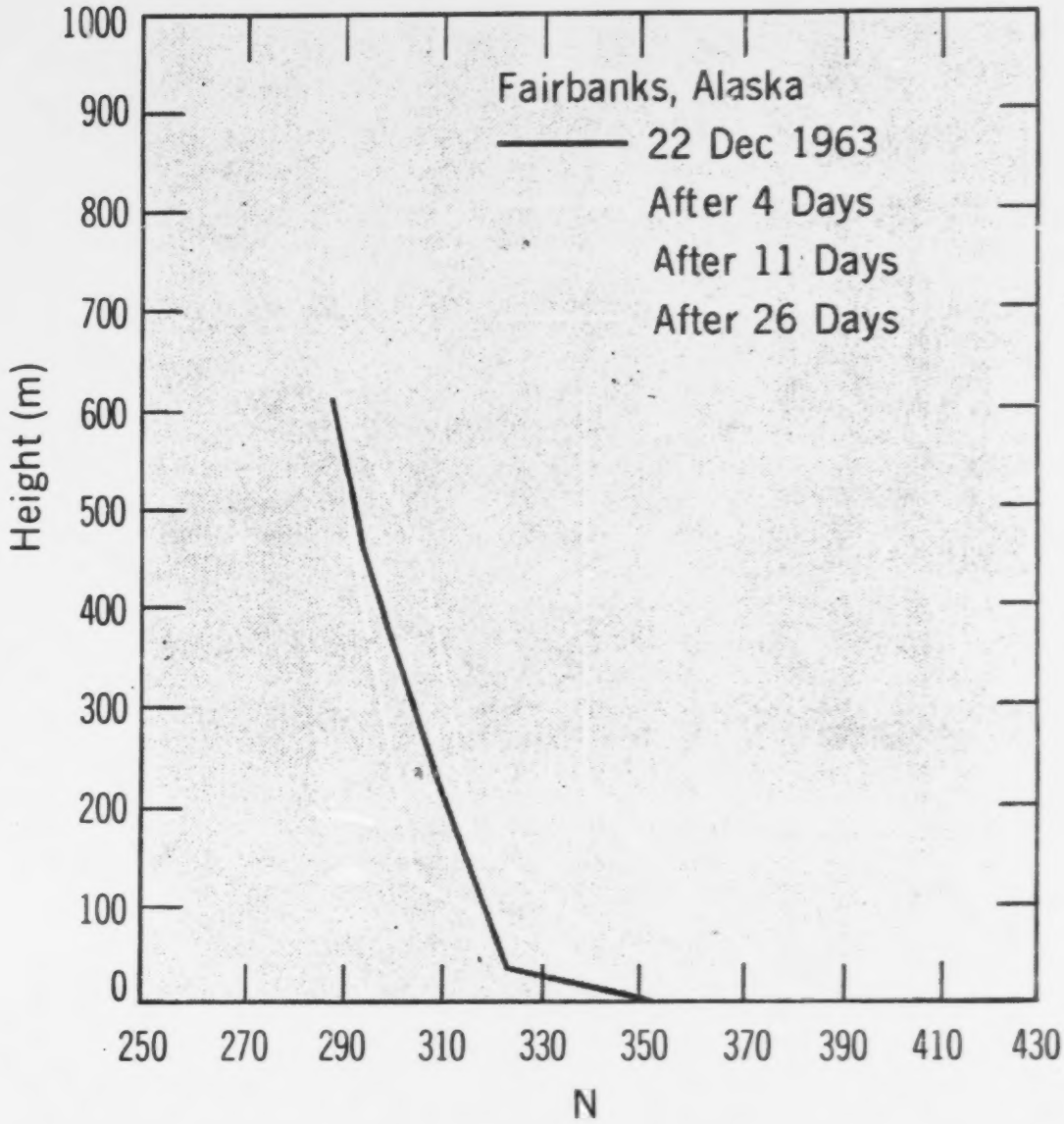

Modification of the surface layers of an air mass in its source region as radiational cooling of the underlying surface proceeds.

Figure 1.23.--Modification of the surface layers of an airmass in its source region as radiational cooling of the underlying surface proceeds (adapted from Plank, 1952).

BEST DOCUMENT AVAILABLE

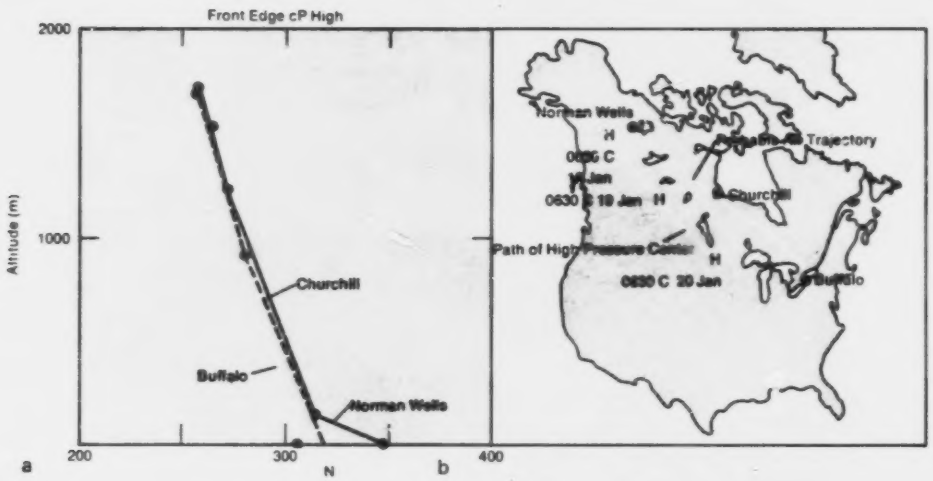

Figure 1.24.--Case illustrating how the surface layers of an airmass are modified by passage over a warmer lower boundary as it follows the trajectory shown (adopted from Plank, 1952).

One of the most important modification processes occurs when an air mass formed above one kind of surface flows over an underlying surface of different temperature or humidity.

Figure 1-24 shows the modification of the refractive index profile as an air mass formed in northern Canada moves southward to Churchill and Buffalo. The solid trajectory shows the progress of the front (edge) of the continental Polar (cP) high pressure region and the dashed curve shows the path of the center of the high.

When a mass of homogeneous air formed over land moves over water of different surface temperature, important modification of the refractive structure of the lower layers takes place. If the water is warmer than the air, the modification proceeds very rapidly, and steady state is quickly achieved, with the important refractive index gradients (and the radio duct) confined to a thin layer very near the water surface. If the air is warmer than the water, the transitional region can extend far off-shore with important effects on the horizontal variation of the refractive index profile, as shown in early measurements by Craig, illustrated in Figure 1-25.

If power law height profiles are chosen for the various meteorological properties, such as wind, potential temperature and moisture, the theoretical problem is tractable, and the results are shown in Fig. 1-26 the profile index, m, is chosen to be 1/7. The theoretical development is given in

BEST DOCUMENT AVAILABLE

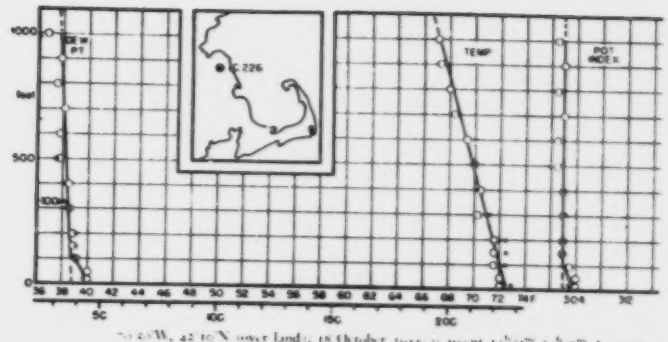

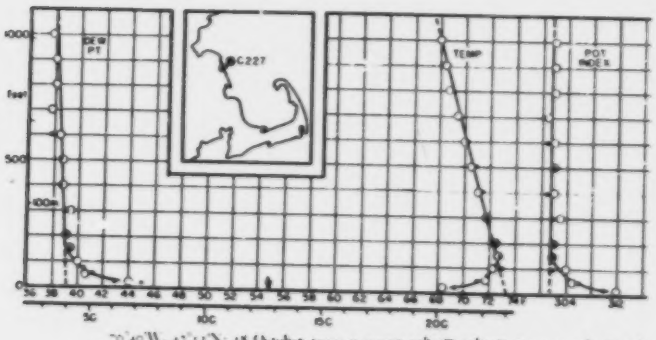

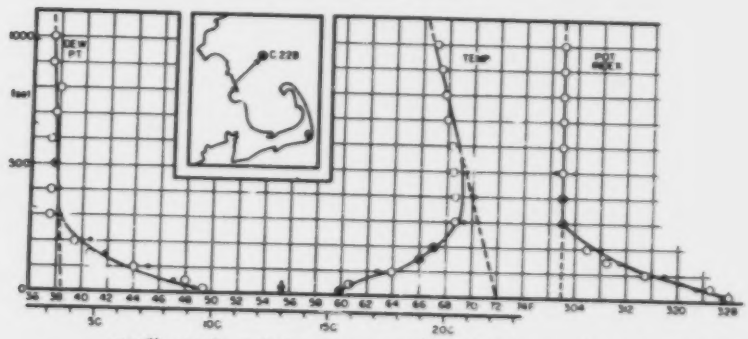

Figure 1.25.--Refractive index profile as land air moves offshore from the U.S. east coast at various locations shown on the insert map (from Craig, 1946).

BEST DOCUMENT AVAILABLE

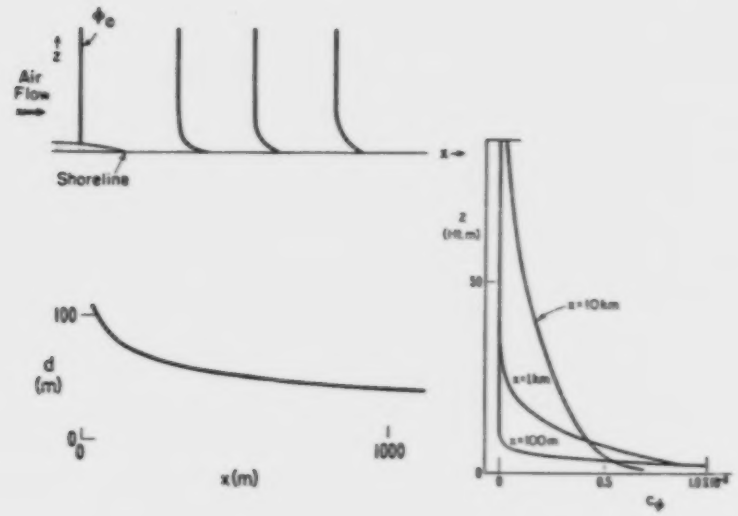

Figure 1.26.--The manner in which duct thickness, d, and C_ϕ are modified with increasing distance off-shore for a simple power-law model of refractive index in which the initial height distribution is given by ϕ_o = constant and m is the power of the height function.

detail in Chapters 9 and 10. Figure 1-26 shows how the height profile of $C_\phi \times 10^{-6}$ (right-hand frame) and duct thickness d (left-hand frame) vary with distance off-shore when the refractive index profile is modified in the manner shown schematically in the top frame, where ϕ_o is the assumed initial distribution of ϕ prior to modification; ϕ_s is its surface value and z is height.

Elevated Layers

Layers capping the convective boundary layer

One class of elevated layer is closely related to the formation of surface layers and the transfer processes that create them. This type of elevated layer is formed when the surface-based nocturnal inversion is erased by surface solar heating following sunrise. It is illustrated schematically in Fig. 1-27. The radar returns from such layers often have a dome-like appearance (Harper et al., 1957; Atlas, 1959; Hardy and Ottersten, 1969; Konrad, 1970; Gossard et al., 1971; Richter et al., 1974). In horizontal section such convective features often resemble doughnuts as seen in Fig. 1-28 from Hardy and Ottersten, 1969). This effect is apparently mainly a result of the entrainment of dry air into the moist rising air at the boundary of the updraft, locally enhancing C_n^2. However, insects can greatly

BEST DOCUMENT AVAILABLE

influence the appearance of the echo unless the resolution of the radar is good enough to resolve them as shown in Fig. 1-29 from Chadwick (private communication). Radar observations of convective dome structures suggest that the sides of the domes are zones of descending mixed air (Arnold et al., 1975) and some relationships between the heat fluxes, the dynamic stability, and the rate of growth of the convective feature have been deduced from radar measurements (Noonkester, 1976, 1978). Readings and Browning have used a balloon-borne turbulence probe to compare radar observations at Defford, England with in-situ measurements of the turbulence structure around convective domes and "hummocks" (Browning et al., 1973; Readings et al., 1973). Substantive transfer of heat and mass across the convective boundary was found which they associated with shear instability near the crest of the domes.

Records of radar return from elevated layers such as that in Fig. 1-29 can easily be converted to a height profile of structure constant of refractive index through the elevated layer from the relation (derived in Chapter 2) between radar reflectivity and C_ϕ^2, which is

$$\eta = (5/6)\pi(2\pi/\lambda)^4(4\pi/\lambda)^{-11/3}\, C_\phi^2 \qquad (1\text{-}17)$$

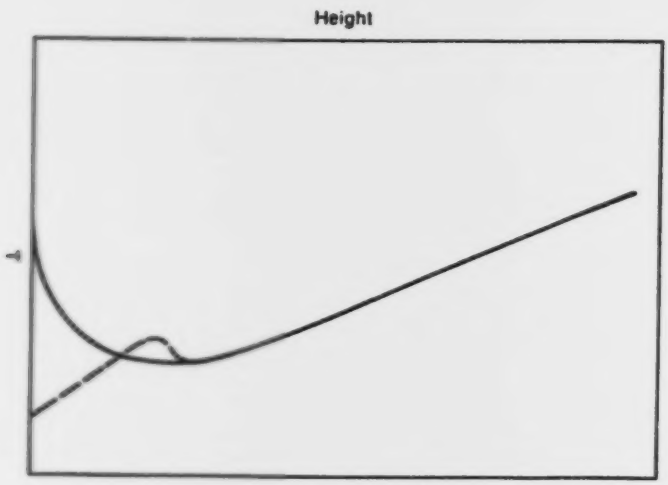

Figure 1.27.--Schematic picture of the formation of a capping inversion when solar heating of the surface begins after sunrise.

BEST DOCUMENT AVAILABLE

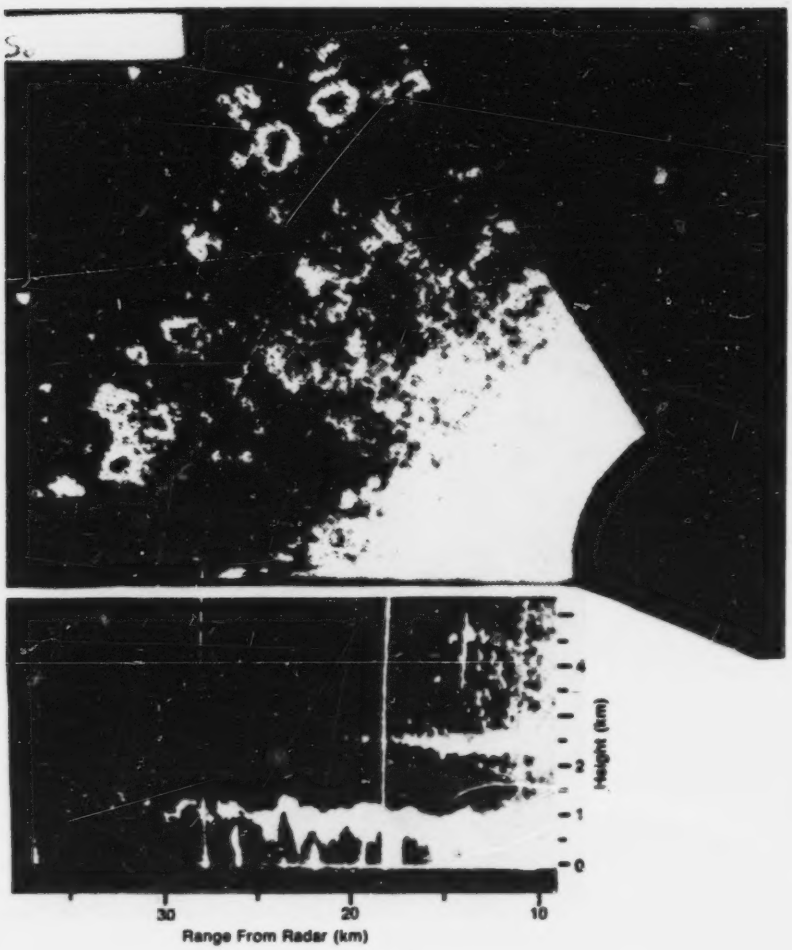

Figure 1.28.--Bottom frame: Dome-like layers at Wallop's Island reported by Hardy and Ottersten (1969). They are height vs. range plots obtained from RHI radar scans. Note resemblance to boundary layer features in Fig. 1.15 obtained with a vertically pointing radar. Top frame: Plan view of features in bottom frame obtained with PPI scans of the radar showing doughnut-like appearance of the convective features in cross-section.

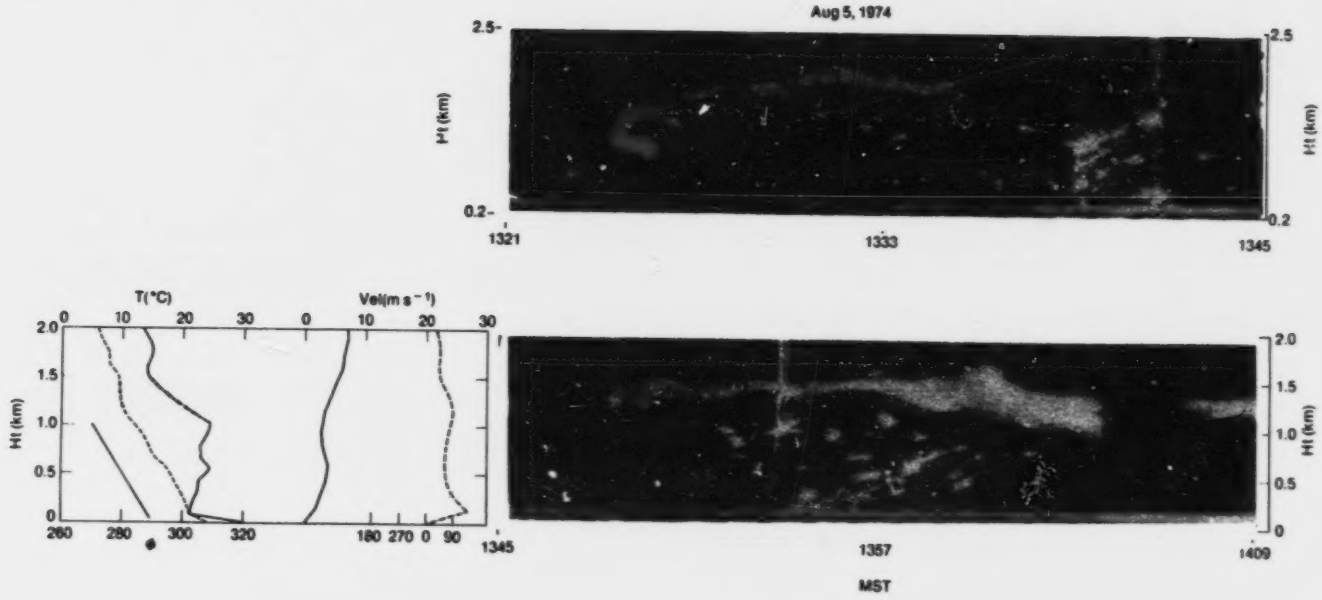

Figure 1.29.--Radar display of the capping layer above the clear convective boundary layer on 23 July 1974 (1200 MST) obtained with a vertically pointing FM-CW radar located at Sterling, Colorado. The height range was changed from 3 km to 6 km midway through the record. The point targets are mainly insects.

BEST DOCUMENT AVAILABLE

In Eq. (1-17) a Kolmogorov -5/3 spectrum has been assumed for the refractive index fluctuations. Layers of this type are predictable if the nature of the heat absorbing/radiating lower boundary is known and if cloud cover is known or predictable. They are found primarily over the land but may also occur over the sea when cool air flows over a warmer sea.

In addition to echoes associated with capping inversions above convective features, low level fog and stratus are often capped by stable layers detectable by high resolution radars. Richter et al., 1973 and Noonkester et al., 1974, 1976 report echoes from the top of advection fog and low stratus clouds. Aircraft measurements by Jensen and Lenshow (1978) show that there is substantial enhancement of C_n^2 near stratus cloud tops apparently due to the entrainment of warm dry air from above the clouds into the zone of the cloud top; they find, in fact, that temperature and humidity are strongly negatively correlated. The large refractive index variance is probably significantly enhanced by wet-bulb cooling producing intense convective mixing in the top of the cloud. Since stratus cloud tops are often accompanied by wind shear, it is not surprising that pronounced radar echoes should be found there. However, the role of change in liquid-vapor phase at the cloud boundary in producing the radar echo should not be over-emphasized. The lower part of temperature inversions, and their associated humidity gradient, are often zones of enhanced refractive index variance and corresponding high values of C_n^2.

Sub-tropical subsidence layers

A type of elevated layer of primary importance in many oceanic areas is found in the eastern sectors of large subtropical high pressure areas which are renowned for their spectacular radio (and optical) refractive effects. In these areas the anticyclonic circulation creates southerly flowing air on the eastern side of such zones in the Northern Hemisphere and northerly flowing air in the Southern Hemisphere. Such an air flow subsides because of divergence in the lower levels, and subsidence causes thermally stable stratification and super refraction. Figure 1-30 shows schematically why subsidence occurs and the effect on the temperature gradient of an air parcel with an adiabatic lapse rate at a height between 500 and 400 mb if it is brought down adiabatically to a height between 900 and 1000 mb. Consider a column of air whose rotation about a vertical axis is given by the angular velocity ω, chosen positive for cyclonic rotation. Define ω to be the angular velocity relative to the surface of the earth. The angular velocity of a point on the earth's surface beneath the air parcel is given by $\Omega \sin\phi$ where Ω is the angular velocity of the rotation of the earth about its axis

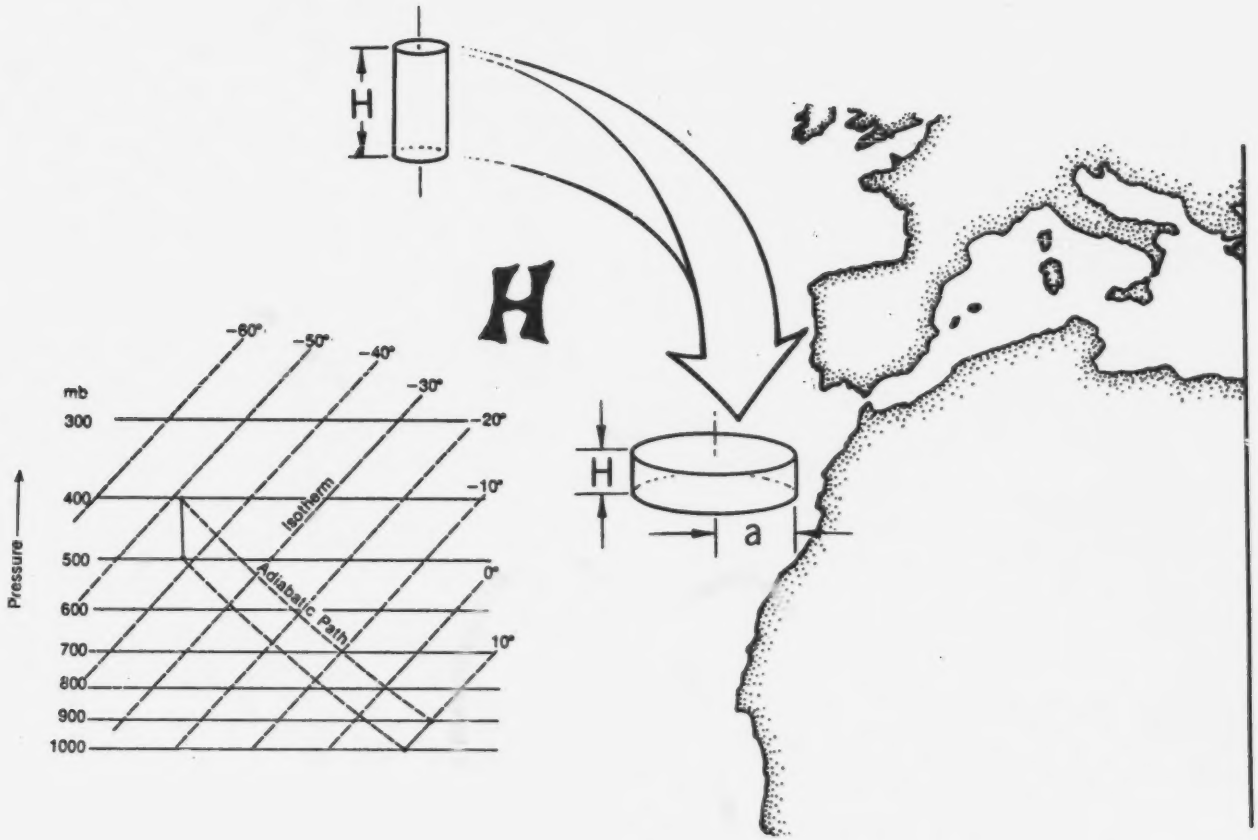

Figure 1.30.--Schematic picture of the way subsidence develops when vorticity is conserved in a southerly flowing airmass in the Northern Hemisphere. Insert shows how the lapse rate of a parcel, initially adiabatic (vertical) between 400 and 500 mb, stabilizes to isothermal as it descends to the 900-1000 mb level.

BEST DOCUMENT AVAILABLE

BEST DOCUMENT AVAILABLE

and ϕ is latitude; Ω is counterclockwise in the Northern Hemisphere. Suppose the cylindrical air column is of height H and radius a as shown in Fig. 1-30. Its total angular velocity will then be $\omega + \Omega \sin\phi$. If its angular momentum is conserved

$$(\omega + \Omega\sin\phi)a^2 = \text{constant.} \tag{1-18}$$

Assume the volume of air within the cylinder is conserved while it undergoes convergence or divergence. The volume

$$V = \pi a^2 H ,$$

so

$$\frac{\omega + \Omega\sin\phi}{H} = \text{constant.} \tag{1-19}$$

Defining $2\,\Omega\sin\phi = f$ as the Coriolis parameter and $\zeta = 2\omega$ as the vorticity of the air column relative to the underlying earth

$$\frac{\zeta + f}{H} = \text{constant} \tag{1-20}$$

where ζ is positive for cyclonic curvature of the airflow. This is one form of Rossby's vorticity equation. We may thus conclude that:

1) Decreasing vorticity resulting from decreasing ϕ causes subsidence; i.e., southerly flowing air in the Northern Hemisphere leads to decreasing H, or subsidence, and vice versa. Such an air flow occurs on the eastern side of large subtropical anticyclones and can lead to strong super refraction. It sometimes manifests itself as a lowering and intensification of the Trade Wind inversion. Figure 1-31 shows aircraft soundings of the refractive index distribution through such a layer and the height gain patterns for four microwave frequencies trapped by the layer (J. B. Smyth, private communication). The aircraft, carrying the four transmitters, was flying off the coast of southern California. The receivers were on the coast at an elevation of 30 m MSL. The intensity of turbulent refractive index fluctuations (C_ϕ^2) is very great in such layers, and radar backscatter can be used very effectively to monitor their existence and height. An example observed by an FM-CW radar, described by Richter (1969), is shown in Fig. 1-32 (J. H. Richter, private communication). Subsidence is also common in air masses moving southward out of their northern continental source regions. An example is shown in Fig. 1-33 adapted from Plank (1952).

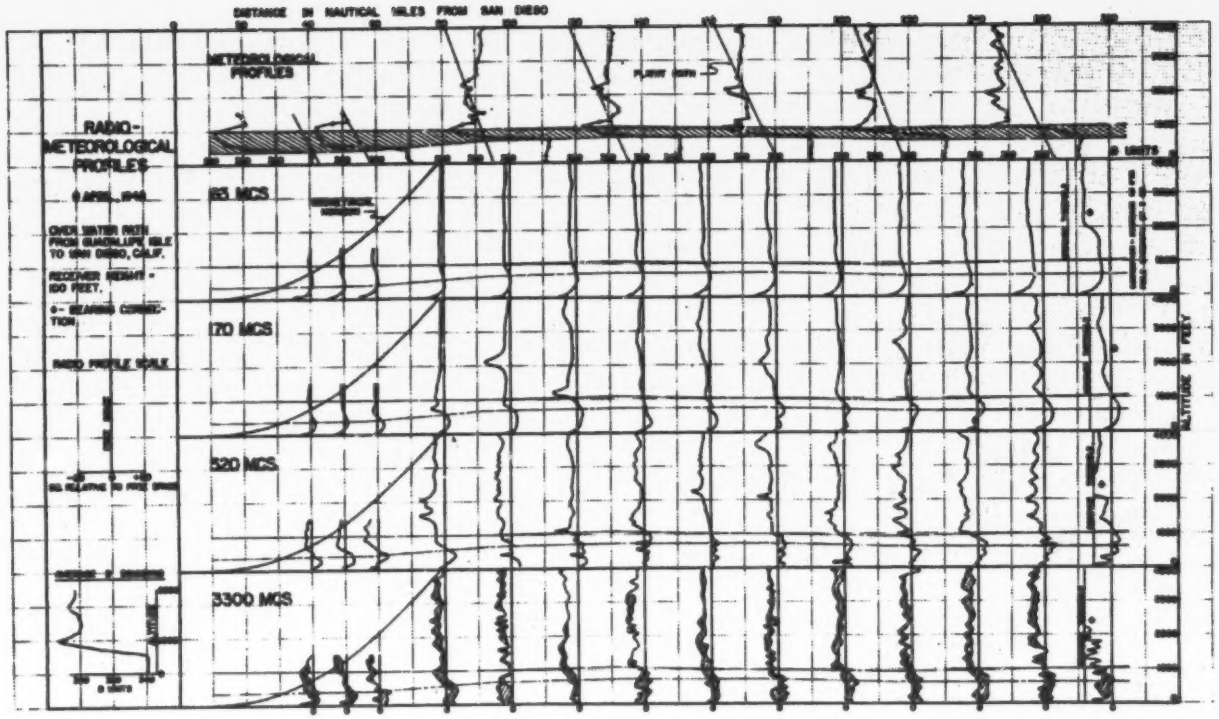

Figure 1.31.--Top Frame: Refractive index distribution on 8 April 1948 west of San Diego. The quantity $B = \phi + 0.013Z$ where Z is in meters. Bottom Four Frames: Height distribution of received power at 100 ft MSL on 4 frequencies as transmitting aircraft flew the slant patterns shown in top frame (J.B. Smyth, private communication).

BEST DOCUMENT AVAILABLE

BEST DOCUMENT AVAILABLE

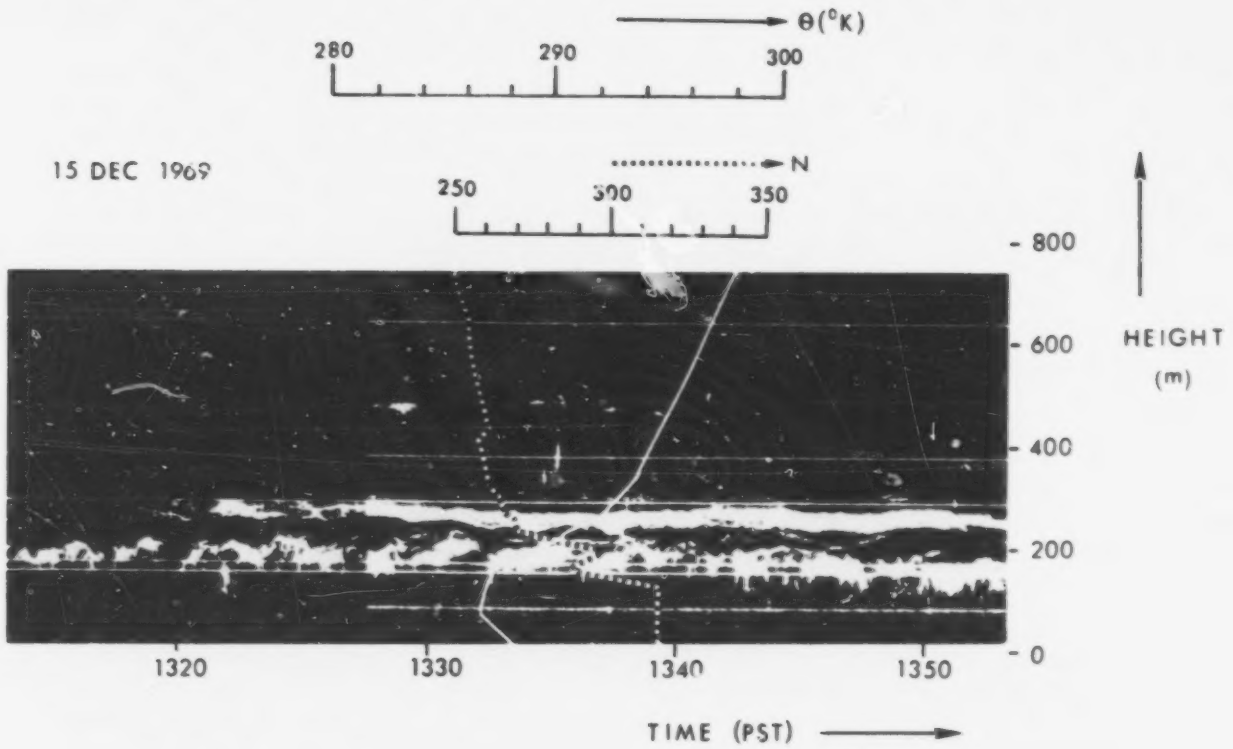

Figure 1.32--Vertically pointing backscatter through layer similar to that of Fig. 1.31 from an FM-CW radar at San Diego. Dashed curve, refractive index N; solid curve, potential temperature. (J.H. Richter, private communication.)

BEST DOCUMENT AVAILABLE

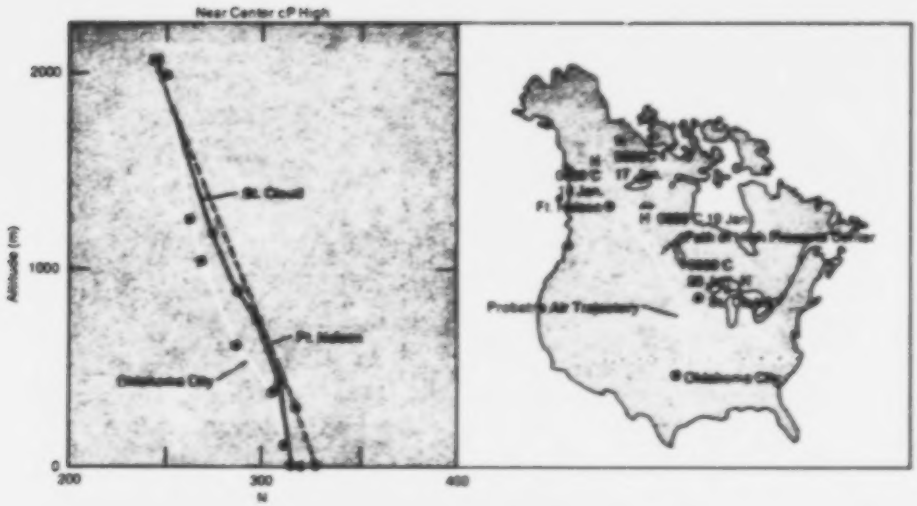

Figure 1.33--Height distribution of radio refractive index N in an airmass which is subsiding as it moves southward anticyclonically along the trajectory shown by the solid arrows on the map in the right-hand frame.

2) Decreasing vorticity at a given latitude (increasing anticyclonic circulation) produces subsidence and superrefraction aloft. Such an effect is common in the U.S. midwest when cold air masses move southward and stagnate, producing pollution over large cities and creating radio and optical superrefraction.

3) In the absence of convergence or divergence, increasing vorticity is produced by equatorward flow. That is, as f decreases ζ increases.

In some areas of the world subsidence conditions are often coupled with a monsoonal type of circulation which brings subsiding dry continental air into juxtaposition with surface marine air. This condition commonly leads to spectacular refractive effects on both radio and optical waves. In southern California a condition called a "Santa Ana" is produced by subsiding flow from the high plateau region of the U.S. southwest over the coastal areas. Figure 1-34 shows a twice inverted optical image from a submarine during such an event. The corresponding optical and radio refractive index profiles are shown in Fig. 1-35. In the Mediterranean the Etesian winds of the Balkan area and the Sirocco of Egypt produce similar effects in coastal zones, but there the subsidence is a lesser factor. During World War II, British radars on the northwest coast of India commonly were able to observe the coast of Arabia 2000 km distant under monsoon conditions.

BEST DOCUMENT AVAILABLE

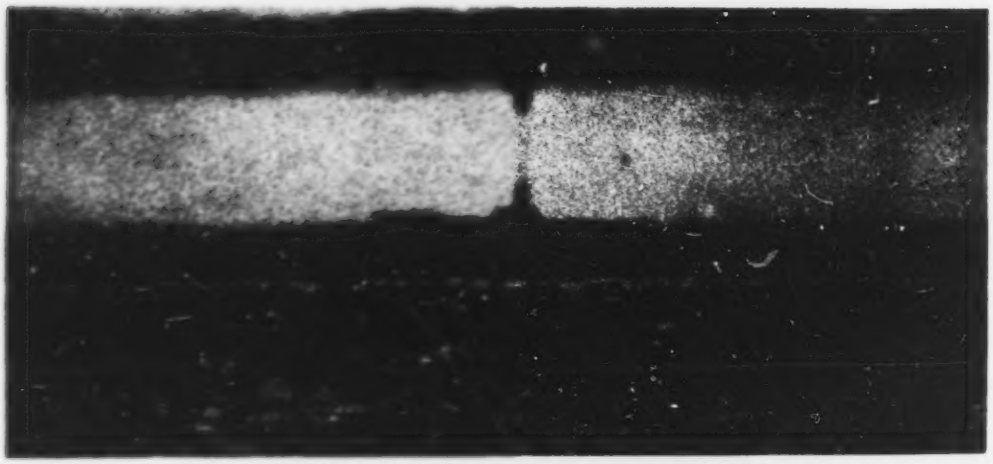

Figure 1.34--Visual evidence of stratification of refractive index in a monsoonal circulation off southern California. Reflection is so specular that the twice-inverted image of the boat is resolvable.

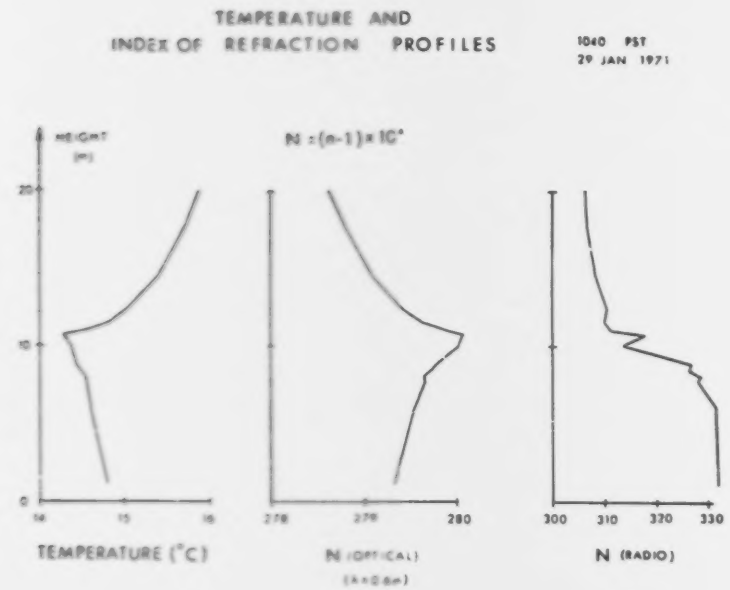

Figure 1.35--Temperature and refractive index height distribution for the case shown in Fig. 1.34, recorded on an oceanographic tower 2 km off-shore at La Jolla California using a height traversing boom with dew-pointer and temperature sensor.

Many of the great desert areas of the world are a direct climatological consequence of their position beneath the eastern part of the major subtropical high pressure zones of the globe and the resulting subsidence with its clear skies and low precipitation amounts. These include the Great American Desert of the U.S. southwest, the Sahara of Africa, the Australian desert and the Chilean desert.

Frontal discontinuities

For decades it has been noted that radars occasionally detect boundaries within air masses such as weather fronts, land and sea breeze fronts (Plank, 1956; Geotis, 1964; Meyer, 1971) and gust fronts (Brown, 1960). An example of the latter is shown in Fig. 1-36 from L. J. Miller (private communication). Such echoes, especially those associated with weather fronts, are often thought to be due to biological targets such as insects with feeding birds (Eastwood, 1967). However, the strong updrafts and rotary motions associated with violent gust fronts can sweep up substantial amounts of debris that is large enough to provide good targets for radars. This is the probable explanation of the record in Fig. 1-36. However fronts and gust fronts are regions of enhanced turbulence so that radar reflectivity from refractive index turbulence may also be a factor. On the eastern slope of the Rocky Mountains in the U.S. a violent Chinook condition can create a rotor in the lee of the mountains that can sweep insects and debris aloft providing a very strong radar echo as shown in Fig. 1-37 acquired by a vertically pointing 8.6 mm wavelength radar (a modified TPQ-11). The upper echoes are clouds but the lower echo, ascending in time, is from surface debris caught up in the lee wave rotor.

The boundaries between adjacent air masses are usually regions of abrupt change in temperature and humidity and are, therefore, commonly zones of large height gradient of refractive index. The variation of refractive index and refractive index structure constant through such layers is of particular interest. The boundaries between air masses are called fronts. Vertical cross-sections and plan views of several types of weather fronts effective in producing refractive index layering are shown in Fig. 1-38. This layering is relatively predictable and is important to many kinds of propagation. Figures 1-39 and 1-40 show examples of frontal systems near Denver, CO, USA. During these events observations were made with a vertically pointing FM-CW radar of 10 cm wavelength; the radar was at Boulder, 60 km north of Denver. The radar returns were compared with radiosonde (raob) balloon soundings taken at the Denver airport supplemented by a Boulder balloon sounding on the

BEST DOCUMENT AVAILABLE

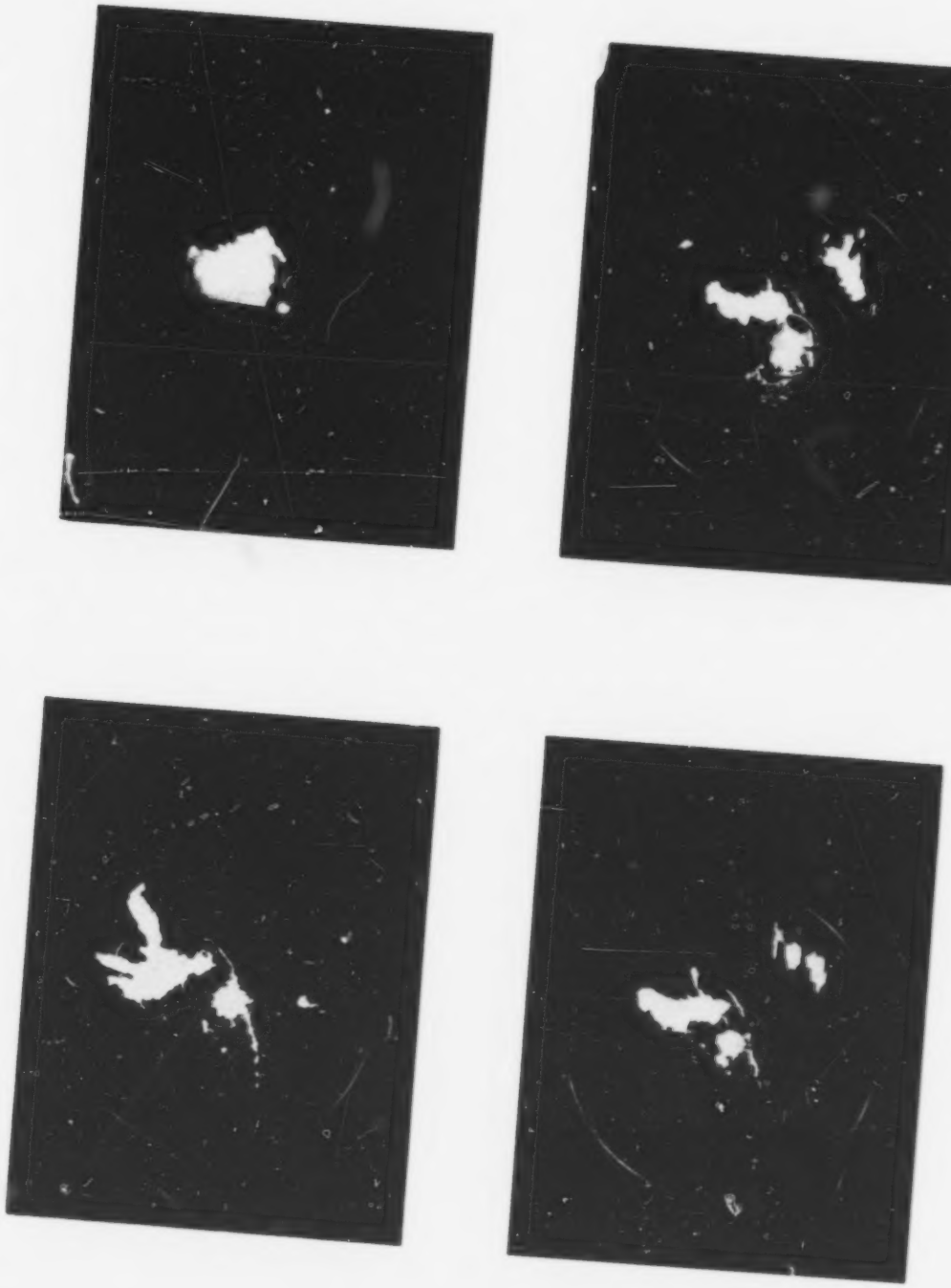

Figure 1.36--Radar returns from a gust front tracked with a 3.2 cm wavelength radar in low elevation angle PPI mode. (L.J. Miller, private communication.) Targets are probably debris swept up turbulence and rotors at the nose of the front.

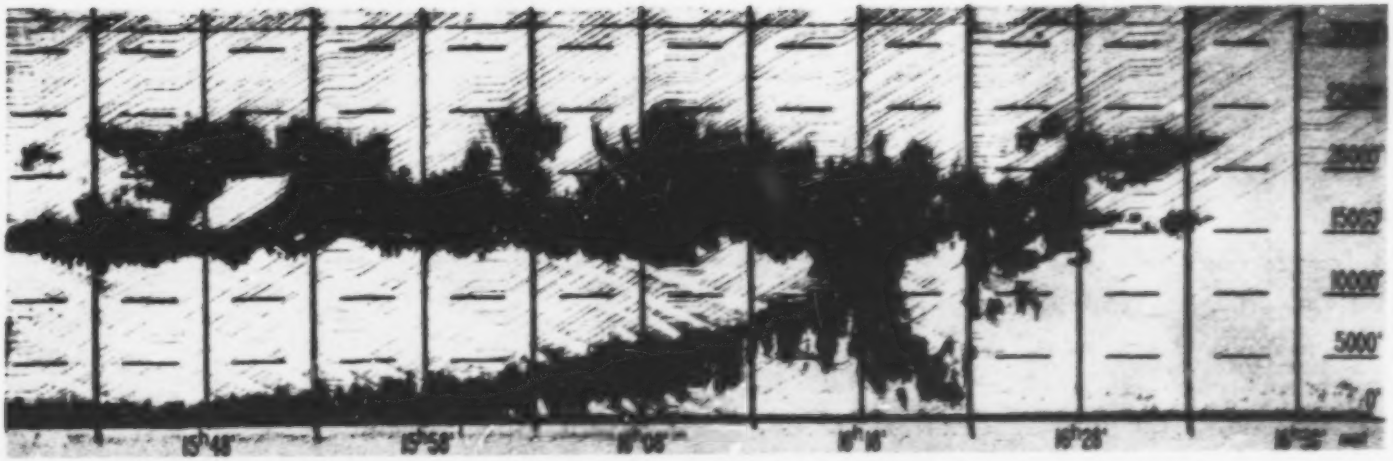

Figure 1.37--Example of radar returns from a debris cloud swept up in violent chinook (down-slope) winds in the lee of the Rocky Mountains at Boulder, CO.

BEST DOCUMENT AVAILABLE

BEST DOCUMENT AVAILABLE

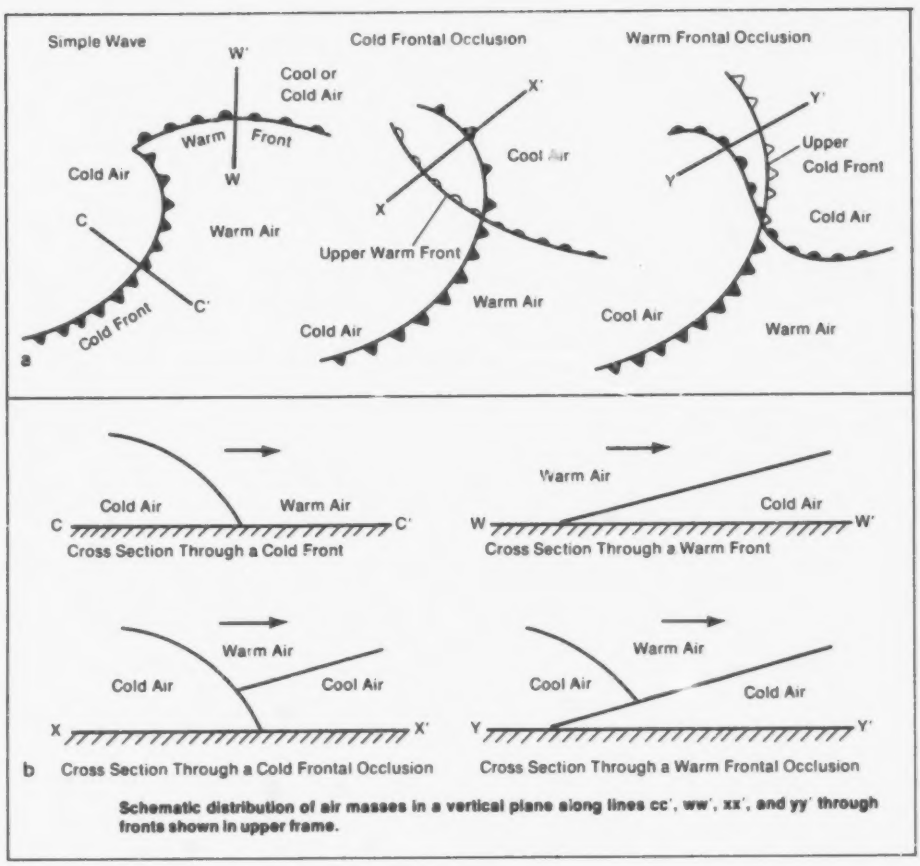

Schematic distribution of air masses in a vertical plane along lines cc', ww', xx', and yy' through fronts shown in upper frame.

Figure 1.38--Schematic picture of some simple frontal structures.

BEST DOCUMENT AVAILABLE

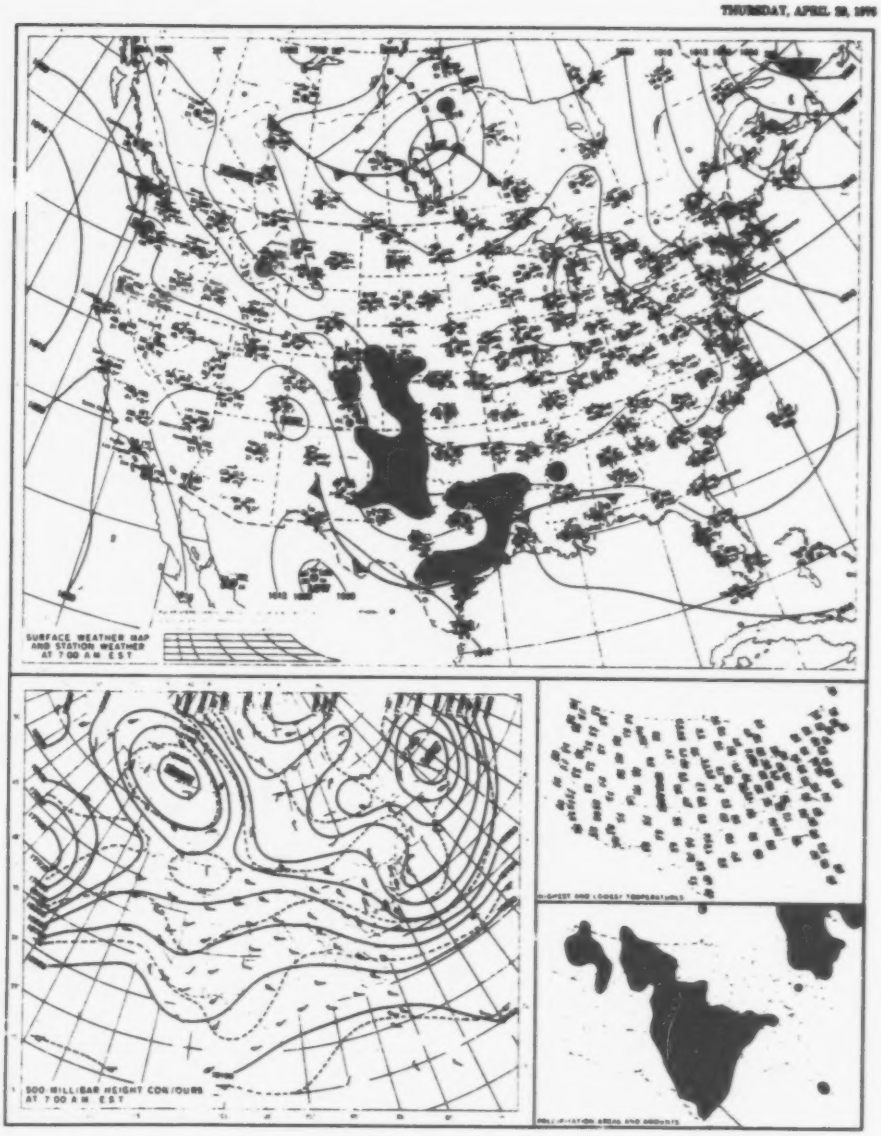

Figure 1.39--Weather maps of 29 April 1976 (0500 MST).

BEST DOCUMENT AVAILABLE

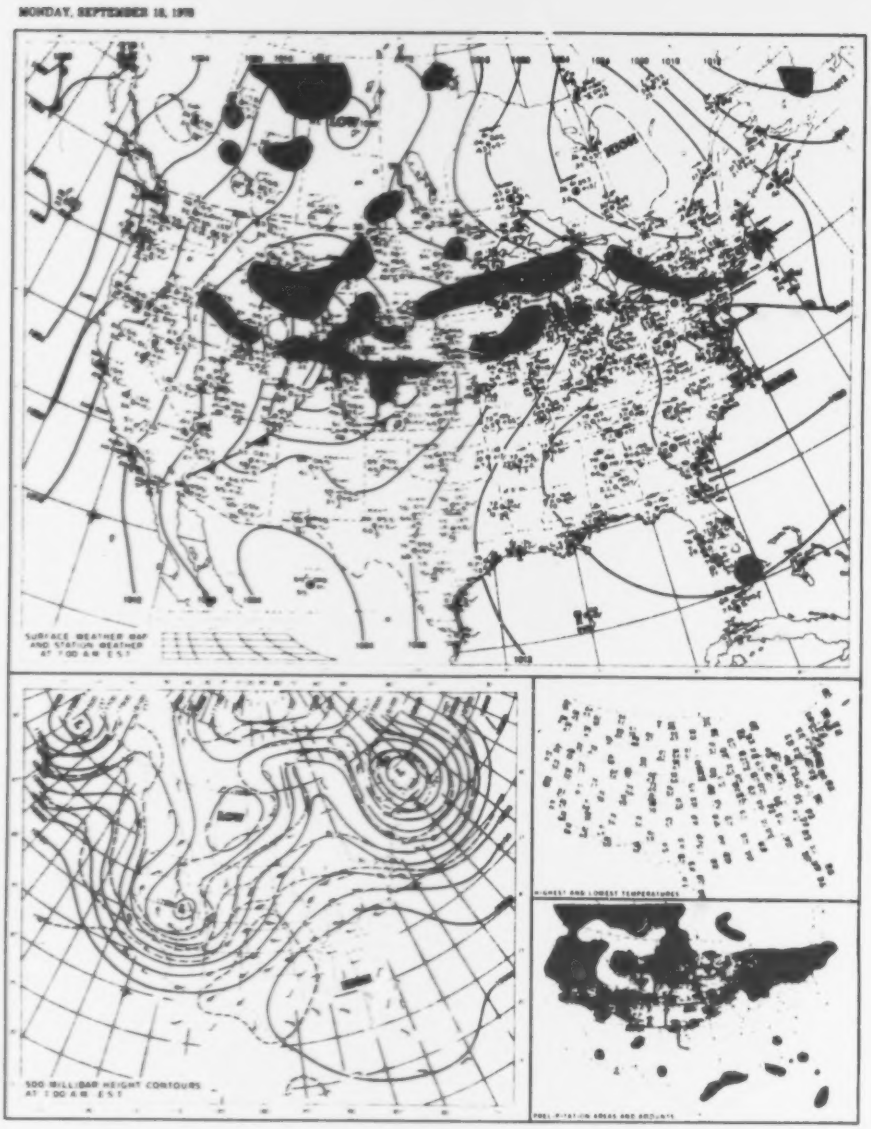
MONDAY, SEPTEMBER 18, 1978
SURFACE WEATHER MAP AND STATION WEATHER AT 7:00 A.M. EST
500 MILLIBAR HEIGHT CONTOURS AT 7:00 A.M. EST
HIGHEST AND LOWEST TEMPERATURES
PRECIPITATION AREAS AND AMOUNTS

Figure 1.40--Weather maps of 18 September 1978 (0500 MST).

18 September 1978 case. The vertically pointing radar sounding data are shown with the balloon sounding data in Figs. 1-41 and 1-42. The profiles of C_ϕ^2 were calculated from Eq. (1-17), derived in Chapter 2. In the case of 29 April, the front was nearly stationary along the eastern edge of the Rocky Mountains and the height of the interface (at 1400 m AGL) was therefore nearly constant. On 18 September the surface front was moving northward, with the cold air wedge becoming thinner with time. The frontal interface at about 500 m AGL is descending and is characterized by very prominent buoyancy oscillations (gravity waves) recorded by both the FM-CW radar (middle frame) and an acoustic sounder (upper frame). The ability of clear-air radars to monitor this type of event is very promising for the study of both the weather phenomenon itself and the associated radio propagation problems. If the radars have Doppler capability they can also monitor the height profile of the wind structure. The prominent wave structures seen on 18 September are common on stable layers in the atmosphere (Gossard and Hooke, 1975) and represent a scale and frequency of perturbation that can, on occasion, cause important fading on tropospheric and satellite paths at small grazing angles. Further examples of wave perturbations of atmospheric layers are shown in Fig. 1-43. The value of high resolution is evident in records of this kind. Such observations are invaluable in the study of dynamic instability in the atmosphere.

The stratosphere and middle atmosphere

Using clear-air radar backscatter, it is now possible to monitor C_ϕ^2 through the whole depth of the lower atmopshere. The tropopause is an elevated layer of particular meteorological interest, and Fig. 1-44 shows an example from Röttger (1980) of tropopause structure measured with a VHF radar at Lindau, West Germany. This example even shows some evidence of differences in the structure of mean reflectivity for different masses. Near-vertically pointing MST (mesosphere, stratosphere, troposphere) radars are now being used on a global scale to observe wind structure. Of course they provide profiles of C_ϕ^2 also. Some locations where these kind of measurements are being made are Jicamarca, Peru; Arecibo, Puerto Rico; Lindau, West Germany; Sunset near Denver, CO, USA; Chatanika and Poker Flats, Alaska USA; Millstone Hill, Mass USA, Kwajalein and Japan in the western Pacific. A global pattern is already emerging for the height distribution of C_ϕ^2. Figure 1-45 is taken from Balsley and Peterson (1980) soon to be published in J. of Appl. Meteorol. It demonstrates that C_n^2 (or C_ϕ^2) apparently decreases with height between altitudes of 10-20 km substantially faster in equatorial latitudes than in the higher latitudes. These new radar observation systems are also revealing wave-like perturbations not unlike those of the lower atmosphere. Observations by radars such as these, and the important design considerations, are discussed in Chapter 11.

BEST DOCUMENT AVAILABLE

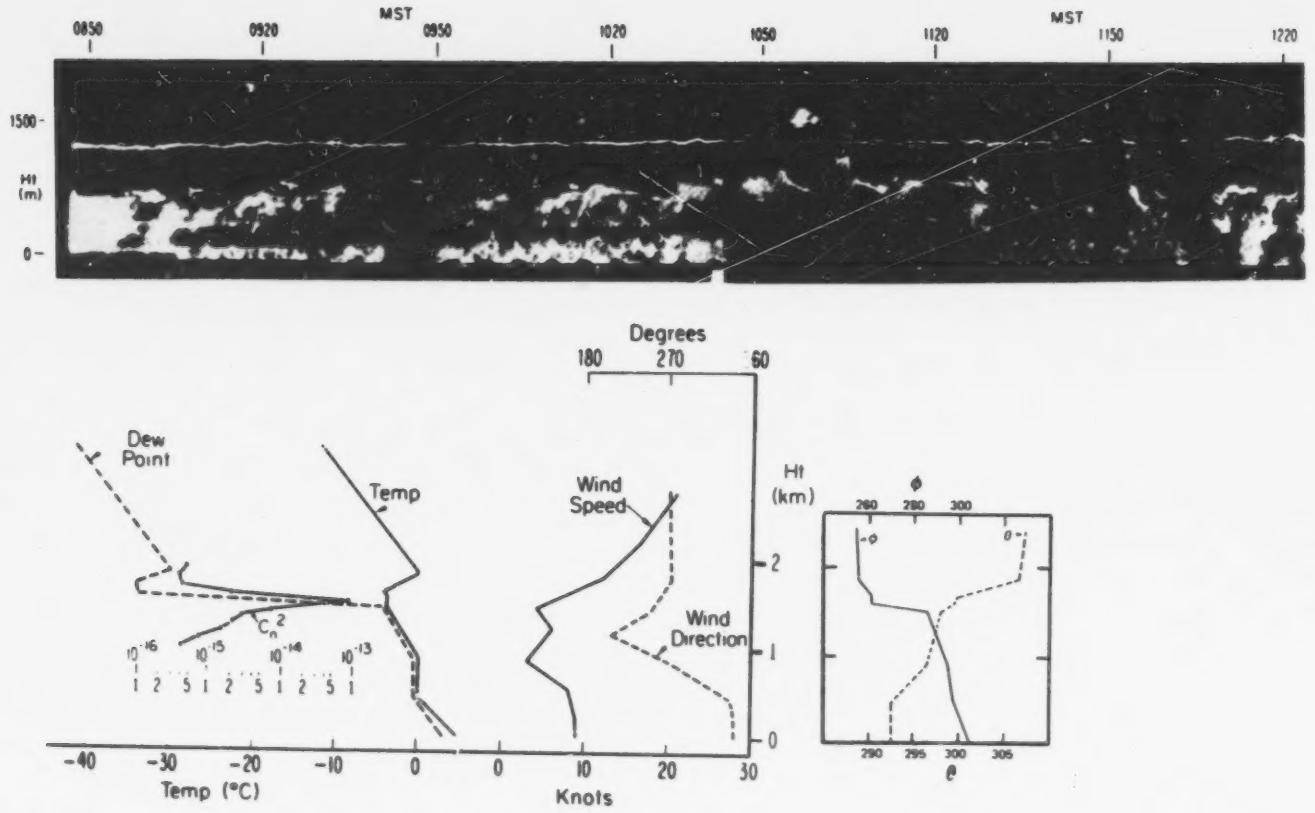

Figure 1.41--Vertically pointing FM-CW radar and balloon sounding data near Denver, Colorado corresponding to weather maps of Fig. 1.39.

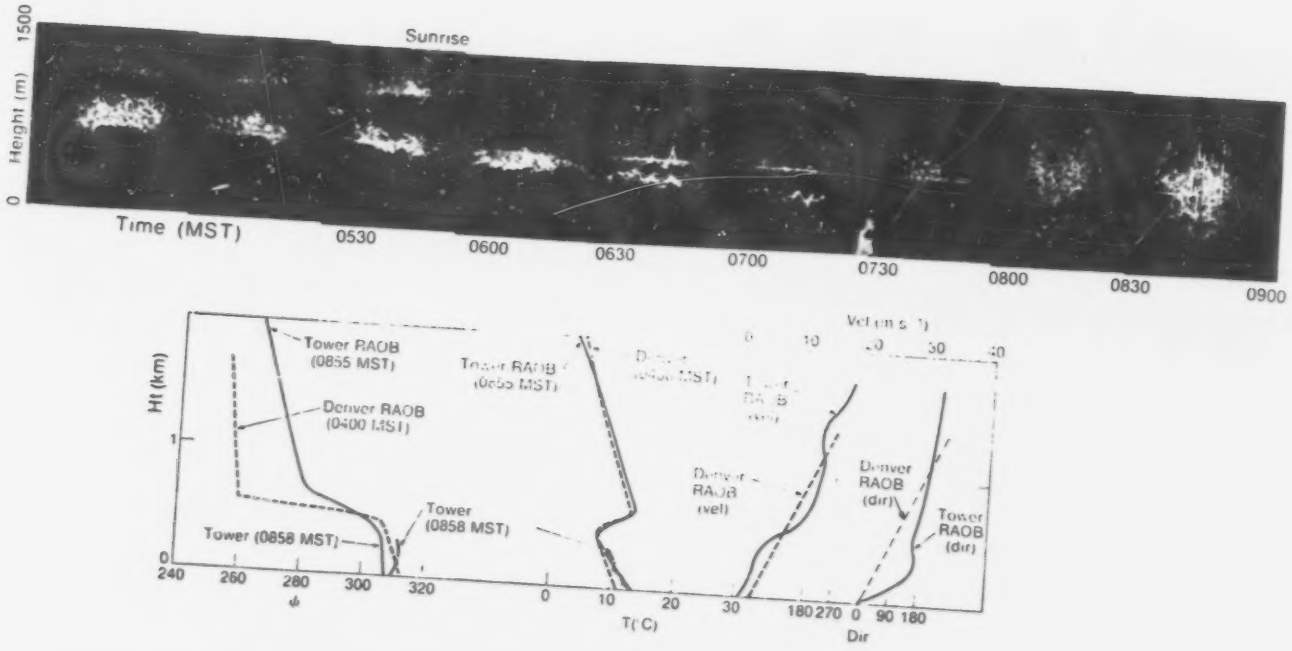

Figure 1.42--Vertically pointing FM-CW radar and balloon sounding data near Denver, Colorado corresponding to weather maps of Fig. 1.40.

BEST DOCUMENT AVAILABLE

BEST DOCUMENT AVAILABLE

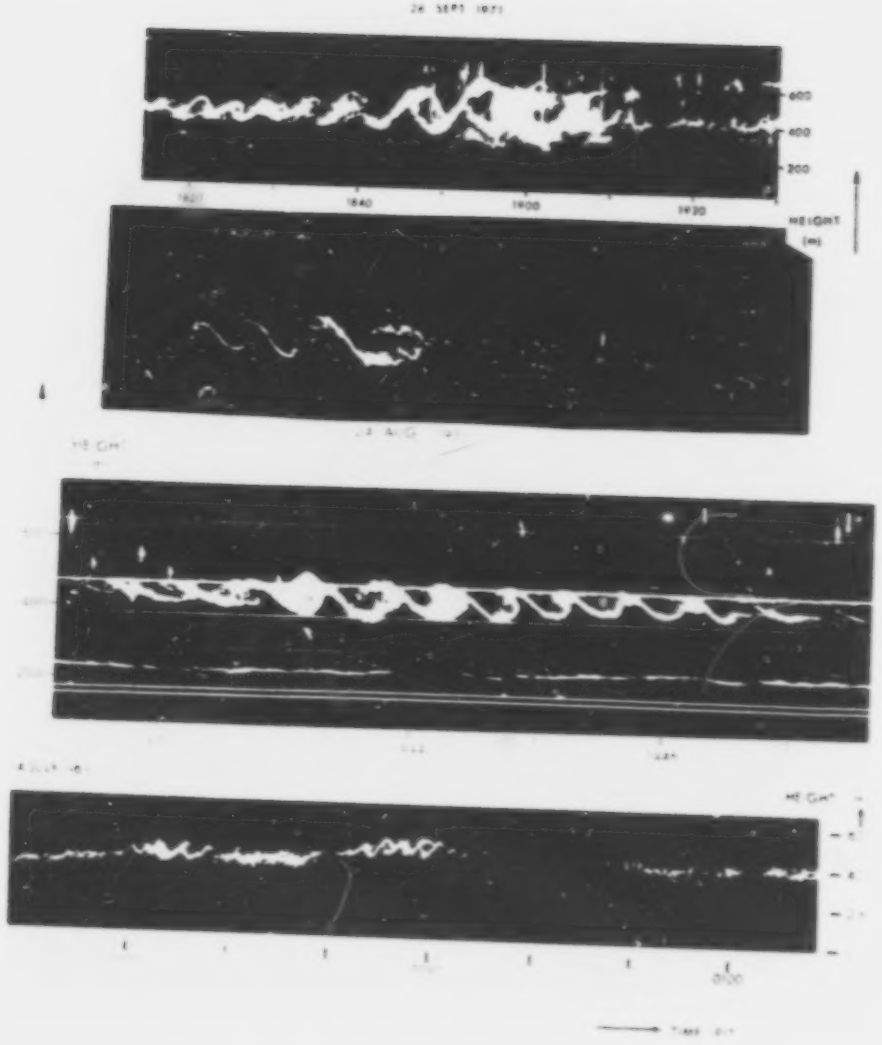

Figure 1.43--Examples of wave perturbations of atmospheric layers observed by the Richter FM-CW radar at San Diego. The value of the remarkable resolution of this radar is evident when attempting to resolve thin, small-scale perturbations.

BEST DOCUMENT AVAILABLE

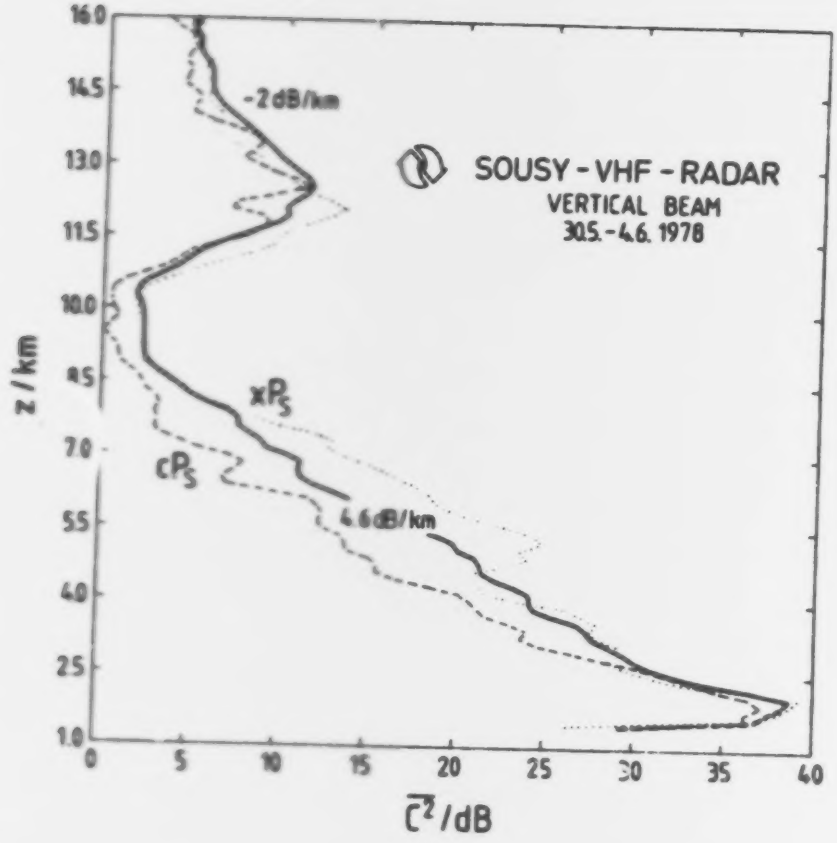

Figure 1.44--Mean reflectivity $\overline{C^2}$ (continuous curve) for 30 May to 4 June 1978. The dashed curve was deduced from the first 24 hours of data when continental polar air (c P_s) dominated, and the dotted curve was deduced from the last 24 hours of data when maritime polar air (x P_s) replaced the continental airmasses. (From Röttger, 1980.)

BEST DOCUMENT AVAILABLE

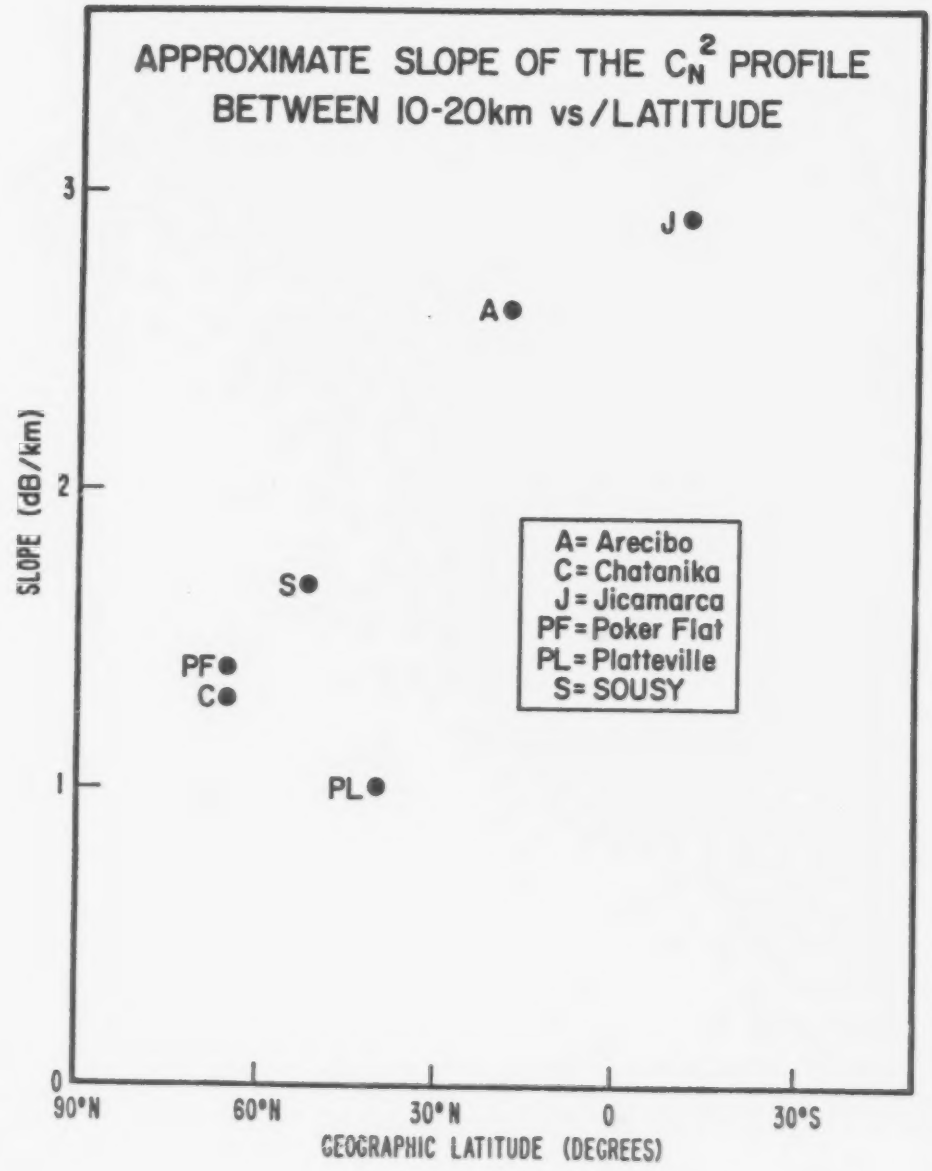

Figure 1.45--The latitudinal variation of rate of drop-off of C_N^2 profiles in the 10-20 km height range. (From Balsley and Peterson, 1980.)

CHAPTER 2 - PHYSICAL EFFECTS OF THE ATMOSPHERE ON RADAR WAVES

2.1 Introduction

At microwave frequencies the refraction, absorption and scattering properties of the non-ionized clear atmosphere result mainly from the fact that the water vapor molecule possesses an electric dipole moment. Of lesser importance, except for millimeter wavelengths, is the magnetic dipole moment of the oxygen molecule. Except near the absorption lines of water vapor and oxygen, the refractive index for microwaves can be considered to be essentially independent of frequency, and gaseous absorption can be considered to be negligible unless very long ranges are involved. For most purposes radar frequencies are deliberately chosen for which these conditions are satisfied. The real part of the refractive index n is then related to the ambient temperature, pressure, and humidity by Eq. (1-12).

In general the non-ionized atmosphere can influence radar in several ways: a) reflection b) refraction c) absorption by atmospheric gases d) absorption by hydrometeors e) scattering by dielectric inhomogeneities and f) scattering by hydrometeors.

2.2 Reflection and Refraction

Refraction and specular reflection usually have important effects on radar systems only when the propagating wave is incident on stratified atmospheric layers at very small angles. This case is important for surveillance systems in which the radar points nearly horizontally in the presence of atmospheric layers with large vertical gradients of temperature and/or humidity. An exception may be found in the backscatter of long wavelength (VHF) radar energy from the tropopause, where there is some observational evidence that a significant coherent (specular) component exists even at vertical incidence (Röttger, 1978; Gage and Green, 1979, Rastogi and Röttger, 1980).

Ray tracing methods in the fields of optics and acoustics as well as radar are discussed in many papers and texts (e.g., Hazelgrove, 1955). Generally speaking, the ray tracing methods are valid in the atmosphere when the refractive index varies slowly in the WKB sense (Budden, 1961). When ray tracing methods are invalid or cumbersome, a wave-guide approach is often more efficient. The waveguide approach is discussed in detail by Budden (1965). Atmospheric waveguides and ducting will be considered in detail in Chapters 9 and 10.

BEST DOCUMENT AVAILABLE

2.3 Absorption

At microwave frequencies, gaseous absorption occurs in the neighborhood of water vapor and oxygen absorption lines in the spectrum. The absorption spectra for oxygen and water vapor in the microwave band is shown in Fig. 2-1 taken from Bean and Dutton (1968). Gaseous absorption is seldom important in atmospheric studies by radar because radar frequencies are usually chosen to minimize this effect.

On the other hand absorption by hydrometeors is important in many meteorological applications. The effect on the attenuation of radar waves by precipitation particles is summarized in Fig. 2-2 for various rainfall rates. However, for cloud studies it only becomes important at the very short wavelengths. For small spherical scatterers, whose size is much less than a wavelength, the Rayleigh approximation is applicable and the absorption crossection Q_a of a single sphere is given by (e.g., see-Batton, 1973)

$$Q_a = (\pi^2 D^3/\lambda)\left[\mathrm{Im}\left(-\frac{m^2 - 1}{m^2 + 2}\right)\right] \qquad (2\text{-}1)$$

where $m = n\text{-}ik$ is the complex index of refraction of the scatterer (e.g., liquid water), λ is wavelength, and D is diameter of the sphere. The attenuation of the radar wave by hydrometeors is the sum of their absorption and the loss of energy scattered out of the beam. The attenuation by clouds (as related to visibility) and precipitation (as related to rainfall rate) is shown in Fig. 2-2.

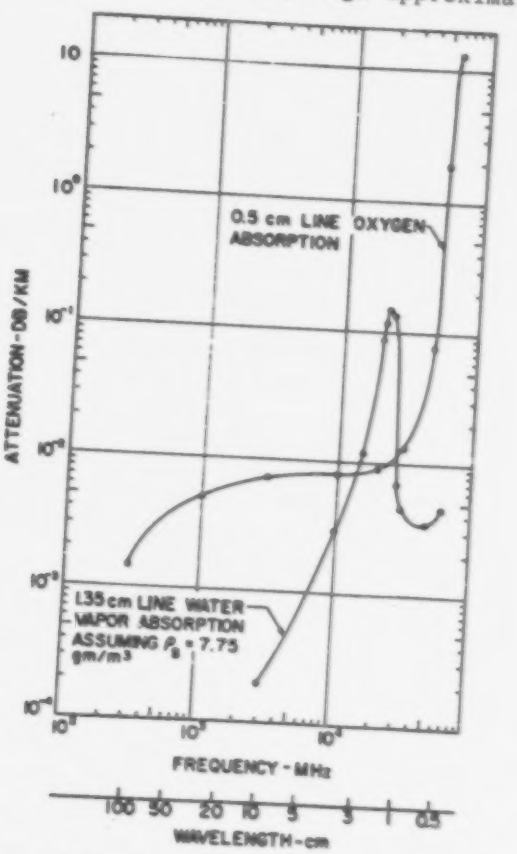

Figure 2.1--Microwave attenuation due to gaseous absorption by water vapor and oxygen (from Bean and Dutton, 1966).

2.4 SCATTERING

Scattering by both hydrometeors and by turbulence in the clear air is very important in many meteorological applications. A concise derivation of the radar equation, which includes

BEST DOCUMENT AVAILABLE

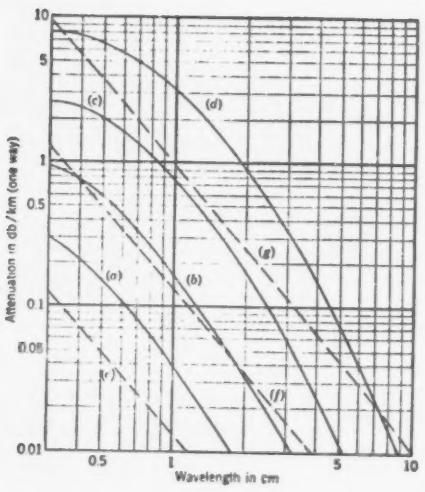

Figure 2.2--Theoretical values of attenuation by rain and fog. Solid curves show attenuation in rain of intensity. (a), 0.25 mm/hr (drizzle); (b) 1 mm/hr (light rain); (c), 4 mm/hr (moderate rain); (d), 16 mm/hr (heavy rain). Dashed curves show attenuation in fog or cloud; (e), 0.032 g/m^3 (visibility about 600 m); (f) 0.32 g/m^3 (visibility about 120 m); (g), 2.3 g/m^3 (visibility about 30 m). (From Kerr, 1951.)

the radar system parameters, is given in the Appendix. At this point it is necessary to introduce the concept of "reflectivity" resulting from scattering. It will be derived in terms of the incident electric field, and independent of radar systems.

The electric moment per unit volume induced in a scatterer is

$$(4\pi)^{-1}\ (\varepsilon-\varepsilon_o)E \qquad (2\text{-}2)$$

where ε is the (uniform) dielectric constant of the scatterer, ε_o is the ambient dielectric constant of the propagation medium and E is the electric field in the scatterer. The total moment for a scatterer of volume V is then

$$f = (\varepsilon-\varepsilon_o)(EV/4\pi). \qquad (2\text{-}3)$$

The scattered field E_s at a distance r_s from a dipole of moment f is given by

$$E_s = \frac{k_s^2\ f\ \sin\psi}{\varepsilon_o\ r_s} \exp(-i\ \underset{\sim}{k}_s \cdot \underset{\sim}{r}_s) \qquad (2\text{-}4)$$

where $k_s = 2\pi/\lambda$ is the wavenumber of the wave scattered in the direction $\underset{\sim}{r}_s$, and ψ is the angle between the direction of polarization of the incident electric field and the direction of $\underset{\sim}{k}_s$.

If some small sphere of undefined composition with dielectric constant ε is considered, the electric field E induced in the sphere is (e.g., Gans, 1912)

BEST DOCUMENT AVAILABLE

$$E = E_o \left(\frac{3}{2+\varepsilon/\varepsilon_o}\right) \exp i(\omega t - \underset{\sim}{k}_o \cdot \underset{\sim}{r}_o) \tag{2-5}$$

where E_o is the magnitude of the incident electric field and ω is the radio-frequency in radians per second. The vectors $\underset{\sim}{r}_o$ and $\underset{\sim}{k}_o$ are the range from the source and the wavenumber of the incident wave respectively, and their dot product gives the phase at the scatterer. Therefore

$$E_s = \{E_o \frac{k_s^2}{r_s} \left(\frac{D}{2}\right)^3 \left(\frac{\varepsilon/\varepsilon_o - 1}{\varepsilon/\varepsilon_o + 2}\right)\} \sin\chi \exp i(\omega t - \underset{\sim}{k}_s \cdot \underset{\sim}{r}_s - \underset{\sim}{k}_o \cdot \underset{\sim}{r}_o) \tag{2-6}$$

where E_s is the scattered field at r_s and $V = (\pi/6)D^3$.

For atmospheric targets there are usually many scatterers within the radar resolution volume. It is convenient to assume a monodispersive drop size distribution whose drops are all of diameter D. This constraint will be relaxed later. Letting $N\, d\underset{\sim}{r}_o$ be the number of drops in the position increment between $\underset{\sim}{r}_o$ and $\underset{\sim}{r}_o + d\underset{\sim}{r}_o$, Eq. (2-6) becomes

$$E_s = E_o(k_s^2/4\pi r_s)\ 3\ KV \sin\psi \int_{\underset{\sim}{r}_o} N(r_o) \exp i(\omega t - \underset{\sim}{k}_s \cdot \underset{\sim}{r}_s - \underset{\sim}{k}_o \cdot \underset{\sim}{r}_o) d\underset{\sim}{r}_o \tag{2-7}$$

where $K = (\varepsilon/\varepsilon_o - 1)/(\varepsilon/\varepsilon_o + 2) \simeq (\varepsilon - \varepsilon_o)/(\varepsilon + 2\varepsilon_o)$ and $V = (4/3)\,\pi(D/2)^3$ is the volume of the spherical scatterer. We have assumed that all the drops in the volume are illuminated by the same incident electric field strength; i.e., the radial extent (Δ) is much smaller than r_s and the cross-beam illumination is a step function. This latter constraint will be eliminated later. From definitions and geometry

$$\underset{\sim}{k}_o \cdot \underset{\sim}{r}_o + \underset{\sim}{k}_s \cdot \underset{\sim}{r}_s = \underset{\sim}{k}_s \cdot (\underset{\sim}{r}_s + \underset{\sim}{r}_o) + (\underset{\sim}{k}_o - \underset{\sim}{k}_s) \cdot \underset{\sim}{r}_o \equiv 2\underset{\sim}{k}_s \cdot \underset{\sim}{r} + \underset{\sim}{\kappa} \cdot \underset{\sim}{r}_o \tag{2.8}$$

where the definitions $\underset{\sim}{\kappa} \equiv \underset{\sim}{k}_o - \underset{\sim}{k}_s$ and $\underset{\sim}{r} \equiv (\underset{\sim}{r}_s + \underset{\sim}{r}_o)/2$ have been adopted. From Fig. 2-3

$$\kappa = 2k \sin(\theta/2) \tag{2-9}$$

where $k = |k_s| = |k_o|$. Recalling that average power is proportional to $\overline{E\,E^*}$, where the overbar indicates time average and the asterisk means complex conjugate, we have for the envelope of the scattered power

$$P_s = P_o\, k_s^4\, 9|K|^2 V^2 (\sin^2\psi)\, I/(4\pi r_s)^2 \tag{2-10}$$

BEST DOCUMENT AVAILABLE

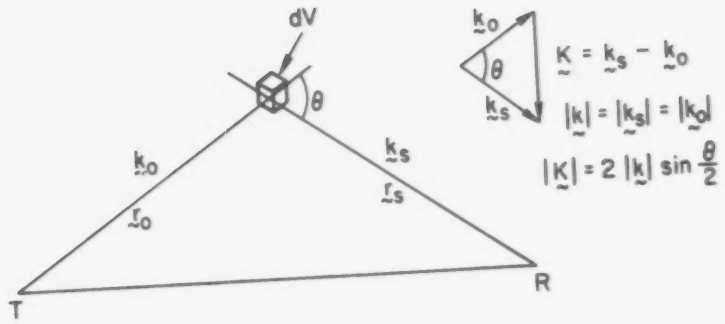

Figure 2.3--Schematic of scattering geometry due to volume element dV between transmitter T and receiver R. Defines the relationship between the various wavenumbers.

where $I = \overline{|\int N(\underset{\sim}{r}_o)\ \exp(-i\ \underset{\sim}{\kappa}\cdot\underset{\sim}{r}_o)d\underset{\sim}{r}_o|^2}$. Now suppose the number density distribution function $N(\underset{\sim}{r}_o)$ to be composed of a deterministic and a random (in some sense) part, i.e., $N = \bar{N}(r_o) + \delta N(r_o)$. The deterministic part will in general lead to partial reflection from large scale gradients of N within the radar beam, and it will be ignored in the present context. Then

$$I = \iint \overline{\delta N(\underset{\sim}{r}_1)\delta N(\underset{\sim}{r}_2)}\ \exp[i\underset{\sim}{\kappa}\cdot(\underset{\sim}{r}_1-\underset{\sim}{r}_2)]d\underset{\sim}{r}_1\ d\underset{\sim}{r}_2 \qquad (2\text{-}11a)$$

$$I = \iint \overline{\delta N(\underset{\sim}{r}_o)\delta N(\underset{\sim}{r}_o+\underset{\sim}{\ell})}d\underset{\sim}{r}_o\ \exp(-i\underset{\sim}{\kappa}\cdot\underset{\sim}{\ell})d\underset{\sim}{\ell} \qquad (2\text{-}11b)$$

where $\underset{\sim}{\ell}$ is the separation of a certain scatterer from some reference position $\underset{\sim}{r}_o$ in the scattering volume. It is convenient to define a spatial correlation function

$$C(\ell) = \frac{1}{\overline{\delta N^2}V}\int_V \overline{\delta N(\underset{\sim}{r}_o)\delta N(\underset{\sim}{r}_o+\underset{\sim}{\ell})}d\underset{\sim}{r}_o\ . \qquad (2\text{-}12)$$

where V is now the scattering volume rather than the volume of a single drop. To carry out the volume integration it is simplest to define a coordinate system relative to the transmission direction, i.e., from transmitter to the scattering element dV. (See Fig. 2-4.) Thus θ is the angle to the scattering element dV off the direction from transmitter to the center of the scattering volume, ℓ is the separation of the scatterer from the volume center and ϕ is the azimuthal angle about the transmission direction. Therefore the differential volume element $d\underset{\sim}{\ell}$ is

BEST DOCUMENT AVAILABLE

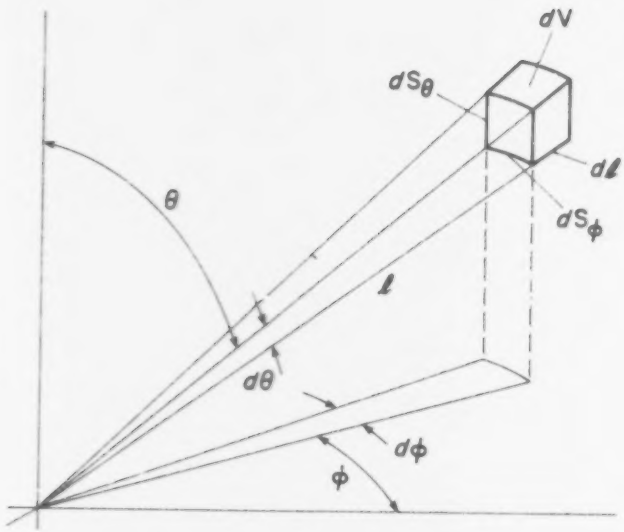

$$dS_\theta = \ell\, d\theta$$

$$dS_\phi = \ell \sin\theta\, d\phi$$

$$dV = d\ell\, dS_\theta\, dS_\phi = \ell^2\, d\ell \sin\theta\, d\theta\, d\phi$$

Figure 2.4--Schematic picture of spherical coordinate system with definition of symbols.

$$d\underset{\sim}{\ell} = dV = \ell^2 d\ell \sin\theta d\theta d\phi \qquad (2\text{-}13)$$

so

$$I = \overline{\delta N^2}\, V \int_0^\infty \ell^2 C(\ell) d\ell \int_0^{2\pi} \int_\pi^{-\pi} [\exp(-i\kappa\ell\cos\theta)]\sin\theta d\theta d\phi \qquad (2\text{-}14a)$$

or

$$I = \overline{\delta N^2} V \frac{4\pi}{\kappa} \int_0^\infty \ell C(\ell) \sin\kappa\ell \, d\ell \, . \qquad (2\text{-}14b)$$

The choice of ∞ as an upper limit for ℓ is justified by the assumption that $C(\ell)$ falls off fast enough so that the contribution for large ℓ is negligible.

A function often chosen for $C(\ell)$ because of its mathematical simplicity is

$$C(\ell) = \exp(-\ell/\ell_o). \qquad (2\text{-}15)$$

BEST DOCUMENT AVAILABLE

Then

$$I = \overline{\delta N^2} V \frac{8\pi \ell_o^3}{(1+\ell_o^2\kappa^2)^2} \quad , \tag{2-16}$$

a result first obtained by Booker and Gordon (1950).

It is easy to establish the relation of scattered power to the power spectrum $\phi(\kappa)$ of scatterer concentration (number per unit volume) by recalling the relation of $\phi(\underset{\sim}{\kappa})$ to the correlation function, i.e., the one dimensional line spectrum is

$$\phi_1(\kappa) = \frac{2}{\pi} \overline{\delta N^2} \int_0^\infty C(\ell) \cos\kappa\ell \, d\ell, \tag{2-17}$$

where ℓ is scalar separation of scatterers along a line. Choosing $C(\ell)$ exponential as before,

$$\phi_1(\kappa) = \frac{2}{\pi} \overline{\delta N^2} \frac{\ell_o}{1+\ell_o^2\kappa^2} \, . \tag{2-18}$$

However, Kovasnay et al. (1949) pointed out that the power spectral density $E(\kappa)$ is related to the one dimensional spectrum of isotropic, homogeneous fluctuations such that [see Eq. (6E) of Appendix E]

$$E(\kappa) = -\kappa \frac{\partial \phi_1(\kappa)}{\partial \kappa} \, . \tag{2-19}$$

Therefore

$$E(\kappa) = \frac{\overline{4\delta N^2}}{\pi} \frac{\kappa^2 \ell_o^3}{(1+\ell_o^2\kappa^2)^2} \, . \tag{2-20}$$

Furthermore, if the scatterer concentration fluctuations are isotropic, the spectrum of vector $\underset{\sim}{\kappa}$ is related to the power spectrum of scalar κ simply as [see e.g., Bolgiano (1958), also Eq. (5E) of Appendix E]

$$\phi(\underset{\sim}{\kappa}) = \frac{E(\kappa)}{4\pi\kappa^2} = \frac{\overline{\delta N^2}}{\pi^2} \frac{\ell_o^3}{(1+\ell_o^2\kappa^2)^2} \, . \tag{2-21}$$

Because $\phi(\underset{\sim}{\kappa})$ is the spectrum of number density it has dimensions of $(\text{length})^{-3}$. Comparing (2-16) and (2-19,20,21) it is readily seen that

$$I = 8\pi^3 V \phi(\underset{\sim}{\kappa}) \tag{2-22}$$

or

$$I = 2\pi^2 V \frac{E(\kappa)}{\kappa^2} = -2\pi^2 V \frac{1}{\kappa} \frac{\partial \phi_1(\kappa)}{\partial \kappa} \, . \tag{2-23}$$

BEST DOCUMENT AVAILABLE

This remarkably simple relationship between the scattered power and the spectrum of the scatterers is perfectly general as pointed out by Villars and Weisskopf (1955).

Scatter from Clouds and Precipitation

In calculating the scatter from cloud and precipitation particles it is usually assumed that the scatterer concentration is random in the sense that the particle concentration in neighboring parcels is completely uncorrelated where the meaning of "parcel" is an atmospheric volume of size approximately $(\lambda/2)^3$. If the number of scatterers $\delta N(\underset{\sim}{r}_1)d\underset{\sim}{r}_1$ is independent of $\delta N(\underset{\sim}{r}_2)d\underset{\sim}{r}_2$, the mean of the product in (2-11a) is zero except when $r_1 = r_2$; then,

$$I = \int_V \overline{[\delta N(\underset{\sim}{r})]^2}\, d\underset{\sim}{r} = \int_V \bar{N}(\underset{\sim}{r})d\underset{\sim}{r} = N_T \,, \tag{2-24}$$

the total number of drops in the volume. That the variance is equal to the mean follows from the assumption of a random array of scatterers [e.g., Present (1958)].

Then from Eq. (2-6)

$$P_s = P_o \frac{k_s^4}{(4\pi)r_s^2} 4\pi\, |K|^2 (D/2)^6 N_T \sin^2\chi \tag{2-25}$$

where N_T is the total number of drops. A scattering cross-section σ is often defined as

$$P_s = \frac{P_o \sigma}{4\pi r_s^2} \tag{2-26}$$

so

$$\sigma = V\eta = 4\pi k_s^4 |K|^2 \left(\frac{D}{2}\right)^6 (\sin^2\chi)\, N_T = (\pi^5/\lambda^4)\, |K|^2 D^6 (\sin^2\chi)\, N_T \tag{2-27}$$

and η is of the same form as σ if N_T is replaced by number of drops per unit volume.

Of course, in the case of cloud or precipitation particles the number distribution is not adequately represented by a single diameter D as assumed above. Instead the population of drops in the volume is represented by some type of size distribution N_D, where the number of drops in the size interval D to D+dD is $N_D\, dD$. The total number of drops in the volume is then

BEST DOCUMENT AVAILABLE

$$N_T = \int_0^\infty N_D \, dD \, . \tag{2-28}$$

The total reflectivity is therefore proportional to

$$Z_T = \int_0^\infty N_D \, D^6 \, dD. \tag{2-29}$$

In order to distinguish this quantity from the reflectivity η, it is called the "reflectivity factor" Z (or Z_T when it is desirable to distinguish total Z from its value for a limited range of drop sizes). Thus, defining the reflectivity as

$$\eta = \frac{\pi^5}{\lambda^4} |K|^2 \sin^2\chi \int_0^\infty N(D) D^6 dD; \tag{2-30}$$

evaluated per unit volume, we find

$$\eta = (\pi^5 |K|^2 / \lambda^4) \sin^2\chi \, Z_T \tag{2-31}$$

which is the usual expression for reflectivity for backscatter from clouds and precipitation found in all textbooks except for the $\sin^2\chi$ factor which is just unity in backscatter.

The possibility that number density in neighboring parcels is not completely uncorrelated in precipitation was considered briefly by Goldstein and by Seifert in Kerr (1951) and rejected as an important consideration. However, it is not so evident that a coherent (Bragg) scatter is negligible in clouds, where number densities can be as high as 1000 cm^{-3}, and this possibility was considered from a theoretical standpoint by Smith (1964), by Naito and Atlas (1964) and by Chernikov (1968). The subject was apparently never pursued further because of the difficulty of measuring cloud number density spatial spectra, which Eq. (2-22) shows to be the decisive factor in the relative importance of incoherent vs. Bragg scatter from clouds. Equation (2-25) shows that incoherent scattered power has an inverse 4th power wavelength dependence, so short wavelength radars favor the incoherent return. If the cloud droplet spatial spectrum is approximately that of a passive scalar mixed by mechanical turbulence, $\phi(\kappa)$ should vary as approximately $\lambda^{11/3}$, nearly canceling the inverse 4th power dependence so the Bragg-coherent backscattered power should fall off only slightly with increasing wavelength. Until recently, most radars used for tropospheric weather observation had wavelengths of 30 cm or less and cloud returns might be ex-

BEST DOCUMENT AVAILABLE

pected to be dominated by incoherent backscatter. With the modern use of radars at several meters wavelength for sounding the clear (and cloudy) atmosphere, the question should be reexamined.

In the case of a cloud at saturation the question arises as to whether condensation will lead to more drops or to growth of existing drops or both. The answer probably depends on the number and kind of nuclei present, the temperature and the degree of super saturation. The question can be largely avoided by dealing with liquid water content rather than number density. Thus a distribution function M_D for mass of liquid water can be defined such that the total mass of liquid water per unit volume is

$$M_T = \int M_D \, D^3 \, dD = \rho_{L,I}(\pi/6) \int N_D \, D^3 \, dD \tag{2-32}$$

where $\rho_{L,I}$ is the density of liquid water or ice. The correlation function analogous to (2-12) is

$$C(\ell) = \frac{1}{\overline{\delta M^2}\, V} \int_V \overline{\delta M(\underset{\sim}{r}_o)\, \delta M(\underset{\sim}{r}_o + \underset{\sim}{\ell})} \, d\underset{\sim}{r}_o \tag{2-33}$$

so Eq. (2-10) becomes

$$P_s = P_o \, k_s^4 \, 9|K|^2 \rho^{-2} \sin^2\psi \; I/(4\pi r_s)^2 \tag{2-34}$$

where

$$I = \overline{\delta M^2}\, V \frac{4\pi}{\kappa} \int \ell C(\ell) \sin\kappa\ell \, d\ell \tag{2-35}$$

$$I = 8\pi^3 \, V \, \phi_M(\underset{\sim}{\kappa}) \; . \tag{2-36}$$

Scatter From the Clear Air

If we consider scatter from the molecules of the clear air, it is evident that the incoherent scatter will be negligible at radar wavelengths because D^6/λ^4 is such a small factor. However, the mean product in (2-11a) may not be zero because of fluctuations in dry air density (temperature) or in water vapor density due to turbulent mixing on scales of the order of $\lambda/2$. If there is variation of dielectric on this scale, the incident electric field will polarize small volumes which deviate from the average by $\delta\varepsilon$ and each small element will behave like a dipole of moment $f = (E/4\pi)\delta\varepsilon \, V$. Substituting f in Eq. (2-5), the power-scattered from such a continuous medium

BEST DOCUMENT AVAILABLE

is found. For small deviations in ε, $3K \approx (\Delta\varepsilon/\varepsilon_o)$. Comparing such a medium with spatial fluctuations in ε instead of the previous medium composed of discrete droplets of constant $\Delta\varepsilon$ but variable concentration N, it is readily seen that $\delta\varepsilon/\varepsilon_o$ is analogous to $3K\,N\forall$ in Eq. (2-10); thus,

$$P_s = P_o[k_s^4/(4\pi r_s)^2]\sin^2\chi\; I \tag{2-37}$$

where

$$I = \overline{\left| \int_V \frac{\delta\varepsilon}{\varepsilon_o}(\underset{\sim}{r}_o)\exp(-i\underset{\sim}{\kappa}\cdot\underset{\sim}{r}_o)d\underset{\sim}{r}_o \right|^2}$$

has dimensions of $(\text{length})^6$. By a derivation analogous to that of Eq. (2-22)

$$I = 8\pi^3 V\phi_\varepsilon(\underset{\sim}{\kappa}) \tag{2-38}$$

where $\phi(\underset{\sim}{\kappa})$ is now the spectrum of atmospheric dielectric fluctuations and has dimensions of $(\text{length})^3$. It is often more convenient to express the problem in terms of the refractive index m given by

$$m = \sqrt{\mu\varepsilon}$$

where the permeability μ is essentially unity for air. But $m = n - ik \approx n$ except near absorption lines in the spectrum, so $\varepsilon \approx n^2$ and $\delta\varepsilon \approx 2n\delta n$. Therefore

$$\overline{\delta\varepsilon(r)\;\delta\varepsilon(r-\ell)} \approx 4\;\overline{\delta n(r)\;\delta n(r-\ell)} \tag{2-39}$$

since $\varepsilon_o \approx n_o \approx 1.0$. Thus, using Eq. (2-20), we see that

$$\phi_\varepsilon(\kappa) = 4\phi_n(\kappa)$$

where $\phi_n(\kappa)$ is the spectrum of n. Therefore

$$P_s = P_o\, V\, \frac{8\pi^4}{\lambda^4}\;\frac{\sin^2\chi}{r_s^2}\;\frac{\phi_n(\kappa)}{\kappa^2}\;. \tag{2-40}$$

Defining the reflectivity η as in Eqs. (2-24,26,27), we find from Eq. (2-40) that

$$\eta = \frac{32\pi^5}{\lambda^4}\;\sin^2\chi\;\frac{\phi_n(\kappa)}{\kappa^2} = 8\pi^2\, k_s^4\,\phi_n(\underset{\sim}{\kappa})\,\sin^2\chi. \tag{2-41}$$

BEST DOCUMENT AVAILABLE

Scattering and the Refractive Index Structure Parameter

It is often convenient to express the scattering properties of the clear atmosphere in terms of the structure parameter of refractive index (C_n^2) which is most easily defined in terms of the structure function $D_n(\ell)$ given by

$$D_n(\ell) \equiv \overline{[\delta n(r) - \delta n(r-\ell)]^2} \quad . \tag{2-42}$$

In the inertial subrange of homogeneous, isotropic turbulence it is found that

$$D_n(\ell) = C_n^2 \, \ell^{2/3} \tag{2-43}$$

where C_n^2 is a proportionality constant called the structure parameter. Ottersten (1969) shows that Tatarskii's (1961) exposition leads to the conclusion that the one dimensional spectrum is given by

$$\phi_{1n}(\kappa) = (1/4) C_n^2 \, \kappa^{-5/3} \tag{2-44}$$

in the inertial subrange of homogeneous, isotropic turbulence. Then, using Eq. (2-19)

$$\phi_{1n}(\kappa) = (3/5) \, \phi_n(\kappa), \tag{2-45}$$

and then Eqs. (2-42) and (2-44), we find

$$\eta = \pi(\tfrac{5}{6}) \, (\tfrac{2\pi}{\lambda})^4 \, C_n^2 \, \kappa^{-11/3} \, \sin^2\psi. \tag{2-46}$$

Therefore, three primary measures of the scattering property of the atmosphere are widely used — Z, η and C_n^2 depending on the nature of the scattering problem to be solved; the scattering cross-section σ is usually used for single discrete targets. The various relationships between reflectivity (η), spectrum (ϕ) and structure parameter (C_n^2) are summarized in Table 2-1. The minimum detectable values of η, Z and C_n^2 are a measure of the sensitivity of the radar and processing system. These are tabulated for a variety of cloud/storm sensing, radars and clear-air radar sounders in Tables 3-1a and 3-1b. We will now discuss the properties of the clear air that determine η and C_n^2.

BEST DOCUMENT AVAILABLE

Table 2-1

$\eta_N = 2\pi^2 k^4 \lvert 3K\rvert^2 V^2 \Phi_N(\kappa) \sin^2\chi$	Reflectivity in terms of concentration spectrum (in vector κ) of spherical particle ensembles.
$\eta_\epsilon = 2\pi^2 k^4 \Phi_\epsilon(\kappa) \sin^2\chi$	Reflectivity in terms of spatial spectrum of fluctuations in gas dielectric constant.
$\eta_n = 8\pi^2 k^4 \Phi_n(\kappa) \sin^2\chi$	Reflectivity in terms of spatial spectrum of refractive index fluctuations.
$\eta_n = 2\pi k^4 \kappa^{-2} \Phi_n(\kappa) \sin^2\chi$	Reflectivity in terms of spatial spectrum in scalar κ for isotropic fluctuations of refractive index.
$\eta_n = (5/6)\pi k^4 \kappa^{-11/3} C_n^2 \sin^2\chi$	Reflectivity in terms of structure parameter of turbulent refractive index fluctuations assuming -5/3 spectrum.

Refractive Index Variance of Clear Air

The radio refractive index of non-ionized air depends on temperature, humidity and pressure (e.g., Bean and Dutton, 1966; Kerr, 1951) as given by Eq. (1-12). It is often convenient to express water vapor pressure in terms of moisture density Q_V. To do this note that the vapor pressure e in millibars is related to Q_V such that

$$e = P(Q_V/\rho)/(0.622 + Q_V/\rho) \simeq P(Q_V/\rho)/0.622 \qquad (2\text{-}47)$$

where 0.622 is the ratio of the molecular weight of water to that of dry air, P is pressure and ρ is air density). Then Eq. (1-12) becomes

$$(n-1) \times 10^6 = (77.6\ P/T)(1 + 7.733\ Q_V/T) \qquad (2\text{-}48a)$$

$$= (77.6/T)(P + 7.733\ R\ Q_V)\ . \qquad (2\text{-}48b)$$

In (2-48b) we have used the equation of state $\rho = PRT$, where R is the gas constant $\simeq 2.88 \times 10^{-3}$ if P is in millibars.

It is useful to consider the influence of fluctuations in P, T and Q_V on n. It is then found (e.g., Gossard, 1977) that

BEST DOCUMENT AVAILABLE

$$\delta n \times 10^6 = -1.43\ \delta T + 7.65\ \delta Q_V + 0.34\ \delta P \qquad (2\text{-}49)$$

where average values of T = 280 K, P = 1000 mb and Q_V = 8 g kg^{-1} have been chosen as representative. The variance in n is then

$$\overline{\delta n^2} \times 10^{12} = 58.5\ \overline{\delta Q_V^2} + 2.04\ \overline{\delta T^2} - 21.9\ \overline{\delta T\ \delta Q_V} + 5.2\ \overline{\delta P\ \delta Q_V} + 0.115\ \overline{\delta P^2} - 0.97\ \overline{\delta T\ \delta P} \qquad (2\text{-}50)$$

in the order of the usual decrease of importance of the terms. The variance of pressure seldom exceeds .01 mb in the turbulence range of wavenumbers and will be ignored for present purposes.

Effect of Temperature-Humidity Covariance

The importance of the cross-product terms depends on the degree of correlation of the different quantities and is quite variable under clear-air conditions. However, it was pointed out by Gossard (1960a) that the temperature-humidity correlation term can be negative under clear-air conditions. He reported measurements obtained with humidity and temperature sensors carried by a captive balloon flown near San Diego in southern California. Figure 2-5 shows spectra obtained with and without the contribution of the cross-spectrum at a height of 420 m MSL (400 m AGL) in (1) a convectively unstable boundary layer and (2) beneath an intense subsidence inversion. The covariance was negative and large under unstable conditions and therefore added (by almost a factor of two) to the power in the refractive index spectrum. Under stable conditions the total power was about two orders of magnitude less and there was no significant consistency to the cross spectral contribution.

Wyngaard et al. (1978) have shown that the spectral form of the cross spectrum in the inertial subrange of turbulence should be the same as the form of the power spectra of temperature and humidity. Using aircraft-borne sensors, they also find negative covariance in the upper portion of convective boundary layers, but they find positive correlation near the surface.

BEST DOCUMENT AVAILABLE

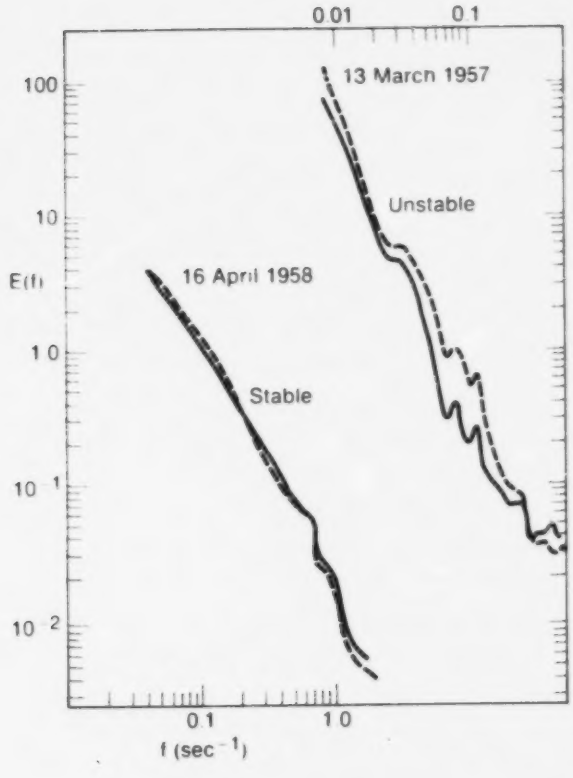

Figure 2.5--Refractive index spectra computed from temperature and vapor pressure spectra with (solid line) and without (dashed line) cospectrum of temperature and humidity. 13 March was convectively unstable; 16 April was relatively stable. (Gossard, 1960.)

2.5 Bragg Scatter from the Air Compared with Bragg Scatter from a Droplet Medium

In order to compare the amount of Bragg scattering from spatial fluctuations of the dielectric constant of air with scattering from fluctuations in the liquid water content of cloud, it is convenient to define an "equivalent refractive index" δn_e for variations in the water droplet population analogous to the refractive index δn representing the variations in the dielectric constant of air. To do this we simply note that equations (2-10) and (2-37) [using (2-39)] have the same form if an equivalent refractive index for the liquid medium is defined such that

$$\overline{\delta n_e^2} \times 10^{12} = (9/4)^2 \, |K|^2 \, \overline{\delta M^2}/\rho_{L,I}^2 \, . \qquad (2\text{-}51)$$

It is more common to express liquid water content, as mixing ratio $Q_{L,I}$, defined as mass of water (or ice) per mass of dry air. The density of dry air is $\rho_a \approx 10^3$ g m^{-3}, so the mass of liquid water per gram of dry air is $M/\rho_a \approx M \times 10^{-3}$, i.e., $Q_L \approx M$ if mixing ratio is expressed in g kg^{-1}. The density of water is $\rho_L \approx 10^6$ g m^{-3} and of ice is $\rho_I \approx 0.9 \times 10^6$ g m^{-3}. Therefore (2-51) shows that

BEST DOCUMENT AVAILABLE

$$\overline{\delta n_e^2} \times 10^{12} = (9/4)\,|K|^2(\rho_a/\rho_{L,I})^2\,\overline{\sigma Q_{L,I}^2} = \begin{cases} 2.09\ \overline{\delta Q_L^2}\ \text{(water)} \\ 0.52\ \overline{\delta Q_I^2}\ \text{(ice)}\ . \end{cases} \qquad (2\text{-}52)$$

Comparing Eq. (2-52) with the first term on the right hand side of Eq. (2-50), it is possible to estimate the relative magnitudes of scattering from clear-air inhomogeneities and of Bragg-coherent scatter from water droplets. However, to do so it is necessary to estimate the relative variances (or structure parameters) of Q_V and $Q_{L,I}$. In general, this is very difficult as no good observational data exist at the relevant scales. However, within a cloud in steady-state at saturation with no precipitation removing water from the cloud and with minimal entrainment, it seems reasonable to assume

$$\delta Q_V = -\delta Q_{L,I}\ . \qquad (2\text{-}53)$$

Equations (2-52) and (2-50) may then be directly compared and we conclude that the dielectric contribution to the Bragg scatter is about 30 times as effective as Bragg scatter from the droplets.

Temperature-Humidity Covariance in Clouds

In addition to the contribution of humidity variance to the refractive index variance, there are contributions from the temperature variance and the cross-covariance between temperature and humidity. The latter contribution could be quite important if they had high negative correlation because a factor of about -22 multiplies the covariance term assuming the mean values chosen for Eq. (2-50).

Based on the Clausius-Clapyron equation, in-cloud temperature perturbations originating in turbulent down-gradient flux should be positively correlated with humidity in saturated air because warm air can hold more water vapor than cold air. However, other models can lead to negative correlation. For example, if dry warm air from outside the cloud is entrained into the cloud, negative correlation might be anticipated in the zone of entrainment, leading to significantly enhanced refractive index perturbations near the edges of the cloud. Furthermore, if the condensation-evaporation process has a finite relaxation time, there is a thermodynamic source of variance. Then the supersaturation resulting from over-shoot leads to nearly perfect, negative covariance between temperature and humidity as shown by Clark and Hall

BEST DOCUMENT AVAILABLE

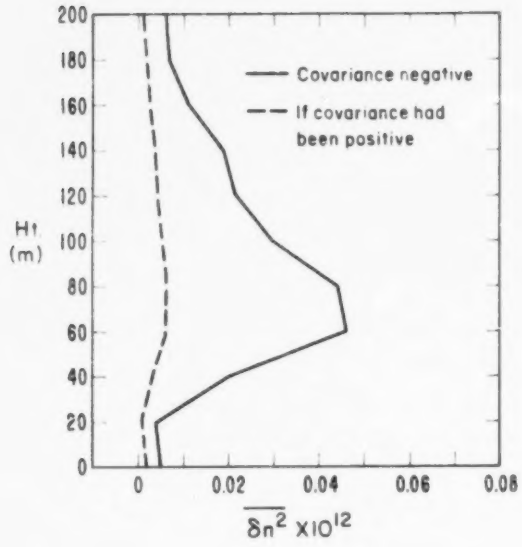

Figure 2.6--In-cloud refractive index variance generated thermodynamically in the Clark and Hill cloud model (solid curve) in which the cross covariance of temperature and humidity is negative. Dashed curve shows the corresponding curve if the covariance had been positive. Here, overbar means spatial average over horizontal planes.

(1979). They deliberately ignored the usual variance generated through turbulence by ignoring large scale gradients of temperature and humidity in their model. The thermodynamic contribution alone was found to produce substantial temperature and humidity variance and covariance. This cross-covariance could thus produce significant enhancement in the general reflectivity of clouds as shown in Fig. 2-6, and the wavelength dependence would certainly depart from that predicted from incoherent scatter from droplets.

2.6 Forward-Scatter Observation of Bragg-Coherence in Clouds

Because the distinction between Bragg-coherent and incoherent scatter reveals itself most clearly in the predicted wavelength dependence, it seems, superficially, that experiments involving several radars of different wavelengths should be used to observe simultaneously the same cloud. There are several difficulties with this experiment: a) Very accurate cross calibration of different radars is necessary. b) The beams of all radars must be matched requiring specially designed, different size antennas. c) The radars must all be observing the same volume which requires that their beams be coaxial. d) The data should all be processed through the same system. The above constraints make such an experiment difficult and expensive, although multiple frequency radar comparisons have been attempted at the Wallops Island facility (Atlas and Hardy, 1966; Naito and Atlas, 1966). Furthermore, a beam matched, bore-sighted pairs of radars (3 and 10 cm) using the same processing system exist at the University of Chicago — Illinois State Water Survey (CHILL) facility.

However, a simpler experiment suggests itself. If we note from Eq. (2-9) that the Bragg wavelength is given by $\lambda_B = (\lambda/2)[\sin(\theta/2)]^{-1}$, it is clear that the effective wavelength λ_B can be used to vary the spectral scale of $\phi(\kappa)$ by varying the scattering angle θ. Thus, a forward scatter experiment in which the beams of the transmitting and receiving antennas are swung simultaneously to vary the scattering angle can be used to obtain the analog of a wavelength dependence using a single radar system, thus avoiding all of the difficulties listed above. Furthermore, the in-cloud spectra can be simply and directly compared with clear-air spectra to reveal possible differences in spectral form of in-cloud and clear air spectra. As of this writing, the only such experiment reported is that described by Gossard and Strauch (1981). In that experiment two Doppler radars of 3.2 cm wavelength were placed at opposite ends of a 28 km baseline between Boulder and Brighton near Denver, Colorado USA. The topography and geometry were carefully chosen such that terrain prevented direct, line-of-sight signal from one radar entering the receiver of the other through antenna sidelobes even when both antennas were aligned along the baseline and pointing toward each other. The terrain profiles along the baseline are shown in Fig. 2-7. The center of the beam is shown at an elevation angle of 1.4° above horizontal at Boulder. At the Brighton site the corresponding elevation angles were 1.7° and 1.9° for the two positions used at Boulder. The lower edge of the beam (the first principal null in the antenna pattern in the vertical plane) was then just tangent to the terrain so that radiation below the main lobe was blocked. The two-way sidelobe suppression was thus about 54 dB and essentially all of the signal can be attributed to the common volume of the main beams of the antenna. The antenna beamwidths (between 3 dB points) were 0.8°. Thus they can be considered to be a narrow beam system in the sense that the effective scattering volume is limited by the common volume of intersection of the transmitting and receiving antennas rather than by the scattering properties of the atmosphere. (Booker and DeBettencourt, 1955.)

The geometry of the forward scatter path is shown in Fig. 2-8 where the scattering angle between the incident and scattered wave directions represented by the vector wave numbers $\underset{\sim}{k}_o$ and $\underset{\sim}{k}_s$ is θ. The distances from the transmitter to the scatterer and from the scatterer to the receiver are $\underset{\sim}{r}_o$ and $\underset{\sim}{r}_s$ respectively. Simple trigonometry shows that the vector difference between $\underset{\sim}{k}_o$ and $\underset{\sim}{k}_s$ has a magnitude of $|k|\ 2\sin(\theta/2)$. It is called the Bragg wavenumber.

The experimental procedure was to vary θ_s by swinging both beams off midpath together. Thus, the altitude of the scattering volume remained the

BEST DOCUMENT AVAILABLE

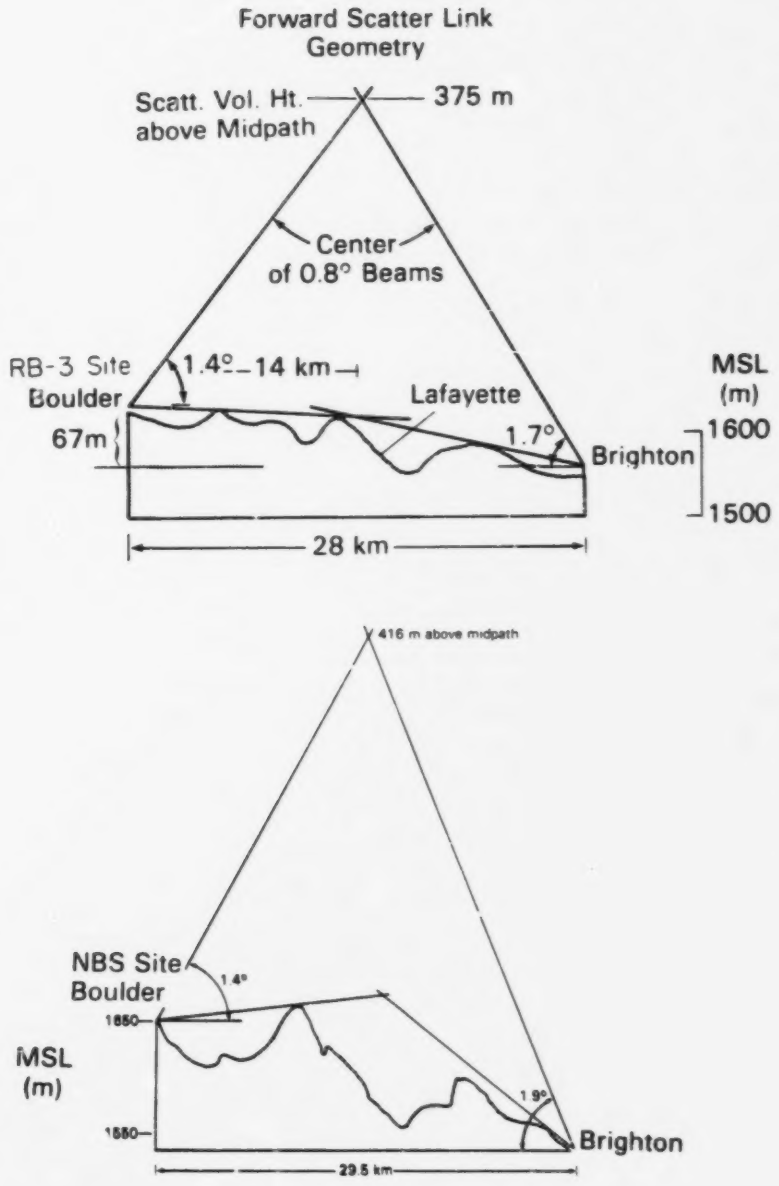

Figure 2.7--Path geometries for in-cloud, forward scatter experiment described in text. (Gossard and Strauch, 1980.)

BEST DOCUMENT AVAILABLE

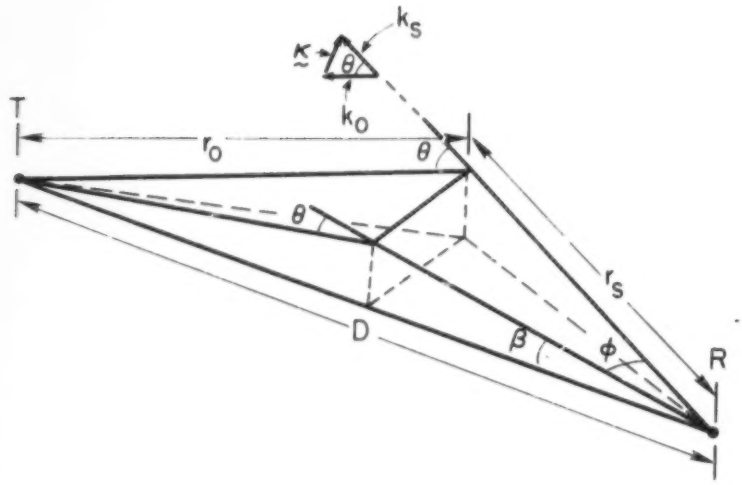

Figure 2.8--Schematic picture of horizontal beamswinging experiment for in-cloud forward scatter experiment described in test. Transmitter and receiver sites are at T and R respectively.

same, and an unambiguous measure of power vs. the Bragg wavenumber was obtained. This relationship will be shown to unambiguously determined the spectrum $\phi(\underset{\sim}{\kappa})$ of the spatial distribution of the scattering ensembles. If the scattering process is coherent in the Bragg sense, the cloud should scatter strongly in the forward direction from transmitter to receiver. If it is fundamentally incoherent, it should be independent of scattering angle because the radars were both vertically polarized. For the geometry given, the minimum scattering angle was 3 - 3.5°. As the beams were swung horizontally, power vs. azimuth patterns were obtained like those shown in Fig. 2-9. The orientation of the baseline from the Boulder site was 91.4° east of true north for one path and 87.1° for the other (labeled NBS). For the site labeled RB-3 the beams were swung toward the south where the path was unobstructed tor 3.5° from the baseline. Farther off-axis, selected azimuths were chosen to ensure that paths were clear of trees or buildings on the horizon. The site labeled NBS was unobstructed on all relevant azimuths. Usually, several elevation angles between 1.4 and 2.0 degrees were used at the Boulder site. Occasional recordings of signal vs. elevation angle on the baseline were made to obtain height profiles of C_n^2 and power spectra.

BEST DOCUMENT AVAILABLE

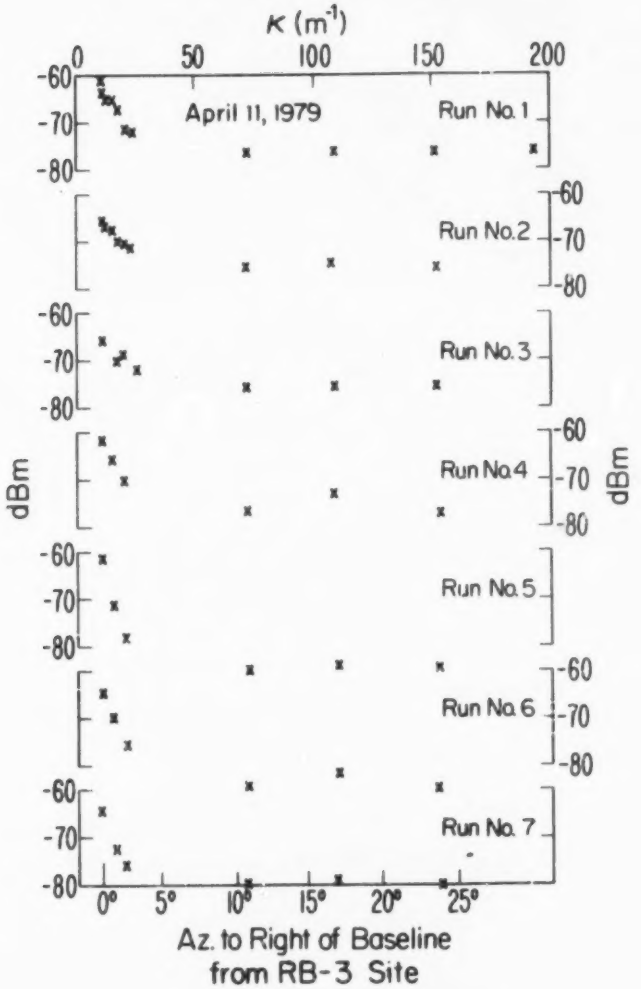

Figure 2.9--Samples of received power in decibels above a milliwatt as beams are swung off the direct path. Decreasing signals at small azimuthal angle represent the region dominated by Bragg scatter. The roughly constant region at azimuths greater than 5° represents the domain dominated by incoherent scatter from hydrometeors.

From Eq. (2-28), the scattered power at distance r_s is

$$P_s = \frac{P_o}{4\pi r_s^2} V\eta \quad . \tag{2-54}$$

The incident power P_o is related to the transmitted power P_T from a source at distance r_o such that

BEST DOCUMENT AVAILABLE

$$P_o = P_T G_T / 4\pi r_o^2 \tag{2-55}$$

where G_T is the gain of the transmitting antenna. The power into the receiver is (see Appendix A)

$$P_R = P_s A_e = P_s G_R \lambda^2 / 4\pi \tag{2-56}$$

where A_e is the effective collecting area of the antenna and where it has been assumed that the gain of the receiving antenna is $G_R = A_e\, 4\pi/\lambda^2 = \pi^2/\alpha_1\alpha_2$ where α_1 and α_2 are two orthogonal one way half power full beamwidths of the antenna.

Combining Eqs. (2-28), (2-55), and (2-56), and assuming $G_R = G_T = G$, $\alpha_1 = \alpha_2 = \alpha$, it is readily found that

$$P_R = \frac{P_T G^2 \lambda^2}{(4\pi)^3 r_s^2 r_o^2} V\eta \ . \tag{2-57}$$

Near midpath $r_s \simeq r_o \simeq D/2$.

If the scattering is completely incoherent in the sense that the total scattered power is just the sum of the powers scattered by all of the individual scatterers, Eq. (2-29) applies and

$$\eta = (\pi/16)k^4 |K|^2 (\sin^2\chi) Z_T \tag{2-58}$$

where $Z_T = \Sigma\, N_i D_i^6$ is a "reflectivity factor" and represents a sum over unit volume of the number of scatterers N_i of diameter D_i per unit volume. For Bragg scatter [Eqs. (2-42) and (2-46)] give

$$\eta = 8\pi^2\, k^4 (\sin^2\chi)\, \phi(\kappa) = (5/6)\pi k^4\, \kappa^{-11/3}\, C_n^2 \ . \tag{2-59}$$

In backscatter, the volume intercepted by the radar beam is

$$V = \pi D^2 \alpha^2\, \Delta/16 \tag{2-60}$$

for a "top-hat" beam, where Δ is the spatial resolution (half the pulse length) and D is the two-way path length.

BEST DOCUMENT AVAILABLE

In forward scatter the total common volume is fairly well represented by two more-or-less conical volumes whose bases are circular sections of diameter $\alpha D/2\cos^2\theta/2$ and whose lengths $L \approx \alpha D/[4 \sin\theta/2, \cos(\theta/2)]$ so

$$V \approx 2(1/3)\pi\alpha^3D^3/64 \cos^5(\theta/2)\sin(\theta/2) \qquad (2\text{-}60a)$$

or

$$V \approx (2\pi/3)\alpha^3D^3/32\theta = \alpha^3D^3/15.3\theta \text{ for } \theta << 1. \qquad (2\text{-}60b)$$

From Eqs. (2-57) and (2-60a) we see that

$$P_R = \{P_TG^2\lambda^2/(4\pi)^2D^2\}\alpha^3D\,\eta/24 \cos^5(\theta/2)\sin\theta/2 \qquad (2\text{-}61)$$

where the factor in braces is often called the "free space" power at distance D, P_F and η is given by either (2-58) or (2-59).

If the spectrum of refractive index for an isotropic medium is presumed to follow some power low, we may write $E(\kappa) = 4\pi\kappa^2\phi(\kappa) = A_n\kappa^{-m}$, where A is a proportionality factor. Then, if θ is small so that $2\sin\theta/2 \approx \theta$, $\kappa \approx k\theta$ and

$$P_R \approx P_F\,\alpha^3Dk^{2-m}(\pi/6)A_n\theta^{-(3+m)}(\sin^2\chi). \qquad (2\text{-}62)$$

For homogeneous, isotropic turbulence in the inertial subrange, $A_n = 5/12\ C_n^2$ where C_n^2 is the turbulent structure parameter and m = 5/3. In the Gossard-Strauch experiment

P_T = 20,000 watts
λ = 0.032 m so k = 196.3 m^{-1}
α = 0.8°
G = $(\pi/\alpha)^2$ = 47 dB
D = 28,000 m
sin χ ≈ 1.0.

From Eq. (2-61) the angular dependence for incoherent scatter will be θ^{-1} for small angles. This dependence results from the change in the size of the scattering volume with angle θ. From Eq. (2-60) the dependence will be $\theta^{-13/3}$ for Kolmogorov spectra in the inertial subrange for small θ.

In addition to the forward scatter measurement, backscatter measurements by both radars were alternated with the forward scatter when the cloud or precipitation conditions provided measurable backscatter.

BEST DOCUMENT AVAILABLE

As seen in the example shown in Fig. 2-9, the forward scatter was always dominated by angle-dependent, Bragg coherent scatter out to about 3-4 azimuthal degrees from the baseline. When there was significant scatter from clouds or precipitation, the return at greater angles was essentially independent of azimuth, providing a clearly identifiable transition from the Bragg-coherent regime to the incoherent regime.

Figure 2-10 shows an example of the kind of observations obtained on a day when clouds and snow precipitation were more-or-less uniformly distributed over the area. The total reflectivity η was computed from the forward scattered power. The incoherent component of the reflectivity was calculated from the backscattered power. In the calculations of $\phi(\kappa)$, the Bragg coherent component was calculated by subtracting the reflectivity in the (incoherent) backscatter from the total reflectivity measured in forward scatter. This procedure was based on the assumption that the coherent component

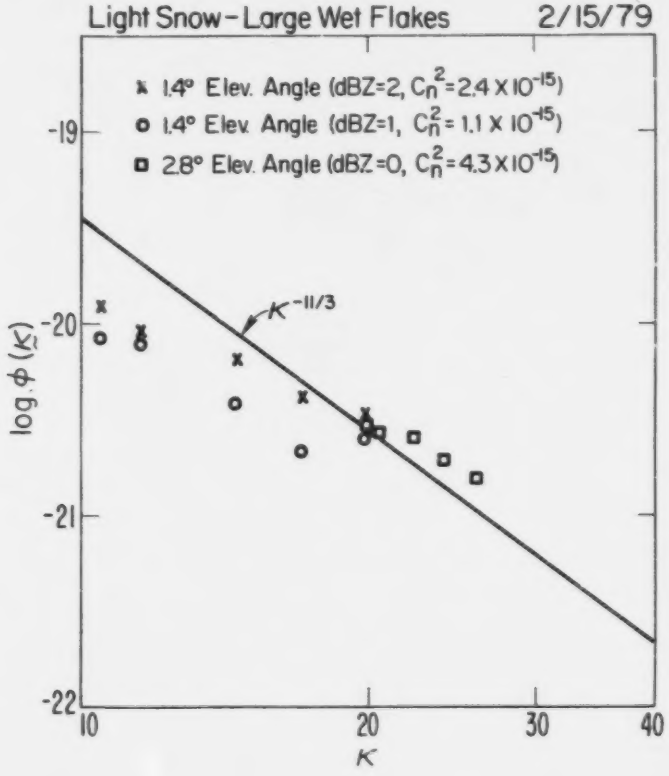

Figure 2.10--Log-log plot of $\phi(\kappa)$ vs. $\kappa = 2k \sin \theta/z$ under light snow conditions. $\phi(\kappa)$ was calculated from received power through equations (2-24) and 2-25). If refractive index fluctuations are created by homogeneous, isotropic turbulence and κ lies within the inertial subrange a slope of -11/3 would be expected.

BEST DOCUMENT AVAILABLE

came from dielectric fluctuations in the gas so that the coherent and incoherent components were additive. Figure 2-11 shows an example from clear air.

Thus, from beamswinging, forward scatter observations can be used to deduce $\phi(\underset{\sim}{\kappa})$ from Eq.(2-62). If the scattering medium is isotropic, the spectrum is independent of the direction of $\underset{\sim}{\kappa}$, so the spectrum (in magnitude of κ) is obtained by integrating over all directions in κ space; thus $E(\kappa) = 4\pi\kappa^2\phi(\underset{\sim}{\kappa})$. If Kolmogorov turbulence in the inertial subrange is assumed to account for the refractive index inhomogeneities, $E(\kappa)$ should obey a $\kappa^{-5/3}$ law and $\phi(\underset{\sim}{\kappa})$ should vary as $\kappa^{-11/3}$. The receiver was at the NBS site for the cases recorded in October 1979..

The average of the least squares fit to all of the data on clear days does, indeed, give a dependence of $\kappa^{-11/3}$. However, data collected in clouds and precipitation show some tendency to fall off less steeply. More quantitative statements are probably not warranted because of the spatial inhomog-

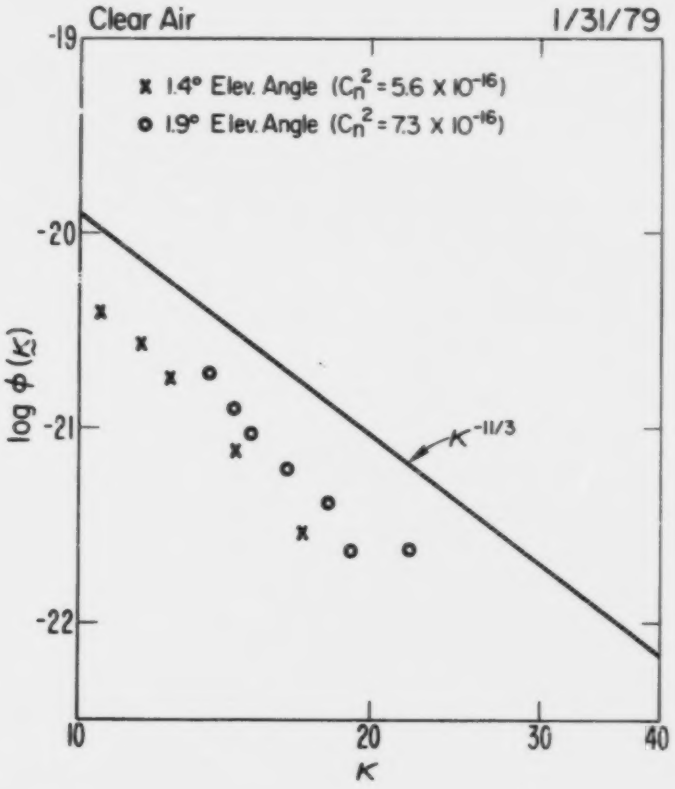

Figure 2.11--Same as 2.10 but under clear-air conditions.

BEST DOCUMENT AVAILABLE

Table 2-2

Date	-(m+2)	$\overline{C_n^2}$	Weather
1/31/79	-4.7	6.5×10^{-16}	Clear
2/15/79	-2.5	2.6×10^{-15}	Cloud
2/27/79	-4.9	4.0×10^{-14}	Clear
3/19/79	-4.2	2.4×10^{-14}	Mixed
4/11/79	-3.43	1.1×10^{-14}	Cloud
10/ 3/79	-2.46	4.4×10^{-15}	Clear
10/ 4/79	-3.10	3.7×10^{-15}	Clear
10/ 9/79	-1.49	1.0×10^{-15}	Cloud/ Lt rain/ snow
	Av. -- 3.7 clear		
	Av. -- 2.9 cloud		

eneity and the rather large temporal variability. These results are summarized in Table 2-2 which is a compilation of the regression coefficients from least-squares fitting of all of the individual beamswinging measurements averaged for each date. The exponent m is the power of the κ dependence of the spectrum if the scatterer spectrum is isotropic; i.e., m = 5/3 for a Kolmogorov spectrum, and m+2 = 11/3. The computation of C_n^2 is done using Eq. (2-63) assuming m = 5/3. An equivalent quantity using the measured value of m has been tabulated as $(C_n')^2$. There is no clear evidence of enhancement of scattered power in cases of clouds, compared with clear air cases, for the winter storm data shown here. The strongest and weakest forward-scattered signals were found on clear days. However, it should be emphasized that all of these observations were made in winter-time, horizontally homogeneous stratiform clouds generated by up-slope flow over the Colorado plains resulting from large scale synoptic conditions. It seems likely that other cloud types, such as violent convective systems, might display drastically different characteristics. Of particular interest is the sign and magnitude of the cross covariance of temperature and humidity in the various cloud types and its spatial distribution.

The regression coefficients were calculated for all cloud cases and used in Fig. 2-12 to plot the regression line representing the crossover between the dominance of Bragg-coherent backscatter and incoherent scatter from droplets for some radars of common wavelength. Thus, for a 6 meter wavelength radar Bragg scatter would dominate for any droplet dBZ values less

BEST DOCUMENT AVAILABLE

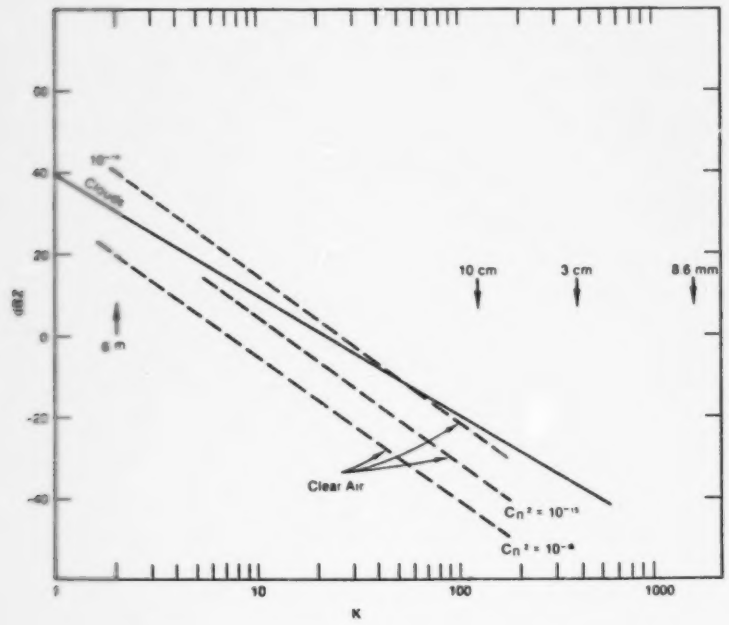

Figure 2.12--A regression fit of power vs. κ for all data under cloud conditions compared with that to be expected for clear-air conditions of various C_n^2 intensity.

than about +57. At the other extreme, for an 8.6 mm wavelength radar, droplet incoherent scatter would dominate for reflectivity factors of dBZ > -43.

On 31 January and 15 February, forward-scatter scans in the vertical crossection including the baseline were made from elevation angles of 1.4° (at Boulder) to about 3.5°. For greater elevation angles there was significant blockage by tree limbs. The case of 31 January is shown in Fig. 2-2-13. The weather was clear with fair skies, and the forward scatter was very weak. Lenticular clouds were present over the mountains and the weather was typical of mild local Chinook conditions. Horizontal beamswinging was done at elevation angles of 1.4° and 1.9°. These data are included on the figure and compared with the free-space, two-way antenna pattern shown in the lower, far-left frame. The height profile of C_n^2 is shown, on a linear scale, at the upper right plotted with the temperature sounding from the Denver RAWIN taken at 1700 MST, two hours after the radar observations. A prominent low-level subsidence inversion characteristic of this kind of weather condition is evident in the sounding. The radar observations were made above the inversion, since the horizon rays intersected at a height of

BEST DOCUMENT AVAILABLE

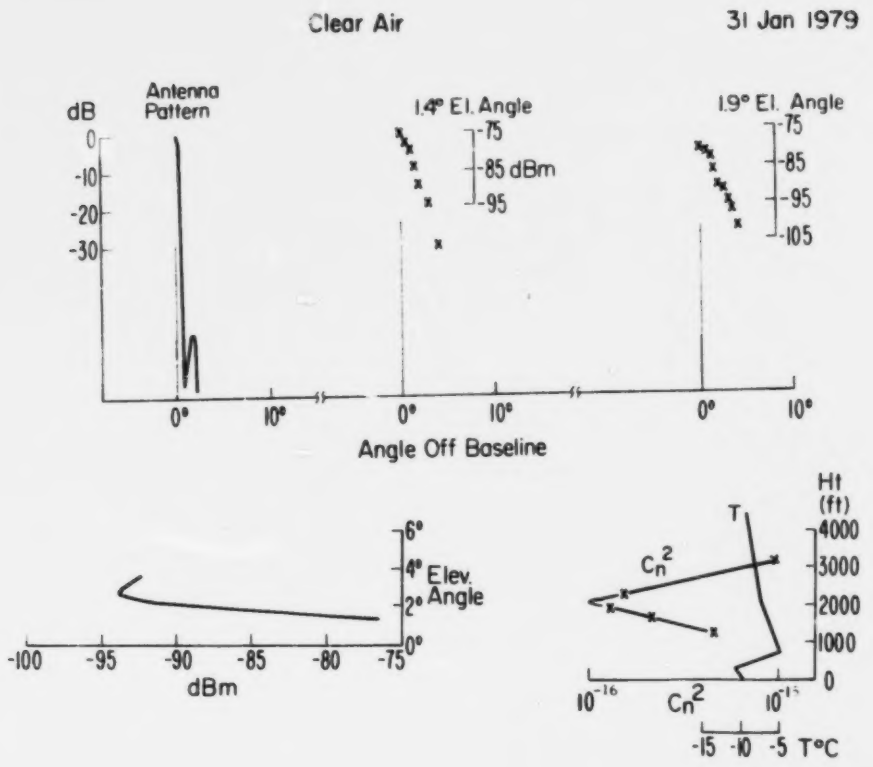

Figure 2.13--Top frame: Power vs. azimuthal angle for horizontal beamswinging compared with free space antenna pattern. Bottom frame: Vertical beamswinging with resulting radar-calculated C_n^2 compared with raob temperature profile. Note very small values of C_n^2 above the inversion and compare with very weak backscatter signals from this region in clear-air radar records shown in Fig. 7.17.

1300 ft AGL at midpath. The observed C_n^2 values are understandably very small under these conditions ranging from 10^{-16} to 10^{-15}.

A vertical beamswinging experiment was also carried out on 15 February and the results are shown in Fig. 2-14. The WPL 8.6 mm, vertically-pointing radar was in operation at the time and its facsimile recorder record is shown as the background of the figure. The 1700 MST temperature sounding from the Denver RAWIN is also shown on the figure. The height profile of C_n^2 calculated from the forward-scatter radar observations is shown plotted on a log scale. Although there was significant precipitation from the clouds, including some large snowflakes, the cloud layer was obviously very thin and capped by a large temperature inversion. From the surface weather map for the period, it is clear that the temperature inversion was a weather front and that the precipitation was related to the local frontal dynamics. Perhaps the most dramatic feature of the forward-scatter data is the very sharp

BEST DOCUMENT AVAILABLE

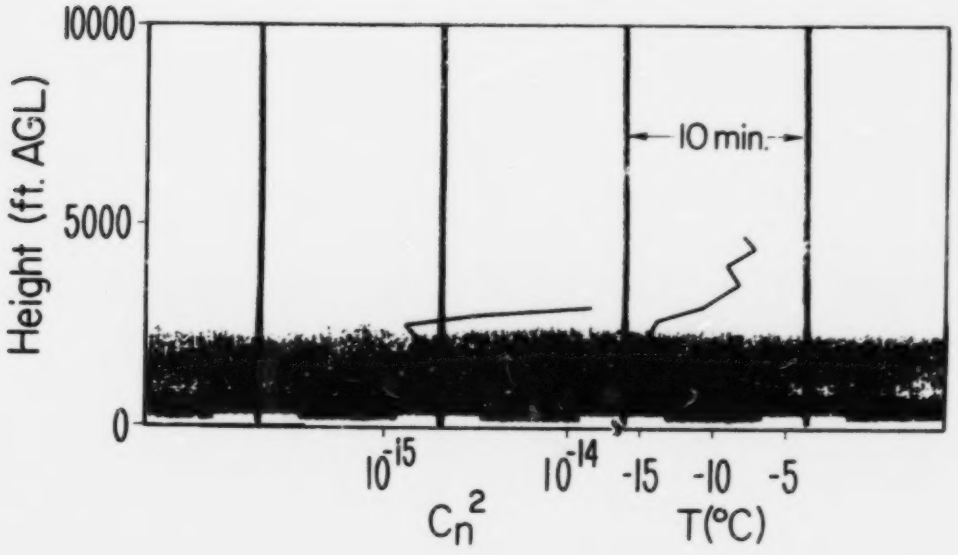

Figure 2.14--Profile of C_n^2 calculated from forward-scatter received power through the boundary between precipitating clouds and the clear air above compared with the temperature profile measured by raob. The cloud backscatter record (shaded background) was from a modified TPQ-11 radar ceilometer of 8.6 mm wavelength.

increase (by an order-of-magnitude) in C_n^2 at the cloud top, which is also the inversion base. This is not altogether unanticipated, since it is to be expected that the entrainment of warm, dry air from above the inversion into the region at the cloud top would produce a locally enhanced variance at that height. Furthermore, this mixing process would lead to a negative covariance between temperature and humidity fluctuations which would further enhance the refractive index variance (Gossard, 1960, 1979). If in-cloud processes alone are considered, and if the cloud is presumed to be everywhere at or very near saturation, the correlation between temperature and humidity might be presumed to be positive because warmer air holds more moisture than colder air (the Clausius-Clapyron relation). This concept would diminish the refractive index variance. Thus the mixing and entrainment occurring at the inversion boundary is likely to produce a pronounced boundary effect detectable by vertically pointing radars (Gossard, 1978). In the presence of cloud the effect may be enhanced by the evaporative cooling of penetrating cloud tongues whose evaporation locally increases the humidity increasing the negative covariance.

2.7 Conclusions

From the theoretical considerations and modeling experiments described in this Chapter:

a) Fluctuations in refractive index due to gaseous inhomogeneities in dielectric constant should be about 30 times more important for coherent radar backscatter than fluctuations in cloud liquid water if the magnitudes of variance of water vapor and liquid water are about the same.

b) Water vapor variance resulting from internal thermodynamic processes coupled to the cloud dynamics through non-linear interaction may be competitive with the corresponding turbulent dynamic variance in water vapor outside the cloud.

c) Negative correlation between temperature and humidity in clouds may lead to substantially greater coherent cloud reflectivity (in the Bragg sense) than previously thought.

From the results of the forward scatter experiment, comparing Bragg scatter from the gas with incoherent scatter from particles:

a) Winter clouds/precipitation near Denver exhibit no evidence of significant departure from the classical concept of incoherent reflection of radar waves in the wavelength range from 20 cm to 50 cm. This conclusion may not be valid for summer convective storms.

b) There is some evidence of less slope to refractive index spectra inside clouds than would be expected if a -5/3 wavenumber dependence were valid.

c) In clear air the radar data substantiate the -5/3 law when all clear-air cases are averaged.

d) Radar wavelengths of 20-30 cm are typical values for cross-over between dominance of coherent to incoherent backscatter in those winter cloud/ precipitation events observed in this experiment which had typical dBZ values of 0-10.

e) There is a dramatic increase in Bragg-coherent return (C_n^2) at cloud tops when they are capped by a temperature inversion with dryer air above.

BEST DOCUMENT AVAILABLE

CHAPTER 3 - VARIOUS RADARS AND THEIR POTENTIAL FOR CLOUD AND CLEAR AIR DETECTION

It is of obvious interest to compare the Z values of various cloud types and the C_n^2 of the clear air with the minimum detectable Z and C_n^2 of various radars. The starting point of such a comparison is Eq. (2-57) and Eqs. (2-58) and (2-59). Obviously, the minimum detectable values of Z and C_n^2 depend on the radar parameters P_t, A_e, $(P_r)_{min}$ and λ. They also depend on the range, r, and range resolution Δ. For a pulse radar, P_t and $(P_r)_{min}$ are usually expressed as peak powers although average powers are readily used if the pulse-repetition period T and the pulse length τ are known.

For single-pulse processing it is convenient to take $(P_r)_{min}$ as the system noise power referred to the receiver input; then

$$(P_r)_{min} = k_B T_e B \tag{3-1}$$

if the noise is uniformly distributed over the receiver bandwidth B. Here $k_B = 1.375 \times 10^{-23}$ is the Boltzman constant. The quality of the receiver can be either expressed in terms of the "effective noise temperature," T_e, or the receiver noise figure, F, related to the noise temperature by

$$F = \frac{T_e + 290^\circ}{290^\circ} \quad . \tag{3-2}$$

F is often given in dB.

Tables 3-1a and 3-1b present the resulting calculations of minimum detectable Z, C_n^2 and η at a range of 10 km for many radars used in atmospheric investigations. Single pulse processing is not usually relevant to the class of radars used in profiling the winds of the clear atmosphere, so these radars, listed in Table 3-1b, are described in a processing mode believed to be typical.

From Table 4-2, to be discussed later, it is immediately evident that cumulonimbus, cumulus congestus and Hawaiian orographic clouds should be detected by almost all radars at a range of 10 km. However, for those radars listed in Table 3-1a fair weather cumulus and continental cumulus should be detected only by the Defford and Wallops Island 10-cm radars and by the 0.86 cm radars. Note that Eqs. (2-57), (2-58) and (4Aa) show that there is an inverse fourth power dependence of Z_{min} on λ, although η_{min} is independent of wavelength; therefore, the short wavelength radars have a very great

BEST DOCUMENT AVAILABLE

TABLE 3-1a CLOUD AND STORM-SENSING RADARS

	Pulse Doppler WPL	Pulse Doppler NSSL	Pulse Doppler Defford	Pulse Doppler Wallops Is	WSR-57 (Hook Mode)	WSR-57	K-Band Doppler WPL	TPQ 11	Chatanika Radar
P_t (w)	0.9×10^5	4.7×10^5	3×10^5	2×10^6	4.1×10^5	4.1×10^5	1.5×10^5	1.2×10^5	3.2×10^6
P_r (dBm)	−106	−111.2	−110	−110	−100	−108	−106	−99	−128
λ (cm)	3.22	10.7	10.7	10.7	10.3	10.3	0.86	0.86	23.25
A_e (m^2)	4.02	31	270	146	5.8	5.8	.64	1.8	310
Δ (m)	75	150	30	195	75	600	37.5	75	1500
R (km)	10	10	10	10	10	10	10	10	10
Min η (m^{-1})	2.7×10^{-12}	9.8×10^{-15}	1.1×10^{-14}	5×10^{-16}	1.6×10^{-12}	3.1×10^{-14}	2.2×10^{-11}	2.2×10^{-11}	3.0×10^{-19}
Min C_n^2 ($cm^{-2/3}$)	1.0×10^{-13}	5.6×10^{-16}	6.8×10^{-16}	2.9×10^{-17}	9.0×10^{-14}	1.8×10^{-15}	5.5×10^{-13}	5.5×10^{-13}	2.2×10^{-19}
Min C_n^2 ($m^{-2/3}$)	2.2×10^{-12}	1.2×10^{-14}	1.5×15^{-14}	6.2×10^{-16}	1.9×10^{-12}	3.85×10^{-14}	1.2×10^{-11}	1.2×10^{-11}	4.9×10^{-19}
Min Z ($mm^6 m^{-3}$)	1.0×10^{-2}	4.5×10^{-3}	5.4×10^{-3}	2.3×10^{-4}	0.625	1.2×10^{-2}	4.2×10^{-4}	4.2×10^{-4}	3.1×10^{-6}
τ (μsec)	0.5	1	1.25	1.3	0.5	4	0.25	0.5	10
T (μsec)	512	768	1250	980	1520	6097	500	1000	3400
Antenna (m)	3.05	8.5	25	18.4	3.65	3.66	1.12	2.14	26.8
Beamwidth (deg)	0.86	1.1	0.33	0.50	0.56	2.0	0.5	0.25	0.6

TABLE 3-1b CLEAR-AIR RADAR WIND SOUNDERS

	FM-CW WPL	Meteorological Profiler WPL	Sunset, Colorado	SOUSY W. Germany	Poker Flat, Alaska
P_t (W)	200 (av)	1.5×10^3 (av)	1.25×10^5	6×10^5	0.15×10^5
λ (cm)	10.2	32.8	741	561	600
Δ (m)	100*	900**	1000	50	750
R (km)	10	10	10	10	10
Min η (m^{-1})	1.8×10^{-14}	4.1×10^{-17}	5.9×10^{-19}	2.1×10^{-20}	1.0×10^{-18}
Min C_n^2 ($cm^{-2/3}$)	9.9×10^{-16}	3.5×10^{-18}	1.4×10^{-19}	4.6×10^{-21}	2.3×10^{-19}
Min C_n^2 ($m^{-2/3}$)	2.1×10^{-14}	7.5×10^{-17}	3×10^{-18}	1×10^{-19}	5×10^{-18}
Min Z ($mm^6 m^{-3}$)	6.2×10^{-3}	1.7×10^{-3}	6.2	7.5×10^{-2}	4.8
Antenna (m)	2.44	10	60 x 30	62	100 x 50
Beamwidth (deg)	2.7	2.3	5 x 9	5	2 x 4
Remarks	Sweep length 50 ms	Integration time 4.6 ms	Integration time 60 ms	Integration time 100 ms	Integration time 60 ms

*Typical. Maximum resolution is 1m.
**High altitude mode. Low altitude, 100 m resolution.

advantage in the detection of targets consisting of small discrete spherical droplets whose reflectivity is describable by Z while Eq. (2-59) shows that there is only a very weak wavelength dependence ($\lambda^{-1/3}$) in the detectability of Bragg scattering targets whose reflectivity is describable by C_n^2.

Comparing Z values for the various clouds with the minimum detectable values shown in Table 3-1a, we see that most clouds would not normally be seen by the 3.2 cm wavelength radar listed in the Table at a range of 10 km based on single pulse processing alone. However, if longer pulse-lengths (e.g., 1-5 μsec) were used and averages taken over many pulses, clouds such as those observed at South Park, Colorado, USA should be detectable. If the Doppler velocity spectra in clouds are narrow, the total processing gain to be realized from Doppler processing and averaging may amount to as much as 10 dB.

Clear-air radars must be very sensitive. Therefore, ground clutter can be a severe limitation unless great care is taken to reduce antenna sidelobes. Because of the low peak power of the modulated CW radars, clutter is not so likely to saturate these systems as in the case of pulse radars with their high peak powers. However, if the CW radar does saturate it is inoperable for all ranges. Although clutter at short ranges typically obscures any clear-air returns close to a pulse radar, the return from longer ranges remains visible. This factor and the transmit-receive switching that is necessary with pulse systems makes them of limited value at short ranges. The FM-CW or pseudo-noise modulation radars which use separate transmit and receive antennas are therefore of more value for short ranges, but considerable care must be taken in ground clutter suppression in the processing and in antenna sidelobe reduction, as well as in siting of the radar. In Doppler-coherent radars, stationary targets (clutter) may be eliminated by removing zero frequency-shift signals. But this technique fails if the rf portion of the receiver saturates. The general procedure for processing radar signals using coherent and incoherent integration is outlined in Chapter 10.

BEST DOCUMENT AVAILABLE

CHAPTER 4 - RADAR REFLECTIVITY AND CLOUD CHARACTERISTICS

4.1 Introduction

This section reviews past work on cloud detection by radar and summarizes some conclusions regarding the detectability of various clouds. Some special drop size distributions are analyzed, and one quite general form is discussed.

4.2 Drop-Size Distribution - Some Special Cases

The results of measurements of cloud drop-size distributions prior to 1949 have been summarized by Best (1951). He concluded that the data fit the relation

$$1 - F = \exp[-(D/D_o)^n] \qquad (4\text{-}1)$$

where F is the fraction of liquid water in drops of diameter less than D. He shows that the mean of values of n found by all investigators is 3.3. Furthermore, of the various choices for D_o, such as the mean, mode or median, Best found that the median drop diameter (the size at which half the water is contained in larger drops) is most independent of n and of the minimum measurable diameter in the sample.

Another widely used distribution is the exponential law, $N_D = N_o e^{-\Lambda D}$, where $N_D dD$ is the number of drops of diameter between D and D + dD. The total mass of water is then given by

$$M_T = \rho \frac{\pi}{6} N_o \int_o^\infty D^3 e^{-\Lambda D} dD = \rho \frac{\pi}{6} N_o \frac{3!}{\Lambda^4} . \qquad (4\text{-}2)$$

If D_o is mass median diameter, $\Lambda = 3.67/D_o$. The total number of drops per unit volume is then $N_T = N_o D_o (3.67)^{-1}$ and the total liquid water content (LWC) is $M_T = \rho \pi N_o D_o^4/3.67)^{-4}$. The water content in the drop-size interval dD is

$$M_D dD = dM = \rho \frac{\pi}{6} N_o D^3 e^{-3.67D/D_o} dD \qquad (4\text{-}3a)$$

so the fractional water content in the interval dD is

BEST DOCUMENT AVAILABLE

$$dM/M_T = [(3.67)^4/6]\ (D/D_o)^3\ e^{-3.67D/D_o} d(D/D_o) \qquad \text{(exponential)}. \quad (4\text{-}4a)$$

This expression can be compared directly with dF, found from Eq. (4-1) to be

$$dF \equiv dM/M_T = 3.3\ (D/D_o)^{2.3}\ e^{-(D/D_o)^{3.3}}\ d(D/D_o) \qquad \text{(Best)}. \quad (4\text{-}4b)$$

We are more interested in the fractional contribution to the total reflectivity factor Z by drops of different size. Note that $dM = \rho(\pi/6)\ e^3\ N_D\ dD$ and, from the definition of Z,

$$dZ = D^6\ N_D\ dD\ . \quad (4\text{-}5a)$$

Therefore,

$$dZ = \rho^{-1}\ (6/\pi)\ D^3\ dM\ . \quad (4\text{-}5b)$$

So from Eqs. (4-4a) and (4-4b) we can find expressions for the fractional contribution to Z analogous to those for liquid water content M. They are plotted in Fig. 4-1. The contribution to reflectivity factor is evidently concentrated near the mass-median of the drop-size population. The total reflectivity factor Z_T is thus related to the mass median drop-size as follows:

$$Z_T = N_o\ \frac{6!}{(3.67)^7}\ D_o^{\,7} = \frac{6!\ M_T}{\rho\ \pi}\ \frac{D_o^{\,3}}{\Lambda^3} \qquad \text{(for Marshall-Palmer type exponential)} \quad (4\text{-}6a)$$

$$Z_T = \Gamma\left(\frac{3}{3.3} + 1\right)\ (6/\pi)\ (M_T/\rho)\ D_o^{\,3} \qquad \text{(for Best's distribution)}. \quad (4\text{-}6b)$$

4.3 A General Drop-Size Distribution Function

The Marshall-Palmer and Best distributions are special cases (or nearly so) of a more general function usually called (see Deirmendjian, 1969; Sal'man, 1973) a "modified gamma distribution." It is given by [see Eq. (1-5)]

$$dN = N_r dr = a\ r^{\alpha}\ \exp(-br^{\gamma})\ dr = a'D^{\alpha}\ \exp(-b'D^{\gamma})\ dD \quad (4\text{-}7a)$$

where, in this section, r is drop radius and $a' = a/2^{\alpha+1}$, $b' = b/2^{\gamma}$; α and γ are free constants. This distribution is shown schematically in Fig. 4-2.

BEST DOCUMENT AVAILABLE

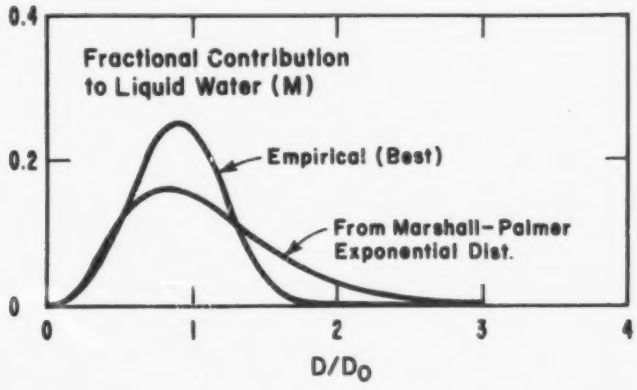

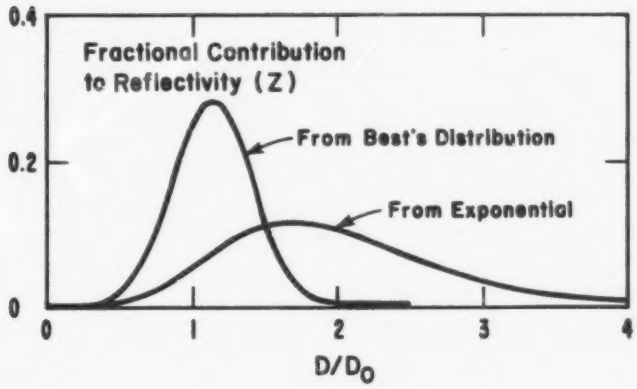

Figure 4.1--Spectrum of fractional contribution to liquid water and fractional contribution to radar reflectivity factor for Best's drop-size distribution and for exponential distribution.

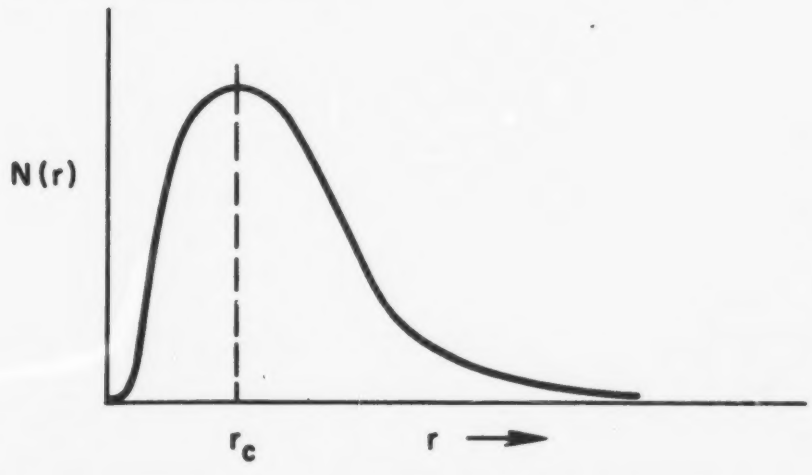

Figure 4.2--Schematic of modified gamma distribution (Deirmendjian, 1969).

BEST DOCUMENT AVAILABLE

As seen above, the mass (or volume) median drop-size (D_o) is a convenient scaling length in radar scattering problems. In terms of D_o and G

$$N_D = a' D_o^{\alpha} (D/D_o)^{\alpha} \exp[-G(D/D_o)^{\gamma}] \tag{4-7b}$$

where G is readily identified as $b(D_o/2)^{\gamma}$. Integration of N_D dD over all D gives

$$N_T = a'\gamma^{-1} D_o^{1+\alpha} G^{-(1+\alpha)/\gamma} \Gamma[(\alpha+1)/\gamma] \tag{4-8}$$

where N_T is the total number of drops per unit volume. The slope of the distribution is zero at r = 0, at $N = N_{max}$ and at $r = \infty$. In Table 4-1 the drop size radius or diameter associated with the maximum of N(r) is called r_c or D_c. At N_{max} where dN/dD = 0

$$b = \frac{\alpha}{\gamma r_c^{\gamma}} \equiv \frac{G}{r_o^{\gamma}}$$

whence it is readily seen that

$$D_o = \left(\frac{\gamma G}{\alpha}\right)^{1/\gamma} D_c \ . \tag{4-9}$$

The corresponding mass of liquid water is given by

$$M(D_1) = \rho \frac{\pi}{6} \int_o^{D_1} D^3 N_D dD \ . \tag{4-10}$$

Using Eq. (4-7b) and integrating over all D

$$M_T = \frac{4}{3} \rho\pi \ a \ \gamma^{-1} G^{-(4+\alpha)/\gamma} \Gamma[(4+\alpha)/\gamma] 2^{-(4+\alpha)} D_o^{4+\alpha}. \tag{4-11}$$

The mass of liquid water contained in drops for which $D < D_1$ is given by

$$M(D_1) = \frac{M_T}{\Gamma(\frac{4+\alpha}{\gamma})} \int_o^{x_1} x^{(4+\alpha-\gamma)/\gamma} e^{-x} dx \tag{4-12a}$$

$$= M_T[1 - e^{-x} (\frac{x^n}{n!} + \frac{x^{n-1}}{(n-1)!} \text{ ---- } x + 1] \tag{4-12b}$$

when $n \equiv 4+\alpha-\gamma$ is integral and where $x = G(D/D_o)^{\gamma}$. (Note also that $\Gamma(n+1) = n!$.) Thus G is uniquely determined for given values of α and γ; it is found for $D = D_o$ from that value of x for which the mass M(D) = 1/2, so that half the volume (or mass of liquid water) lies in sizes less than D_o. A plot of G

BEST DOCUMENT AVAILABLE

Table 4-1 Parameters of modified gamma distribution for some hydrometeors and aerosols (Deirmendjian's values except as otherwise indicated).

	α	γ	r_c(m)	D_o(m)	$N_T(m^{-3})$	G	a	b	VP$(m^3 m^{-3})$***	$Z(mm^6 m^{-3})$	$\sigma_{ext}(m^{-1})$
Haze (Continental)	2	1/2	$.07\times10^{-6}$	1.19×10^{-6}	100×10^{6}	11.669	4.9757×10^{32}	15.119×10^{3}	1.17×10^{-11}	NA	3.64×10^{-5}
Haze (Maritime)	1	1/2	$.05\times10^{-6}$	2.34×10^{-6}	100×10^{6}	9.670	5.3333×10^{22}	8.944×10^{3}	4.95×10^{-11}	NA	8.25×10^{-5}
Haze (High Altitude)	2	1	$.10\times10^{-6}$	0.57×10^{-6}	100×10^{6}	5.671	4.000×10^{29}	20.000×10^{6}	3.14×10^{-12}	NA	1.88×10^{-6}
Cloud (MDP **)	8	3	2×10^{-6}	4.45×10^{-6}	100×10^{6}	3.677	5.5556×10^{60}	3.333×10^{17}	3.77×10^{-9}	6.91×10^{-7}	3.05×10^{-3}
Cloud (Double Corona)	8	3	2×10^{-6}	4.45×10^{-6}	100×10^{6}	3.677	5.5556×10^{60}	3.333×10^{17}	3.77×10^{-8}	6.91×10^{-7}	3.05×10^{-3}
Cloud (Corona)	8	3	4×10^{-6}	8.90×10^{-6}	100×10^{6}	3.677	1.0851×10^{58}	4.17×10^{16}	3.02×10^{-8}	4.42×10^{-5}	1.22×10^{-2}
Cloud (Cumulus)	6	1	NA	12.89×10^{-6}	100×10^{6}	9.670	2.3730×10^{48}	1.50×10^{6}	6.255×10^{-8}	3.74×10^{-4}	1.56×10^{-2}
Rain * (Drizzle)	0	1	NA	667×10^{-6}	1450	3.673	8×10^{6}	5.5×10^{3}	2.74×10^{-8}	3.77x10	4.73×10^{-7}
Rain * (Light, 1 mm hr^{-1})	0	1	NA	900×10^{-6}	1960	3.673	8×10^{6}	4.1×10^{3}	9.09×10^{-8}	3.07×10^{2}	1.86×10^{-6}
Rain * (Moderate, 4 mm hr^{-1})	0	1	NA	1200×10^{-6}	2610	3.673	8×10^{6}	3.1×10^{3}	2.87×10^{-7}	2.30×10^{3}	4.20×10^{-6}
Rain * (Heavy, 16 mm hr^{-1})	0	1	NA	1600×10^{-6}	3490	3.673	8×10^{6}	2.3×10^{3}	9.08×10^{-7}	1.72×10^{4}	1.21×10^{-5}
Snow * (Moderate)	0	1	NA	2980×10^{-6}	930	3.673	1.14×10^{6}	1.2×10^{3}	1.56×10^{-6}	1.91×10^{5}	6.78×10^{-5}
Rain (Maritime)	1	1/2	50×10^{-6}	2338×10^{-6}	1000	9.670	0.533×10^{12}	2.828×10^{2}	4.95×10^{-7}	1.83×10^{4}	8.26×10^{-4}
Rain (Continental)	2	1/2	70×10^{-6}	1191×10^{-6}	1000	11.669	4.98×10^{16}	4.781×10^{2}	1.17×10^{-7}	1.33×10^{3}	3.63×10^{-4}

* From stratiform rainfall rate relations given by Gunn and Marshall (1958) assuming Marshall-Palmer distribution.

** Mother of Pearl

*** Volume of particulates per cubic meter, snow is volume of equivalent spherical liquid drop.

BEST DOCUMENT AVAILABLE

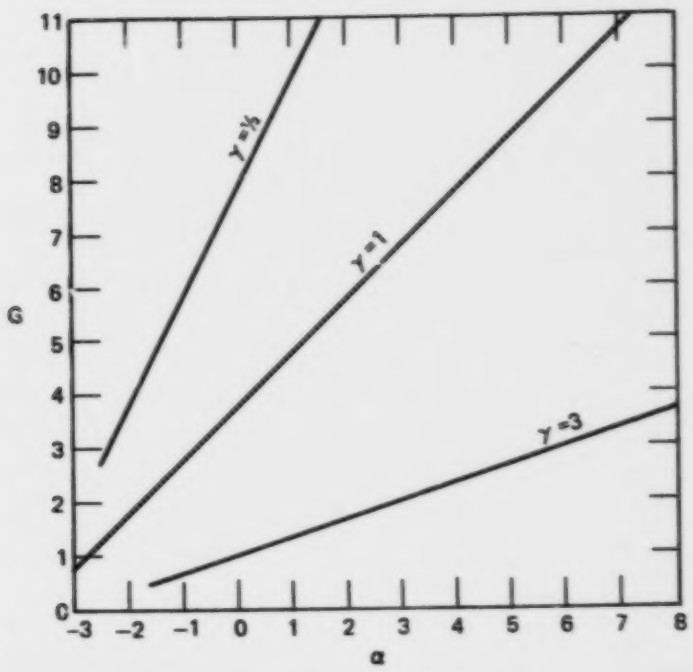

Figure 4.3--Relationship between the coefficients of the modified gamma distribution and the exponential factor G.

is shown in Figure 4-3. From (4-7b) we see that the exponential distribution results when $\alpha = 0$, $\gamma = 1$. Then $G \equiv \Lambda D_o = 3.67$ and $a' = N_o$. It is therefore no surprise that Eq. (4-8) then yields $N_T = a' D_o (3.67)^{-1} \equiv \frac{a}{2} \Lambda^{-1}$ whence we identify N_o with a/2. Then Eq. (4-11) becomes

$$M_T = \frac{4}{3} \rho\pi \, aG^{-4} \, \Gamma(4) \, 2^{-4} \, D_o^{\,4} \qquad (4\text{-}13)$$

in agreement with the above discussion of the exponential distribution.

The distribution of Best, (Eq. 4-4b), does not conform precisely to a special case of Eq. (4-7a). Note that $G \simeq 0.5$ instead of unity when $\gamma = 3.3$ and $\alpha = 0.7$. Also, in his discussion of Eq. (4-7a), Deirmendjian chooses to constrain α to be integral.

Here, we are more interested in the reflectivity factor Z than in M so, as in Eq. (4-5b) of the previous section, we note that $dZ = D^6 N_D dD = (6/\rho\pi) D^3 dM$. Using Eq. (4-7b) and Eq. (4-10) and transforming to x as in (4-12a), the integration is straightforward and we find

BEST DOCUMENT AVAILABLE

$$dZ = (6/\rho\pi)\, M_T\, \Gamma^{-1}[(4+\alpha)/\gamma]\, G^{-3/\gamma}\, D_o^3\, x^{(7+\alpha-\gamma)/\gamma}\, e^{-x}\, dx \qquad (4\text{-}14a)$$

and

$$Z_T = \frac{6M_T D_o^3}{\rho\pi G^{3/\gamma}}\, \frac{\Gamma[(7+\alpha)/\gamma]}{\Gamma[(4+\alpha)/\gamma]}\,. \qquad (4\text{-}14b)$$

Some parameters that have been suggested for the modified gamma function are shown in Table 4-1 for selected aerosols and hydrometers. The values of r_c, N_T, α and γ are taken from Deirmendjian (1969) except as indicated, but the values of G, M_T, D_o, Z_T and σ have been calculated from those values. Using the relations (4-8), (4-9), (4-11), (4-14b), and (5-6c). (The value of r_c = 4 μm given by Deirmendjian for a Double-Corona cloud seems to be an error. In our Table 4-1 we have assumed that it should have been r_c = 2 μm.) For comparison with the Deirmendjian models, we have also calculated the corresponding quantities from the Marshall-Palmer distribution for rainfall assuming the coefficients found by Gunn and Marshall (1958) for various rainfall rates. They find

Rain	Snow
$\Lambda(m^{-1}) = 4.1 \times 10^3\, R^{-0.21}$	$\Lambda(m^{-1}) = 2.29 \times 10^3\, R^{-0.45}$
$N_o(m^{-4}) = 0.08 \times 10^8$	$N_o(m^{-4}) = 0.038 \times 10^8\, R^{-0.87}$

in the exponential distribution, where $N_D = N_o\, e^{-\Lambda D}$. All lengths are in meters except rainfall rate R which is in mm hr^{-1}. In Table 4-1, it has been assumed that R = 1, 4 and 16 mm hr^{-1} for light, moderate and heavy precipitation respectively in accordance with the convention in Kerr (1951).

In the following paragraphs, observed cloud drop-size parameters have been compiled and tabulated, and it will be seen that the Deirmendjian parameters drastically underestimate the total liquid water content measured in natural clouds. Better in-situ measurements combined with good radar measurements are obviously needed.

4.4 Methods for Measuring Drop-Size In-Situ

Most in-situ measurements of drop size distribution have been made with powered aircraft, because the required instruments are complicated and relatively heavy. Exceptions are the measurements made on Mt. Washington and those made from a sailplane and reported by workers at the National Center

for Atmospheric Research (NCAR) near Boulder, CO. The advantage of the latter systems is that the air stream is relatively undisturbed.

Conceptually, the simplest method is direct photography if an arrangement is achieved that allows an undisturbed sample of air to be photographed. Unfortunately this is difficult, and the method is expensive requiring a great deal of time to collect and process enough data to represent a significantly large sample.

One of the oldest methods is to expose slides to the air stream and count individual drops and their sizes. Such slides may be coated with grease (Weickmann and aufm Kampe, 1953) or with soot (e.g., Breed et al., 1976). This method is fairly accurate, but it is slow and laborious, requiring human measurement and counting of individual drops. The photography and slide collection methods are most accurate for drops larger than 100 μm.

An earlier method, used extensively by Diem (1948) and by Boucher (1952) on Mt. Washington, employed a cylindrical "impinger." It is probably the least reliable of the widely used techniques.

Two recently developed methods that are now becoming widely used depend on the scattering properties of spheres for optical wavelengths. A simple natural example of optical scattering is the halo that some clouds produce around the solar disk. The instrument is called the Axially Scattering Spectrometer Probe (ASSP), best for particles 2-30 μm in diameter; and the Forward Scattering Spectrometer Probe (FSSP), best for particles 3-45 μm in diameter. Such instruments aboard sailplanes probably provide the best data that can be collected in quantity (Dye, 1973). Unfortunately the lack of powered flight limits the mobility of the sailplane and makes it difficult to sample different parts of a cloud system rapidly. The various measuring techniques recommended by Particle Measuring Systems Incorporated of Boulder, Colorado for the different particle size ranges are summarized in Fig. 4-4.

4.5 Observations of Drop-Size Distribution in Natural Clouds

In 1953 Weickmann and aufm Kampe reported measurements of drop-size spectra in cumulus clouds. Observations were made at many locations within the clouds and the drop-size spectra from all observations were compiled into average spectra for three cumulus types: fair weather cumulus (cumulus humulis), cumulus congestus, and cumulonimbus. Photographs of typical drop

BEST DOCUMENT AVAILABLE

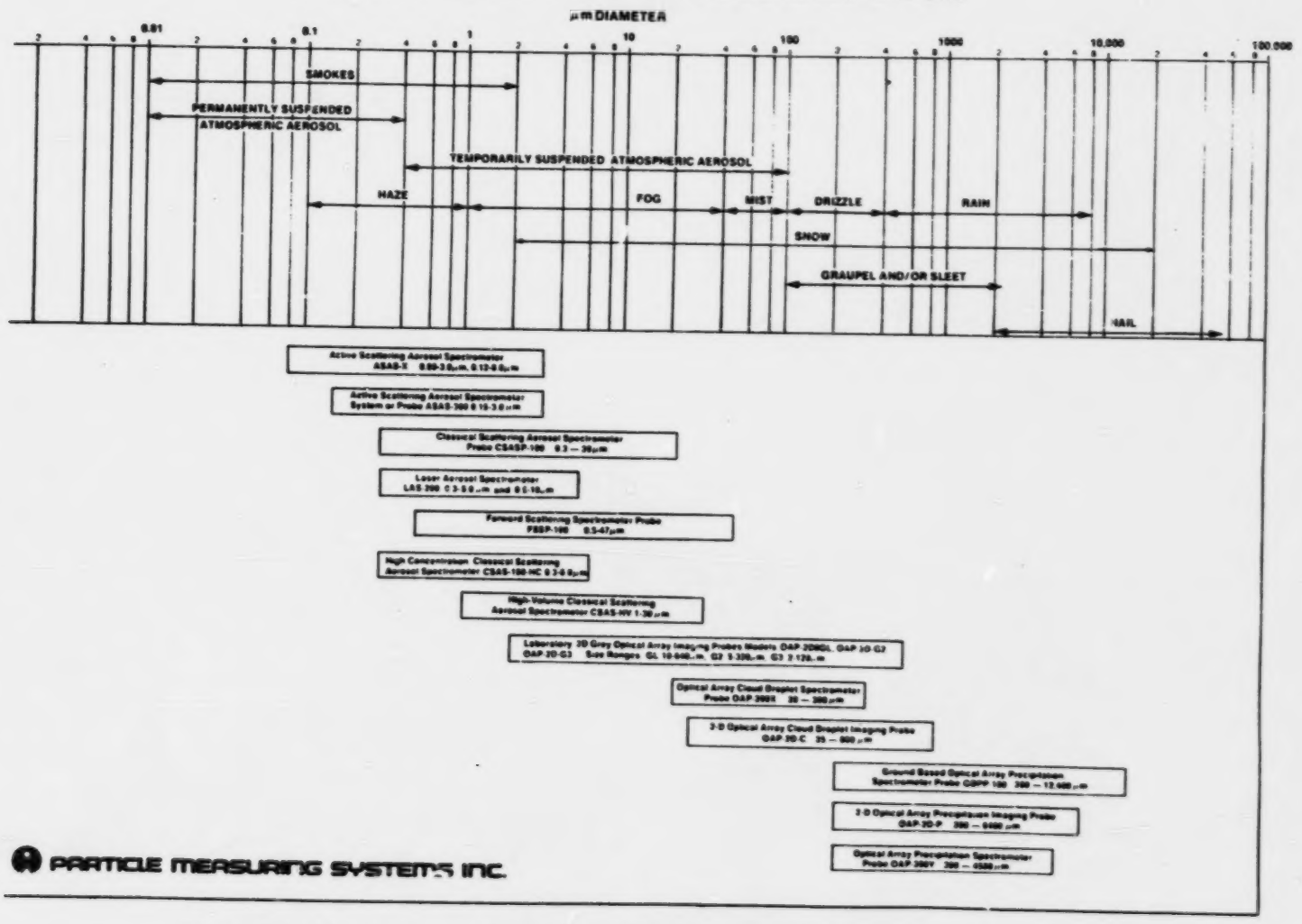

Figure 4.4--Size ranges of atmospheric particles sampled by particle size spectrometers (courtesy of Particle Measuring Systems Inc.)

BEST DOCUMENT AVAILABLE

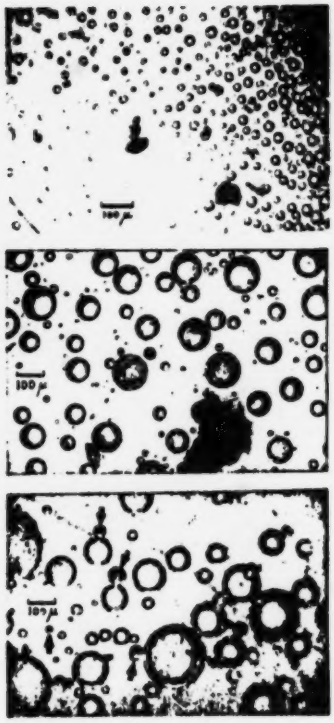

Figure 4.5--Samples of natural drop-size distributions in various clouds. (Weickmann and aufm Kampe, 1953).

distributions are shown in Fig. 4-5. In addition to drop-size distributions that allow the median diameter D_o to be calculated, the average liquid water content M(g m^{-3}) and the average number of drops are given in Table 4.2. From these data a radar reflectivity factor (Z) can be calculated using the Atlas Bartoff method (see Section 4.6). The height distribution of cloud radii and of spectral spread are shown in Fig. 4-6. The rms drop size reaches a maximum near cloud base. The total water content is concentrated in drops of much larger radius in cumulus congestus than in fair weather cumulus as shown dramatically in Fig. 4-7. This fact has important implications for cloud detecting radars. However, some caution in accepting these data as typical is suggested by the fact that the median diameters of the clouds investigated by Weickmann and aufm Kampe are much larger than those of other investigators, so the reflectivity factors given in Table 4.2 may not be very typical.

Squires (1958) has compared clouds of maritime origin near Hawaii with cumulus clouds of continental origin in Australia. Multiple exposure samplers were used, and the drop-size concentrations showed spatial variations on scales down to 300 m or less. Clear patches were often found even in dense clouds. However, characteristic differences were found. Squires studied

BEST DOCUMENT AVAILABLE

Table 4-2 Cloud parameters.

	Cloud type	Number density (N) (m^{-3})	Water content (M) ($gr\ m^{-3}$)	Reflectivity z ($mm^6\ m^{-3}$)	Median diameter (D_o) (m)	6th power mean diameter (m)	Atlas Barthoff (Z) z ($mm^6\ m^{-3}$)	$N_T D_o^6$ ($mm^6\ m^{-3}$)
Weickmann-aufh Kampe	Fair weather cumulus	302×10^6	1.0		32×10^{-6}		0.0845	
	Cumulus congestus	64×10^5	3.9		108×10^{-6}		12.7	
	Cumulonimbus	72×10^6	2.5		108×10^{-6}		8.1	
		$\sum_i N_i$ (m^{-3})	$\rho \frac{\pi}{6} \sum_i N_i D_i^3$ ($gr\ m^{-3}$)	$\sum_i N_i D_i^6$ ($mm^6\ m^{-3}$)				
Squires	Continental cumulus	495×10^6	0.35	1.82×10^{-3}	13.2×10^{-6}	12.4×10^{-6}	2.1×10^{-3}	2.6×10^{-3}
	Trade wind cumulus	72.5×10^6	0.81	5.3×10^{-2}	26.5×10^{-6}	30.0×10^{-6}	3.9×10^{-2}	2.5×10^{-2}
	Hawaiian dark stratus	23.3×10^6	0.335	4.0×10^{-2}	34.0×10^{-6}	34.7×10^{-6}	3.4×10^{-2}	3.6×10^{-2}
	Hawaiian orographic	5.2×10^6	0.523	1.35	92.0×10^{-6}	80.0×10^{-6}	1.05	3.15

BEST_DOCUMENT AVAILABLE

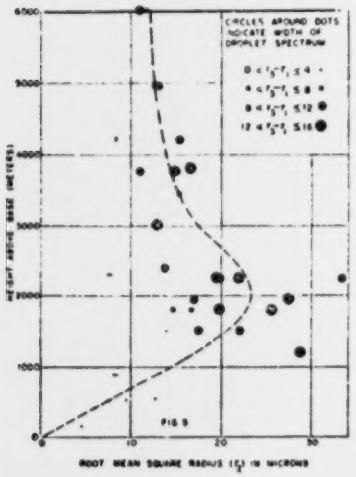

Figure 4.6--Root-mean-square radii in cumuliform clouds versus height above base. (Weickmann and aufm Kampe, 1953.)

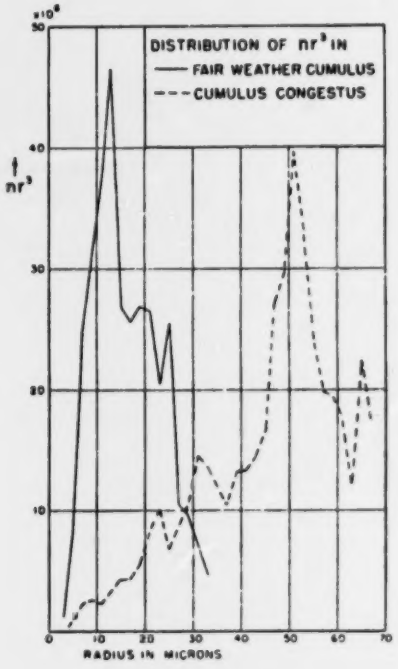

Figure 4.7--Water-content spectra in fair-weather cumulus and cumulus congestus. (Weickmann and aufm Kampe, 1953.)

BEST DOCUMENT AVAILABLE

Table 4-3. Cloud parameters (after Diem).

Diem's cloud types	$\rho \frac{\pi}{6} \sum_i N_i D_i^3$ (gr m^{-3})	$Z = \sum_i N_i D_i^6$ Z (mm^6 m^{-3})	D_o (m)
CU_1	0.32	1.18×10^{-3}	11.2×10^{-6}
CU_2	0.87	2.76×10^{-2}	20.6×10^{-6}
SC	0.09	3.53×10^{-4}	10.1×10^{-6}
AS	0.28	2.40×10^{-3}	12.8×10^{-6}
NS	0.40	1.40×10^{-2}	23.4×10^{-6}
ST	0.29	1.29×10^{-2}	24.1×10^{-6}

orographic clouds 600 m to 1500 m thick with updrafts of 0.1 to 0.25 m sec^{-1}, dark stratus clouds about 300 m thick, and cumulus clouds over the sea with updrafts at about 1 m s^{-1}. He compared the results of the maritime cumulus with Australian continental cumulus of similar size and found very significant differences. Maritime cumuli showed relatively low drop concentrations (45 cm^{-3}) when compared with the continental cumuli which contained about 228 drops cm^{-3}. The liquid water content was similar in both, so the drops in the marine clouds were significantly larger than their continental counterparts. The cloud characteristics as measured by Weickmann aufm Kampe and by Squires are compiled in Table 4-2. Table 4-3 summarizes aircraft observations over Germany reported by Diem (1948). Figure 4-8 (from Boucher, 1952) shows cloud data collected at Mt. Washington along with Diem's aircraft observations.

In experiments at South Park, near Denver, Colorado, Knollenberg's Axially Scattering Spectrometer Probe (ASSP) was used to measure drop-size distributions. Soot-coated slide samples were also taken. The results were reported by Breed et al. (1976) in the Proceedings of the International Cloud Physics Conference. The authors reported drop number density, mean diameter $\bar{D}$ of the drops and total liquid water content for five cases from both the ASSP and the slide observations. The results are shown in Table 4-4. Assuming an exponential distribution, D_o has been calculated from $\bar{D}$, and Z has been calculated from Eq. (4-6a).

BEST DOCUMENT AVAILABLE

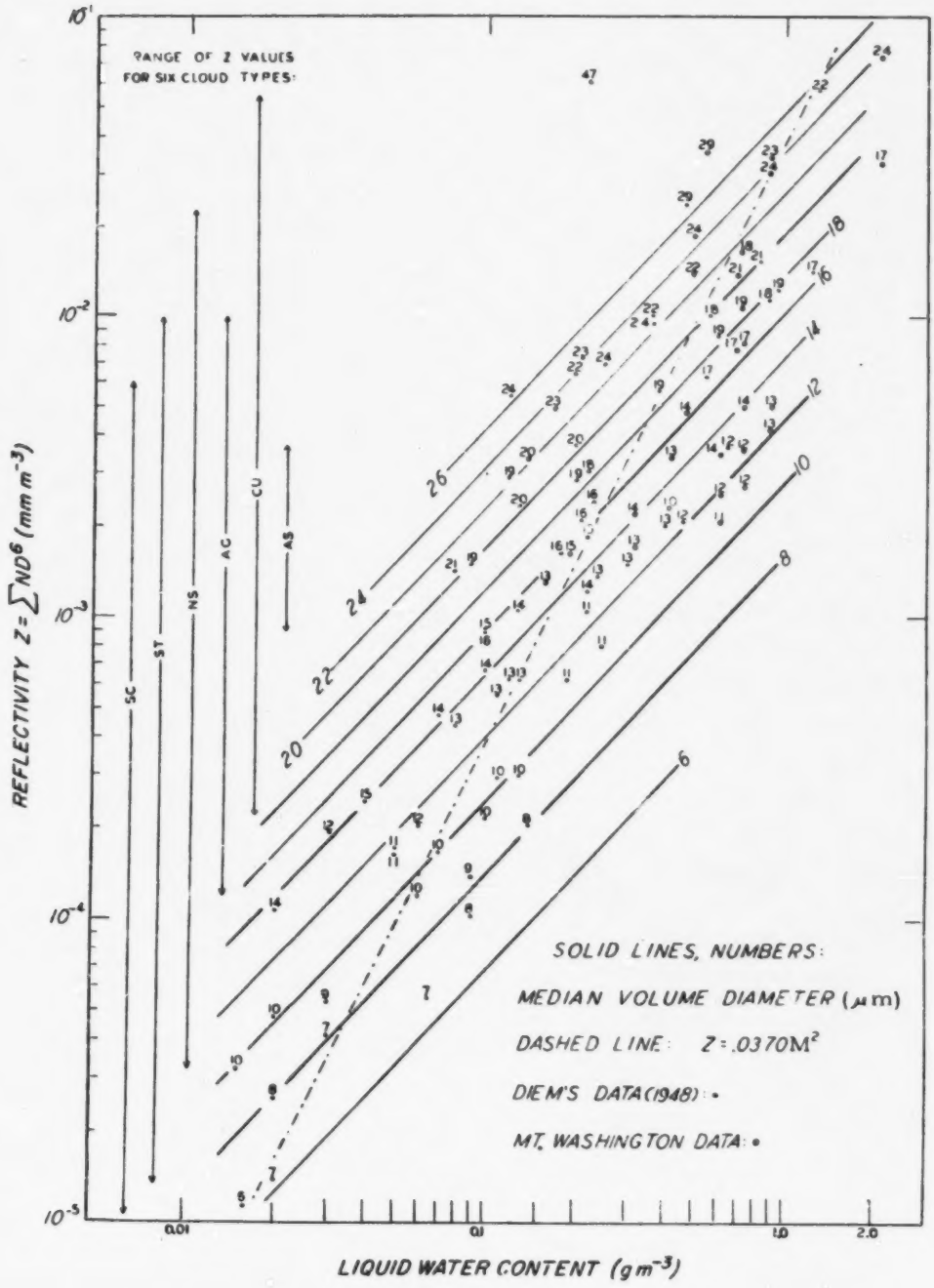

Figure 4.8--Diagram showing the correlation between radar reflectivity factor, the median volume diameter and the liquid water content for clouds, based on 38 impinger observations at Mt. Washington NH, and 67 aircraft observations by Diem in Germany. (Boucher, 1952.)

Table 4-4. Cumulus cloud parameters; South Park, Colorado.

N_T (m^{-3})	$\bar{D}$ (μm)	M ($gr\ m^{-3}$)	D_o (μm)	Z ($mm^6\ m^{-3}$)
687	8.4	.216	30.8	.0163
72	7.4	.015	27.2	7.8×10^{-4}
487	9.7	.234	35.6	2.7×10^{-2}
565	9.3	.236	34.1	2.4×10^{-2}
461	9.9	.233	36.3	2.9×10^{-2}
559	9.7	.405	35.5	4.7×10^{-2}
104	7.1	.028	26.1	1.3×10^{-3}
64	8.3	.027	30.5	2.0×10^{-3}
209	8.1	.085	29.7	5.8×10^{-3}
352	9.5	.234	34.9	2.6×10^{-2}

It is clear from the various observations tabulated here that the liquid water content of the Deirmendjian clouds is an underestimate of what has been measured in natural clouds. This is most clearly true of cumulus types, for which much observational data exist; there have been few in-situ observations in the corona producing clouds.

4.6 Observations of Drop-Size Distribution in Man-Made Clouds

In recent years there has been concern about the ways in which man's activity may affect the environment. One concern has centered on problems of heat and moisture "pollution" and the resulting modification of local climate. Thus cooling tower plumes associated with the various kinds of power generating plants have been studied and their modification of the environment examined. Huff (1972) and Agee (1971) have demonstrated that snowfall is enhanced downwind of power plants. The physical explanation is not clear though mechanisms have been proposed (Hanna and Gifford, 1975). The drop size distribution within the plume is a critical factor in the physics. It is exceptionally difficult to measure in a plume because tower-mounted in-situ sensors are seldom feasible and aircraft-borne penetrations are expensive and

too brief to provide satisfactory data. It is therefore of interest to examine the utility of short wave-length radars (e.g., 8.6 mm) to probe plume structure remotely. The problem has also been studied by Ricks (1977).

Few data sets are available, and we use here data acquired by Pena (1977) from aircraft penetrations of a power plant plume at Keystone, Pennsylvania. The same data set was used by Ricks. The drop size spectra are listed in Table 4-5 along with the conditions under which the data were collected. We have used these data to calculate (by numerical integration) the total number of drops (N_T), the total volume of liquid particulates (V_T) and the total reflectivity factor (Z_T). Because of the importance of the large drops ($Z \propto D^6$), the distributions have been extrapolated by fitting an exponential distribution to the measured distribution at the large-drop tail of the spectrum. The resulting Z values from manmade clouds are very similar to the values found in natural clouds, for example in South Park (see Table 4-4), but they are almost 2 orders of magnitude larger than Z's found from the Deirmendjian distribution for cumulus.

4.7 Observations of Cloud Reflectivity

Few radar observations of clouds are to be found in the literature; most observations reported have been confined to precipitating systems, primarily because of the radar wavelengths used. The status of cloud observations using millimeter wavelength radars prior to 1964 has been presented by Plank et al. (1954) and by Harper (1964). At that time radar was not an impressive tool for cloud observation.

Based on observations relating the percentage mass distribution by size to drop-size distributions as measured at Mt. Washington Observatory, Bartoff and Atlas (1951) undertook to relate median diameter to the radar reflectivity factor Z. They arrived at the following relationship between reflectivity factor, median diameter, and total water content M (where the subscript T is dropped from now on):

$$Z = 1.35\ (6/\pi)\ D_o^3\ (M/\rho) \times 10^{12}\ (mm^6\ m^{-3}) \qquad (4\text{-}15)$$

where D_o is in meters and M is g m^{-3}. Although Eq. (4-15) is empirical, it is similar in form to (4-6b). The difference between $\Gamma[(3/n) + 1)]$ and 1.35 is probably not significant. Of course, D_o and M are not unrelated; in fact,

BEST DOCUMENT AVAILABLE

Table 4-5 Observed plume data (drop number is various size intervals).

Droplet Diameter (μm)	Sample Identifier						
	#1	#2	#3	#4	#5	#6	#7
1							
2	69	164	666	183			
3							
4							
5	553	366	732	289	27	56	36
6							
7							
8	374	486	659	361	90	86	72
9							
10	466	427	792	897	123	115	96
11							
12							
13	95	295	390	370	104	120	107
14							
15	8	143	216	99	23	66	25
16							
17							
18		21	33	47	2	17	2
19							
20			18			12	2
Plume Temp (°C)	20	20	20	20	20	20	20
Air Temp (°C)	5.8	5.8	5.8	5.8	16.6	16.6	16.6
Pressure (mb)	990	990	990	990	990	990	990
Water Vapor Density (gr m^{-3})	4.06	4.06	4.06	4.06	8.3	8.3	8.3
N_T (m^{-3})	3664×10^{6}	5151×10^{6}	9566×10^{6}	5808×10^{6}	963.5×10^{6}	1210×10^{6}	897.5×10^{6}
V_T ($m^3 m^{-3}$)	2.54×10^{-6}	5.57×10^{-6}	8.91×10^{-6}	7.37×10^{-6}	1.36×10^{-6}	2.165×10^{-6}	1.32×10^{-6}
Z_T ($mm^6 m^{-3}$)	3.45×10^{-3}	1.45×10^{-2}	2.66×10^{-2}	2.13×10^{-2}	3.01×10^{-3}	7.93×10^{-3}	3.15×10^{-3}

BEST DOCUMENT AVAILABLE

Atlas (1954) finds

$$D_o(m) = 26.5 \times 10^{-6} M^{1/3} \qquad (4\text{-}16)$$

so

$$Z = 0.048 M^2 \quad (mm^6 m^{-3}) \qquad (4\text{-}17a)$$

or

$$Z = 139 D_o^6 \times 10^{24} \quad (mm^6 m^{-3}) . \qquad (4\text{-}17b)$$

If radar reflectivity is used to calculate D_o and M, Atlas estimates that Eq. (4-15) gives a standard error of estimate of only 6.5% for D_o and 21% for M. Equation (4-16) yields D_o with a standard error of 33%. Using (4-15), Eq. (4-17a) is found from which M is obtained with a standard error of 53% and (4-17b) is found yielding D_o with an error of 16%. Apparently these relations might be useful for some practical problems such as estimating visibility within clouds, but they are not accurate enough to test the microphysics of cloud models.

For advection fogs, Donaldson (1955) finds the following relationships corresponding to the cloud Eqs. (4-15, 16, 17):

$$Z = 3.26 D_o^3 M \times 10^{12} \quad \begin{cases} +34\% \\ -53\% \end{cases} , \qquad (4\text{-}18)$$

$$Z = 8.2 M^2 \quad \begin{cases} +115\% \\ -53\% \end{cases} \qquad (4\text{-}19)$$

and

$$Z = 2.7 D_o^6 \times 10^{24} \quad \begin{cases} +91\% \\ -48\% \end{cases} . \qquad (4\text{-}20)$$

In Table 4-3, the Atlas-Bartoff relationship, (Eq. (4-15), has been used to compute Z for the Weickmann aufm Kampe data and the Squires data. These may be compared with $\Sigma N_i \Delta D_i^6$ calculated from Squires' data*. For comparison, $N_T D_o$ has also been computed, and it is clear that the Atlas-Bartoff equation is better, though not dramatically better, and it might sometimes be useful to substitute information about N for information about M when computing Z.

---

* Squires' data are presented as drop size histograms in size increments of typically $\Delta D = 10$ μm.

Conclusions

Experience gained in the 1950's and 1960's does not demonstrate that radar reflectivity is a very useful quantity in the observation and study of clouds. However, with the advances in radar technology in the 1970's, and with the inclusion of dual-frequency attenuation measurements, dual polarization and Doppler, the utility of radars for cloud investigations should be re-evaluated.

There is a wide range in measured values of cloud drop size distributions. This is partly due to the variety of measurement methods used, but present evidence suggests that the large variation may be real. There has probably been some bias because most experimental programs have been aimed at storm and precipitation research, and aircraft penetrations have tended to occur under conditions prior to or during precipitation conditions. This may partly explain why larger drop sizes and higher Z values are found from in-situ measurements than are deduced from optical techniques and the Deirmendjian model.

BEST DOCUMENT AVAILABLE

CHAPTER 5 - RADAR ATTENUATION AND CLOUD OBSERVATION

5.1 Introduction

The previous Chapter addressed the question of useful data that might be obtained with a cloud detecting radar and considered what information might be available from reflectivity measurements alone. In this section we consider what information might be extracted if both reflectivity and attenuation measurements were available from radars with different wavelengths. Such methods have been used with some limited success in studies of precipitation (Goldhirsh and Katz, 1974), but the problem is different (and in some ways simpler) if it were to be used with clouds. It could, in principle, provide a spatial picture of the drop-size distribution in the early stages of a developing storm.

5.2 Attenuation of Radar Waves by Small Water Drops

Attenuation of radar waves may result from gaseous absorption, particle absorption (say by water droplets) or from particles scattering energy out of the beam. If radar wavelengths are chosen which avoid the water vapor and oxygen spectral lines (say 3.2 cm, 0.86 cm, or 0.31 cm), gaseous absorption can be considered small. If the water drops are very small compared with the radar wavelength, the Rayleigh approximation for the scattering and absorption cross-sections gives (Battan, 1973 pg. 67):

$$Q_s = \frac{2}{3}\frac{\pi^5}{\lambda^4}|K|^2 D^6 \qquad (5\text{-}1a)$$

$$Q_a = \frac{\pi^2}{\lambda} I(-K) D^3 \qquad (5\text{-}1b)$$

where D is drop-size diameter, $K = (m^2 - 1)/(m^2 + 2)$, m is the complex index of refraction, λ is radar wavelength and $I(-K)$ is the imaginary part of minus K shown plotted in Fig. 5-1. Obviously, for very small D, as in clouds, the absorption cross-section is the important consideration. Then k (the absorption coefficient) is the sum of the absorption cross-sections of all the particles within a unit volume; so

$$k = \sum_{vol} Q_a = \frac{\pi^2}{\lambda} I(-K) \int_0^\infty N_D D^3 \, dD \qquad (5\text{-}2a)$$

BEST DOCUMENT AVAILABLE

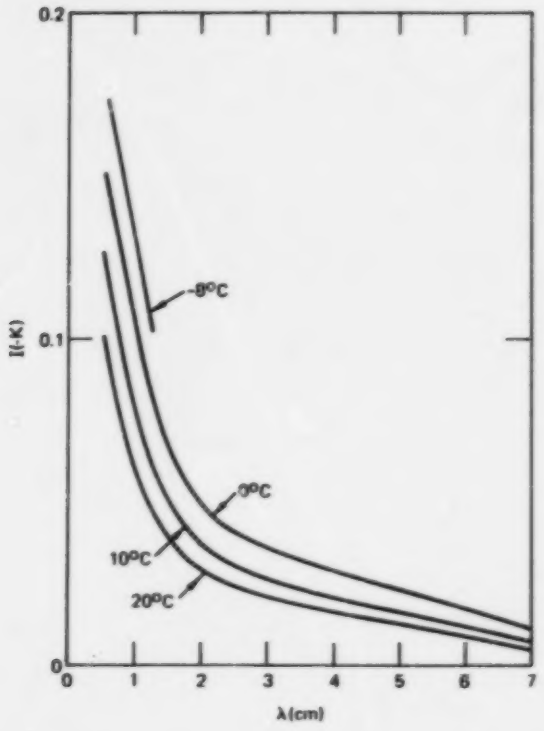

Figure 5.1--Imaginary part of $-K = -(m^2-1)/(m^2+2)$ as a function of wavelength and temperature.

where $N_D\,dD$ is the number of drops in the size interval from D to D + dD. However, note that total mass of liquid water

$$M_T = \rho \frac{\pi}{6} \int_0^\infty N_D D^3 \, dD$$

so

$$k = \frac{6\pi}{\rho\lambda} I(-K) M_T \qquad (5\text{-}2b)$$

and is independent of the drop-size distribution. Thus, for water clouds, attenuation provides a simple, direct measure of liquid water content if temperature can be estimated so that I(-K) is known. From Chapter 4 the reflectivity factor Z is given by:

$$Z = N_0 \frac{6!}{(3.67)^7} D_0^7 \qquad \text{(for exponential distribution)} \qquad (5\text{-}3a)$$

$$Z = \frac{6}{\rho\pi} \Gamma(1.91) D_0^3 M_T \qquad \text{(for Best's cloud drop-size distribution)} \qquad (5\text{-}3b)$$

BEST DOCUMENT AVAILABLE

where $N_o = N_D e^{3.67\ D/D_o}$ and D_o is the drop-size above which half the liquid water is found. From (5-2b) and (5-3a,b) it is easy to verify that

$$D_o^3 = \frac{\pi^2}{\lambda} \frac{I(-K)}{\Gamma(1.91)} \frac{Z}{k} \text{ (Best)}, \quad D_o^3 = \frac{\pi^2}{\lambda} I(-K) \frac{(3.67)^3}{120} \frac{Z}{k} \text{ (exponential)}. \quad (5\text{-}4a,b)$$

If we consider the more general drop size distribution, Eq. (4-7a), we see from Eq. (4-14b) that

$$D_o^3 = \frac{\pi^2}{\lambda} |I(-K)|\ G^{3/\gamma}\ \Gamma[(4+\alpha)/\gamma]/\Gamma[(7+\alpha)/\gamma]\ \frac{Z}{k}\ . \quad (5\text{-}4c)$$

Apparently radar measurements of both reflectivity and attenuation can provide information about important microphysical cloud quantities.

5.3 Optical Extinction by Small Water Spheres

The extinction coefficient σ_{ext} is defined by the relation $I/I_o = \exp(-\sigma_{ext} r)$ where I is the intensity of the transmitted light at range r and I_o is the intensity at $r = 0$. If Q_e is the extinction efficiency of a drop, then the extinction from a single drop is $Q_e A$, where $A = \pi r^2$ and r is the radius of the spherical drop. For a distribution of drops of uniform size the extinction coefficient is $\sigma_{ext} = N\ Q_e\ \pi r^2 \equiv N\ Q_e (\pi/4) D^2$ where N is the number of drops per unit volume. For number density distribution N_D

$$\sigma_{ext} = (\pi/4) \int_o^\infty Q_e\ D^2\ N_D\ dD \quad (5\text{-}5a)$$

(see Van de Hulst, 1957, pg. 129). In the Mie scattering limit of drops very large compared with wavelength, which is the usual condition for visible wavelengths, $Q_e \to 2$ if the absorption is relatively small; then

$$\sigma_{ext} = (\pi/2) \int_o^\infty D^2\ N_D\ dD. \quad (5\text{-}5b)$$

It follows that

$$\sigma_{ext} = \frac{3\ \Gamma(0.7)}{\rho} \frac{M_T}{D_o} \text{ (Best)}, \quad \sigma_{ext} = 367 \frac{M_T}{\rho\ D_o} \text{ (exponential)}\ . \quad (5\text{-}6a,b)$$

Again, the result may be calculated for the modified gamma function using Eqs. (4-7b) and (5-5b) and we find

$$\sigma_{ext} = 3\ \rho^{-1}\ M_T\ G^{1/\gamma}\ D_o^{-1}\ \Gamma[(3+\alpha)/\gamma]/\Gamma[(4+\alpha)/\gamma]. \quad (5\text{-}6c)$$

The assumption that $Q_e = 2$ has been examined by Hodkinson (1966) and Jiusto (1974). They find that it actually varies from 1 to 2 depending on the angle and range to the scatterer.

Apparently combinations of optical and radar systems have potential for remotely acquiring information about drop size distribution when the attenuation of the optical wavelengths is not too large.

5.4 Cloud and Rain Parameter Diagrams

From Eqs. (4-13), (4-14b), (5-2b) and 5-6c) it is clear that Z, k, D_o, M and σ_{ext} are inter-related in a simple way if γ and α are known (as, for example if the drop size distribution is exponential). Atlas and Ulbrich (1974) have made use of this fact and have constructed a "rain parameter diagram" describing the relationships between the above quantities and rain-rate R (mm hr^{-1}) assuming a Marshall-Palmer distribution in which $\Lambda = 41\ R^{-0.21}$ (cm^{-1}). For particles of precipitation size, the Rayleigh approximation is not necessarily valid. Atlas and Ulbrich therefore write $M = \ell A^{\beta}$ where the attenuation in dB per unit distance is $A = 10\ k \log e = 4.34\ k$. Actually, they express A in dB km^{-1}. In the Rayleigh approximation $\beta = 1$. On the other hand, when the drops are very large with respect to wavelength $\beta = 3/2$ for a monodisperse size distribution. In general the functional behavior of β is quite complicated because the full Mie scatter calculation is needed and the drop size distribution must be known. Assuming a Marshall-Palmer distribution, Atlas and Ulbrich made the necessary calculations for $\lambda = 3.22$ cm and $T = 10°C$. Their results are shown in Fig. 5-2. The inter-relationships are much simpler for clouds because the Rayleigh approximation is valid for the usual radar wavelengths. We have calculated the corresponding "CLOUDPAD" shown in Fig. 5-3. On the cloud diagram R of course is not relevant. In the cloud case, the diagram can be very general if a dimensionless attenuation $A\lambda/I(-K)$ is defined and used as a parameter. The diagram then applies to all temperatures in the Rayleigh size range. In Fig. 5-3 an exponential drop size distribution is assumed but no assumption of a value for N_o is necessary.

If Z and k can be observed by radar, some of the most important cloud quantities such as liquid water content, drop size (D_o) and extinction coefficient can be monitored continuously in time and space about the radar. If

BEST DOCUMENT AVAILABLE

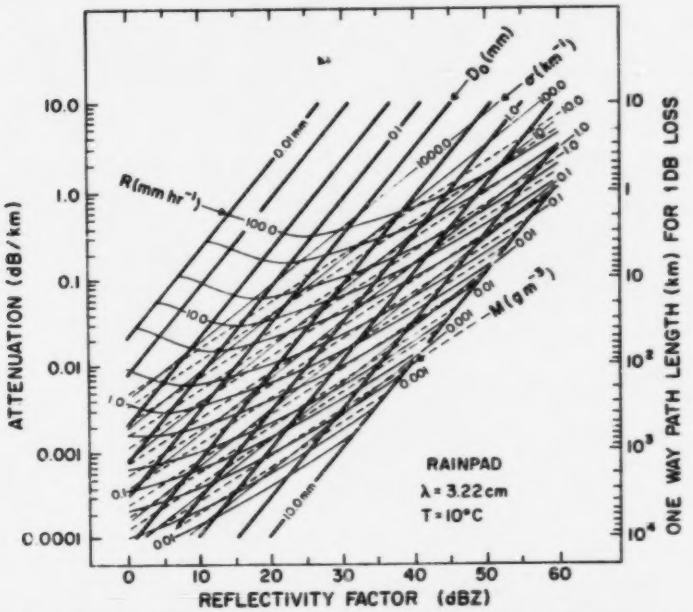

Figure 5.2--Rain parameter diagram of Atlas and Ulbrich (1974) graphically demonstrating relationships between attenuation A, reflectivity factor Z, total mass of liquid water M, rainfall rate R, and optical extinction coefficient σ. Calculations assume a Marshall-Palmer distribution and fit a power law $M = \ell A^{\beta}$ to the Mie scattering solution. Temperature and wavelength must be assumed.

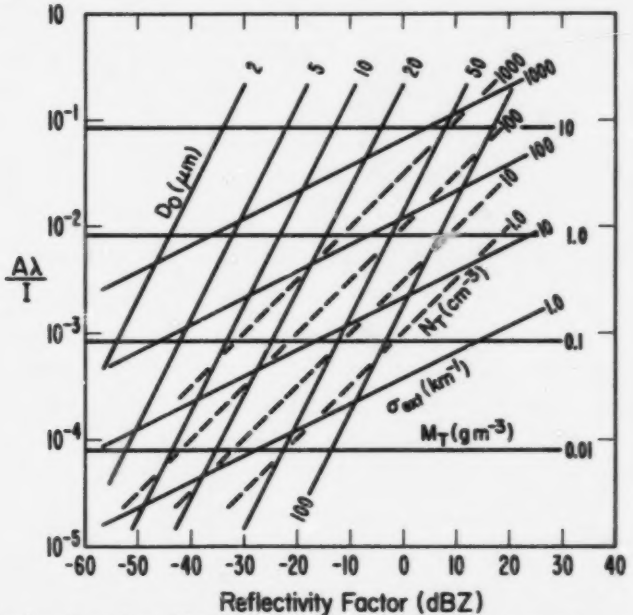

Figure 5.3--Cloud parameter diagram in which Rayleigh scattering is assumed. Shows relationships between attenuation A, reflectivity factor Z, total mass of liquid water M_T, total number density N_T and optical extinction coefficient σ_{ext}. When attenuation is plotted as the dimensionless quantity Aλ/I, diagram applies for all temperatures and wavelengths. The quantity I = Imaginary part of $-(m^2-1)/(m^2+2)$.

BEST_DOCUMENT AVAILABLE

extinction coefficient can be obtained optically, the observational errors can be estimated and the relevance of the assumed spectral functions could then be judged.

5.5 Measuring Z and k

Suppose we make cloud reflectivity measurements with two radars of different wavelengths, one having a wavelength that is essentially unattenuated and the other heavily attenuated. Then for the unattenuated radar the received power P_r is

$$P_{r1} = \frac{C_1}{r^2} Z \tag{5-7a}$$

and from the other

$$P_{r2} = \frac{C_2}{r^2} Z \, e^{-2 \int_o^r k \, dr} \tag{5-7b}$$

where r is range and C_1 and C_2 are known constants depending on the radar parameters. Then it is easy to see that

$$Z = \frac{P_{r1}}{C_1} r^2 \tag{5-8a}$$

and

$$k = \frac{1}{2} \, d \, \ell n(P_{r1}/P_{r2})/dr \, . \tag{5-8b}$$

From Z and k the cloud information is readily calculated from (5-4a,b) and (5-2b).

Unfortunately Eq. (5-8b) depends on absolute calibrations of both radars (C_1 and C_2), so the ratio P_{r1}/P_{r2} cannot be as accurate as comparative measurements made by a single radar. However, a single radar can yield k if the gradients in Z are not large. To see this, write the integral over k from some range r_o to $r = r_o + \Delta$ where Δ is some small increment of range over which backscattered powers are to be compared. Then

$$\int_{r_o}^{r_o+\Delta} k \, dr = -\frac{1}{2} \ell n \left. \frac{P_r(r) \, r^2}{C_2 Z} \right|_{r_o}^{r_o+\Delta} \, . \tag{5-9a}$$

BEST DOCUMENT AVAILABLE

If k and Z can be considered constant over the increment Δ, this gives

$$k = \frac{1}{2\Delta} \frac{r_o^2 \, P_r(r_o)}{(r_o+\Delta)^2 \, P_r(r_o+\Delta)} \quad . \tag{5-9b}$$

Now the ratio of powers applies to a single radar so only relative power at different positions is needed, and relative powers can be measured quite accurately. However, (5-9b) requires that Z be constant over the increment Δ. In principle Δ can be as small as the range resolution of the radar. If the antenna is stationary, many pulses can be integrated to obtain accurate power estimates. Thus the variance of received power,

$$\text{VAR } P_r(r_o) = \text{VAR } P_r(r_o+\Delta) = \frac{31(\text{dB})^2}{N}$$

where N is the number of independent samples (pulses).

5.6 Analysis of Errors

If we presume that careful calibration of the radars will allow absolute power to be observed to an accuracy of ± 3 dB then Eq. (5-8a,b) and Eq. (5-4a,b) lead to error bars on M shown in Fig. 5-4a. If relative powers for a single radar have an accuracy of ± 0.3 dB, Eq. (5-9b) gives the much smaller error range shown in Fig. 5-4b, integration over many pulses could substantially improve this accuracy figure.

However, it is to be remembered that the validity of (5-9b) depends on Z remaining constant over the range of Δ. In severe storms there are many times when this approximation is not valid even when Δ is chosen as small as 1 km. However, in the case of cloud systems that are more-or-less stratiform, or of storms in the early stages of development, the approximation that Z is roughly constant over increments of a kilometer may be much more realistic. It is likely that both (5-8b) and (5-9b) will be useful, with (5-8b) used mainly through regions of large gradients of Z.

Figures (5-5a) and (5-5b) show the corresponding errors in D_o to be expected for average reflectivities of -20 and -30 dBZ if Z can be estimated to an accuracy of ± 3 dBZ and $P_r(r_o)/[P_r(r_o+\Delta)]$ is known to ± 0.3 dB. We see that regardless of average reflectivity, the expected range of error is about ± 25% which is probably not bad for many purposes since the range of D_o is so great.

BEST DOCUMENT AVAILABLE

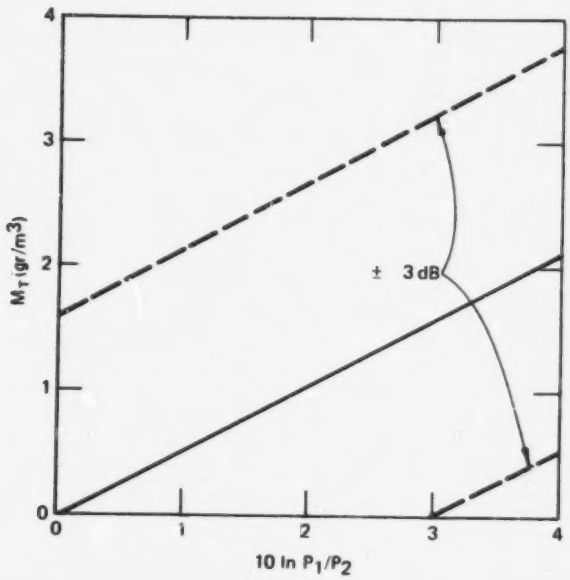

Figure 5.4a--Error in calculation of mass of liquid water assuming an error of ± 3 dB in measured power difference between radars of two different wavelengths.

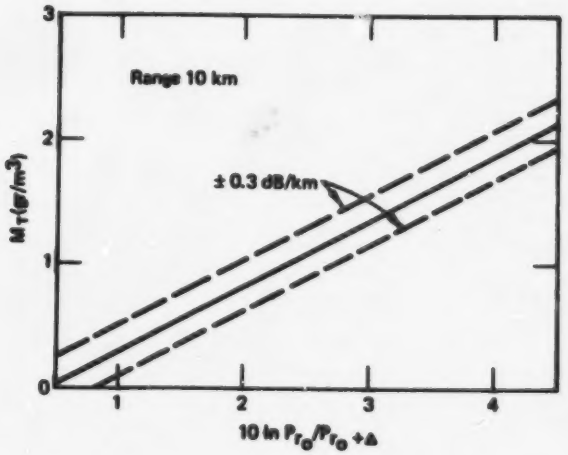

Figure 5.4b--Error in calculation of mass of liquid water assuming an error ± 0.3 dB/km in measured attenuation between ranges r_o and $r_o + \Delta$.

BEST DOCUMENT AVAILABLE

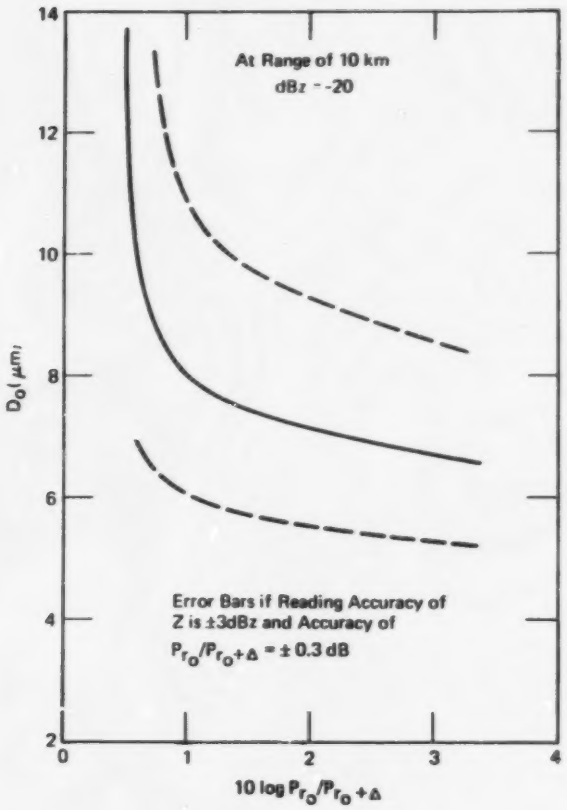
At Range of 10 km
dBz = -20
Error Bars if Reading Accuracy of
Z is ±3dBz and Accuracy of
$P_{r_o}/P_{r_o+\Delta}$ = ± 0.3 dB
D_o (μm)
10 log $P_{r_o}/P_{r_o+\Delta}$

Figure 5.5a--Error in calculation of median mass diameter for assumed conditions in dicated on figure.

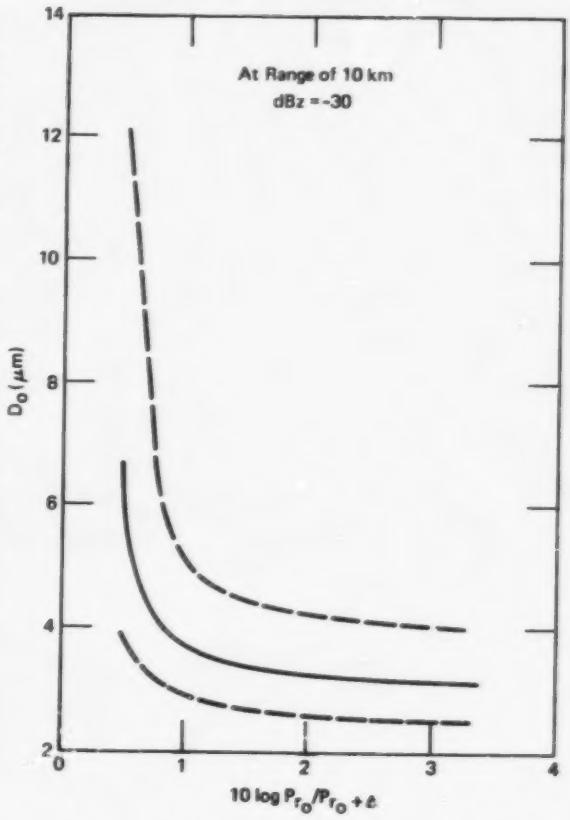

Figure 5.5b--Error in calculation of median mass diameter for an assumed reflectivity of dBZ = -30. Conditions otherwise as in Fig. 5.5a.

5.7 Conclusions

In some ways clouds are more convenient to work with than precipitation because the Rayleigh approximation can be used.

Multi wavelength radar observations can provide information about microphysical quantities. We see from Eq. (5-2a) that there is almost a factor of four difference in the attenuation of 3.2 cm radars and 0.86 cm radars. This should be enough difference to provide valuable information on spatial drop-size distribution and on its evolution. If a 10 cm radar were used, its waves could be considered as unattenuated and even better quantitative observations could be made. This kind of information could be of great value in understanding the microphysics of nucleation and precipitation. As an aid to short-term forecasting at a Weather Service site, a forecaster might find it of value to watch for a rapid growth in D_o^3 (by watching Z/k) as a predictor of place and time of the onset of local precipitation.

CHAPTER 6 - POLARIZATION AND SCATTERER CHARACTERIZATION

6.1 Introduction

One of the impressive results of past radar cloud observations was the conclusion that high reflectivities in non-precipitating clouds were often associated with the presence of ice particles. More recently measurements of signals from satellites received on two polarizations have sometimes shown significant signal in the cross-polarized channel even when there is little attenuation along the path. These observations could result from the polarizing effects of ice particles located somewhere on the path. Finally, cloud studies with radars have always produced cases for which there was significant backscatter from the apparently clear air. Some of these observations undoubtedly resulted from backscatter from turbulent inhomogeneities in the dielectric structure of clear air, but some of them might well result from enhanced backscatter from particles having a favorable alignment relative to the radar's polarization. The depolarization of satellite signals under conditions that occasionally are visually "clear" suggests that such events may be associated with ice crystals.

Additional support for this hypothesis comes from observations made with the 10 cm FM-CW radar pointing vertically. Strong and consistent returns were observed at Fraser, Colorado from particles identified as ice blown off the peaks and ridges surrounding the site. An example is shown in Fig. 6-1, in which both cloud particles and dielectric backscatter are shown. The dielectric backscatter is seen in the breaking wave structure faintly visible at a height of 2 km. The identification of the scattering particles was substantiated by simultaneous lidar observations.

Immediately we are presented with a mystery, of sorts, if we assume an expression similar to (Eq. A17) to be valid, because $K \equiv (m^2-1)/(m^2+2) \approx 0.97$ for water and only 0.45 for ice. The situation is even more drastic for snow because $K/\rho \approx$ constant and the density of snowflakes is only about 0.05 that of ice. Thus $K_{snow} = 0.05\ K_{ice}$, and we would expect water drops to be much more effective scatterers than ice or snow. A possible explanation lies in polarization effects and the possibility that ice particles are often water coated. Growth and nucleation processes may also be important because particles with ice centers may grow to drop-sizes relatively large compared with coexisting water drops.

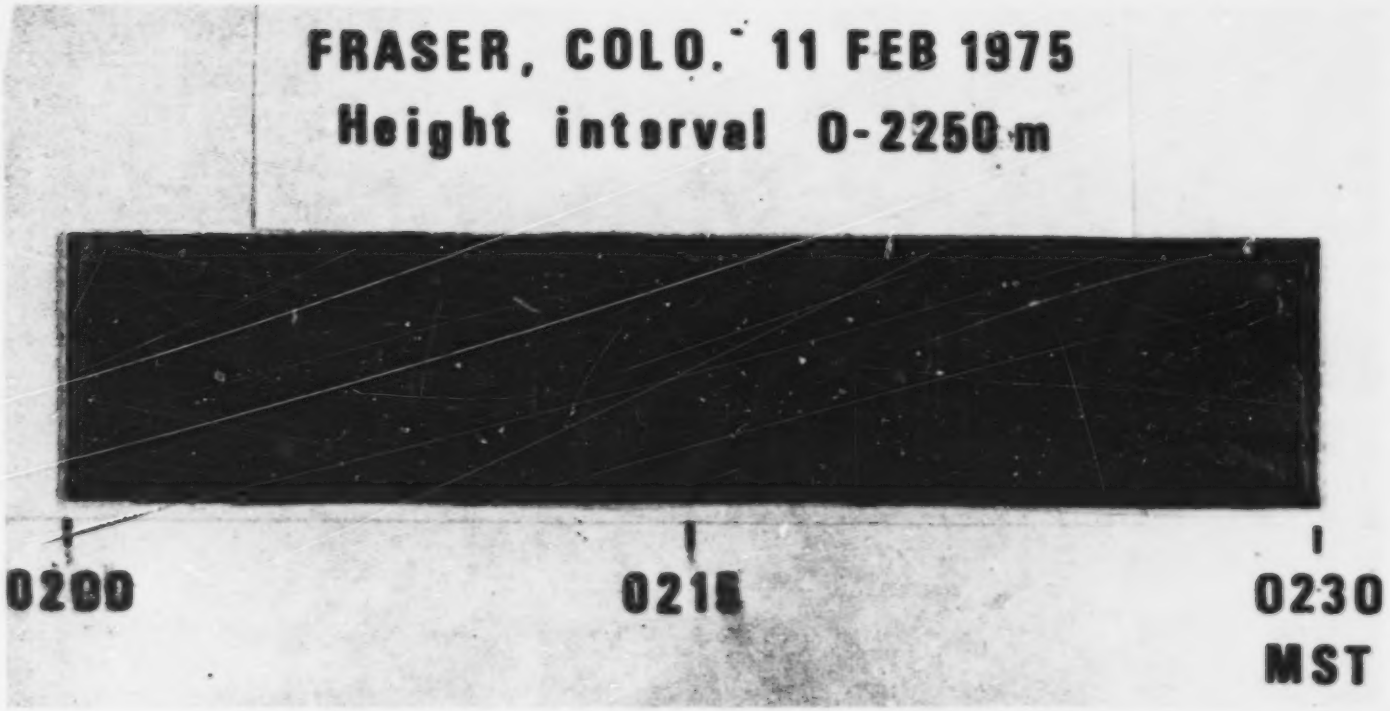

Figure 6.1--Record from frequency-modulated continuous wave, 10 cm wavelength radar described by Chadwick, et al. [1976] showing backscatter from ice clouds and from clear-air (the braided structure of Kelvin-Helmholtz waves near top center). Gain was reduced near center of record to better display the clear-air return. Note the two classes of return are of comparable magnitude.

BEST DOCUMENT AVAILABLE

These observations suggest that it is imperative that more information be acquired on the relationship between cloud types and radar backscatter; they demonstrate the potential importance of radar as an observational tool in a weather observing facility but emphasize the gaps in present knowledge that prevent its use in a quantitative and explicit way.

The observational results summarized above suggest an experimental program in which radar polarization might be exploited to fill some of the crucial information gaps.

6.2 Backscatter by Non-spherical Particles

Discussion

There has been increased interest in methods of calculating the polarization effects of non-spherical scatterers because of the anomalous depolarization events that are now recognized to occur commonly on earth-satellite paths. There are three primary ways in which the effect of scatterer shape on incident radiation may be analyzed. The theory of Gans (1912) is an amplification and extension of Lord Rayleigh's earlier theory (1881) for scattering from small spheroids. With the availability of computers, scattering theories based on Waterman's (1965) "extended integral equation" technique have been used (e.g., Bringi and Seliga, 1977) to treat non-spherical scatterers with dimensions up to about 3λ. It provides an exact solution, but computers are generally needed for solution of the transition, or T-matrix. Finally, numerical solution for the scattering from bodies of arbitrary composition and shape is possible by dividing the scattering volume into incremental volume elements and matching the (complex) boundary conditions at all inter-volume-element boundaries. Only the Gans method provides results parametrically simple enough to make conceptually general statements about the effects of non-sphericity on scattering.

Theory

It is presumed in Gans theory that a uniform plane electromagnetic wave intercepting an ellipsoid excites dipole moments that can be resolved into three components along the orthogonal axes of the ellipsoid. The length of the axes are presumed small compared with the wavelength, and multi-pole moments are neglected. The Gans theory has been adopted by Atlas, Kerker, and Hitchfeld (1953) to deduce some effects of scatterer shape on radar backscatter.

BEST DOCUMENT AVAILABLE

The electric moment per unit volume induced in the scatterer is E $(m^2-m_o^2)$ so the total moment is (see Section 2.4)

$$f = m_o^2 EV\ (m^2/m_o^2-1)/4\pi \tag{6-1}$$

where V is volume of the scatterer, m is its refractive index, m_o is the refractive index of the propagation median, and E is the electric field induced in the scatterer. Gans (1912) finds the induced field in a spheroid to be related to the incident field E_o as

$$E_\xi = \frac{E_{o\xi}}{1+\frac{m^2/m_o^2-1}{4\pi}\,p} \tag{6-2a}$$

$$E_\eta = \frac{E_{o\eta}}{1+\frac{m^2/m_o^2-1}{4\pi}\,p'} \tag{6-2b}$$

$$E_\zeta = \frac{E_{o\zeta}}{1+\frac{m^2/m_o^2-1}{4\pi}\,p'} \tag{6-2c}$$

where ξ is the direction of the axis of rotation (or figure axis) of the ellipse and η and ζ are the directions of two orthogonal diameters. Therefore, from Eq. (6-1),

$$f_\xi = (4\pi)^{-1}\, m_o^2 g\, E_{o\xi},\quad f_\eta = (4\pi)^{-1}\, m_o^2 g'\, E_{o\eta},\quad f_\zeta = (4\pi)^{-1}\, m_o^2 g'\, E_{o\zeta} \tag{6-3}$$

where g is the complex quantity

$$g,\ g' = \frac{V[(m/m_o)^2-1]}{4\pi + [(m/m_o)^2-1]p,p'} \equiv \frac{3V}{4\pi}\, L,\ L'\, e^{-i\chi,\chi'} \tag{6-4}$$

where

$$p' = 2\pi - p/2.$$

The quantities L, L', χ, χ', and g, g' are defined by the identities in Eq. (6-4). For an oblate spheroid (flattened at the poles of the major axis) Gans finds

$$p = \frac{4\pi}{e^2}\left[1 - \left(\frac{1-e^2}{e^2}\right)^{1/2} \text{arc sin } e\right] \tag{6-5a}$$

BEST DOCUMENT AVAILABLE

and for a prolate spheroid

$$p = 4\pi \frac{1-e^2}{e^2} \left[\frac{1}{2e} \ln\left(\frac{1+e}{1-e}\right) - 1\right] \tag{6-5b}$$

here $e = (a^2-b^2)^{1/2}/a$ is the eccentricity and a and b are the semi axes of the elliptical cross-section.

The scattered field E_s at distance r from a dipole of moment f is given by Eq. (2-5), that is,

$$E_s = \frac{k_s^2 f}{m_o^2 r} \exp(-i \underset{\sim}{k}_s \cdot \underset{\sim}{r}) \tag{6-6}$$

where $k_s = 2\pi/\lambda$. The r.f. phase factor, $\exp(-i \underset{\sim}{k}_s \cdot \underset{\sim}{r})$, will be neglected because we are interested in the signal magnitude. Also, the scattered power P_s at r is related to the incident power P_o as

$$P_s = \frac{P_o \sigma}{4\pi r^2} \tag{6-7}$$

where σ is the equivalent cross-section of a target isotropically scattering the same power in the direction $\underset{\sim}{r}$ as the real scatterer. Noting that P_o, P_s, $\propto E_o^2$, E_s^2 and that $V = \frac{\pi}{6} D^3$ is the volume of the equivalent sphere; Eqs. (6-3), (6-6), and (6-7) give

$$\sigma_i,\ \sigma_i' = \left(\frac{4\pi}{3}\right)^2 \frac{\pi^5 D_e^6 (m^2-1)^2}{\lambda^4 [4\pi + (m^2-1)p,p']^2} = \frac{64\pi^5}{\lambda^4} D_e^6 S,\ S' \tag{6-8}$$

where σ_i is the cross-section of an individual drop scattering parallel to the principle axis and σ_i' is the scattering cross-section for the two remaining orthogonal axes, D_e is the diameter of a sphere of equal volume, and S and S' are here defined by (6-8) for later use. If we examine the limiting case as $e \to 0$, and expand both the arc sin factor and the radical in Eq. (6-5a) for small e, it is found that $P \to P' \to 4\pi/3$ so that

$$\sigma_i = \frac{\pi^5}{\lambda^4} D^6 \frac{|m^2-1|^2}{(m^2+2)^2} = \frac{\pi^5}{\lambda^4} D^6 |K|^2 \tag{6-9}$$

in agreement with the well known result for Rayleigh scattering from small spherical particles (e.g., Battan, 1973).

BEST DOCUMENT AVAILABLE

Of course, Eqs. (6-8) and (6-9) give the scattering cross-section for a single particle only. The total scattered power is therefore proportional to $\sigma = \sum_{vol} \sigma_i$ where the summation is over a unit volume presumed to be uniformly filled with scatterers. If the size distribution of particles is described by N_D where N_D is the number of drops in the size interval D to D + dD, Eq. (6-9) gives

$$\sigma = \frac{\pi^5}{\lambda^4} |K|^2 \int_o^\infty D^6 N_D \, dD \tag{6-10}$$

over the whole size range of spherical particles and for spheroidal particles in general Eq. (6-8) gives

$$\sigma,\sigma' = \left(\frac{4\pi}{3}\right)^2 \frac{\pi^5}{\lambda^4} \int_o^\infty \frac{(m^2 - 1)^2}{[4\pi+(m^2-1)p,p']^2} D^6 N_D \, dD \tag{6-11a}$$

and therefore from the definitions of L and χ in Eq. (6-4)

$$\sigma,\sigma' = \frac{\pi^5}{\lambda^4} \int_o^\infty L,L' e^{-i\chi,\chi'} D^6 N_D \, dD \, . \tag{6-11b}$$

Seliga and Bringi (1976) define the quantity

$$Z_{DR} = 10 \log (\sigma/\sigma')$$

as the "differential reflectivity" where σ,σ' are given by Eqs. (6-11a) and (6-11b), and N_D is assumed to obey a Marshall-Palmer distribution, i.e., $N_D = N_o e^{-3.67/D_o}$. Some insight is provided by first assuming a uniform size distribution and assuming that all particles are oblate spheroids with vertical axes, equal eccentricity and equal volume. Then Eq. (6-8) gives

$$\sigma/\sigma' = g^2/g'^2.$$

Geometry of Scattering

We first consider the radar backscatter problem, then generalize it to the case of forward scatter because of the interest in scattering on earth-satellite paths. The orientation of the axis of symmetry (figure axis) of the ellipsoid is in the direction ξ and two orthogonal minor axes are chosen in the directions η and ζ. The geometry assumed is shown in Fig. 6-2 and is summarized as follows:

BEST DOCUMENT AVAILABLE

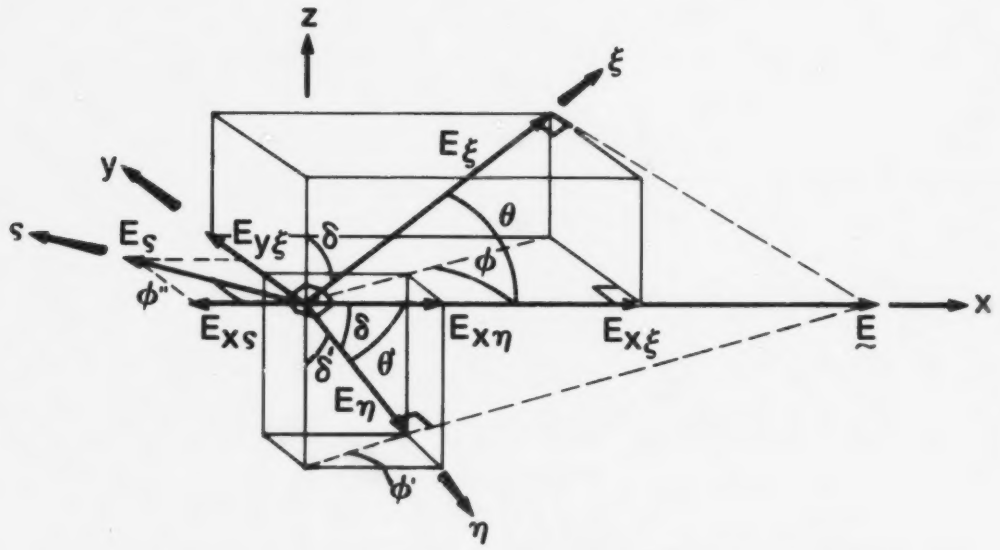

Figure 6.2--Schematic illustration of assumed geometry defining symbols and quantities used in polarization analysis.

a) choose ξ to be the direction of the rotational or figure axis of the ellipsoid,

b) choose z to be the propagation direction of both the incident and (with opposite sense) the radar backscattered energy,

c) choose the x axis to be in the direction of the incident field $\underset{\sim}{E}_o$ where the zero subscript is dropped from now on.

d) without loss in generality, choose one minor axis E_ζ of the ellipsoid to lie in the xy plane (i.e., $\phi' = \phi + 90°$) and the other to lie in the ξz plane (i.e., $\phi' = \phi$, $\delta' = \delta - 90°$).

e) make θ and δ the angles between the ξ direction and the x and z axes respectively. ϕ is the angle between x and the direction of E_ξ projected onto the xy plane. θ' and δ' are the angles between the η direction and the y and z axes respectively, and ϕ' and ϕ'' are the angles between x and the azimuthal directions of E_η and E_ζ.

Dropping the zero subscript the projections of $\underset{\sim}{E}$ onto the three axial directions are

BEST DOCUMENT AVAILABLE

$$E_\xi = E\cos\theta = E\ell, \qquad E_\eta = E\cos\theta' = Em, \qquad E_\zeta = E\cos\phi'' = En$$

and the projections on x are

$$E_{x\xi} = E_\xi\cos\theta = E_\xi \sin\delta\cos\phi, \quad E_{x\eta} = E_\eta\cos\theta' = E_\eta\cos\delta\cos\phi, \quad E_{x\zeta} = -E_\zeta\sin\phi.$$

Similarly, on y and z,

$$E_{y\xi} = E_\xi \sin\delta \sin\phi \qquad E_{y\eta} = E_\eta \cos\delta \sin\phi \qquad E_{y\zeta} = E_\zeta \cos\phi$$

$$E_{z\xi} = E_\xi \cos\delta \qquad E_{z\eta} = -E_\eta \sin\delta \qquad E_{z\zeta} = 0$$

so

$$E_{x\xi} = E \sin^2\delta \cos^2\phi \qquad E_{x\eta} = E \cos^2\delta \cos^2\phi \qquad E_{x\zeta} = E \sin^2\phi$$

$$E_{y\xi} = E \sin^2\delta \cos\phi \sin\phi \qquad E_{y\eta} = E \cos^2\delta \cos\phi \sin\phi \qquad E_{y\zeta} = -E \sin\phi \cos\phi \quad (6\text{-}12)$$

$$E_{z\xi} = E \sin\delta \cos\delta \cos\phi \qquad E_{z\eta} = -E \cos\delta \cos\phi \sin\delta \qquad E_{z\zeta} = 0$$

and

$$f_{x\xi} = m_o^2 g\, E_{x\xi} = CLe^{-i\chi}E_{x\xi}, \qquad f_{x\eta} = m_o^2 g' E_{x\eta} = CL'e^{-i\chi'}E_{x\eta},$$

$$f_{x\zeta} = m_o^2 g' E_{x\zeta} = CL'e^{i\chi'}E_{x\zeta} \quad \text{etc.}$$

where $C = 3\, m_o^2\, V/4\pi$ and V is the volume of the scatterer. Summing all components along x, y, and z,

$$f_x = CE\,(Le^{-i\chi}\sin^2\delta\cos^2\phi + L'e^{-i\chi'}\cos^2\delta\cos^2\phi + L'e^{-i\chi'}\sin^2\phi)$$

$$= CE\left\{(Le^{-i\chi} - L'e^{-i\chi'})\ell_1^2 + L'e^{-i\chi'}\right\} \quad (6\text{-}13a)$$

$$f_y = CE\left\{Le^{-i\chi}\sin^2\delta\,\sin\phi\cos\phi + L'e^{-i\chi'}\cos^2\delta\,\sin\phi\cos\phi - L'e^{-i\chi'}\sin\phi\cos\phi\right\}$$

$$= CE\left\{(Le^{-i\chi} - L'e^{-i\chi'})\ell_1\ell_2\right\} \quad (6\text{-}13b)$$

$$f_z = CE\cos\phi\cos\delta\sin\delta(Le^{-i\chi} - L'e^{-i\chi'}) = CE\,(Le^{-i\chi} - L'e^{-\chi'})\ell_1\ell_3 \quad (6\text{-}13c)$$

BEST_DOCUMENT AVAILABLE

where $\ell_1 = \sin\delta\cos\phi$, $\ell_2 = \sin\delta\sin\phi$, $\ell_3 = \cos\delta$ are the direction cosines of E_ξ projected onto the x, y, and z axis respectively.

If z is chosen to be the propagation direction, $E_z = f_z = 0$. If the $\underset{\sim}{E}$ vector lies on the x axis, the propagation plane is yz, and if the x axis is horizontal the radiation is horizontally polarized. If xz is the propagation plane, containing the $\underset{\sim}{E}$ vector, the radar is vertically polarized. In either case, f_y is the cross-polarized component of the radiation.

Of course, in reality we are not dealing with single scatterers but with ensembles of scatterers oriented in some manner only describable statistically. Atlas, Kerker, and Hitchfeld suggest three cases of particular interest: (a) the case of random orientation, (b) the case uniform orientation of oblate spheroids with figure axes vertical, and (c) the case of prolates with their major axis arbitrarily oriented in the horizontal plane. From Eqs. (6-13a,b)

$$f_x^2 = C^2E^2\left\{\ell_1^4L^2e^{-2i\chi} + (1-2\ell_1^2+\ell_1^4)(L')^2e^{-2i\chi} + (\ell_1^2-\ell_1^4)LL'e^{-i(\chi+\chi')}\right\} \qquad (6\text{-}14a)$$

$$f_y^2 = C^2E^2(\ell_1\ell_2)^2\left\{L^2e^{-2i\chi} - 2LL'e^{-i(\chi+\chi')} + (L')^2e^{-2i\chi'}\right\} . \qquad (6\text{-}14b)$$

If an average is taken over a complete cycle of the incident wave propagating such that $L\exp(-i\chi)$, $L'\exp(-i\chi') \propto \exp i(\omega t - k_o z - \chi,\chi')$

$$\overline{f_x^2} = \frac{C^2E^2}{2}\left\{\overline{\ell_1^4}|L|^2+(1-2\overline{\ell_1^2} + \overline{\ell_1^4})|L'|^2 + 2(\overline{\ell_1^2} - \overline{\ell_1^4})|L||L'|e^{-i(\chi-\chi')}\right\} \qquad (6\text{-}15a)$$

$$\overline{f_y^2} = \frac{C^2E^2}{2}\,\overline{(\ell_1\ell_2)^2}\left\{|L|^2 - 2|L||L'|e^{-i(\chi-\chi')}+|L'|^2\right\} . \qquad (6\text{-}15b)$$

Perfect Sphere

Return to Eqns. (6-4) and (6-5) and consider their limiting form for a perfect sphere. Note that e = 0 for a sphere. If the $\sin^{-1}$ factor and the radical in Eq. (6-5a) are expanded in series for small e, it is found that $p = p' \to 4\pi/3$ as $e \to 0$ so that

$$g = g' = \frac{3V(m^2 - 1)}{4\pi(m^2+2)} = a^3\,\frac{|m^2-1|}{(m^2+2)} \equiv a^3K \qquad (6\text{-}16a)$$

for a sphere, i.e., $Le^{-i\chi} = K$. Noting that $\ell_1 = \ell_2 = 0$ if we choose a coordinate system for the sphere such that $\xi = z$, Eq. (6-14a) gives

BEST DOCUMENT AVAILABLE

$$f^2 = m_o^4\, a^6 K^2 E^2 \equiv (3/4\pi)^2 m_o^4\, V^2 K^2 E^2 \qquad (6\text{-}16b)$$

in agreement with the classical result for the dipole moment of a sphere.

Random Orientation

If the orientation of the axis is entirely random

$$\overline{\ell_1^2} = \frac{1}{2}\int_{-1}^{1} \ell_1^2 d\ell_1 = \frac{1}{3},\ \overline{\ell_1^4} = \frac{1}{2}\int_{-1}^{1} \ell_1^4 d\ell_1 = \frac{1}{5} \text{ etc.}$$

Then

$$\overline{f_x^2} = \frac{C^2E^2}{2}\left\{\frac{1}{5}|L|^2 + \frac{8}{15}|L'|^2 + \frac{4}{15}|L||L'|\cos(\chi-\chi')\right\} \qquad (6\text{-}17a)$$

$$\overline{f_y^2} = \frac{C^2E^2}{2}\cdot\frac{1}{15}\left\{|L|^2 - 2|L||L'|\cos(\chi-\chi') + |L'|^2\right\} . \qquad (6\text{-}17b)$$

Oriented Oblate Spheriods

Suppose the scatterers are all oblate spheriods, oriented with their figure axes vertical. The vertical direction is then ξ. Also, choose the x axis to be horizontal. Since z is by definition the propagation direction, the propagation plane is then zy; it must contain E_ξ (i.e., $\theta = 90°$) if ξ is to be vertical and x horizontal. Therefore, the projection of E_ξ on x, is $\ell_1 = 0$ and on y is $\ell_2 = \sin\delta$.

Note that the polarization has not been specified. Equations (6-15a) and (6-15b) are written assuming $\underset{\sim}{E}$ to be horizontal, lying along x. For vertical polarization the x and y axes can be exchanged. Then f_x and f_y must be interchanged and also ℓ_1 and ℓ_2. Thus for horizontal polarization

$$\overline{f_x^2} = \frac{C^2E^2}{2}|L'|^2 \qquad (6\text{-}18a)$$

$$\overline{f_y^2} = 0 \qquad (6\text{-}18b)$$

and for vertical polarization

BEST DOCUMENT AVAILABLE

$$\overline{f_x^2} = 0 \tag{6-19a}$$

$$\overline{f_y^2} = \frac{C^2E^2}{2} \left[|L|^2 \sin^4\delta + |L'|^2(1-2\sin^2\delta + \sin^4\delta) \right.$$

$$\left. + 2|L||L'|(\sin^2\delta - \sin^4\delta)\cos(\chi-\chi') \right] . \tag{6-19b}$$

Thus with horizontal polarization the $\underset{\sim}{E}$ vector is perpendicular to the y, z, and ξ axes, so only f_x^2 is non zero. Furthermore, since the x axis of the spheroid is independent of δ, the moment f_x does not depend on elevation angle. When the propagation plane $y\xi$ contains the $\underset{\sim}{E}$ vector, the polarization is said to be vertical. The projection of $\underset{\sim}{E}$ onto the x axis is then zero so $f_x = 0$, but the projection onto ξ clearly depends on the angle between ξ and the propagation direction z, so f_y depends strongly on δ.

Oriented Prolate Spheroids

Suppose the scatterers are prolate spheroids with their major axis lying in the horizontal plane. Then ξ is horizontal as is x by assumption.

Therefore the horizontal plane is $x\xi$ and ℓ_1, the projection of E_ξ onto x, is just $\ell_1 = \cos\theta$, and ℓ_2, the projection of E_ξ onto y, is $\ell_2 = \sin\theta \sin\delta$. Thus

$$\overline{\ell_1^2} = \frac{1}{2}, \qquad \overline{\ell_2^2} = \frac{\sin^2\delta}{2\pi} \int_{-\pi}^{\pi} \sin^2\theta d\theta = \frac{\sin^2\delta}{2}$$

$$\overline{\ell_1^4} = \frac{3}{8}, \qquad \overline{(\ell_1\ell_2)^2} = \frac{\sin^2\delta}{2\pi} \int_{-\pi}^{\pi} \cos^2\theta \sin^2\theta d\theta = \frac{1}{8}\sin^2\delta$$

$$\overline{\ell_2^4} = \frac{3}{8}\sin^4\delta;$$

so for horizontal polarization and horizontal prolates,

$$\overline{f_x^2} = \frac{C^2E^2}{2}\left\{\frac{3}{8}|L|^2 + \frac{1}{4}|L||L'|\cos(\chi-\chi') + \frac{3}{8}|L'|^2\right\} \tag{6-20a}$$

$$\overline{f_y^2} = \frac{C^2E^2}{2}\left[\frac{1}{8}\sin^2\delta\,|L|^2 - 2|L||L'|\cos(\chi-\chi') + |L'|^2\right] \tag{6-20b}$$

BEST_DOCUMENT AVAILABLE

and for vertical polarization and horizontal prolates

$$\overline{f_x^2} = \frac{C^2E^2}{2}\left\{\frac{1}{8}\sin^2\delta\,|L|^2 - 2|L||L'|\cos(\chi-\chi') + |L'|^2\right\} \tag{6-21a}$$

$$\overline{f_y^2} = \frac{C^2E^2}{2}\left\{\frac{3}{8}|L|^2\sin^4\delta + (\sin^2\delta - \frac{3}{4}\sin^4\delta)|L||L'|\cos(\chi-\chi')\right.$$

$$\left. + (1-\sin^2\delta + \frac{3}{8}\sin^4\delta)|L'|^2\right\}. \tag{6-21b}$$

6.3 Differential Reflectivity from Non-Spherical Particles

Suppose a volume containing oblate spheroidal scatterers of common size and shape is viewed simultaneously by radars of horizontal and vertical polarization. Furthermore, assume that the axes of rotation of the spheroids are all vertical. Then the ratio of powers in the two polarizations will be given by the ratio of Eqs. (6-18a) and (6-19b). The ratio will generally vary dramatically with zenith angle as shown in Fig. 6-9 parametric in the ratio a/b where a is the semi axis of rotation (principle axis) and b is the orthogonal semi axial dimension. However, if the two radars are viewing the volume horizontally ($\delta = 90°$) a rather simple relationship is obtained as shown in Figs. 6-3 and 6-4. For either water or ice the ratio of the powers in the two polarizations depends mainly on the ratio a/b with only a weak dependence on radar wavelength λ or temperature. Therefore, a simple measure of power backscattered on the two polarizations provides a direct measure of drop shape.

In order to obtain information on actual drop-size, it is necessary to use either a relationship between absolute reflectivity and drop size or a relationship between drop shape and drop size. The latter relationship has been investigated by Pruppacher and Beard (1970). They studied water drops falling at terminal velocity in a wind tunnel at 20°C at a pressure of sea level in a nearly saturated environment. They obtained drop-shape photographically, and examples of various size drops are shown in Figs. 6-5 and 6-6. At first glance the drops in Fig. 6-5, which are between 30 and 450 μm radii appear to be spherical. However, with magnification even drops as small as 155.5 μm radius were found to be deformed. In summary, drops less than about 140 μm (Reynold's number ≈ 20) showed no deformation; drops such that 140 μm $\leq$ a $\leq$ 500 μm were slightly, but measurably, deformed oblated

BEST DOCUMENT AVAILABLE

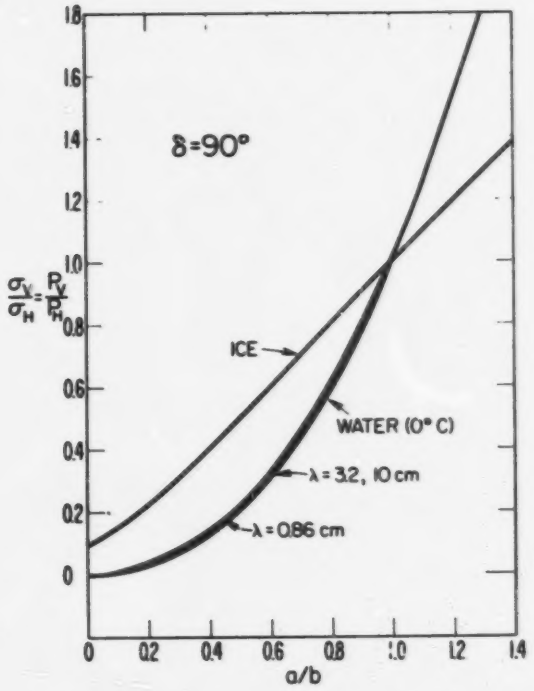

Figure 6.3--Relationship between drop-shape (a/b) and ratio of backscattered power at vertical and horizontal polarizations for horizontal propagation.

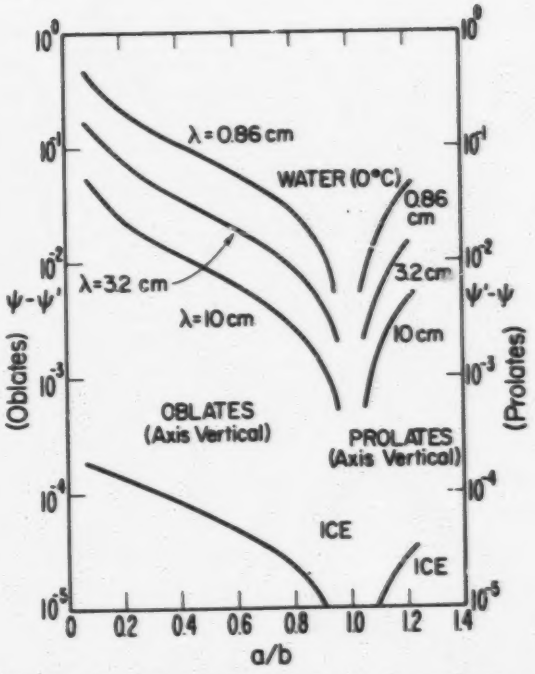

Figure 6.4--Relationship between drop-shape (a/b) and phase difference between vertical and horizontal polarizations for horizontal propagation (δ = 90).

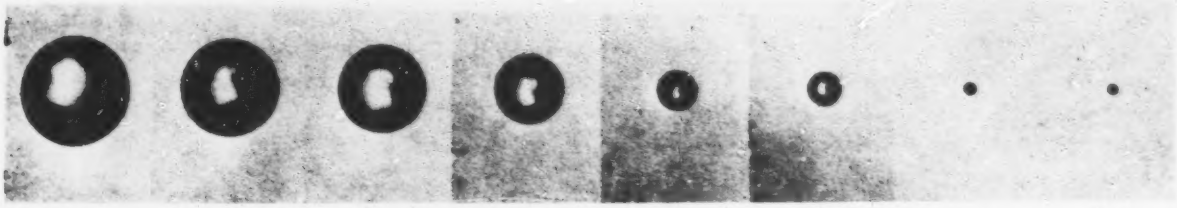

Typical shape of small water drops falling at terminal velocity (from left to right a_0 : 432, 393, 354, 262, 155·5, 130·9, 44·5, 33·8 μm corresponding to the following values for V'_z : 351, 319, 289, 229, 119, 98, 21, 14 cm s^{-1}).

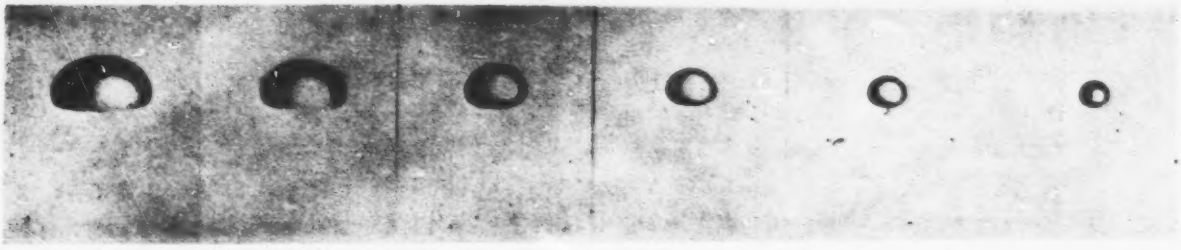

Typical shape of large drops falling at terminal velocity (from left to right a_0 : 4·50, 3·675, 2·90, 2·05, 1·725, 1·35 mm corresponding to the following values for V'_z : 920, 930, 917, 913, 886, 770 cm s^{-1}).

Figure 6.5, 6.6--Photographs of shape of water drops falling at terminal velocity in the laboratory for various mean radii, a_0. (From Pruppacher and Beard, 1969.)

BEST DOCUMENT AVAILABLE

conforming fairly well to the relations obtained by Imai (1950) which can be combined (Pruppacher and Beard) into the expression

$$a/b = [1-(9/16)\ a_o \rho V_t^2/s]^{1/2} \qquad (6\text{-}22)$$

where a_o is drop radius, in cm, ρ is saturated air density ($\sim 1.19 \times 10^{-3}$ g cm^{-3}), V_t is terminal fall velocity in cm s^{-1}, and s the surface tension of water at 20°C ($\sim$72.75 erg cm^{-2}).

Figure 6-6 shows drops in the size range $0.5 \leq a_o \leq 4.5$ mm. It shows that the shape deviates markedly from spherical in this range, but up to 1.5 mm radius the shape is still well approximated by an oblate spheroid. At larger sizes the bottom of the drop is flattened. The various experimental results to be found in the literature were collected by Pruppacher and Beard and are summarized in Fig. 6-7. In the size range $0.5 \leq a_o \leq 4.5$ mm the deformation a/b is linearly related to size a_o by the empirical expression

$$a/b = 1.030 - 0.124\ a_o \qquad (6\text{-}23)$$

where a_o is in mm.

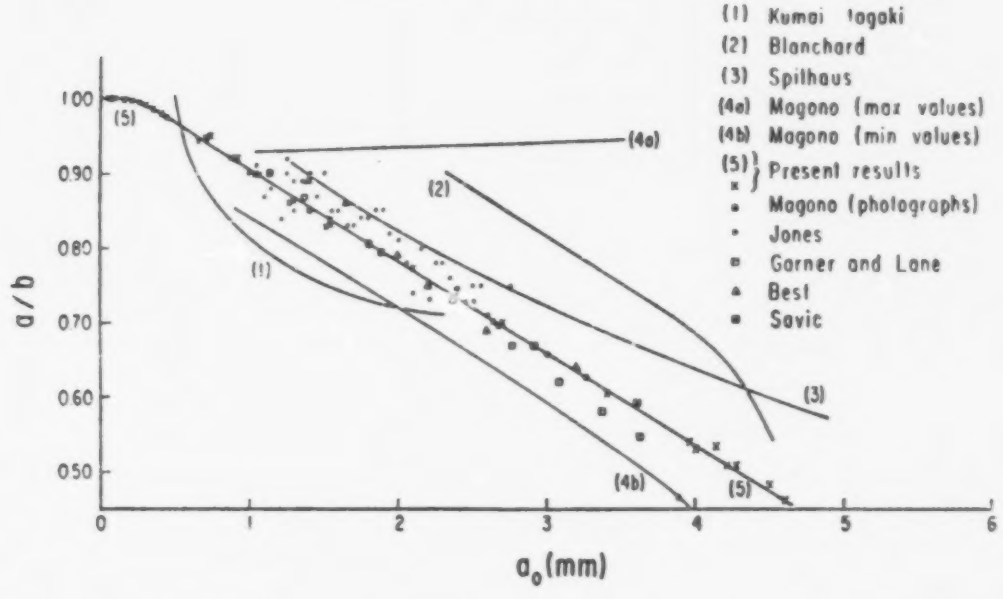

Figure 6.7--Drop deformation versus drop-size from sources indicated on figure.

BEST DOCUMENT AVAILABLE

Pruppacher and Pitter (1971) have presented a method with more physical basis for calculating drop shape but the method requires assumptions about the appropriate pressure distribution over the drop and requires computer calculation. From the radar-observed deformations a/b it is easy to calculate effective values of drop radius a_o using Eqs. (6-22) and (6-23). Then, using empirical fall velocity-size relations given by Gunn and Kinzer (1949) or by Foote and DuToit (1969), the fall velocity in quiet air can be retrieved. Finally, with Doppler observation of total fall velocity, the contribution from vertical air motion can in principle be deduced.

The discussion above has been based on the assumption that all drops in the volume are of the same size and shape. Seliga and Bringi (1976) adopt the more reasonable assumption that the drop sizes form an exponential number distribution $N_D = N_o \exp-(\Lambda D_e)$. The total backscattered power

$$P = \int_{D=0}^{\infty} \sigma_D N_D dD_e$$

where the index "e" refers to a sphere of equal volume. So from Eq. (6-10),

$$\frac{\sigma'}{\sigma} = \frac{\int_o^{\infty} D_e^6 S_i' \, N_D dD_e}{\int_o^{\infty} D_e^6 S_i N_D dD_e} = \frac{Z'}{Z} \qquad (6\text{-}24)$$

where S, S' are defined by the identity, Eq. (6-8). Bringi and Seliga (1976) call 10 log(Z'/Z) the "differential reflectivity" = Z_{DR} although "differential reflectivity factor" would be a more appropriate term, as Z is conventionally called reflectivity factor to distinguish it from the reflectivity η. In their interpretation Z' is the value for horizontally polarized incident radiation and Z is that for the vertically polarized wave. When the distribution for N_D is inserted in Eq. (6-24), N_o cancels and D_e disappears in the integration. Therefore, since the mass median diameter $D_o = 3.67/\Lambda$, the quantity D_o is uniquely determined by the radar power measurement Z_H/Z_V. Then, from an absolute measurement of either Z_H or Z_V, the value of N_o can be found. Using the results of Pruppacher and Beard to relate a/b to D_e and thus to calculate P, P' and S, S'; Seliga and Bringi compute the integrals in Eq. (6-24) by numerical methods and obtain the results shown in Fig. 6-8 (solid curves) where Z_{DR} is defined above and where N_o is related to the horizontal polarization reflectivity factor through the quantity 10 log(Z_H/N_o).

It is noteworthy that essentially the same relationship between Z_{DR} and size scale is found from Eqs. (6-18a) and (6-19b) by suitable definition of

BEST DOCUMENT AVAILABLE

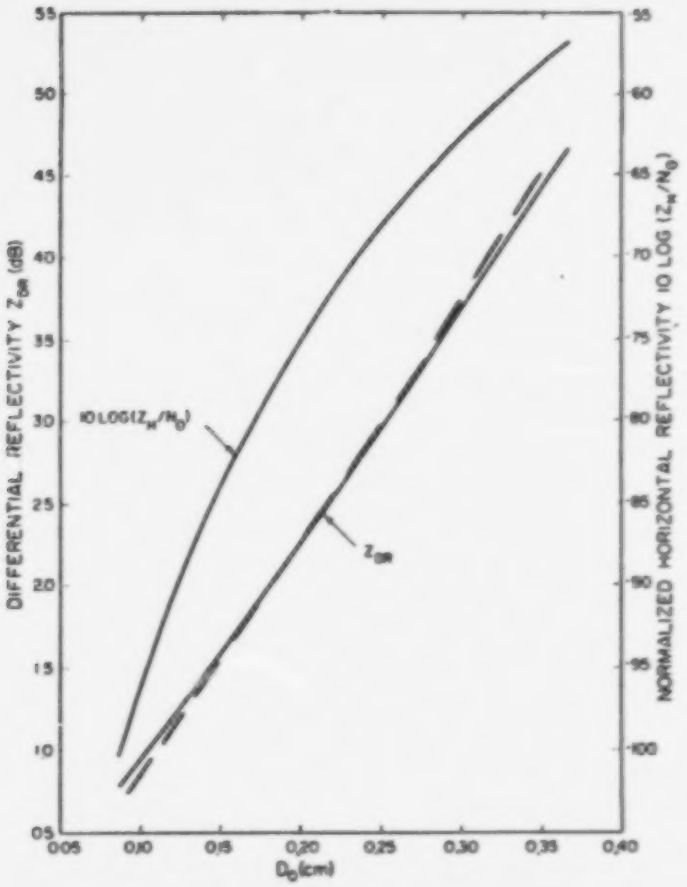

Figure 6.8--Variations of Z_{DR} and normalized horizontal reflectivity 10 log (Z_H/N_0) with D_0. The drop-size distribution is assumed to be exponential with coefficient N_0. Dashed curve is obtained from Eqs. (6-18a), and (6-19b) by assuming a homogeneous distribution of drops by rescaling D_0.

the size scale (say D_1) to use in the uniform size model assumed in the use of (6-18a) and (6-19b). The dashed curve shown in Fig. 6-8 for Z_{DR} is found if the abcissa is D_1 instead of the mass median diameter D_0, where AD_0 = 2.0. (Note that AD_0 = 3.67.) Thus, defining $D_1 = 0.54D_0$, the rather simple reasoning that led to Figs. 6-4 and 6-5 can be used to deduce the drop-size scale D_0 from the differential reflectivity, effectively by-passing the numerical integration of Seliga and Bringi and the shape-scale-fall velocity relations of Pruppacher and Beard.

6.4 Attenuation by Non-Spherical Particles

The total attenuation, Q_t, of radar waves by small particles is made up of attenuation due to the scattering of energy out of the beam, Q_s, and of

BEST DOCUMENT AVAILABLE

attenuation due to absorption Q_a. That is, $Q_t = Q_s + Q_a$. In the Rayleigh approximation for very small spherical particles (e.g., see Battan, 1973)

$$Q_s = \frac{128}{3}\frac{\pi^5 a^6}{\lambda^4}\left|\frac{m^2-1}{m^2+2}\right|^2 = \frac{24\pi^3}{\lambda^2}\left(\frac{V}{\lambda}\right)^2 |K|^2 \qquad (6\text{-}25)$$

$$Q_a = \frac{8\pi^2 a^3}{\lambda}\ \mathrm{Im}\ -\frac{m^2-1}{m^2+2} = 6\pi\left(\frac{V}{\lambda}\right) I(-K)\ . \qquad (6\text{-}26)$$

In order to generalize these results to the case of non-spherical particles, return to Eqs. (6-4) and (6-5a,b) and consider their limiting form for the case of a perfect sphere. In Eq. (6-5a) if the $\sin^{-1}$ factor and the radical are expanded in series for small e, it is found that $P \to 4\pi/3$ as $e \to 0$ and Eq. (6-16a) is obtained. Equations (6-25) and (6-26) can then be written

$$Q_s = \frac{8\pi}{3m_o^4}\left(\frac{2\pi}{\lambda}\right)^4 |g|^2$$

$$Q_a = \frac{8\pi^2}{\lambda m_o^2}\ \mathrm{Im}(-g)\ .$$

Generalizing to the case of spheroids of random orientation

$$Q_s = \frac{8\pi}{9\,m_o^4}\left(\frac{2\pi}{\lambda}\right)^4 (|g|^2 + 2|g'|^2) \qquad (6\text{-}27)$$

$$Q_a = \frac{8\pi^2}{3\lambda m_o^2}\ \mathrm{Im}(-g - 2g')\ . \qquad (6\text{-}28)$$

We see from Eqs. (6-25) and (6-26) that $Q_s \propto (V/\lambda)^2$, whereas $Q_a \propto V/\lambda$. Therefore, when considering liquid cloud droplets and cm or mm radar wavelengths, Q_a should easily dominate Q_s because of the relatively small volume of each cloud droplet. However, the imaginary part of the refractive index of ice is very small, i.e., $m \simeq 1.78 - i7.9 \times 10^{-4}$ at -10°C, whereas for liquid water $m \simeq 7.14 - i2.89$ at 0°C for a 3.2 cm wavelength radar (Battan, 1973). Obviously Eq. (6-27) can be used to calculate the attenuation in water clouds, but for ice particles the scattering cross-section is the important component and Eq. (6-28) must be used.

BEST DOCUMENT AVAILABLE

6.5 Scattering in an Arbitrary Direction

We have so far considered only backscatter because that is the case of most interest in radar. However, in bistatic radar systems or in analysis of the effect of spheroidal scatterers on one-way communications and telemetry paths it is necessary to generalize the previous expressions.

If the scatterers are not spherical, the scattered electric field may have components E_x, E_y, and E_z in all coordinate directions. The dipole moments f_x, f_y, and f_z may exist along all three axes as shown in Fig. 6-9. We consider the scattering to be along the dashed vector at an angle γ with the z axis and let the angle γ lie in the xz plane. The total electric field associated with the wave scattered at the angle γ is therefore the vector sum of the y component and the components of E_x and E_z projected onto AB, the normal to the propagation direction in the xz plane. The scattered field has dipole moments f_x, f_y, and f_z, and the intensity of the power radiated is

$$I(\gamma) = (2\pi/\lambda)^4(f_y^2 + f_x^2 \cos^2\gamma + f_z^2 \sin^2\gamma). \qquad (6\text{-}29a)$$

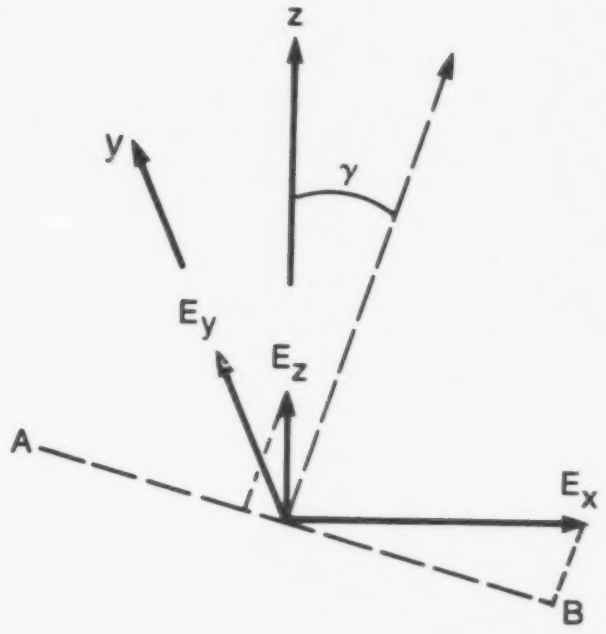

Figure 6.9--Ratio of backscattered power in vertical and horizontal polarizations for various zenith angles assuming spheroidal scatterers whose axes of symmetry are vertical. Plot is parametric in the ratio a/b. Conditions otherwise as indicated on figure.

BEST DOCUMENT AVAILABLE

In the backscatter direction, for which $\gamma = 180°$, this reduces to simply

$$I(\gamma) = (2\pi/\lambda)^4(f_y^2 + f_x^2) \qquad (6\text{-}29b)$$

as is to be expected.

Polarization effects in the forward scatter direction have recently assumed great importance. The depolarization that results from non-spherical scatterers imposes a major limitation on the possible use of polarization diversity as a means of increasing channels on satellite-to-earth paths. It is readily seen from the above, that both attenuation and depolarization are simply calculated within the approximations contained in the Gans theory. If the (spheroidal) shape of the scatterers is known; the depolarization and the attenuation are intimately linked through Gans' factor g.

Imagine, then, the surprise of experimentalists when the phenomenon of "anomalous depolarization" without attenuation was discovered on satellite to earth paths.

The answer, of course, is to be found in the comparison of Eqs. (6-14), (6-15), and (6-19). If we consider ice needles, it is immediately clear from Eq. (6-14b) and (6-15a) that there will be significant cross-polarized scatter from ice prolates unless $\delta = 0$. On the other hand the imaginary part of the refractive index of ice is very small ($k \simeq 8 \times 10^{-4}$) so Eq. (6-19) will yield very small attenuation. It seems clear (Cox et al., 1976) that the depolarization results from ice particles in the atmosphere.

6.6 Conclusions and Possible Observational Applications

1) When the incident electric vector is perpendicular to a plane containing one of the spheroid axes, there is no dipole moment excited along that axis so there will be no cross polarized component in the scattered wave.

2) Ice spheroids are relatively weak backscatterers compared with water spheroids of comparable volume, and their backscatter and attenuation depend only weakly on shape. On the other hand, water spheroids are very shape-dependent. It is pointed out by Atlas, Kerker, and Hitchfeld, (1953), that the shape effect should be completely negligible for snow. They base their conclusions on the fact that $(m^2-1)/(m^2+2) \propto \rho$ where ρ is density, and note that P is proportional to m^2-1. Since the density of ice is about 0.9 and that of snow is about an order of magnitude less, the very weak shape

dependence of pure ice is further greatly reduced when it occurs in the form of snow. However, for melting snow, when the flakes are water coated, the reflectivity might become very shape-dependent.

3) Kerker, Langleben, and Gunn (1951) and Warner (1977) have made computations on the basis of theory assumming an ice sphere to be surrounded by a thin water film. They find that even a very thin water coating is sufficient to make the scatterer behave like a water droplet of the same mass.

4) For oblates the backscattered power does not change with zenith angle δ for horizontal polarization, but for vertically polarized transmission the backscattered (parallel polarized) power decreases dramatically as δ increases. This is also true if prolates (needles) have their major axis horizontal but are randomly oriented in azimuth.

5) For prolate spheroids whose principal axes are vertical, the backscatter increases as the zenith angle δ increases.

6) The ratio of the backscattered power in vertical and horizontal polarization and their phase difference is a sensitive measure of drop-shape. If both radars view the volume at horizontal grazing angle ($\delta = 90°$) especially simple relations are found as seen in Figs. 6-3 and 6-4. The ice phase differs greatly from the water phase. Drop shape a/b is closely related to drop-size so the dual polarization measurement is of significant potential value to the meteorologist monitoring locally changing conditions. The drop-shape deviates significantly from spherical only for drops greater than about 200 microns, so such a measurement may not be of much use in studies of non-precipitating clouds. However, it should be a sensitive indicator of when the first few large drops appear and permit the observer to monitor the occurrence and growth rate of precipitation-size particles within clouds.

7) Polarization measurements can reveal to the meteorologist much about conditions near the freezing level by exploiting the bright-band phenomenon. As pointed out above, the reflectivity of snow above the freezing level should be very small and independent of polarization at all zenith angles δ. However, a region of high reflectivity occurs just below the zero degree isotherm. Suggested reasons for the enhanced reflectivity producing the bright band include (1) transition from ice to water (Austin and Bemis, 1950) and (2) change in shape as particles melt (Wexler, 1955). Based on depolarization measurements, Wexler concluded that shape changes accounted for only about 1.5 dB of enhancement. Because flat oblates with vertical axes would

BEST DOCUMENT AVAILABLE

not be expected to produce depolarization, but should produce significant aspect vs. reflectivity changes, an experiment should be done using two polarizations to measure the relative backscatter dependence on elevation angle in an RHI scan. However, horizontally oriented prolates (or needles) could cause significant depolarization, so measurements of both the co-polarized and cross-polarized backscatter on both polarizations would be of value to the meteorologist wishing to monitor the change of state and distribution of particles in his vicinity. The dependence of the ratio of backscattered power in the vertical and horizontal polarizations on zenith angle δ and on wavelength λ is shown in Figs. 6-10 and 6-11.

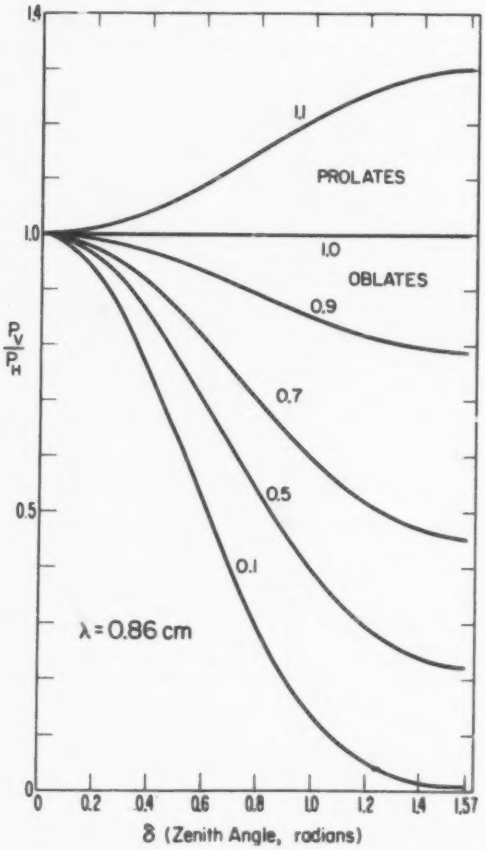

Figure 6.10--Ratio of backscattered power in vertical and horizontal polarizations for various zenith angles assuming spheroidal scatterers whose axes of symmetry are vertical. Plot is parametric in the ratio a/g. Conditions otherwise as indicated on figure.

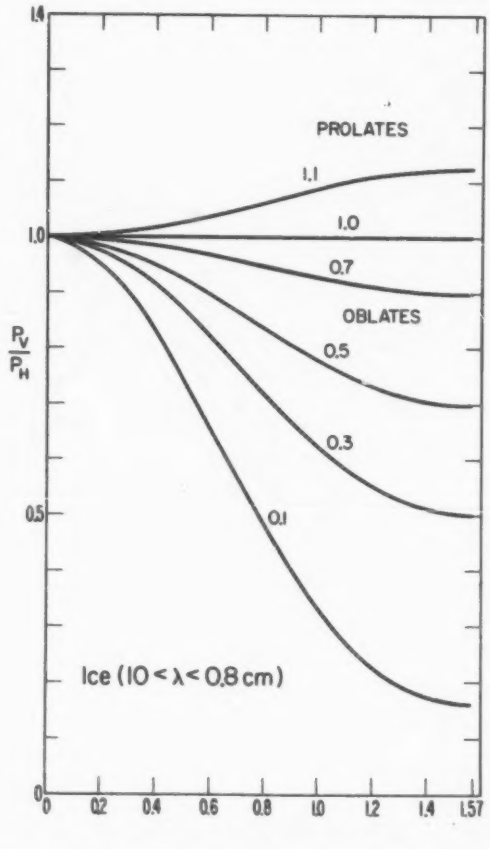

Figure 6.11--Geometry of off-path scattering in arbitrary direction γ; general picture with z not necessarily the propagation direction.

BEST DOCUMENT AVAILABLE

8) For ice, k (the imaginary part of the refractive index) is very small so χ is small and attenuation due to absorption is very small. Attenuation is almost entirely due to scattering.

9) Equations (6-18b) and (6-19a) show that no cross-polarization results from oblate spheroids whose axes are vertical for either horizontal or vertical polarization.

10) Prolate spheroids whose major axes are randomly oriented in horizontal planes produce significant cross polarization of the backscattered signal.

11) When the electric vector is parallel to a plane containing the major or minor axis of the spheroid only the dipole moment along that axis is excited.

12) By monitoring the height region containing the freezing level, the meteorologist could tell when an ice cloud begins to precipitate, because the bright-band phenomenon depends on particles falling through the freezing level. In fact the distinctive banding is partly a result of the change in particle fall velocity as they change state from snow to liquid (see Fig. 6-12, taken from Lhermitte and Atlas, 1963). In Fig. 6-12 the radar was of

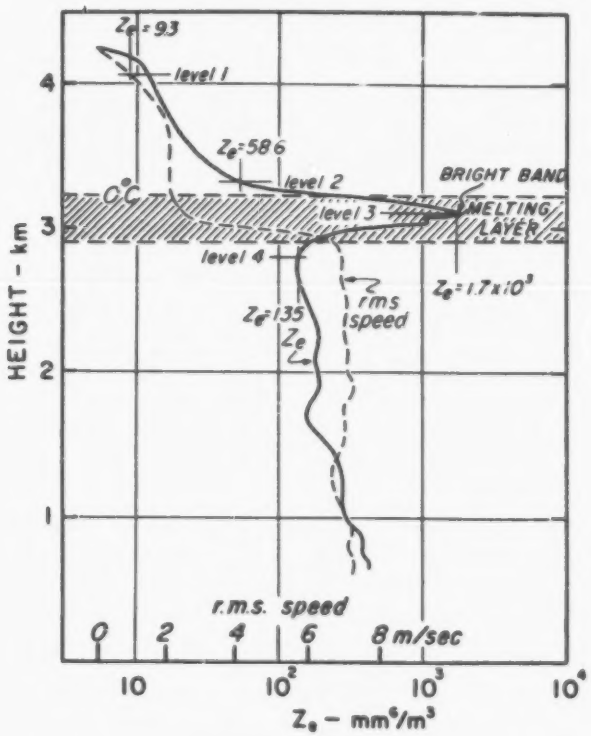

Figure 6.12--Simultaneous profiles of reflectivity factor Z and root-mean-square particle-fall speed in light (1 mm/hr), steady precipitation with a bright band. (From Lhermitte and Atlas, 1963.)

BEST DOCUMENT AVAILABLE

wavelength λ = 3.2 cm and pointing vertically. The bright-band is often more intense than would be expected simply from the change in state from ice to snow. Note that Z_e increased by a factor of 30.6 between level 2 and level 3 in Fig. 6-12. Referring to Eq. (6-9) and noting that $|K|^2 \simeq 0.92$ for water and $|K|^2 \simeq 0.21$ for ice, we see that the change from ice to liquid can only account for a factor of about 5. This fact caused Lhermitte and Atlas (1963) to propose that rapid aggregation of ice crystals into larger and larger snowflakes proceeded down to level 3 within the bright-band. Even when randomly oriented, nonspherical particles can be much more effective backscatterers than spheres as shown by Fig. 6.14. For particles with an axial ratio of 10 to 1, the normalized backscatter intensity in the parallel polarized channel $\overline{I_p^n}$, is about 10 for oblates and about 25 for prolates. Furthermore randomly oriented particles can produce substantial power in the cross polarized receiver channel. Figure 6.15 shows that water drops with axial ratios of about 10 lead to depolarization ratios of about 10% for oblates and about 30 percent for prolates. For randomly oriented particles typical values of the depolarization ratio, expressed in decibels range from -10 to -25 dB. By comparison, the backscattered power from oriented particles is shown in Fig. 6.16 and may be compared directly with Fig. 6.14; from Atlas, Kerker and Hitschfeld (1953).

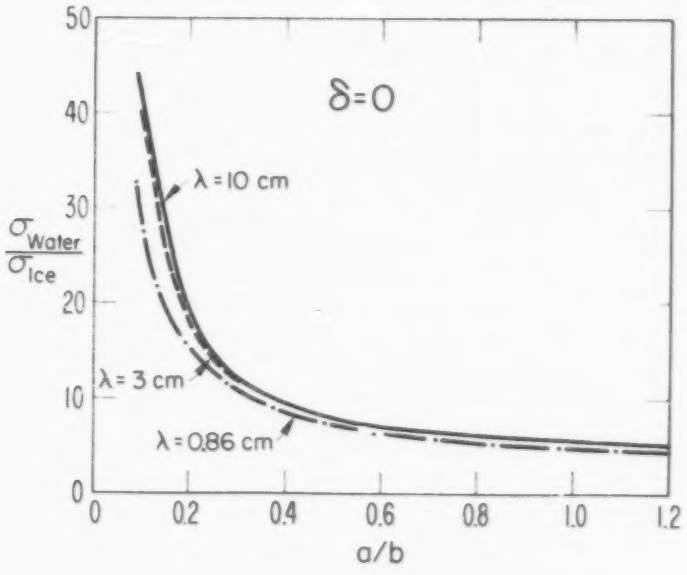

Figure 6.13--Ratio of backscattering cross-section for water and ice particles as a function of shape assuming vertically pointing radar.

BEST DOCUMENT AVAILABLE

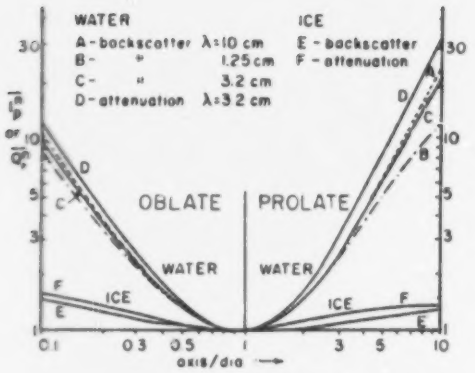

Figure 6.14--Parallel-polarized backscatter and attenuation by randomly oriented water and ice spheroids, relative to return and attenuation by equivolume spheres. From Atlas, Kerker and Hitchfeld.

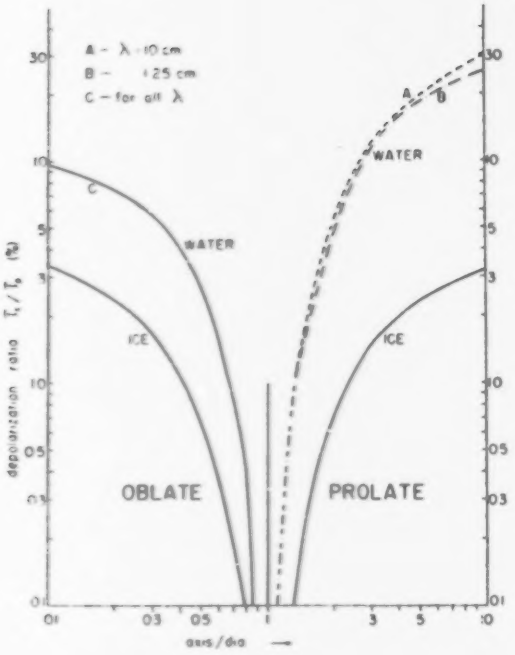

Figure 6.15--Depolarization ratio (ratio of cross-polarized component of backscattered energy to parallel-polarized component) for randomly oriented water and ice particles. From Atlas, Kerker and Hitchfeld.

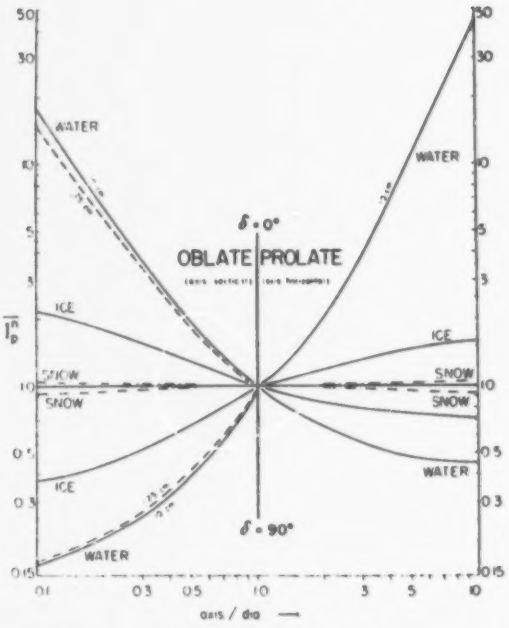

Figure 6.16--Parallel-polarized component of backscattered intensity from oriented particles (relative to backscatter from equivolume spheres) for the two extreme cases of vertically (δ = 0°) and horizontally (δ = 90°) pointing, vertically polarized antennas. From Atlas, Kerker and Hitchfeld.

CHAPTER 7 - DOPPLER RADAR OBSERVATION OF CLOUDS AND CLEAR-AIR

7.1 Doppler Radar Measurements

The radar techniques so far described for observing the atmosphere use the magnitude of the backscattered power, the relative power backscattered at different wavelengths, or the relative power backscattered on different polarizations. However, radar systems can also measure the Doppler shift of the backscattered signal which is due to movement of the scatterers toward or away from the radar. The use of Doppler radar for research in the dynamics of mature storms is not new and the imminent incorporation of Doppler capability into National Weather Service radars gives it new potential importance. Until recently, Doppler radars have been limited to observations on systems containing precipitation size particles. However in the last decade important observations have been possible in the optically clear atmosphere using Doppler radars with wavelengths of 0.1 to 10 meters. It now seems likely that Doppler radar capability will be extended to study non-precipitating clouds. Therefore, at this point Doppler radar systems will be considered briefly and their potential for cloud observations assessed.

The conventional, non-Doppler radar, measures the total power backscattered from each radar resolution cell. The radar resolution cell is defined by the two-way antenna pattern and the resolution along the antenna axis which depends on the bandwidth of the transmitted signal (pulse width for a pulsed radar) and the receiver response. Doppler radars measure radar reflectivity in each resolution cell but they also measure the reflectivity-weighted distribution of radial velocity (the Doppler velocity spectrum) in each cell. These data are obtained simultaneously for all resolution cells along the antenna pointing direction. Typical observation times are about 0.1 sec. Real-time estimates of the mean radial velocity (first moment of the Doppler spectrum) and width of the spectrum (second central moment) can be made with presently available hardware. The complete Doppler spectrum can be found in real time for a limited number of resolution cells. Figure 7.1 is an example of the Doppler spectrum observed with a vertically pointing radar. In this case both rain and hail were present in the resolution cell and the Doppler spectrum shows two distinct fall speeds. In many cases the spectra are very much broader than that shown in Fig. 7.1.

The primary information provided by a Doppler radar is the three dimensional fields of radar reflectivity, mean radial velocity, and spectral width. Radar reflectivity provides insight into the type of scatterers

BEST DOCUMENT AVAILABLE

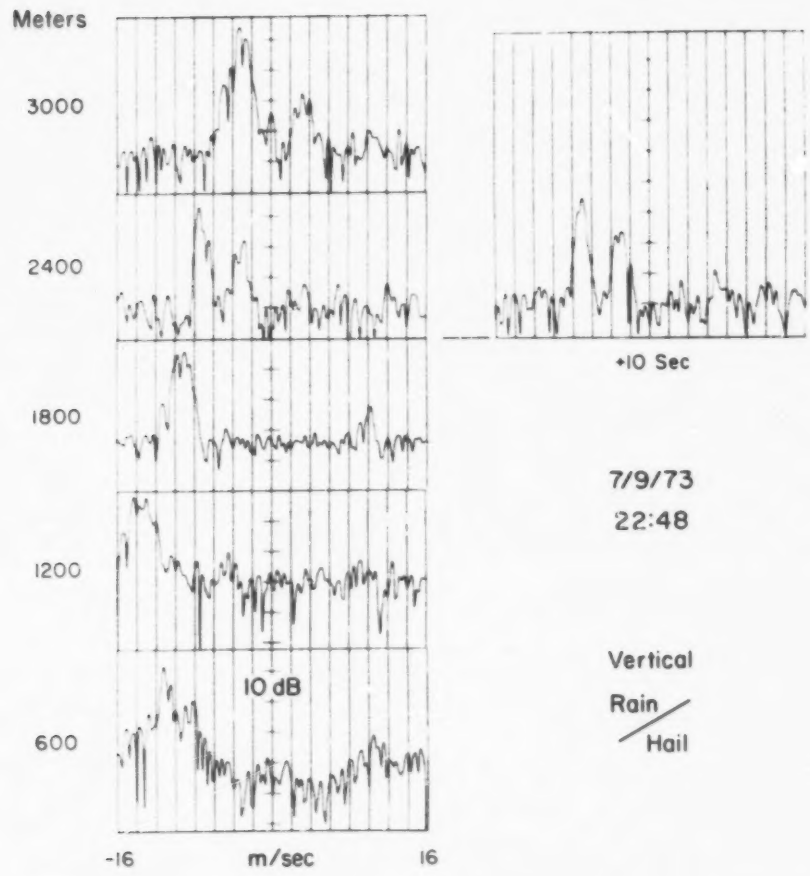

Figure 7.1--Top frame: Schematic illustration of the Doppler spectra of two successive pulses in a pulse radar system illustrating the ambiguity in interpretation called velocity folding; if signal #1 corresponds to pulse #1, the radial velocity is just $V = + V_J$. However, if the radial velocity of the target is greater than V_M, signal #1 goes with pulse #2 and $V = -2 V_M + V_J$. Bottom frame: Schematic appearance of folding on an "A" scope display.

present; mean radial velocity fields are used to construct the wind field (scatterers are assumed to move horizontally with the mean wind and to have a fall speed which depends on particle size); the width of the spectrum can be used to infer atmospheric turbulence. Radar reflectivity and mean velocity are widely used by radar meteorologists whereas estimates of spectral width are not. The reason for this is two-fold: (a) reliable estimates of width are more difficult to obtain and (b) the meteorological interpretation of width estimates is not as straight forward. Spectral width depends on a number of factors as discussed in Section 7.2.

BEST DOCUMENT AVAILABLE

Meteorological Doppler radars measure the velocity of the scatterers by observing the phase change of the returned signal from pulse-to-pulse. The need to observe signals scattered by a sequence of transmitted pulses leads to restrictions on the maximum range and maximum velocity that can be measured unambiguously. As will be shown, these limitations are more severe for shorter wavelength radars.

A pulsed radar (conventional or Doppler) transmits a series of pulses of temporal duration τ and of pulse repetition interval T. If a target at range r is so far away that the travel time of the microwave energy to the target and back ($t = 2\ r/c$) exceeds T, then the succeeding pulse is transmitted before the preceding signal returns, so the signal appears at the same range as that of a target whose range is $r = \frac{c(t-T)}{2}$. The maximum unambiguous (or folding) range is:

$$r_m = \frac{1}{2}\, cT \ . \qquad (7\text{-}1)$$

The minimum scale the radar can resolve in the radial direction is

$$\Delta r = \frac{1}{2}\, c\tau \ . \qquad (7\text{-}2)$$

In both cases the factor of 1/2 appears because target range is one-half the total travel distance of the radar pulse.

In the pulsed Doppler radar, the phase of the transmitted pulse is known and the phase of the returned signal is compared with that transmitted to obtain the range to the target. If the target radial velocity is so large that target range changes more than $\lambda/4$ between succeeding pulses, then the signal phase change will be more than π radians. But this phase change could have been caused by a target moving in the opposite direction at a slower radial velocity. The unambiguous (or folding) velocity is therefore

$$V_m = \pm \frac{\lambda/4}{T} \ . \qquad (7\text{-}3)$$

Note that the maximum frequency that can be observed without ambiguity is $f = \pm \frac{1}{2T}$ to satisfy the Nyquist sampling criterion and, since Doppler frequency and velocity are related by

$$f = 2V/\lambda \ , \qquad (7\text{-}4)$$

$V_m = \frac{\lambda}{2} f_m = \pm \frac{\lambda}{4T}$ so that V_m is usually referred to as the Nyquist velocity. Velocity resolution depends on observation time; that is, if N pulses are used to observe the target, the frequency resolution is $\frac{1}{NT}$ so the velocity resolution is

$$\Delta V = \frac{\lambda}{2NT} \quad . \tag{7-5}$$

The range at which aliasing (or folding) occurs is proportional to the pulse repetition period while the velocity at which aliasing (or folding) occurs is inversely proportional to pulse repetition period. Thus, for a given radar wavelength and with uniformly spaced pulses we can only minimize range aliasing at the expense of velocity aliasing and vice versa. Since the product of unambiguous range and unambiguous velocity is

$$R_m V_m = \pm \frac{c\lambda}{8} \tag{7-6}$$

aliasing problems are more troublesome for shorter wavelength radars.

It should be noted that velocity aliasing can often be resolved using spatial and temporal continuity constraints or from additional meteorological information. The velocity of range-aliased targets can be measured if they do not coincide in range with echoes that are not aliased. Also, range aliasing is not a problem at higher elevation angles so that the maximum velocity can be increased by decreasing the pulse repetition interval as the elevation angle increases.

7.2 Atmospheric Turbulence and Doppler Velocity Spectral Width

If all particles within the pulse volume of a very narrow beamwidth Doppler radar were moving in the same direction with the same velocity, a single Doppler frequency spectral line could be unambiguously identified. Actually, the Doppler spectrum of atmospheric backscatter has finite width. In fact, it may often be quite broad. There are several reasons for spectral broadening:

a) If the air within the pulse volume is turbulent, the various air parcels are moving randomly in all directions with a wide range of velocities. The Doppler spectral width therefore contains valuable information about the turbulence intensity throughout the volume of space being probed.

BEST DOCUMENT

b) If there is shear in the mean wind, the speed and direction of the mean wind may vary significantly within the pulse volume causing broadening of the Doppler spectrum. Usually, the important shear is the transverse variation in the radial wind component because the transverse dimensions of the resolution value are greater than the radial dimensions. If this is significant, a correction for it must be applied before the turbulence information can be extracted. According to Sloss and Atlas (1968), the contribution to the variance by shear transverse to the beam is given by

$$\sigma^2 = \frac{\beta_T^2 \, r^2 \theta_3^2}{2.76} \tag{7-7}$$

where β_T is the transverse shear (s^{-1}), r is range to the pulse volume, θ_3 is the half beamwidth to the half power (3 dB) point on the (Gaussian) mainlobe of the antenna pattern and the constant 2.76 results from a Gaussian beam assumption and the definition of antenna width.

The contribution of radial shear in the mean radial wind has been given by Sirmans and Doviak (1973) as

$$\sigma^2 = (\beta_R \, \Delta)^2/12 \tag{7-8}$$

where β_R is the radial component of shear in the mean radial wind and Δ is range cell length.

c) The Doppler spectrum is broadened if the antenna is in motion. Sloss and Atlas find this contribution to the variance to be

$$\sigma^2 = \Omega^2 D^2/2.76 \tag{7-9}$$

where D is antenna diameter and Ω is angular rate of rotation in radians s^{-1}.

d) Even if there is no turbulence or shear in the mean wind, so that it is completely uniform in speed and direction, and even if the reflectivity is constant over the pulse volume, the Doppler spectrum would have appreciable width when measured with any real radar because of the finite width of the radar beam; that is, if the beamwidth is not infinitesimal, the radial direction from the radar varies over the beam so that a range of radial velocities is sensed even if the wind is perfectly uniform. In practice this effect is

BEST DOCUMENT AVAILABLE

very small if the beamwidth is small. Formally its contribution is given by

$$\sigma^2 = V_T^2 \, \theta_3^2/2.76 \qquad (7\text{-}10)$$

where V_T is the component of the mean wind that is transverse to the beam axis, θ_3 is the half width to the half power (3 dB) point in the antenna pattern assuming a Gaussian beam.

e) If the radial velocity includes a component of particle fall speed there is a spectral broadening because not all the particles fall at the same velocity. This effect is negligible at low antenna elevation angles or for non-precipitating clouds. The variance caused by particle fall speed is given by

$$\sigma^2 = \sigma_D^2 \sin^2 \theta_E \qquad (7\text{-}11)$$

where θ_E is the antenna elevation angle and σ_D^2 is the variance of the fall speed of the scatterers. For rainfall, σ_D^2 is about 1 m^2/sec^2.

f) Gradients in reflectivity within the pulse volume influence the spectral breadth because the influence of a given air parcel on the Doppler spectrum is weighted according to its reflectivity.

Because the total variance of a group of Gaussian broadening processes is the sum of the individual processes if they are independent, they simply contribute additively. Thus by subtracting the effects of (b) through (f) it is possible to deduce turbulent intensity within the pulse volume from Doppler radar observations. However, in addition to the contaminating effects listed above there are other complications. For example, it is necessary to assume that:

1) The outer scale of the turbulence is large compared with the largest dimension of the pulse volume, so that the inertial subrange of the turbulence is fully established.

2) The form of the turbulence spectrum is known. This restriction could be relaxed if the radar had provision for varying the pulse length. By systematically varying the pulse length (and therefore the pulse volume) the form of the spectrum can be directly inferred if the turbulence is statistically stationary in time and if it is spatially homogeneous.

BEST DOCUMENT AVAILABLE

However, within the constraints imposed by the assumptions listed above, the spectral width can be used to calculate the turbulent dissipation rate in the pulse volume. The general technique seems to have been first discussed by Gorelik and Mel'nichuk (1963, 1968), but they did not explicitly include the spectral filtering that results from the limited transverse extent of the radar beam, and their results were only applicable to the case where the pulse width was much greater than the beamwidth. The general problem was treated by Srivastava and Atlas (1972) and by Frisch and Clifford (1974). Frisch and Clifford assumed a Gaussian beam crosssection and a Gaussian pulse shape, and they included both the case of pulse length greater than beamwidth and less than the beamwidth. The problem was further generalized by Labbit (1979) and he corrected an error in the Frisch and Clifford results for the case of pulse length greater than beamwidth. The correct treatment is not trivial and has been included here as Appendix D in which the derivation follows closely that of Labbit. Kolmogorov turbulence is assumed in which the energy spectrum is given by

$$E(k) = \alpha\, \varepsilon^{2/3}\, k^{-5/3}. \tag{7-12}$$

It is further assumed that the illuminated pulse volume is represented by a Gaussian antenna pattern and a Gaussian pulse length so that the antenna pattern, normalized to the pulse volume, is

$$P = \exp\left[-\frac{z^2 + y^2}{2a^2} - \frac{x^2}{2b^2}\right] \tag{7-13}$$

where x is the propagation direction and a and b depend on the beamwidth and pulse length respectively. Then to 2nd order of a hypergeometric expansion in γ^2 (see Appendix D),

$$\varepsilon = \delta^{-1}\left[\frac{\sigma_{11}^2}{1.35\,\alpha\left(1 - \frac{\gamma^2}{15}\right)}\right]^{3/2} \tag{7-14}$$

where

$$\left.\begin{aligned} \delta &= a \\ \gamma^2 &= 1-(b/a)^2 \end{aligned}\right\} \quad \text{when } b \leq a$$

$$\left.\begin{aligned} \delta &= b \\ \gamma^2 &= 4[1-(a/b)^2] \end{aligned}\right\} \quad \text{when } a < b$$

BEST DOCUMENT AVAILABLE

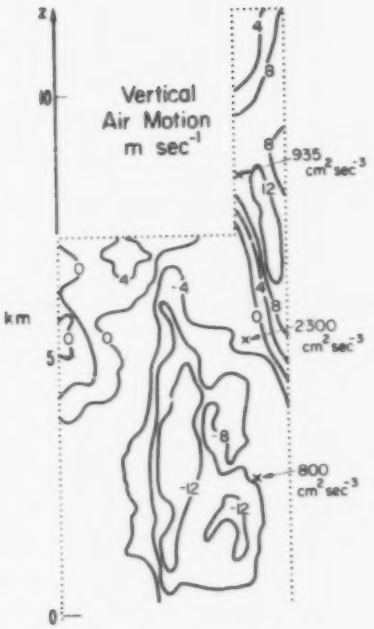

Figure 7.2--Distribution of vertical velocity and turbulent kinetic energy dissipation rate, ε, in a convective storm that was observed simultaneously by a vertically pointing Doppler radar and a distant radar observing it nearly horizontally. Contours are vertical air motion measured by zenith-pointing radar. Vertical velocity measurements were corrected for the fall velocity of the particles in still air. Note that high dissipation rates were measured between updraft and downdraft. The spatial scale was obtained by assuming $x = \bar{u}t$, *where* $\bar{u}$ *was approximately 7 m* s^{-1}. *(From Frisch and Strauch, 1976.)*

σ_{11}^2 is the variance of the radar Doppler velocity spectrum.

Strauch and Merrem (1976) and Frisch and Strauch (1976) have used the method to observe the spatial distribution of turbulent dissipation rate in a convective storm. An example is shown in Fig. 7-2 in which computed values of ε are superimposed on the vertical velocity pattern observed by a vertically pointing Doppler radar as the storm cell moved overhead. Clearly, very strong turbulence was found (>2300 cm^2 sec^{-3}) in the zone between updraft and downdraft.

The method has also been used by Frisch and Clifford (1974) and Moninger et al. (1978) to observe the distribution of turbulence in the planetary boundary layer by injecting chaff into the airstream. Figure 7-3 from Moninger et al. (1978) shows an example in which chaff was injected from a point source on a 152 m tower. The spatial and temporal patterns of diffusion of the chaff are shown for two releases.

The measurement of Doppler spectral width offers considerable promise for measuring the distribution of turbulence within developing clouds and relating it to drop size growth. Such a program would require the development of millimeter wavelength radars with Doppler capability because longer wavelength radars can detect refractive turbulence in the optically clear air which can mask the signal scattered from the small droplets.

BEST DOCUMENT AVAILABLE

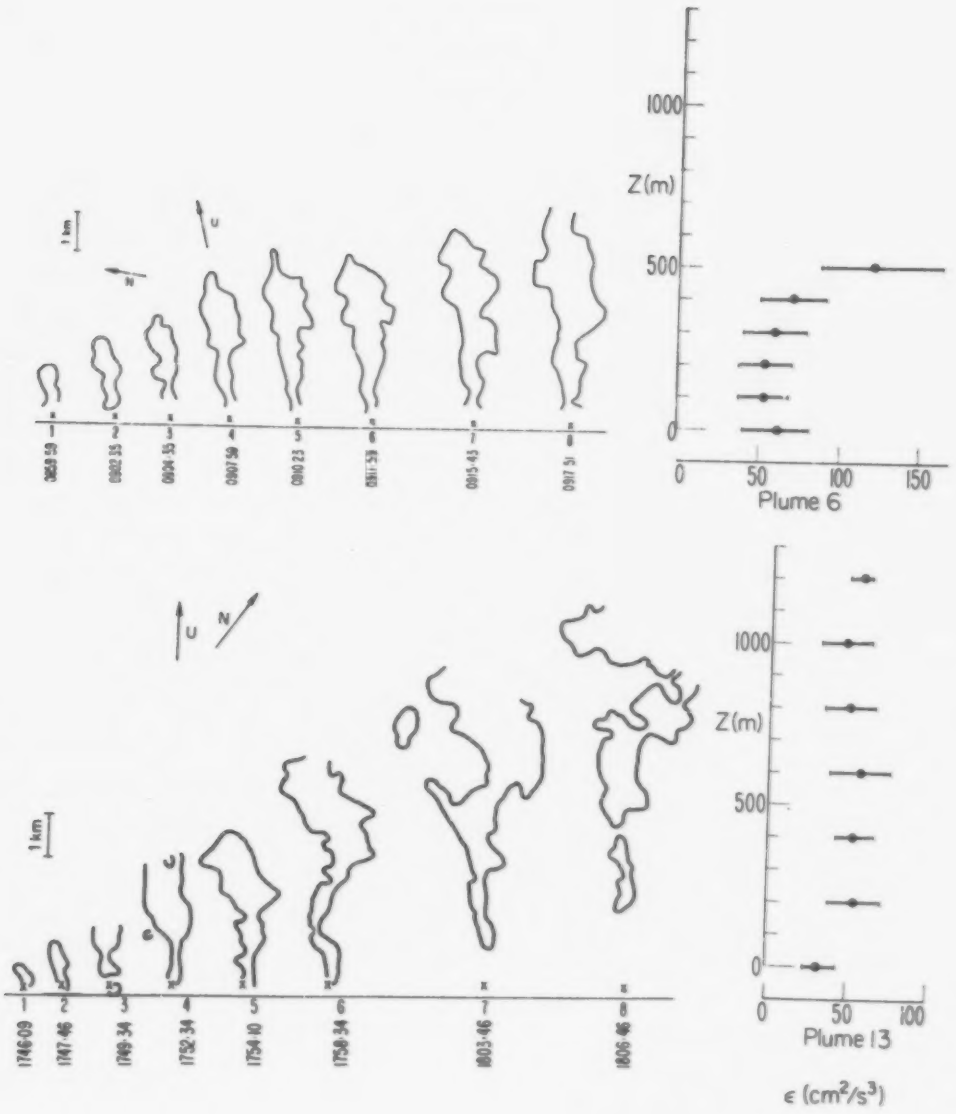

Figure 7.3--Diffusion of chaff released into the convective boundary layer from a continuous point source on a 152 m tower. Left frames show how the chaff concentration evolved with time shown along the horizontal axis. Right frames show the height distribution of ε calculated from the spectral width (2nd moment) and Eq. (7-10). (From Moninger et al., 1978.)

7.3 Multi-Radar Doppler Systems

A technique that has provided dramatic new insight into the small- and mesoscale dynamics of storms is the dual Doppler or multi-Doppler radar system. The technique is very simple in principle and very sophisticated in practice — particularly in the methods of collecting, processing, and displaying the data and analytical results. It has been used extensively in the study of mature, precipitating convective storms and even frontal systems (see Fig. 7-4) in which the drop sizes are large enough to serve as targets for conventional radars. The method holds great promise for cloud studies, but the necessary radar wavelengths are then very short and relatively highly attenuated.

The system uses two or more Doppler radars, separated by baselines, to scan a common volume of space with significantly different viewing angles. The radar receivers are gated to collect data in increments of range, and their beams are swept in elevation and azimuth, thus scanning a pre-selected volume of a storm. Each radar measures the velocity component toward or away from the radar (radial component) within each incremental volume of the region scanned. It is necessary that there be particles of sufficient size for the radar to "see" within the volume of interest, such as naturally occurring rain or snow or artificially injected chaff or insects. Some radars may be sufficiently sensitive to use return from refractive index fluctuations in the clear air to operate in this mode as discussed in Section 7.5.

The concept was first actively promoted by Lhermitte (1967), and such systems are presently operational at the University of Miami in Florida, the Wave Propagation Laboratory at Boulder, Colorado, the National Severe Storms Laboratory at Norman, Oklahoma, the National Center for Atmospheric Research (NCAR) at Boulder and at the Centre National de la Recherche Scientifique in France.

Key factors in the success of the multi-Doppler radar systems have been the technique of scanning the volume and the method of processing the data, and the various programs have differed mainly in their approach to these problems and in the missions for which the systems were designed.

The Miami program has aimed at a real-time processing capability, and special hard-wired logic was developed for rapid calculation of the wind fields from the combined radar observations. The data were collected in

BEST DOCUMENT AVAILABLE

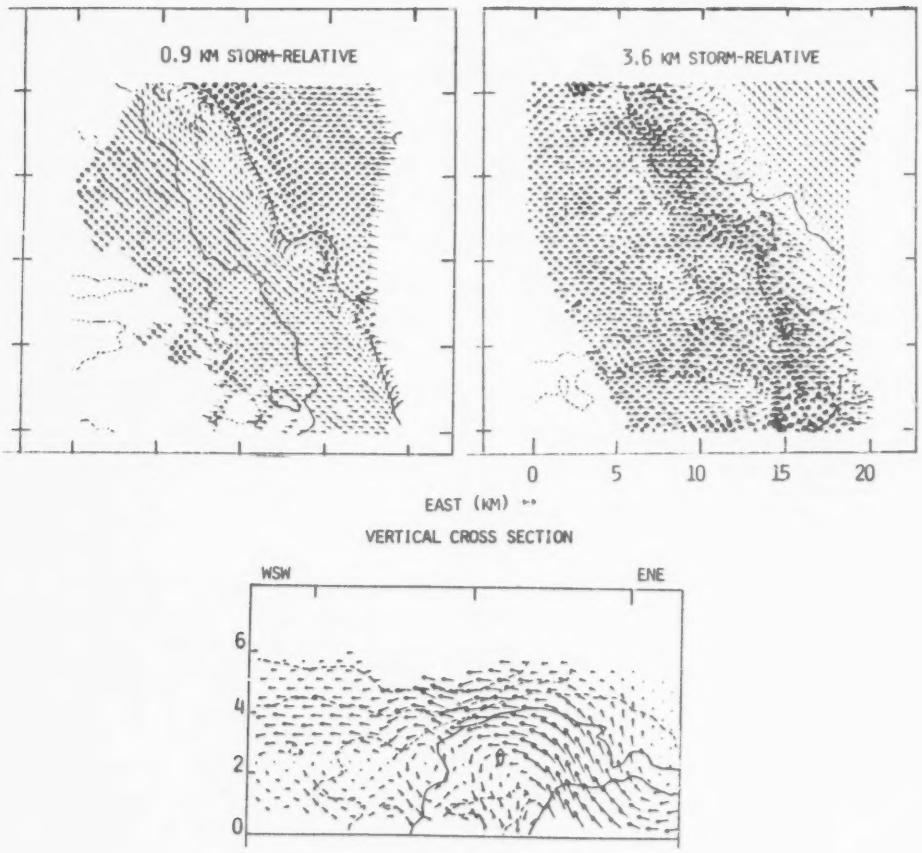

Figure 7.4--Example of three-dimensional wind fields reconstructed from multi Doppler radar observations. Top frames: Plan views of horizontal flow fields through a front approaching the Sierra Nevada foothills near Auburn, California. Note the cyclonic feature at right center of the left-hand frame. A small tornado was observed on the ground at this point. Bottom frame: Vertical cross-section through the front.

planes common to both radars so that the radial velocities from the two radars could be simply combined to yield the total velocity vector in that common plane. Note that this does not mean that the two radars scan at a common, constant elevation angle, but rather that the radars must be programmed to scan in a fairly complicated manner. For low plane angles the technique provides a method for quickly and simply calculating the approximately horizontal field of the wind. The University of Miami system has been used effectively to provide wind fields for the weather modification experiments conducted by the Equatorial Meteorological Laboratory (EML) of NOAA.

Unlike the University of Miami radars which transmit 3 and 5 cm waves, the Norman radars use 10 cm waves. That system was designed specifically for

studying the generation and evolution of severe weather, and the identification and prediction of those severe weather cells which spawn tornadoes. The 10 cm wavelength of the Norman radars provides them with a generally greater range and smaller attenuation than the shorter wavelengths of the Miami and WPL systems. However, the components are larger, and the radars must have much larger antennas for comparable beamwidths; the Norman system is therefore confined to one area of operation.

The Wave Propagation Laboratory system is designed to be capable of being moved to various meteorological regimes and participating in various field experiments. It is therefore a 3 cm-wavelength system mounted on trailers. It is used as a research tool, so the processing of the data is done off-line by general purpose computers rather than in real-time. This permits computer calculation of the full, three-dimensional velocity field in a Cartesian coordinate system by methods which will be described below. The Doppler frequency information is extracted either by the covariance ("pulse-pair") method (Rummler, 1968; Miller and Rochwarger, 1972) or by a full Fourier transformation of the time series of information collected in each range "bin" of each individual "beam" using FFT (Fast Fourier Transform). The latter method provides information about spectral shape in addition to the Doppler shift information provided by other processors. Display of the full spectrum also aids in editing the data if multiple peaks are present, or if ground return must be removed, or if a threshold is to be adjusted to eliminate "noise." The spectral shape and width contains information about the turbulence within the pulse volume of the radar, as will be described later.

Three-Dimensional Wind Fields in Storms Observed by Doppler Radar

In the co-plane method the radial velocity data are collected in common tilted planes scanned azimuthally by two radars. The two radars scan independently in azimuth through a predetermined number of "beams" in their common plane and then together step up to the next plane and independently scan it, etc. The original WPL system used 24 range gates, so for a typical number of beams and gates it required about 30 seconds to scan a single plane. In order to minimize the effect of temporal changes in the wind field during the scanning time, the field is referred to a common time by moving each parcel forward or backward according to its temporal displacement from the average time for each plane. If the storm system is changing rapidly, as few as 64 pulse samples may be collected in each volume increment so that the

storm may be scanned very quickly. For cloud observations in which the system may be changing rather slowly, but in which the signal is likely to be very weak, as many as 512 pulses may be used to measure the Doppler signal.

In processing coplane data, a cylindrical coordinate system is used because such a system is natural for the dual radar baseline geometry, and it leads to very simple expressions for combining the radial velocities into the total velocity field in the planes (Lhermitte and Miller, 1970). The situation is shown schematically in Fig. 7-4. The technique is described in detail, along with the relevant equations, by Miller and Strauch (1974). After the 2-dimensional velocity field in the common planes has been found, the divergence of the wind field in the plane is computed. The equation of mass continuity as formulated in cylindrical coordinates is then used to calculate the velocity component normal to the plane by integrating the velocity divergence starting with the 0 deg elevation angle plane where the normal velocity component must be zero over level ground. This yields the total velocity field in the volume in cylindrical coordinates, and it only remains to interpolate the velocities from grid points in the cylindrical system to grid points in a Cartesian system and to transform the r, s, α velocity components into x, y, z components (see Fig. 7-5). Typically two or more radars interrogate radial winds in about 20,000 volume increments in about 4 minutes for a total period of an hour or more depending on the speed of storm motion and the size of the radar network. The quantity of data so collected is enormous and usually processing has been done off-line by high speed computers. One such software package has been developed by the Wave Propagation Laboratory and has been titled MUDRAS (Multiple Doppler Radar Analysis System). It has been published as NOAA Technical Memorandum ERL WPL-35 by Kohn, Johnston and Mohr (1978). Another software package that has been published is called MASTER, documented in Technical Memorandum ERL WPL-55 by Moninger and Sanders (1980). It is suitable for small computers but is designed to process the data only through the stage of interpolating the radar data into a Cartesian grid. Further manipulation of the data and display is most conveniently done in the SKY program published in MUDRAS.

An example of a single-cell storm in Northeastern Colorado is shown in Fig. 7-6 taken from Kropfli and Miller (1973). In this case only two Doppler radars were available in the experiment and the coplane method was used for its simplicity. However, if three or more radars are used to scan the same volume the coplane method is not feasible. The concept of synchronous scanning of common planes must then be abandoned, and a plan for synchronous

BEST DOCUMENT AVAILABLE

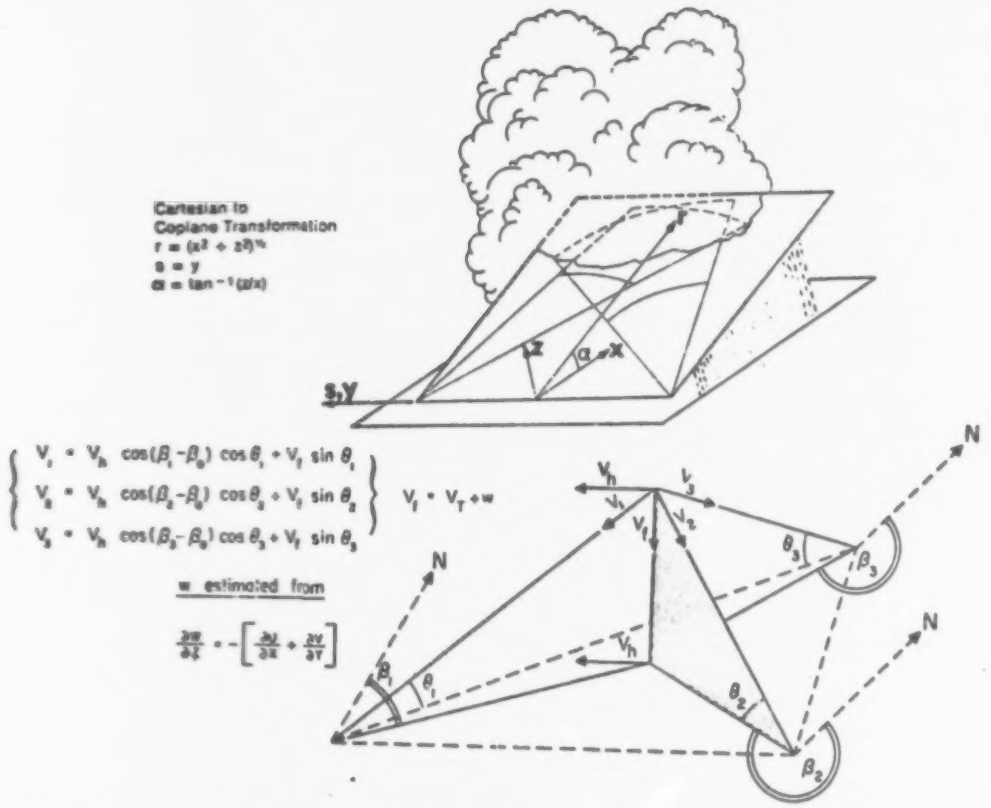

Figure 7.5--Top frame: Schematic picture of the coplanar scan commonly used in dual-Doppler wind field observations. Bottom frame: Schematic picture for 3 radars with equations relating the indicated velocity components. V_T is the terminal fall velocity in quiet air.

scanning of the common volume adopted. There are a variety of options for such scanning. However, if it is decided to begin and end the volume scan simultaneously at all radars, it must be recognized that those radars close to the storm have much wider angular sectors to scan and must therefore scan much faster than radars farther away. It should also be recognized that the shape of the pulse volume of radars close to the scan volume can be very different from those farther away so that care must be taken in combining the measurements to produce three dimensional measurements. When more than two radars are used, it is usually most practical to interpolate immediately from the spherical coordinate system in which the radars collect their data into a Cartesian grid common to all the radars.

Particle Fall Velocity

Of course Doppler radars do not measure the air motion directly but rather the velocity of tracers within the air volume. Such tracers have a

BEST DOCUMENT AVAILABLE

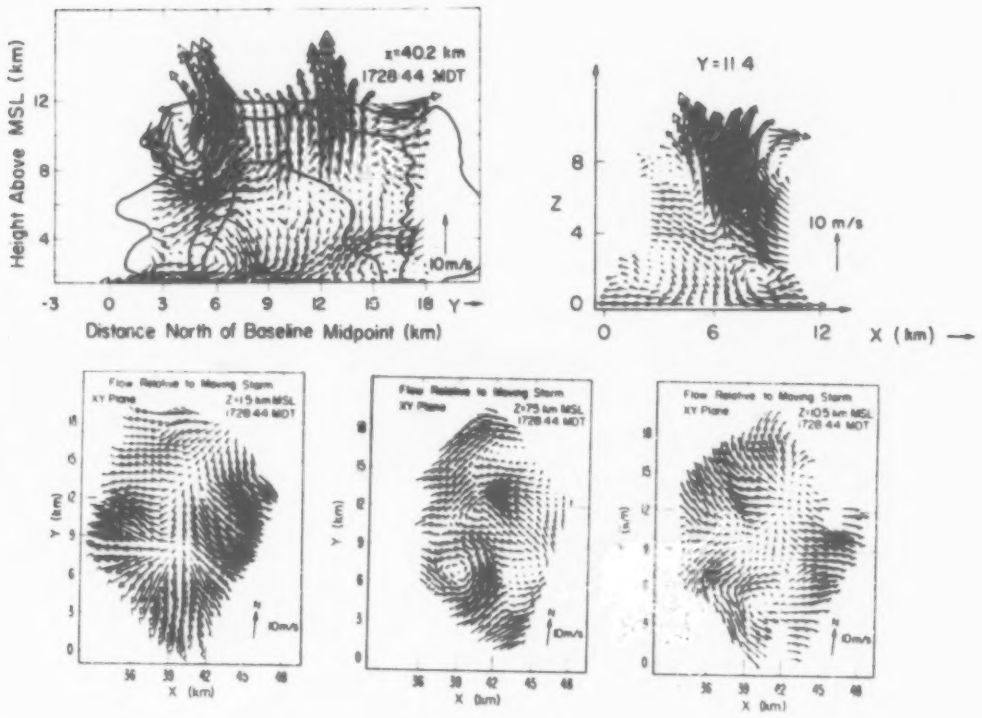

Figure 7.6--Example of wind fields observed with dual Doppler radars (top frame) compared with a model of a simple single-cell convective storm (bottom frame). The volume mean flow has been subtracted from the total wind leaving the residuals. Note the gust front, the inflow at the front, the flow forward into the anvil, the flow of dry air at mid-cloud level into the back of the storm exiting at the rear at surface level and the downdraft produced by evaporative cooling in the precipitation shaft. (From Kropfli and Miller.)

terminal fall velocity in still air which is added to the natural vertical velocity of the air itself. Since multi-Doppler radar systems view the atmospheric volume at very low elevation angles (maximum typically 15 deg), and since the terminal velocity only enters the problem as the product of the sine of the elevation angle, the effect is generally small. The fall velocity of chaff is about 0.3 m s^{-1} and the fall velocity of snow is about 1 m s^{-1}. However, the fall velocity of water drops is highly variable depending on drop size and may reac 9 meters per second. Furthermore, in convective storms the drop size distribution may be highly variable throughout the storm. It is therefore sometimes necessary to take account of the terminal fall velocity of the water drops in a more rigorous way. This is most accurately done by relating the fall velocity to the easily measurable reflectivity distribution through the storm. The relation between fall velocity and drop size is rather well established. Furthermore there is a

large body of experimental data relating rainfall rate to drop size distribution and radar reflectivity to rainfall rate. These various relationships can be combined to provide a relationship between terminal fall velocity and the radar reflectivity factor. One relationship commonly used in multi-Doppler radar software is that proposed by Joss and Waldvogel (1969).

Boundary Conditions

Although three or more Doppler radars can, in principle, directly observe the 3-dimensional velocity of a target, in practice it is found to be necessary to use the equation of continuity regardless of the number of radars in the experiment for two main reasons:

1) The vertical component of the velocity of precipitating particles is contaminated by a "fall velocity" that is often difficult to estimate.

2) The antenna elevation angles needed to obtain a reliable estimate of the vertical velocity component are only found for targets in the upper levels of storms in typical situations.

Therefore the combination of multiple-radar geometrical estimates and estimates using the equation of continuity are found to be optimum. The resulting redundance, in principle, allows the vertical particle velocity and vertical air velocity to be separated. Miller (1979) has in fact calculated reflectivity vs. fall velocity estimates using this technique.

In order to integrate vertically the horizontal divergence patterns, a starting boundary condition must be known. Over water or over flat terrain such as the Great Plains it is usually adequate to assume the lower (rigid) boundary to be horizontal and flat so that the condition $w = 0$ at $z = 0$ can be imposed. If the lower boundary is not flat it is usually desirable to work from an upper boundary condition rather than a lower boundary. For one thing, any errors introduced by the erroneous assumption that the lower boundary is level and flat grow in the course of integration upwards because of the exponential decrease in atmospheric density with height, whereas the corresponding errors are damped in the course of downward integration. If three or more radars are available the particle vertical velocity at the top of the storm where the elevation angles are large can be measured accurately geometrically. Furthermore, high in the storm the particle fall velocities are small and fairly accurately estimated. Thus the geometrical vertical

velocities can yield a fairly accurate upper boundary condition with which to start the downward integration of the horizontal divergence. Moninger (1980) has described a refinement of the technique in which the integration is begun with the boundary condition as described and carried down to the next grid point where the calculated velocities are compared with the geometrical velocities and values which are weighted toward the geometrical are used to restart the integration. As the integration is carried downward through the top four levels, the calculated values are successively weighted more heavily. From the fifth level down only calculated values of vertical velocity are used. Figure 7-7 shows an example of a penetrative downdraft in a cell analyzed by Moninger (1980) using this technique for establishing an upper boundary condition for beginning the integration.

The multi Doppler-radar analysis of cloud dynamics is simpler in some respects than that for storms. For example, the problem of estimating the particle fall velocity in quiet air is absent with very small drops. Furthermore, the potential mixture of hail, water drops and snow found in mature storms will not be present in clouds. Although water drops and ice crystals may be present, they will not severely degrade the kinematic observations. On the other hand, the cloud medium will not normally extend to the ground providing a lower boundary condition; so an upper boundary condition is needed requiring three or more radars. The clouds that can usefully be observed by this method are therefore limited to geometrical relationships with the radars that permit accurate vertical velocities to be measured near cloud tops.

7.4 Choice of Wavelength in Cloud-Sensing Doppler Radar Systems

Figure 2-2 shows that the attenuation of radar waves due to absorption by water droplets increases strongly as wavelength is shortened. Consequently most radars used in severe storm studies have employed the longer wavelengths, i.e., 5 or 10 cm. However, radars used to study clouds whose drops are small must use very short wavelengths so that the factor D^6/λ^4 (see Eq. 2-41) will be as large as possible.

The disadvantages of short wavelength radars are mainly:

1) Their relatively high attenuation (see Fig. 2-2).

BEST DOCUMENT AVAILABLE

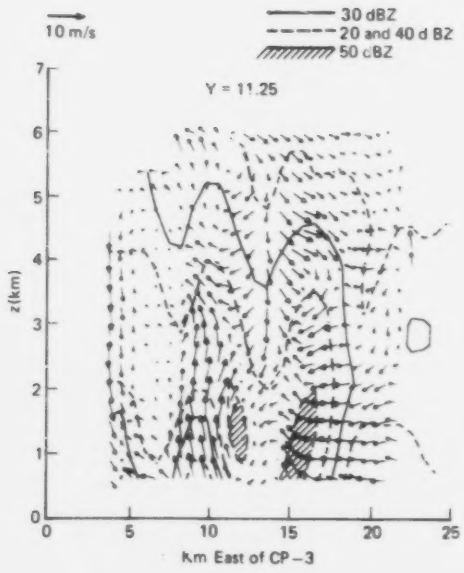

Figure 7.7--Example of multiple-Doppler radar observation of a convective storm in the Sacramento valley. Storm shows evidence of a well developed penetrative downdraft. In this case the integration of the continuity equation was done from the top down with the boundary condition chosen at storm top, as described in the text, because of the complicated terrain at the lower boundary. Note the unusual positive correlation between reflectivity pattern (contours of Z units at 10 dBZ intervals) and vertical velocity. (From Moninger, 1980.)

2) The severe aliasing that occurs if the particle velocities become large (see Eq. 7-6). Sophisticated modulation schemes can aid in solving this problem. For example pairs of pulses separated by a longer period can minimize the velocity-range folding ambiguity. Thus the small separation of pulses in the pair can provide a relatively large value for V_M, while the large separation between pairs of pulses can provide a large r_M.

However, there are important advantages of short wavelength radars.

BEST DOCUMENT AVAILABLE

1) Multi-Doppler-radar analysis has always shown that the limitation in spatial resolution, primarily depending on beamwidth, is the limiting factor in resolving the important vertical scales. Thus, the shorter wavelength radars have significant advantages because narrow beams can be achieved with reasonable apertures. Furthermore, for low angle coverage ground clutter-induced velocity errors are often very significantly reduced by narrow beams. Experience has shown that this is a factor that is hard to over-emphasize.

2) Another factor favoring the shorter wavelength radars is that the accuracy of Doppler estimates (for large SNR and reasonably narrow spectra) is given by

$$\hat{\sigma}_{v_r} = \left[\frac{\lambda\sigma}{8\sqrt{\pi}\ T_d}\right]^{1/2} \tag{7-14}$$

where

T_d = dwell time

σ = width of Doppler spectrum.

Thus, shorter wavelengths lead to more accurate velocity estimates in a given dwell time, provided that spectral widths are small compared to the Nyquist value. Also favoring the shorter wavelength radars is the fact that the reflectivity (η) is proportional to the inverse 4th power of wavelength, and for Doppler work the important consideration is the trade-off between the reflectivity (in dB) and the attenuation. For drops whose diameters are much less than a wavelength, Eqs. (2-25,29) and (5-7b) show that

$$P_R \propto \underbrace{\frac{\pi}{1c}\frac{(2\pi)^4}{\lambda^4}|K|^2 Z}_{\eta} G^2 e^{-2\int_o^{p_o} kdp} \tag{7-15}$$

where p_o is the attenuation path length through the precipitation. The reflectivity η is thus proportional to λ^{-4} and to the reflectivity factor $Z = \Sigma N_i D_i^6$ where N_i is the number of drops of diameter D_i in a unit volume, $|K|^2 \simeq 0.93$ and k is the absorption coefficient. Then, expressed in decibels, $P_R(dB) = \text{const} + 20 \log G - 40 \log \lambda - 4.343(2\int_o^{p_o} kdp)$. Recalling that the gain $G = (\pi/1.22)^2(Dia)^2/\lambda^2$, we distinguish two cases of interest: (1) the case of <u>constant aperture</u> of dish diameter (Dia) which is of overriding importance for transportability and (2) the case of <u>constant gain</u> G which is the important case for fixed sites where large antennas are feasible.

BEST DOCUMENT AVAILABLE

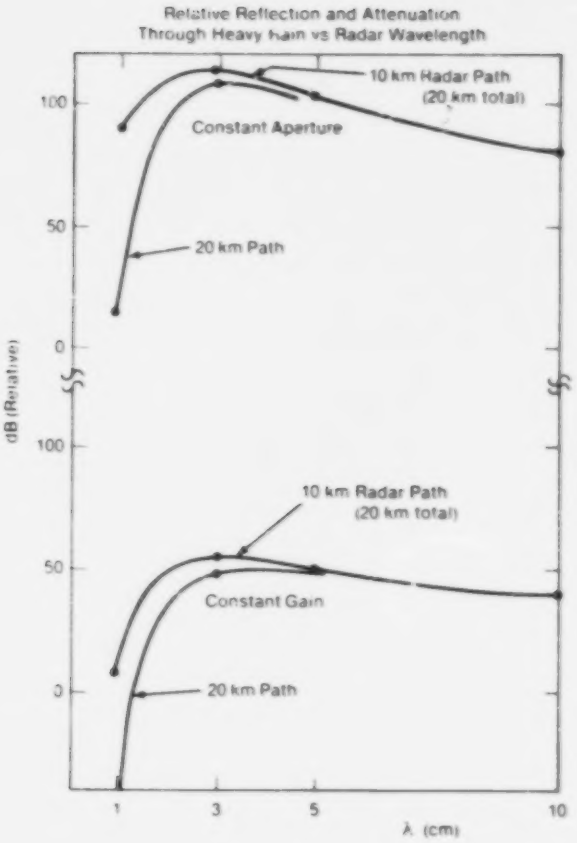

Figure 7.8--Received power resulting from relative reflection and attenuation as a function of wavelength in 16 mm hr^{-1} precipitation for the same aperture (top) and same antenna gain (bottom).

For (1)

$$P_R(dB) = \text{const} - 80 \log \lambda - 4.3\ k\ p_o.$$

For (2)

$$P_R(dB) = \text{const} - 40 \log \lambda - 4.3\ k\ p_o.$$

The two cases are shown in Fig. 7-8 where relative power is plotted for 0.9, 3.2, 5, and 10 cm radars assuming values of absorption coefficient in heavy rain taken from Fig. 2-2. Curves for 2-way paths (radar range) of 10 and 20 km are shown. It seems probable that depths of heavy precipitation should very seldom exceed 10 km. For Doppler work it should be noted that even in precipitation there is little to choose between the various 3-10 cm radar systems with realistic attenuation paths. If accurate reflectivities or very long ranges are required, it is desirable to have 10 cm radars in the system. As the drop sizes within the cloud grow, the millimeter wavelength radars will become heavily attenuated and longer wavelength radars must then "take over" as a storm develops.

There are several reasons why a cloud sensing Doppler capability is important:

1) It would allow developing storms to be observed in their early evolutionary stage. The variety of quantities observable with multi Doppler-radar is exemplified in Table 1-2 taken from Kropfli and Miller (1973). Cloud sensing capability would extend these observations into the cloud phase.

2) Present radar wavelengths permit only a relatively small volume of a storm to be observed. This is illustrated by the lower frame in Fig. 1-11 in which the velocity field of the storm shown in Fig. 7-6 has been superimposed by Browning on a realistic schematic picture of a storm. (The solid circular points are the calculated trajectory of a hailstone.)

3) The ability to superimpose microphysical information (from dual wavelength, dual polarization observations) along with turbulent intensity (from spectral width observations) on the detailed kinematic morphology of clouds would help in cloud model verification.

7.5 Doppler Radar Studies of Clear-Air Structure

The Use of Chaff in Studies of the Clear Air

An obvious extention of the multi-Doppler radar techniques now commonly used in storm research is their application in clear air conditions by use of chaff. The chaff usually is formed of thread-like pieces of aluminum-coated mylar, cut to one-half the wavelength of the radar. It can be dispensed by a variety of techniques. Small rockets, capable of releasing a chaff package up to heights of a few hundred meters, are commercially available. Other dispensers include shot-gun shells having a small explosive charge and a chaff package. The most useful method for filling a substantial volume of the lower atmosphere employs a chaff cutter that produces a continuous stream of chaff cut to the desired wavelength. Such cutters are easily adapted for use aboard aircraft or ground vehicles. They are fairly effective as fixed, ground-based dispensers, especially under convective conditions. The chaff is then quickly mixed through the whole depth of the convective boundary layer and provides very suitable tracers of the air motion. The chaff density needed is very low — one element per 30,000 cubic meters is adequate for most geometries.

The multi-Doppler radar technique using chaff was very effectively employed by NOAA's Wave Propagation Laboratory in 1975 in the METROMEX program carried out at St. Louis, Missouri, in the USA. In this program, one goal was determining the modification of the local meteorology by large urban areas (Auer, 1975). Some of the effects investigated in the total program included 1) urban influences on the amount and patterns of precipitation, resulting perhaps from "seeding" by nuclei produced by industrial areas; 2) the manner in which diffusion of nuclei and pollutants takes place; 3) possible heat island effects on circulation patterns in the volume above the city. A comprehensive description of the program, with contributions by many participants, is included in Vol. 17, No. 5, of J. of Appl. Meteorol., 1978 (Special issue on METROMEX, S. Changnon, ed.)

Multi-Doppler radars are especially well suited to provide the three-dimensional wind patterns needed to evaluate many of the hypothesized effects. Figure 7-9, adapted from Kropfli and Kohn (1978), shows a flow pattern that was reproduced in the clear convective boundary layer whenever the mean flow was from the northeast. Figure 7-9 includes a background map of the area, showing the position of the Mississippi River, the siting of the two (NOAA/WPL) radars, and the location of Granite City. Granite City is an industrial suburb of the St. Louis complex. The presence of a substantial number of industrial plants suggests that it may be an important heat source, and this hypothesis is confirmed by temperature sensors aboard the University of Wyoming aircraft. A striking feature of Fig. 7-9 is the vortex roll existing downwind of Granite City. It is revealed in several cross-sections transverse to the mean flow at distances downwind indicated by the Y value of each cross-section. The corresponding convergence pattern 300 meters above the city and the divergence pattern at 1300 meters are shown by the plan views of the residual fields of the horizontal vector wind, shown below and above the vertical cross-sections in the figure.

Figure 7-10 shows examples of flow patterns under conditions of substantial mean wind, i.e., 6 m s^{-1} from the ESE (top frame) and under conditions of relatively low mean wind, i.e., 3 m s^{-1} from the south (bottom frame). The alignment, presumably resulting from shear in the mean wind, is clear in the fields shown in the top frame. More examples of the phenomena shown in Figs. 7-9 and 7-10 may be found in Kropfli and Kohn (1977). Other examples in which multi-Doppler radar techniques have been used with chaff to study flow patterns under clear-air conditions have been reported by Frisch et al. (1976), Gossard and Frisch (1976), Kropfli and Hildebrand (1980), and Hooke (editor) (1980). Figure 7-11 shows examples extracted from Frisch et

BEST DOCUMENT AVAILABLE

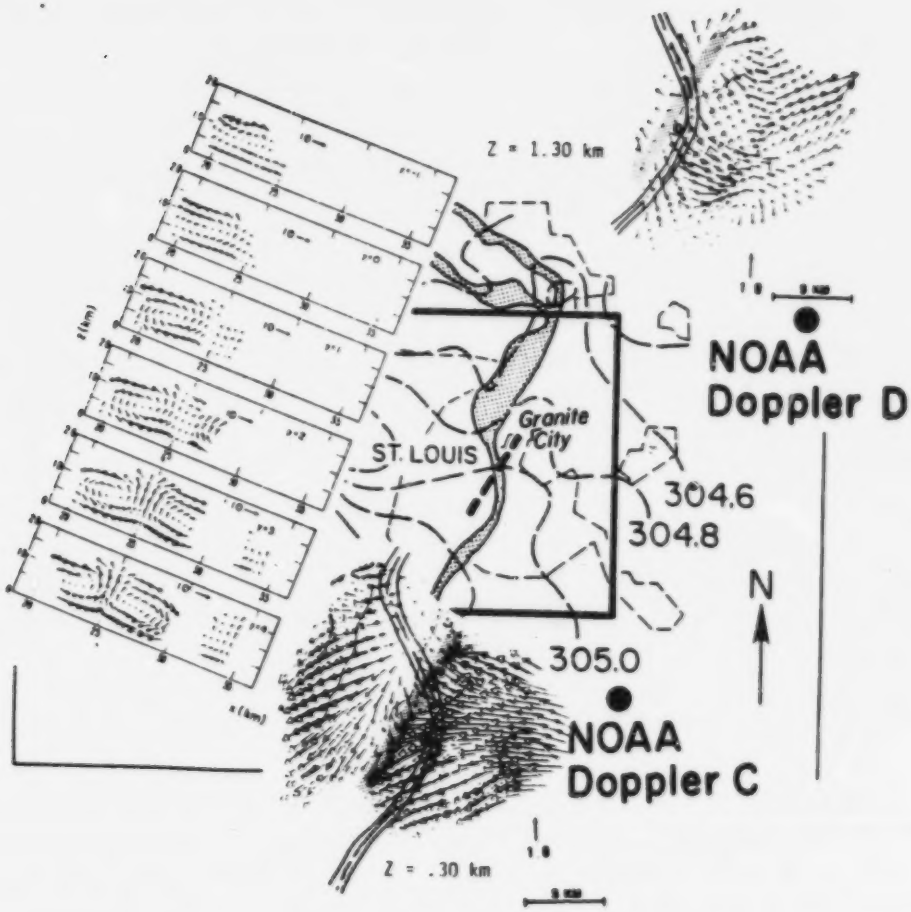

Figure 7.9--Flow patterns observed by dual Doppler radar in the convective boundary layer at St. Louis, MO during the METROMEX. The wind fields were measured in the vicinity of the heavy dashed line crossing the Mississippi river in the center map downwind of the industrial heat source at Granite City. Lower plan view of residual wind field is at a height of 300 m and shows pronounced convergence along stippled zone. Upper plan view at a height of 1300 m shows convergence has been replaced by divergence suggesting a vortex role — a suggestion borne out by the vertical cross-sections of velocity transverse to the dashed line spaced at 1 km intervals shown in left-hand frames. Dashed contours over city show potential temperatures measured by a University of Wyoming aircraft at an altitude of 1300 m. (From Kropfli and Kohn, 1977.)

BEST DOCUMENT AVAILABLE

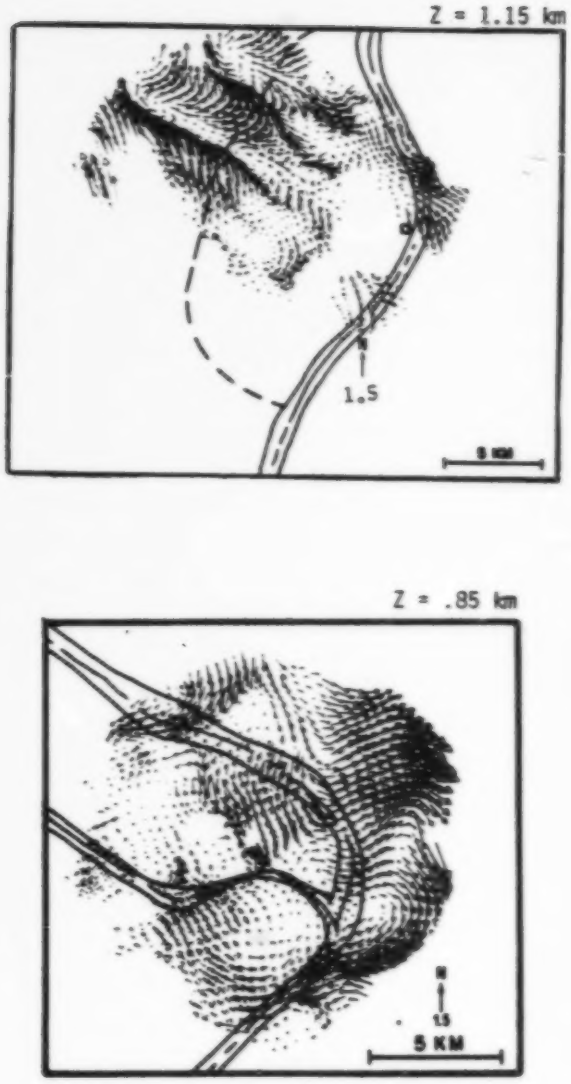

Figure 7.10--Examples of flow patterns under unstable conditions with substantial mean wind; i.e., 6 m s^{-1} from the ESE (top frame) and under conditions of relatively low mean wind; i.e., 3 m s^{-1} from the south (bottom frame). The pronounced alignment evident in the top frame presumably results from vertical shear in the mean boundary layer wind. (From Kropfli and Kohn, 1977.)

BEST DOCUMENT AVAILABLE

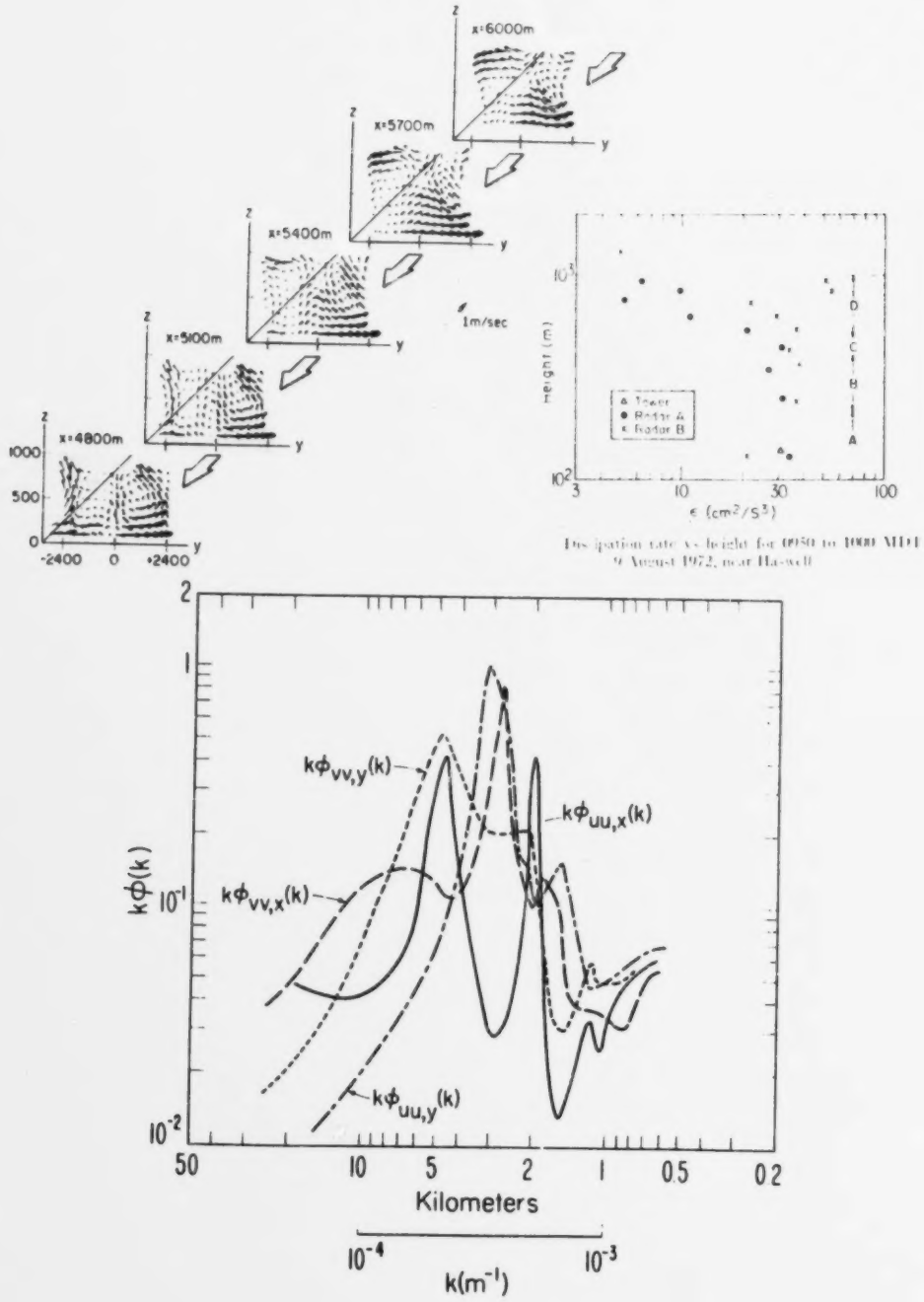

Dissipation rate vs. height for 0950 to 1000 MDT 9 August 1972, near Haswell

Figure 7.11--Upper left-hand frame: Vertical cross-sections of wind transverse to the mean flow (large open arrows) measured by dual Doppler radar using chaff targets. Upper right: Height distribution of turbulent kinetic energy dissipation rate in the convective boundary layer from Doppler spectral width, compared with in-situ measured value on 152 m tower. Bottom: Spectra of various velocity components and cross-components from the radar-chaff data. (From Frisch et al., 1976.)

BEST DOCUMENT AVAILABLE

al. (1976). In addition to research, the technique clearly shows great promise in the investigation of the diffusion of pollutants under conditions when simple statistical models are inapplicable. However, as of this writing, it has not been used in programs of this kind.

7.6 Dual Doppler Radar Measurements in the Clear Air Without Chaff

Doviak and Berger (1980) have reported returns from the clear atmosphere that were strong enough to use for dual-Doppler synthesis of three-dimensional wind fields in the clear air without the need for chaff. They interpret their radar backscatter to be a result of the kind of clear-air Bragg scatter discussed in Section 2.5 of Chapter 2. The PPI display for the example they analyzed is shown in Fig. 7-12, and the residual wind field, after the mean wind is removed, is shown in Fig. 7-13. The wind was 10 m s^{-1}

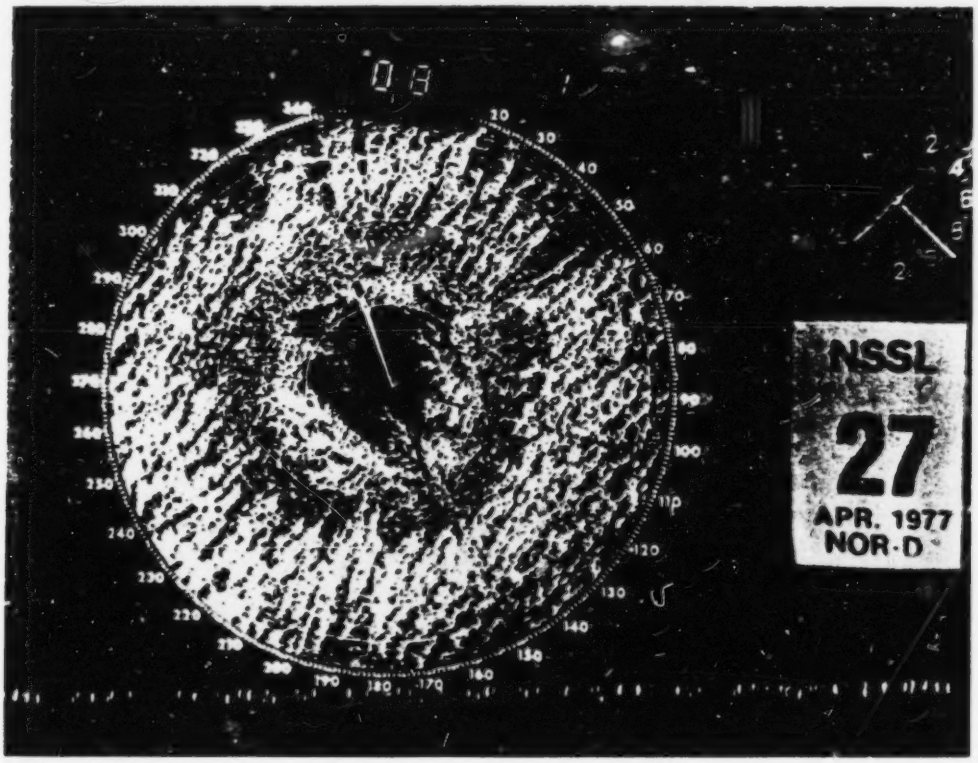

Figure 7.12--PPI contour display of reflectivity xR^{-2} (R is range) from NRO Doppler. Bright area of higher reflectivity is aligned parallel to mean wind and the bands are spaced about 4 km apart. Range marks are 20 km apart. Elevation angle = 0.8°. (April 27, 1977, 1350 CST).

BEST DOCUMENT AVAILABLE

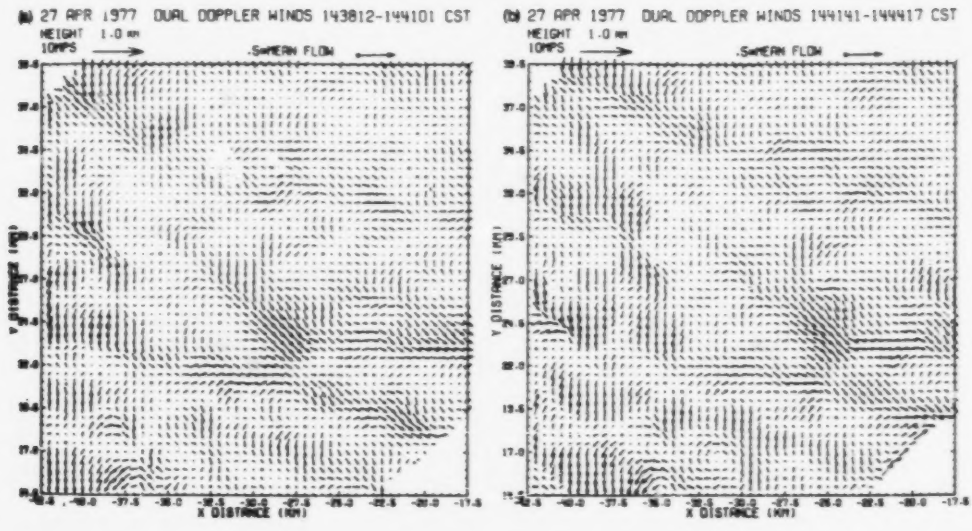

Figure 7.13--Horizontal wind fields in the clear air measured by dual Doppler radar without chaff. Note high correlation between successive patterns about 2 1/2 minutes apart.

at the surface on this day and shows considerable shear with height so elongation of the convective features might be anticipated, and indeed, seems evident in both Figs. 7-12 and 7-13. The resemblence to the chaff cases discussed above is apparent. A major question in the interpretation of this kind of observation is whether the return is from the basically uncontaminated clear air or from a significant population of particulates. In the United States midwest, a very dense population of insects is present in the boundary layer, as seen in Figs. 1-27 in Chapter 1 and Figs. 8-2 and 8-5 in Chapter 8. The subject of insects will be discussed in more detail in Chapter 8. Without the very high resolution ($\sim$1-6 m) provided by the FM-CW radar, or without frequency polarization diversity, it is virtually impossible to distinguish radar signals caused by an insect/seed population from the diffuse return due to Bragg scatter from the clear air. However, these particulates themselves provide excellent air-motion tracers, except in the rare cases when the dominant insect species is not a "weak flyer," so they are seldom a detriment to the use of radar as a meteorological tool.

7.7 Frequency-Modulated, Continuous-Wave (FM-CW) Radar

The first successful radar designed specifically for use in clear-air research was the FM-CW radar (Richter, 1969). It immediately provided spectacular observations of buoyancy (gravity) waves and convective perturbations in

BEST DOCUMENT AVAILABLE

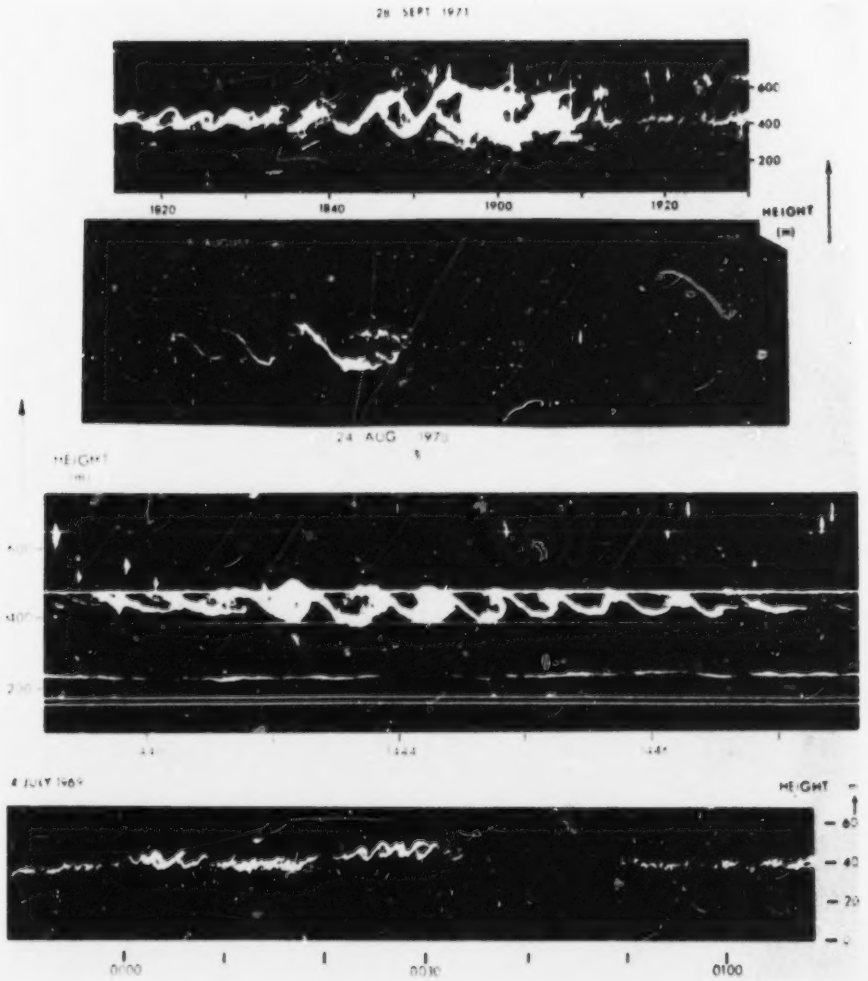

Figure 7.14--Examples of gravity (buoyancy) wave structure on elevated stable layers in the atmosphere observed by the Richter FM-CW radar at San Diego. Horizontal lines are range markers or clutter from fixed targets. The dots and vertical streaks are point targets — usually insects and birds. (From Gossard and Hooke, 1975.)

the lower atmosphere (Gossard et al., 1970; Richter and Gossard, 1970; Atlas et al., 1970; Gossard and Richter, 1970). It provided pictures of atmospheric perturbations with unparalled resolution and detail, as shown in Fig. 7-14. However, this development was not actively pursued elsewhere, although a similar system was used for a time at ESSA, and results from operations in Colorado were reported by Bean et al. (1971, 1972). The reason this development was not pursued seems to lie in the almost concurrent development of the

BEST DOCUMENT AVAILABLE

acoustic sounding system, sometimes called SODAR, described by McAllister et al. (1968) and Little (1969). The scientific community generally turned to the acoustic system as a boundary layer remote-sensing tool, even though it did not have as great range or range-resolution as the FM-CW radar. Furthermore, the acoustic sounders are generally inoperative during high wind or precipitation events. The main reasons the community turned to the acoustic system were that 1) it is basically cheaper than the radar, and 2) it is easy to incorporate Doppler capability into the pulsed acoustic system. It was widely thought that an FM-CW radar, designed for use with a distributed target such as the atmosphere, could not have a Doppler capability. Such a radar uses the frequency difference between the transmitted signal and the returning signal to provide range information. It therefore seemed impossible to extract velocity information from an additional Doppler shift in frequency. (For further discussion see Chapter 19.) Thus, the apparent inability to sense velocity within a continuous target was probably a major factor in the lapse of interest in the radar. However, in 1974, the practical use of Doppler in this type of radar was demonstrated (Strauch et al., 1976), and its use in providing clear-air wind profiles to heights of 1 km or more was reported (Chadwick et al., 1976a,b). Figure 7-15 shows the first radar-measured wind profiles, compared with measurements by tethered balloon (solid curves) and RAWIN (circled points). The details of the incorporation

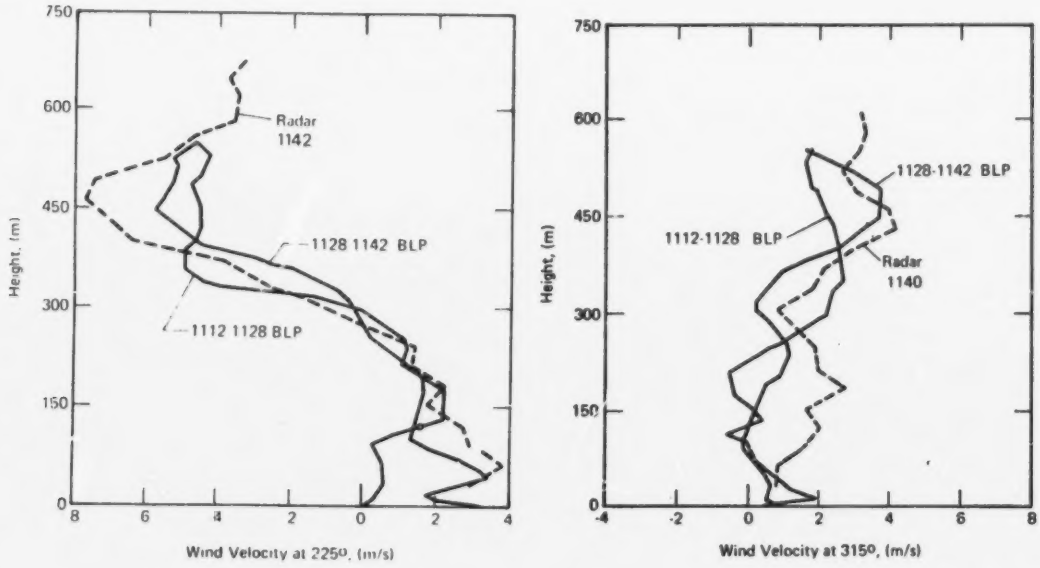

Figure 7.15--Wind profiles measured by an FM-CW Doppler radar (dashed curves) compared with tethered balloon profiles (BLP, solid curves).

of Doppler processing in the radar are given in Chapter 10. After its discovery, it was evident that Doppler processing in this type of radar is very simple in practice, because the radar processing is done in the frequency domain and the usual transformation from time to frequency is unnecessary. The Doppler capability opens up a wide range of possibilities for use of the FM-CW radar in boundary layer research. In addition to continuous monitoring of mean wind profiles, the following quantities can be observed in the clear air:

a) Height profiles of divergence and deformation can be monitored by the methods summarized in Fig. 1-9. Information about the spatial spectrum of these quantities can be obtained by varying the radius of the cone of the VAD scan.

b) Velocity variance and turbulent energy dissipation rate (ε) can be monitored by the Frisch-Clifford method described in Appendix D.

c) The inherent ability of this radar to vary range resolution continuously provides information on spectral shape and outer scale in the planetary boundary layer.

d) Because the radar transmits and receives continuously, wind information can be acquired at very low altitudes ($\sim$20 m above the radar).

e) Spatial radial wind velocity information can be acquired and displayed in a PPI mode (called plan-shear indicator, PSI), as shown in Fig. 7-16. In Fig. 7-16, shear conditions along the glide path at the Denver Airport (Stapleton Field) were being monitored by the radar.

This type of radar has been used by Gossard et al. (1978) to measure the velocity variance and the turbulent dissipation rate inside a frontal inversion. The synoptic situation is shown in Fig. 1-37, and the meteorological soundings from the Denver RAWIN are shown along with the radar backscatter vs. height and time in Fig. 1-39. The height profile of Doppler spectra and the A-scope display of backscattered power are shown with a portion of the time-height display in Fig. 7-17. During these observations, the radar was pointed vertically so the vertical scale is both height and velocity for the Doppler record. Since the mean vertical velocity is virtually zero, there is no detectable Doppler shift of the spectra from their zero position in each range cell. Therefore, the important information is contained in the width, or 2nd moment, of the Doppler spectra. Using Eq. (7-10), the variance σ_{11}^2

BEST DOCUMENT AVAILABLE

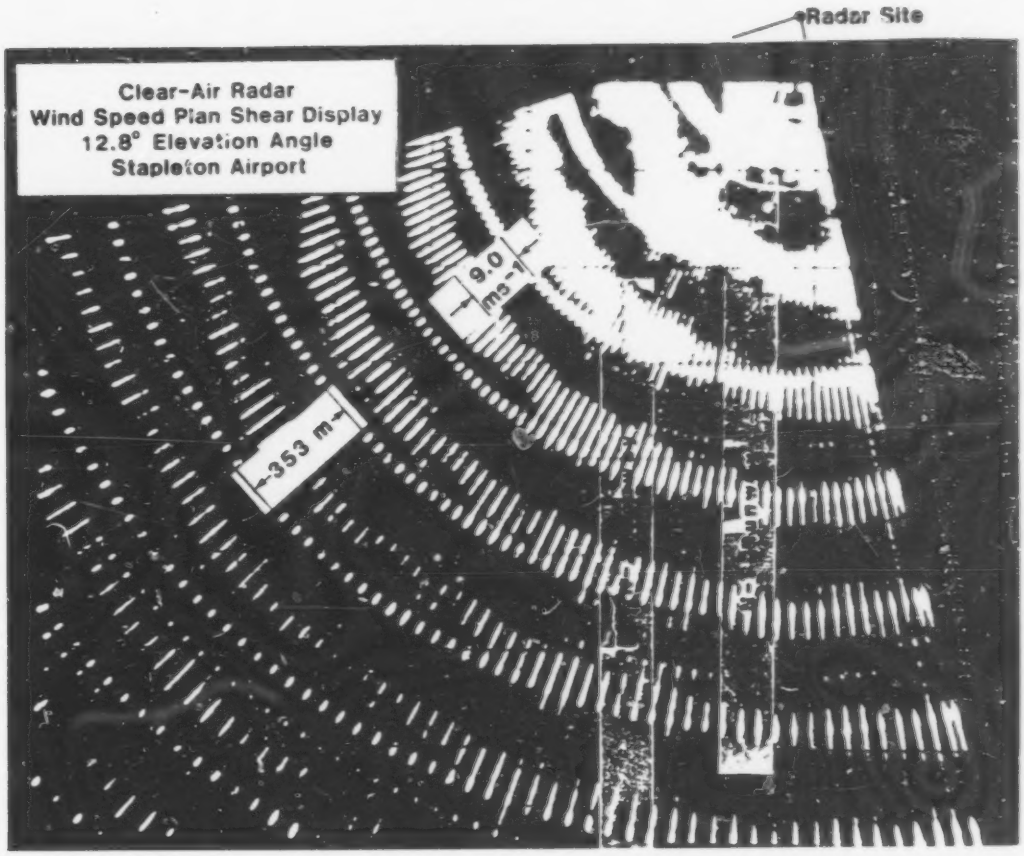

Figure 7.16--Plan-shear indicator (PSI) display of radial winds in the clear air above Stapleton International Airport at Denver, Colorado. The display may be understood by referring to Fig. 7.1 and imagining a plan view of the spectral peaks as viewed from above over an azimuthal sector. The radial dimension is both range and velocity. The concentric circles of dots correspond to the zero radial velocity position in each of 9 range cells 353 in size. The clear air return is in the form of the velocity spectra (see Fig. 7.1) seen as the elongated radial streaks. Their displacement from the zero velocity circles is the radial velocity Doppler shift. If the echoes from successive range cells come close or cross each other, large shear in the radial wind exists. (From Campbell et al., 1980.)

Figure 7.17--Left frame: Height-time display of backscatter power from vertically pointing FM-CW radar. It is a section of Fig. 1.41. Right frame: A-scope display of backscattered power for a single scan compared with the Doppler spectra in height increments of 87 m. Reference signal shown at height of 1500 m AGL. Compare Doppler display with Fig. 7.1. (From Gossard et al., 1981.)

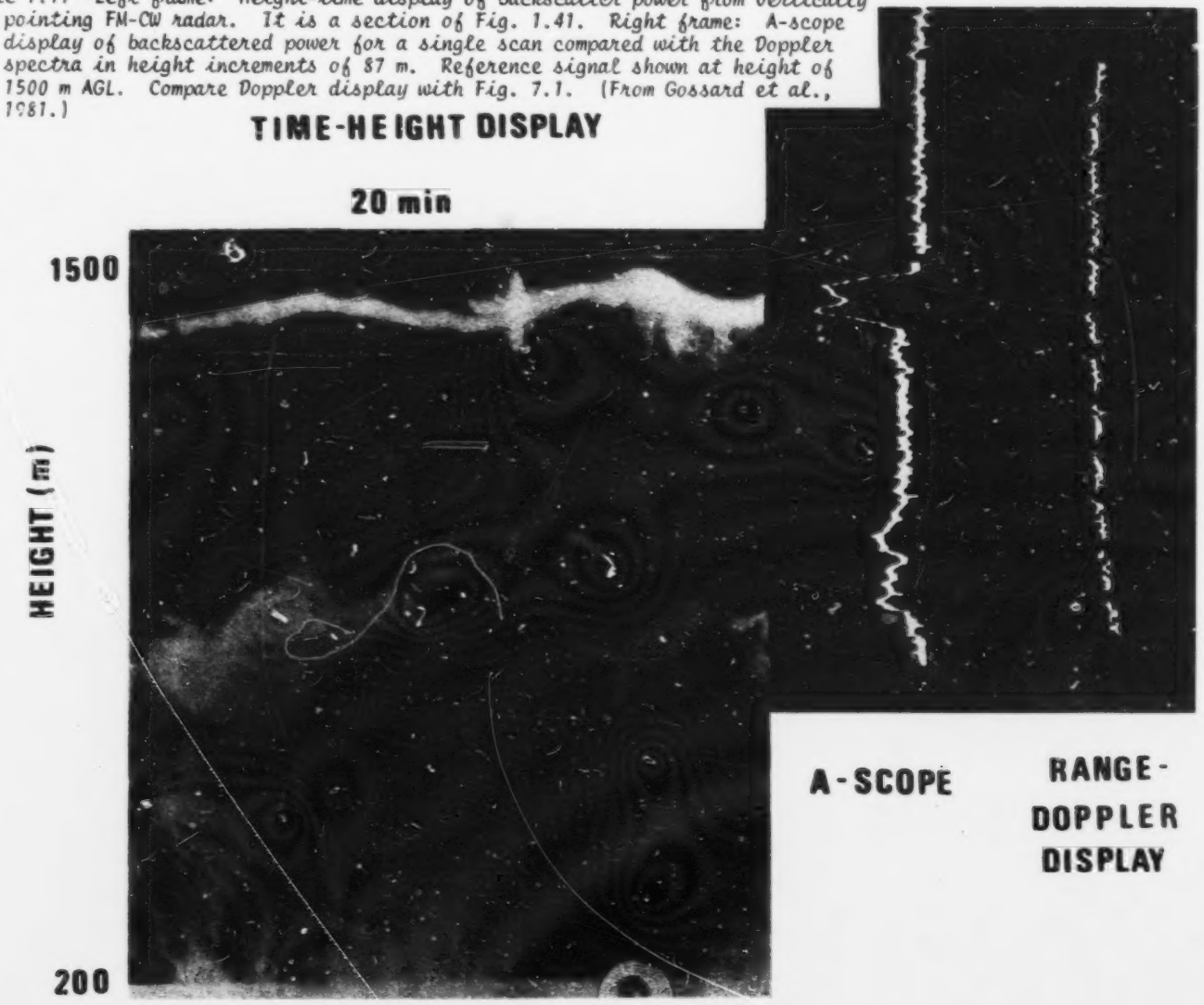

BEST DOCUMENT AVAILABLE

BEST DOCUMENT AVAILABLE

and the turbulent energy dissipation rate ε were calculated. The results of Gossard et al. (1978) were based on the values of the universal constants originally proposed by Frisch and Clifford (1974). It has since been pointed out by several workers that the constant A should be 55/11 = 1.35 and the values of ε shown in the profile in Fig. 7-18 are based on the corrected value. The height profile of C_n^2 in this figure is based on the non-Doppler backscattered power, so the resolution is 6 m and the maximum value of C_n^2 at the center of the layer is 4.8×10^{-13}. From the discussion in Appendix E, observations of ε and C_n^2 allow estimates of the flux quantity $\overline{w'\phi'}$ to be made. Thus,

$$\overline{w'\phi'} \simeq - \frac{C_\phi^2 \, \varepsilon^{1/3}}{B_\phi \, (\partial\bar{\phi}/\partial z)} \qquad (7\text{-}16)$$

where C_ϕ^2 is related to C_n^2 as given in Appendix B; i.e., $C_\phi^2 \simeq C_n^2 \times 10^{12}$. If $B_\phi \, \varepsilon = 10 \text{ cm}^2 \text{ s}^{-3} = 10^{-3} \text{ m}^2 \text{ s}^{-3}$, $d\bar{\phi}/dz \simeq -0.2$ and $C_\phi^2 \simeq 0.3$, we find

$$\overline{w'\phi'} \simeq - .05$$

within the refractive layer produced by the inversion.

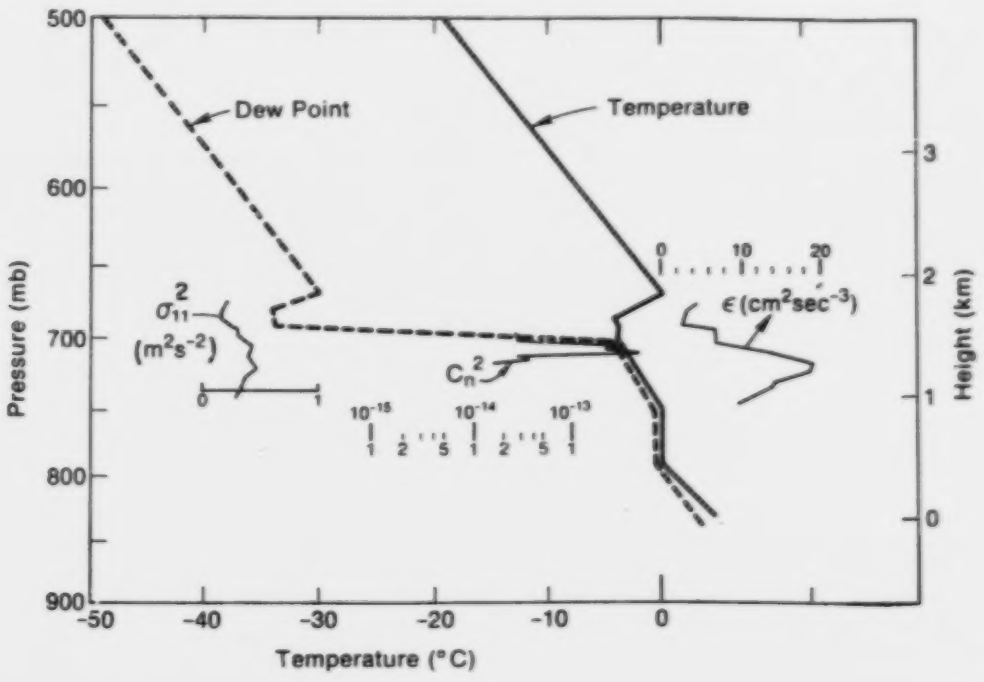

Figure 7.18--Vertical profiles of temperature and dew point from Denver raob compared with C_n^2, calculated from backscattered power shown in Fig. 7.17, and radial velocity variance found from width of Doppler spectra in Fig. 7.17 and ε calculated from Eq. (7-10).

BEST DOCUMENT AVAILABLE

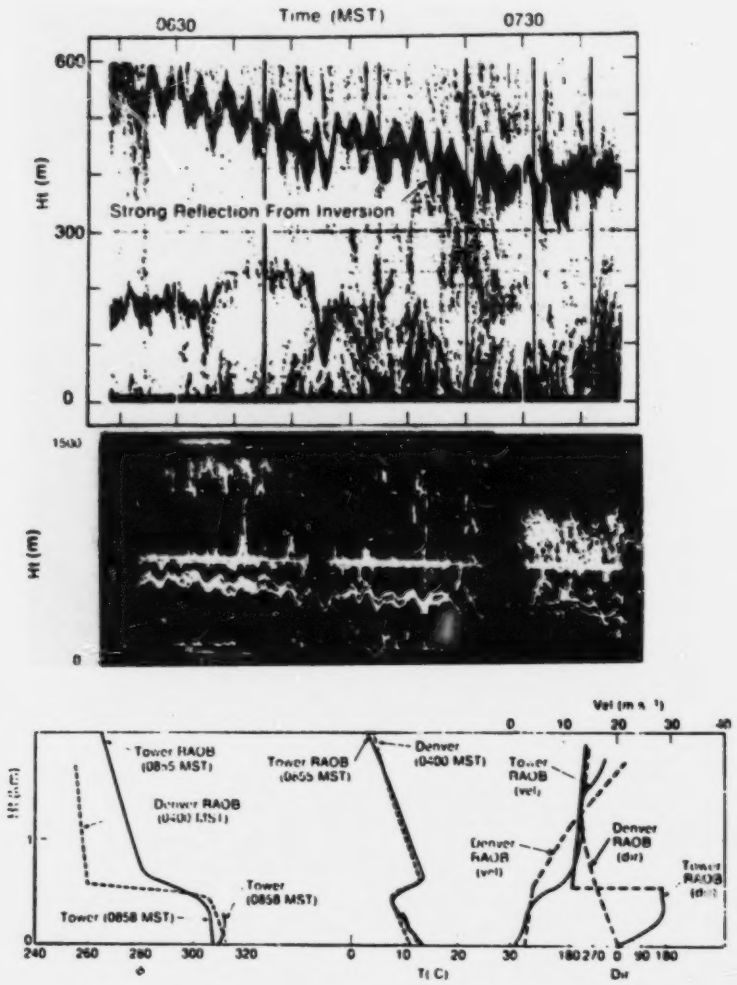

Figure 7.19--Section of Fig. 1.40 (middle frame) compared with simultaneous acoustic sounder record (top frame).

A frontal situation similar to that shown in Fig. 1-39 is shown in Fig. 1-38. The vertically pointing radar record is shown with the Denver and Boulder (tower) sounding data and an acoustic sounder record in Fig. 7-19. Unfortunately, this event occurred early in the morning when the radar was unattended and no Doppler observations were obtained. However, the radar was operating near an acoustic sounder. Both sensors clearly recorded the frontal interface and the wave event on it. The acoustic backscatter depends only on C_T^2, so C_T^2 can be calculated by a technique similar to that used to calculate C_ϕ^2 from the radar backscatter. However, C_T^2 and C_N^2 are related to the structure parameter of humidity C_e^2 through the relation (see Eq. 2-50)

BEST DOCUMENT AVAILABLE

$$C_N^2 = a^2 C_T^2 + b^2 C_e^2 - 2ab C_{Te}^2 \qquad (7\text{-}17)$$

where (Gossard, 1977)

$$a = \frac{77.6\ p}{T^2} + 7.46 \times 10^5 \frac{e}{T^3},\quad b = \frac{3.73 \times 10^5}{T^2} \qquad (7\text{-}18)$$

when e and p are in millibars. It is usually more useful to express Eq. (7-17) in terms of the potential quantities θ, e_p and C_ϕ^2 where θ is potential temperature and e_p is potential vapor pressure (see Appendix B), and p = 1000 mb. C_{Te}^2 depends on the cross covariance (or cross-spectra) of temperature and humidity. Its importance in calculating refractive index spectra from spectra of temperature and humidity was pointed out by Gossard (1960).

From Eq. (7-17), $C_{e_p}^2$ can be deduced if the correlation between temperature and humidity is known. Alternatively, the moisture density q may be used where $q = 0.62\ e_p$ (gr m^{-3}). From the soundings of temperature and refractive index shown in Fig. 7-19, we see that the gradients of temperature and humidity are large and of opposite sign within the inversion layer. Therefore, it seems reasonable to suppose that mixing will create perturbations in temperature and humidity that are strongly negatively correlated. Assuming a correlation of -1, $C_{e_p}^2$ can be calculated from the observed values of C_ϕ^2 and C_θ^2. The results are shown with the C_θ^2 values in the left frame of Fig. 7-20. The truncation of the profiles is a result of the quantization of the radar and acoustic records.

Using Eq. (7-16), $\overline{w'\theta'}$ and $\overline{w'e_p'}$ can be estimated if it is assumed that $\varepsilon \simeq 10$ cm^2 s^{-3} as it was on 29 April. Thus, if we choose the 0858 Boulder raob for the gradient quantities,

$$C_\phi^2 \simeq .3,\ C_\theta^2 \simeq C_e^2 \simeq 8 \times 10^{-3},\ \frac{d\phi}{dz} \simeq -0.1,\ \frac{d\theta}{dz} \simeq +.03,\ \frac{dq}{dz} = -.01$$

$$\overline{w'\theta'} = -8.1 \times 10^{-3},\ \overline{w'e'} \simeq 0.028 \text{ mb ms}^{-1},\ \overline{w'q'} \simeq 0.017 \text{ g m}^{-2} \text{ s}^{-1}$$

and the corresponding flux quantity for ϕ is

$$\overline{w'\phi'} = -0.02$$

BEST DOCUMENT AVAILABLE

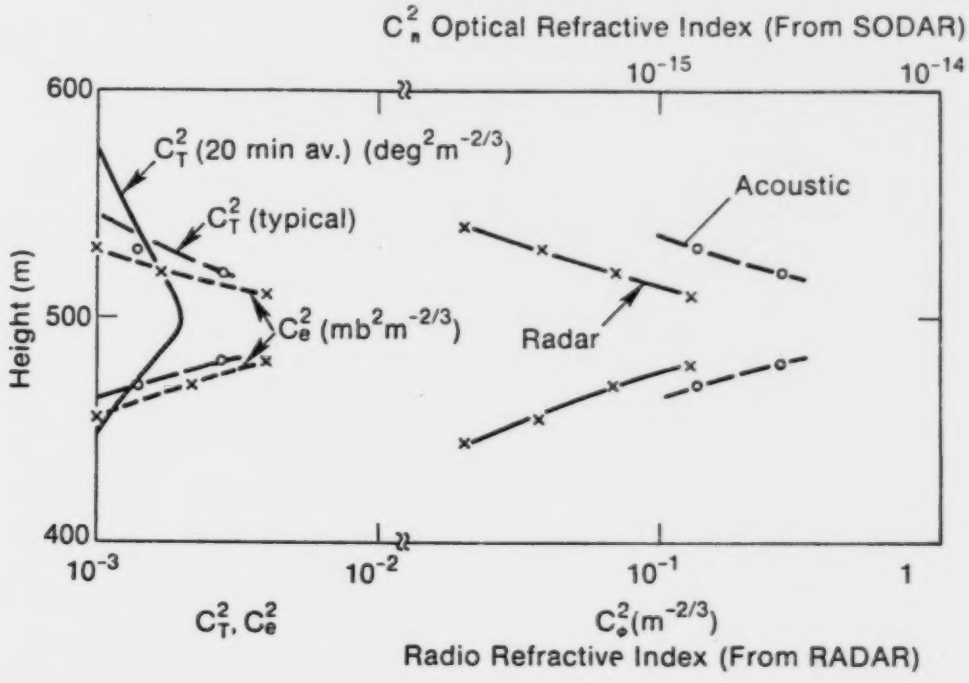

Figure 7.20--Height distribution of C_ϕ^2 and C_T^2 through the frontal zone of the event shown in Fig. 7.19.

in reasonable agreement with the 29 April case. These calculations are only intended to illustrate a method by which clear air radars can, in principle, remotely sense flux in elevated layers if the gradients of the mean quantities can be estimated (perhaps from local raobs). They probably provide correct fluxes through frontal inversions to within an order-of-magnitude, but it is important to verify the method with aircraft-borne sensors of w' ' w'θ' and w'φ'. In both of the cases shown, the lower atmosphere was not really "clear" because fog was present to a height of more than 100 m AGL in both events. However, the primary backscatter is thought to result from Bragg return because the droplets were not precipitating at the time of the radar observations and were therefore very small. No hint of a fall velocity appears in either Fig. 1-39 or 1-40.

7.8 Doppler Radar Winds in the Stratosphere and Middle Atmosphere

With the powerful clear-air VHF radar systems described briefly in Chapter 1 (Figs. 1-41, 1-42), it is now possible to monitor continuously the winds nearly up to the stratopause; with some of the more powerful systems

BEST DOCUMENT AVAILABLE

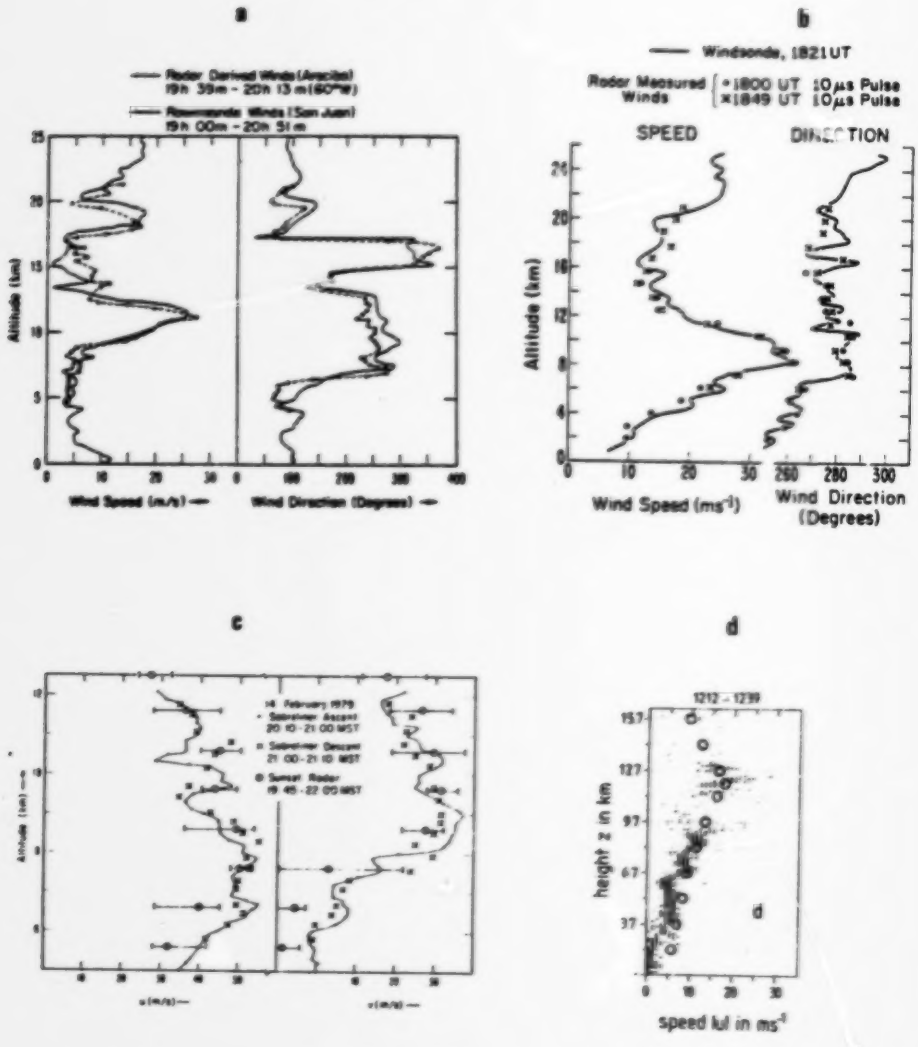

Figure 7.21--Wind profiles into the stratosphere measured by radar compared with RAWIN soundings from Arecibo (7.21a); Chatanika, Alaska (7.21b); Sunset, Colorado (7.21c) and Lindau, German Democratic Republic (7.21d).

such as that at Poker Flats, Alaska, it is possible to monitor winds continuously into the ionosphere. Some examples of wind soundings into the stratosphere are shown in Fig. 7-21. These systems have been demonstrated from equatorial latitudes, such as Arecibo and Puerto Rico (7-21a), to Chatanika, Alaska (7-21b), and from the North American midwest (7-21c) to central Europe (7-21d). They have been compared with winds from balloon soundings and with in-flight aircraft winds. Their ability to measure winds is now well established, and they can routinely monitor important aspects of the coupling between the upper and lower atmosphere. Such coupling has been

an intriguing and controversial subject for many years. More details, and the important design factors for such radars are given in Chapter 11. Combined with microwave radiometric monitoring of temperature and humidity from surface and satellite platforms, such radar systems, deployed globally, could make it possible to establish whether various proposed mechanisms for coupling the lower and upper atmosphere are, in fact, important. Some reported and hypothesized coupling between the troposphere, upper atmosphere and solar activity include:

1) Solar correlated variation of winds in the neutral middle atmosphere.

2) Variations in height of tropical tropopause related to variations in solar constant.

3) Vertically propagating energy from planetary waves — importance of the shutter effect of seasonal wind shear variations.

4) Sudden stratospheric warmings. Increases in temperature of 50°C have been observed in the polar stratosphere followed by reversal of mean zonal winds above 65° latitude.

5) Possible coupling between the ozonosphere and lower atmosphere through dynamic instability.

6) Solar/magnetospheric control of the earth's electric field and its possible modulation of thunderstorm activity.

7) Correlation between vorticity area index and geomagnetic index (Roberts-Wilcox effect).

CHAPTER 8 - BIOLOGICAL TARGETS AND THEIR ROLE IN RADAR BACKSCATTER

For decades the possible role of birds and insects in the composition of clear-air returns from airmass targets and elevated layers was argued and discussed under the general headings of "angels" and "ghosts." The question of whether the clear-air returns resulted from Bragg backscatter, focusing reflective bubbles or biological targets was finally largely resolved by the advent of high resolution atmospheric radars. The FM-CW radar was able to separate and distinguish both the Bragg return from refractive index fluctuations and the biological targets. Records such as that shown in Fig. 1-15 unambiguously demonstrate that both Bragg backscatter and insect scatter often make comparable contributions to the radar return and must be considered to be almost inseparable in low resolution radar systems.

The ability of radars to track insects and to continuously monitor their concentration and movements suggests that they may become an important tool in entomology and in the development of methods for insect control in agriculture. A fairly large body of observational data already exists. A good summary of radar observations of angels into the early 1950's, and the conclusions drawn from them, was provided by Plank (1956). More recent reports on the subject using conventional pulse radars include Glover and Hardy (1966); Lhermitte (1966); Browning and Atlas (1966); Eastwood (1967); Shaefer (1976) and Riley (1979). Shaefer (1976) has reported data collected from many parts of the world. An example from his observations is shown in Fig. 8-1. The tendency for echoes to form an annulus results from the conical scan of the radar beam. This pattern is evidence that the insect population occurs in an elevated layer which the beam intersects at a range equal to the layer height divided by the tangent of the elevation angle.

Another noteworthy feature of Fig. 8-1 is the tendency for the echo to be stronger along one axis than the other. This is an indication that the insects have a common orientation so that they are broadside to the radar beam in the direction of strong signal return with their small dimension in the orthogonal orientation. The reason for their common orientation is uncertain as is the means by which it is created and maintained.

In the midwestern United States insects are sometimes so dense that they completely dominate radar return in the boundary layer. They seem to be generally "weak flyers" and can serve as excellent tracers of the kinematic structure of the boundary layer. They are often too dense to be resolved by the usual pulse radar whose spatial resolution is seldom better than 50-75

BEST DOCUMENT AVAILABLE

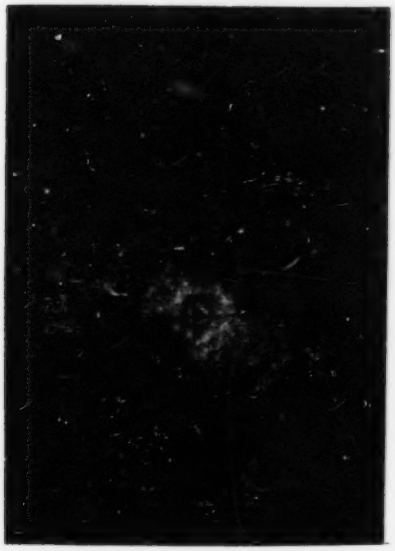

Figure 8.1--PPI display of radar returns from insects. The appearance of an annulus in the insect distribution results from the radar's conical scan and indicates that the insects occur in an elevated layer. The tendency for the echo to be stronger along one axis indicates a strong tendency for the individuals to be oriented in the same direction.

meters in range and considerably poorer in angle for useful ranges. However, radars with other modulation schemes, such as the FM-CW radar, can have range resolution of about 1 meter (Richter, 1969); the insects are then readily resolvable as shown in Fig. 1-27. This type of radar uses two different antennas for transmitting and receiving, so transmit/receive switching is not used, as in the pulse systems. Therefore, there is no fundamental limitation on minimum range so the resolution in angle can be very good if targets are examined close to the radar. This type of radar has been used in insect studies by Richter et al. (1973), Richter and Jensen (1973) and by Gossard and Chadwick (1979).

A record from such a radar is shown in Fig. 8-2 (Chadwick, private communication). Although very dense, the insects are being resolved by the radar. In fact, the insects reveal details of the particle motion within the boundary layer as well as its morphology. Figure 8-3 (enlarged from 8-2) shows a wave structure commonly seen under the stably stratified conditions that occur at night. (This record was obtained about 0200 in the morning.) The wave shape departs significantly from sinusoidal showing that the wavelength is long compared to the boundary layer depth. It is thus a "shallow water" wave that is roughly trochoidal in shape like that analyzed by Gossard and Richter (1971).

From high resolution radar measurements of this kind it is possible to separate the discrete insect echoes from the clear-air returns, and it is immediately clear that insects are a major source of radar return at the time of year when these observations were made. Therefore, such biological targets

BEST DOCUMENT AVAILABLE

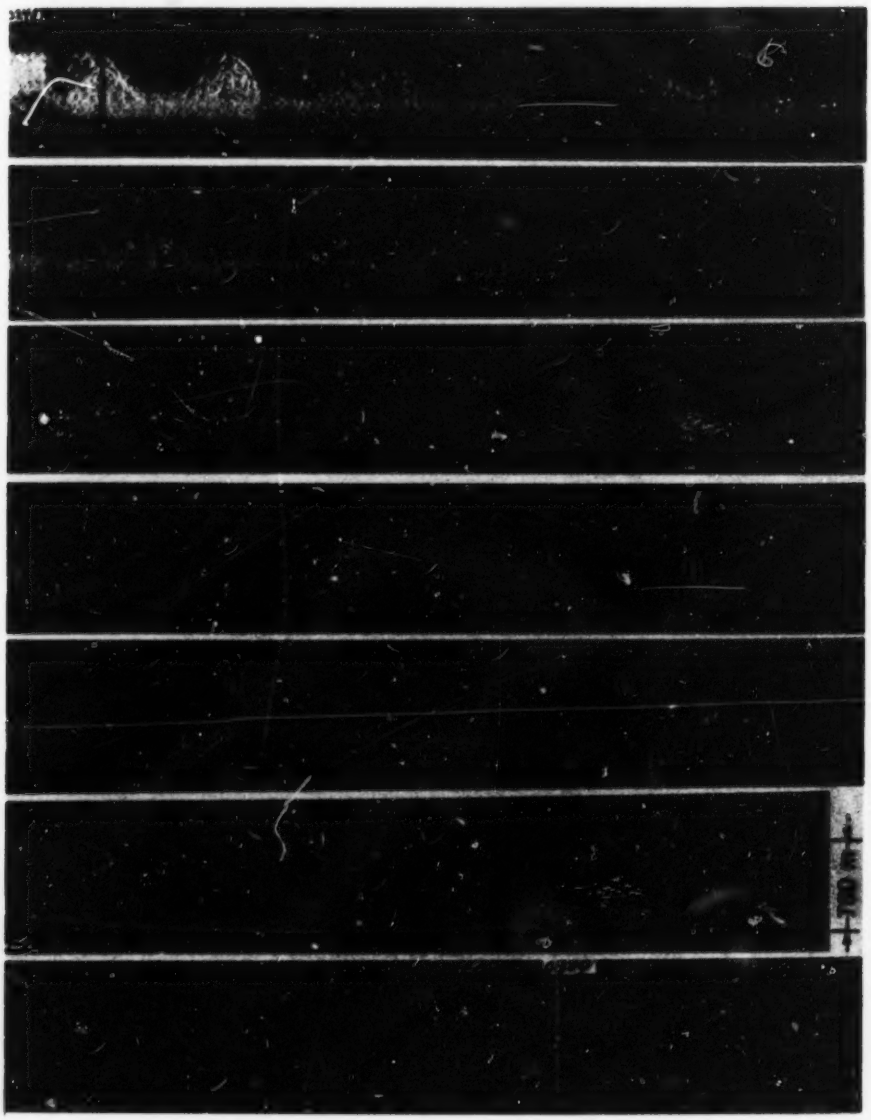

0145-0730 MST (0245-0830 MDT) 19 July 1974

Figure 8.2--Insects in the night-time boundary layer at Sterling Colorado observed by a vertically pointing FM-CW radar (R.B. Chadwick, private communication).

BEST DOCUMENT AVAILABLE

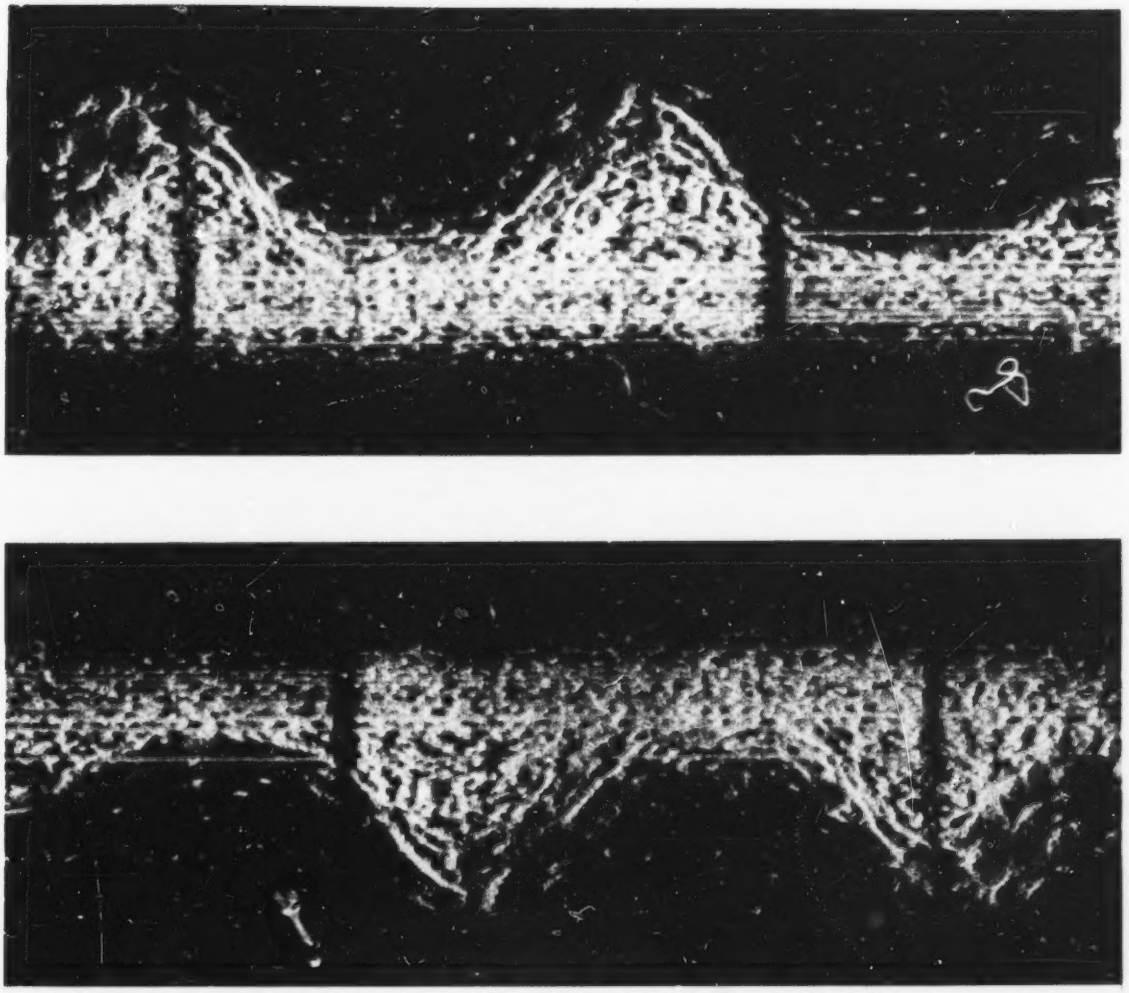

Figure 8.3--The fine height resolution of the FM-CW radar allows a count of individual insects. It indicates an average concentration during this interval of about one insect per 12 m cube of atmosphere.

are an important concern for many applications in the midwestern United States. Insects in this area become important at temperatures above about 10°C (50°F).

The observations in Figs. 8-2, and 8-3 were acquired on the night of 19 July 1974. This record was one of many with comparable numbers of insects. It was chosen because of the interesting wave events on the nocturnal inversion displayed by the insects. A balloon sounding was taken at 0655 Mountain Standard Time (0755 MDT) the following morning, and is shown in Fig. 8-4. The insect distribution in the early portion of the record suggests

BEST DOCUMENT AVAILABLE

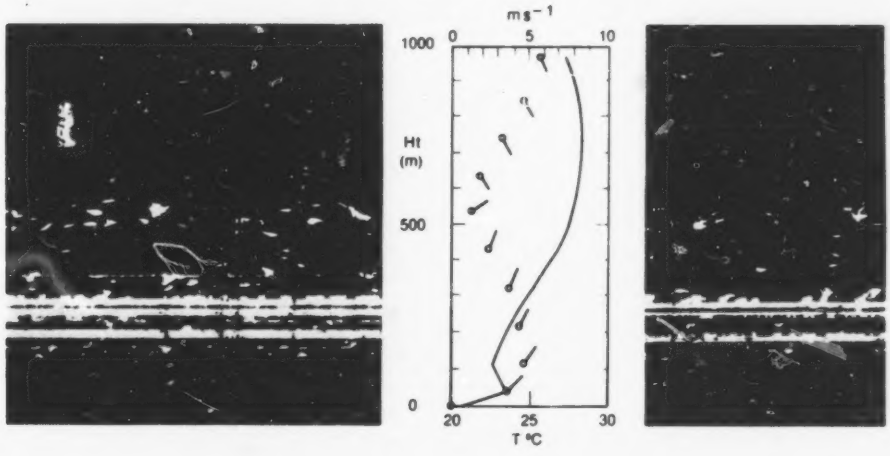

Figure 8.4--Temperature and wind profile at 0655 MST the following morning with insect record of that time.

that the insect population, whose source is presumably the surface, is strongly confined to the surface layer by the strong thermal stratification; although there are insects above the surface layer, the relative numbers above the inversion become greater as the night progresses. There is in fact some suggestion in Fig. 8-2 (waves 4, 5, 6 of top frame that the waves may play a role in entraining insects (or rather projecting them) into the region above the inversion. Meanwhile, the population near the surface is decreasing, leaving a substantial elevated layer of insects apparently bearing little relation to the temperature profile revealed by the balloon sounding at 0655 MST. If a wind speed of 4 m s^{-1} is assumed, a count of the number of insects in the early part of the record yields an insect density of about one insect per 2000 m^3 or a cube about 12 m on a side. No attempt has been made to correct for the larger volume intercepted by the beam at greater heights nor to account for the fact that the side-by-side transmit and receive antennas used in this type of radar have beams that only partially intercept near the ground because of their spatial separation.

Figure 8-5 shows an afternoon case in which insects dominate the return, although a clear-air return associated with the capping inversion seen in the balloon sounding appears at the upper edge of the insect layer. Superfically, this record looks much like the nighttime records of Figs. 8-(2-4), but the scale in Figs. 8-(2-4) is 0-750 m whereas that in Fig. 8-6 is 0-3000 m. In Fig. 8-5 the insects are being convectively mixed more-or-less uniformly through the whole depth of the planetary boundary layer. It is perhaps

BEST DOCUMENT AVAILABLE

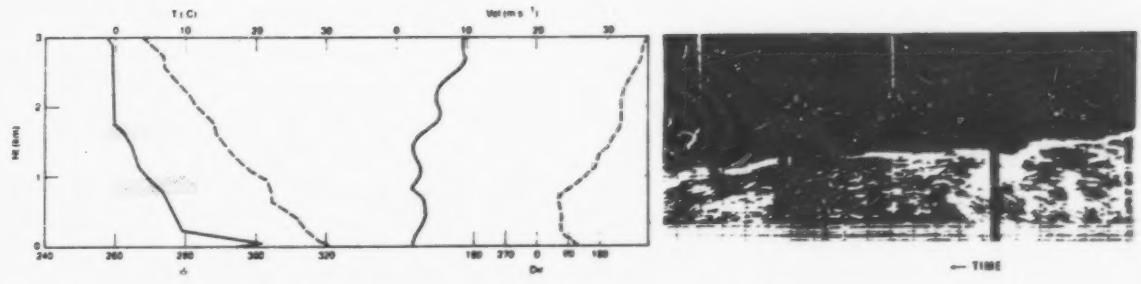

Figure 8.5--Case of afternoon record dominated by insect return with clear-air return from capping inversion, compared with raob-measured profiles of temperature, potential refractive index and wind. (R.B. Chadwick, private communication.)

significant that the insects reveal little evidence of any entrainment through the capping inversion.

The records so far shown emphasize the role of insects in radar returns from the boundary layer and their relation to convective features and thermal stratification. However, their concentration may also be related to layers aloft (Figs. 1-16, 8-6 and 8-7). These records were obtained in southern California with the Richter radar system. There appears to be no consistent relationship between the insect concentration and the layer height — sometimes the insects are concentrated below, sometimes above and sometimes within the backscattering layer. In Southern California the advection of air from the continental interior is common under conditions of strong refractive layering. It is probable that advection of insects and debris is decisive in determining where the insects are found relative to the temperature inversion (which nearly always coincides with the refractive layer in this climatic regime).

Figure 1-27 reveals in detail the way insects are swept up and entrained into convective features and illustrates the complexity that must characterize any analysis of such features using a radar with less resolution than that provided by the FM-CW system. The presence of insects contaminates the radar returns in such a way that predictions of wavelength dependence based on Bragg backscatter are seriously in error. Particulates such as insects produce a λ^{-4} wavelength dependence for backscattered power if they are Rayleigh scatterers, whereas clear-air Bragg backscatter should have a dependence of about $\lambda^{-1/3}$ as pointed out in Chapter 2.

BEST DOCUMENT AVAILABLE

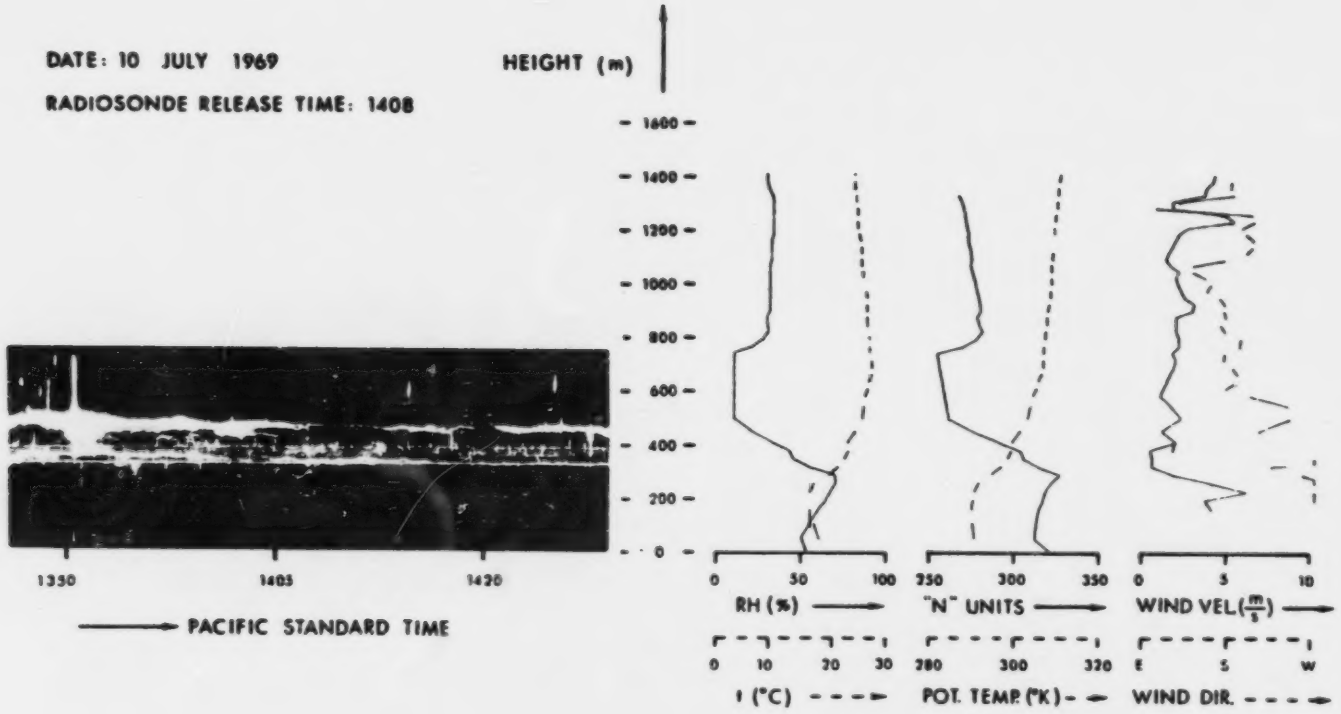

SIMULTANEOUS RADAR AND RADIOSONDE SOUNDINGS LOCATION: 32°42' N. LAT., 117° 13' W. LONG., 31 m ABOVE MSL

Figure 8.6--Insect returns from FM-CW radar at San Diego with associated meteorological profiles.

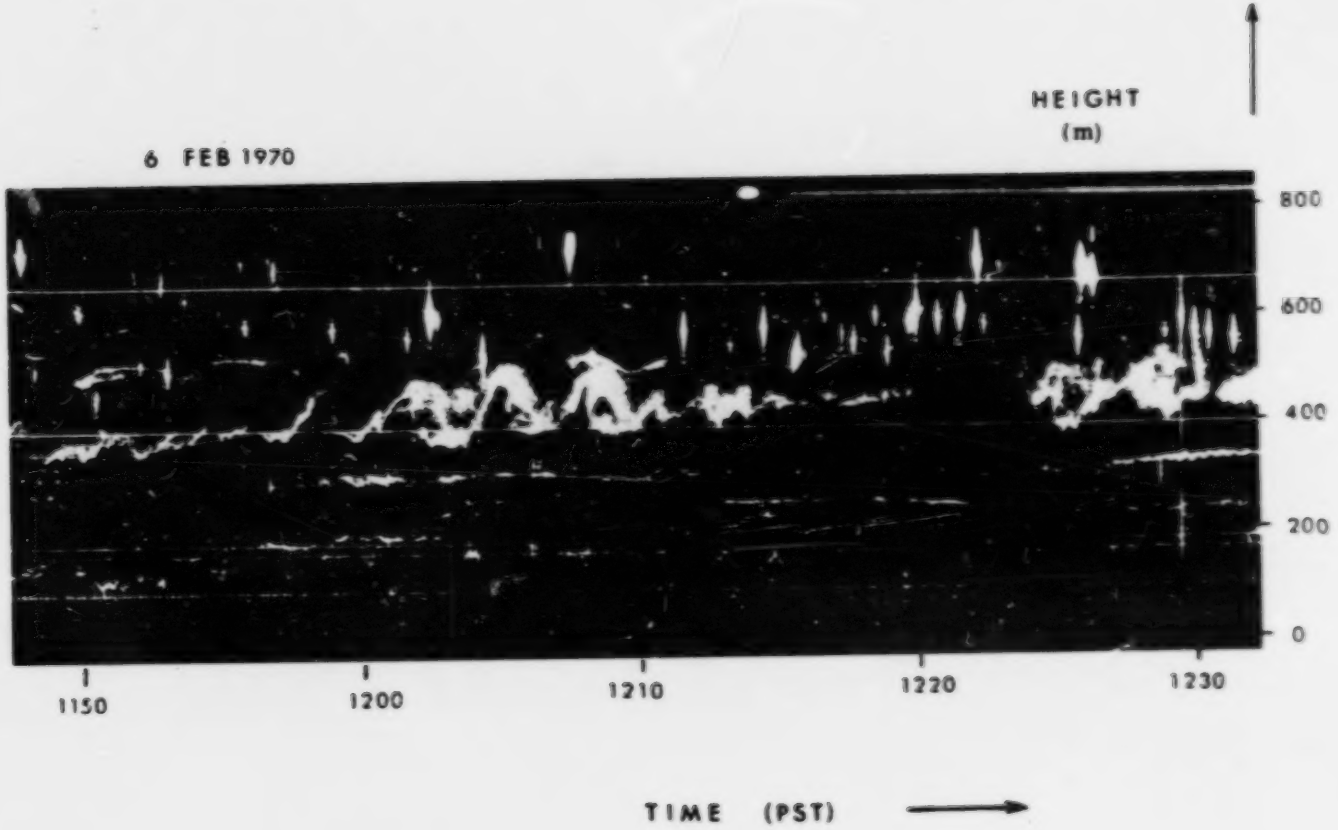

Figure 8.7--Examples of insects (point and streak targets) concentrated above an inversion layer characterized by Kelvin-Helmholtz waves (see Gossard and Hooke, 1975).

BEST DOCUMENT AVAILABLE

CHAPTER 9 - BOUNDARY LAYER STRUCTURE AND RADAR REFRACTION, DUCTING AND SCATTERING

9.1 Introduction

The curvature of rays in two dimensions is proportional to the gradient of refractive index transverse to the propagation direction. If the ray is propagating nearly horizontally, its curvature is nearly equal to dn/dz where z is height and n is refractive index. Because n is very close to unity for both optical and microwaves, it is common to define a quantity $N = (n-1) \times 10^6$ in order to avoid handling many digits. The quantity N depends on temperature, humidity and pressure (see Eq. 1-12) and decreases with height in the earth's atmosphere. Since its height gradient is negative, horizontal rays in the atmosphere are bent downwards. When they curve downward by an amount equal to the earth's curvature they are said to be trapped or ducted. The duct thickness or duct height (see Fig. 9-1) occurs where $(dN/dz) \times 10^{-6} = -z/a$, where a is the earth's radius.

In the boundary layer the height profiles of temperature and humidity are approximately logarithmic. Therefore, over the ocean where evaporation is occurring, so that humidity decreases with height, the gradient of N will exceed the ducting gradient near the sea surface. If this height is sufficiently great compared with wavelength, the waves will be trapped and propagation well beyond the horizon can occur. Over water surfaces this boundary layer phenomenon is often referred to as the "evaporation duct." However, a similar phenomenon commonly occurs over land due to the increase of temperature with height in nocturnal radiation inversions.

The evaporation ducting phenomenon seems to have been first reported formally by Katzin et al. (1947). Subsequently it has been periodically investigated with some vigor (e.g., Anderson and Gossard, 1953; Jeske, 1965; Richter et al., 1973). An example of the effect of the duct on the trapping of radio waves of 3 cm wavelength, when a crucial ducting condition, here represented by the quantity χ, is reached, is shown in Fig. 9-1. An example of the way in-situ profiles of refractive index are modified by passage over a sea surface is shown in Fig. 1-23 taken from Craig (1946). Its effects are sometimes optically spectacular as shown in Fig. 1-32, but Fig. 1-33 shows that the profiles resulting from the over-water modification are drastically different in this case from those observed by Craig.

BEST DOCUMENT AVAILABLE

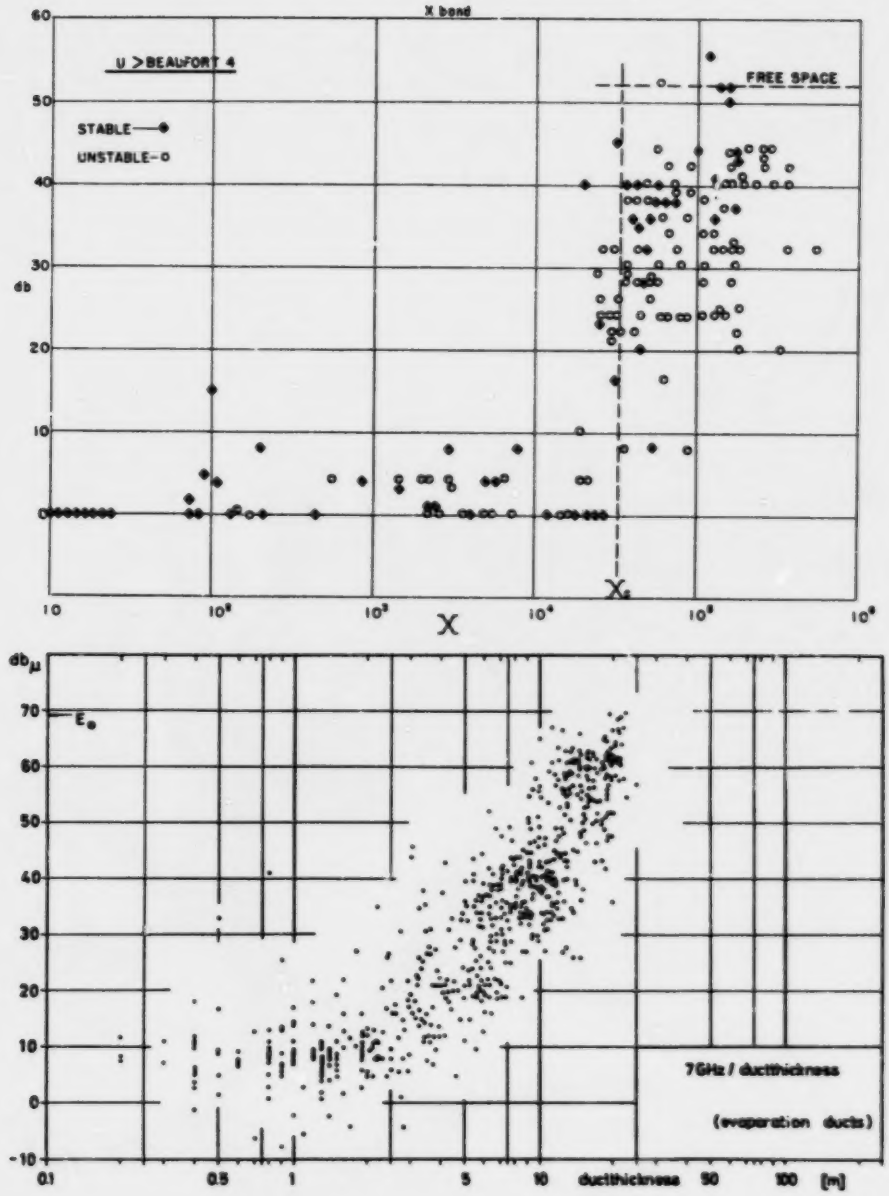

Figure 9.1--Example of enhance beyond-the-horizon signals on over water paths in the presence of strong air-sea contrast in temperature and humidity. Top frame: Received power over Cardigan Bay in the U.K. for a 3 cm wavelength path vs. a ducting parameter that depends on wavelength, thickness of duct and air-sea contrast in refractive index (from Anderson and Gossard, 1953). Bottom frame: Received power vs. duct thickness defined by the condition dM/dz = 0 (see text) for a 7 GHz path over the North Sea (from Jeske, 1965).

BEST DOCUMENT AVAILABLE

The corresponding phenomenon during radiational cooling at night is very well illustrated by Fig. 9-2 taken from Day and Trolese (1950). The lower frame shows how profiles of temperature (as represented by the quantity B, Eq. (1-15) are modified to produce a ducting condition after sunset. The upper frames show the onset of ducting on 5 microwave frequencies for various combinations of transmitter and receiver heights within and above the duct.

It is awkward to plot curved rays above a curved earth. It is usually more satisfactory to "map" the ray diagram into a frame in which the earth's surface is flat and the rays are given an appropriate relative upward curvature. Then horizontal rays that are just trapped appear as straight lines, while more super refractive rays are bent downward and less refracted rays are bent upward. This is accomplished by using a modification of the refractive index called M where

$$M = N + \frac{z}{\bar{a}} \times 10^6 = N + 0.157\ z \qquad (9\text{-}1)$$

where $\bar{a} = 6.371 \times 10^6$ meters and z is in meters. When $\partial M/\partial z = 0$, a horizontally propagating wave is just trapped; i.e., it follows the curvature of the earth.

Another refractive index parameter called potential refractive index (ϕ) is most useful for reasoning about the behavior of refractive index in a dynamic atmosphere; especially the boundary layer. It is approximately given by $\phi = M - 0.13\ z$ where z is in meters. The profiles of the various refractive index parameters are shown schematically in Fig. 1-17. All three

BEST DOCUMENT AVAILABLE

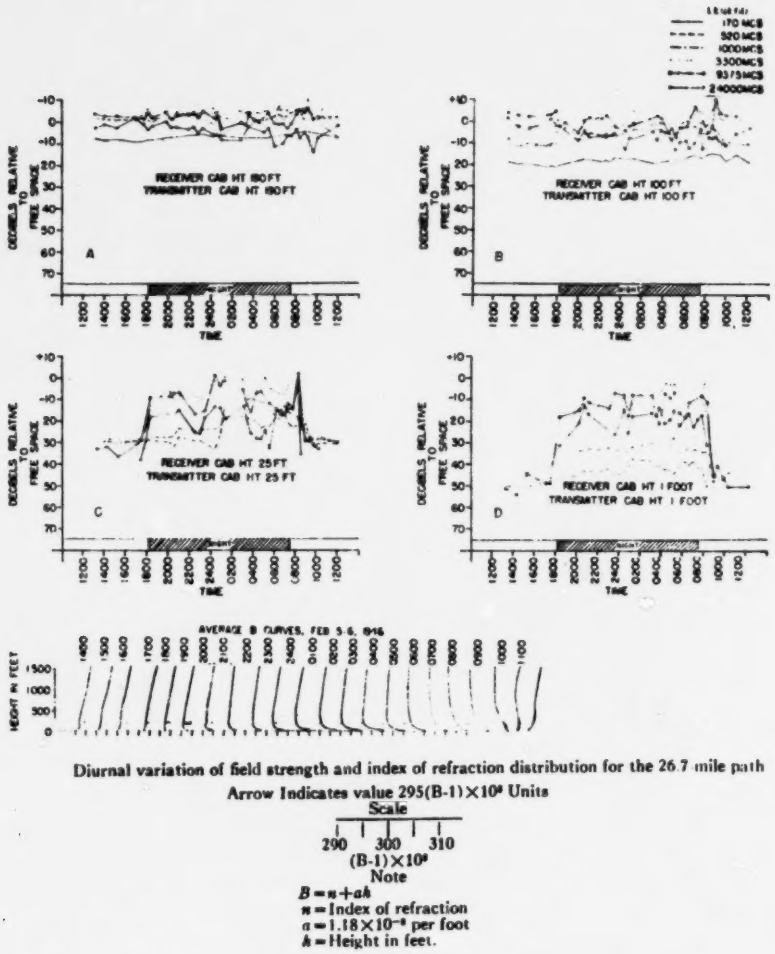

Diurnal variation of field strength and index of refraction distribution for the 26.7 mile path

Arrow Indicates value $295(B-1)\times10^6$ Units

Scale

290 300 310

$(B-1)\times10^6$

Note

$B = n + ah$

n = Index of refraction

$a = 1.18\times10^{-6}$ per foot

h = Height in feet.

Figure 9.2--Example of enhanced beyond-the-horizon signals on an over land path at several frequencies resulting from radiational cooling of the surface at night reported by Day and Trolese (1950). The refractive index parameter B is given by Eq. (1-15).

concepts will be useful in considering the refractive and scattering behavior of microwaves in the planetary boundary layer.

The potential refractive index, ϕ, is important because motions can be considered to take place adiabatically for the temporal and spatial scales relevant to the boundary layer. It is defined by replacing the temperature and vapor pressure in Eq. 1-12 by the potential temperature θ and potential vapor pressure e_p and referring the refractive index to a reference pressure level of 1000 millibars. Then

BEST DOCUMENT AVAILABLE

$$\phi = \frac{77.6}{\theta} \left(1000 + \frac{4810\ e_p}{\theta}\right) \qquad (9\text{-}2)$$

where

$$\theta = T \left(\frac{1000}{p}\right)^{R/c_p} \quad , \quad e_p = e \left(\frac{1000}{p}\right) . \qquad (9\text{-}3a,b)$$

The relationships between the various refractive index parameters and their schematic behavior in the boundary layer is summarized in Fig. 1-17 of Chapter 1. The relationships between refractive index quantities written in N(z) and those in $\phi(z)$ are developed in Appendix B.

9.2 Refractive Index Structure of the Boundary Layer

Important effects of boundary layer structure on radio and radar propagation have been recognized for decades, but the subject has taken on new interest with the new technology that makes possible the sensing of winds in the clear air. Earlier work emphasized the radio refractive effects of the boundary layer while more recent interest has centered on the scattering and scintillation resulting from the turbulent refractive structure and its temporal and spatial distribution.

By analogy with the stress exerted by a nonturbulent fluid on a bounding surface, it is common to represent the shearing stress τ exerted by a turbulent flow on a lower boundary as

$$\tau = \rho K \frac{du}{dz} \qquad (9\text{-}4)$$

where K is a turbulent "eddy viscosity," ρ is density of the fluid, u is the fluid velocity in (say) the x direction and z is the direction perpendicular to x. The x direction will be considered to lie in the horizontal plane while z is vertical. The shearing stress τ is, by definition, $\rho\ \overline{u'w'}$ where u' and w' are the turbulent perturbations of velocity in the x and z directions, respectively. It is therefore possible to interpret τ as the flux of u momentum in the z direction in the boundary layer. In a horizontally uniform steady flow over a nonrotating earth, it is physically implausible for momentum to accumulate at any height under steady state conditions so it is commonly assumed that the flux of momentum (and other passive properties) is constant in the atmospheric surface layer, i.e., τ = constant. When assumptions of steady state or horizontal homogeneity are invalid, the vertical fluxes of properties are not constant even in the surface layer. The

BEST DOCUMENT AVAILABLE

quantity $(\tau/\rho)^{1/2}$ has the dimensions of velocity and is commonly called the friction velocity; so $u_*^2 = -\overline{u'w'}$.

Generalizing the classical logarithmic profile of wind applicable under neutral stability conditions, assume

$$\frac{du}{dz} = \frac{u_*}{k_o z}\left(1 + \alpha \frac{z}{L}\right) , \tag{9-5}$$

where $k_o \simeq 0.4$ is von Karman's constant and the length

$$L = \frac{u_* \theta (du/dz)}{g k_o (d\theta/dz)} \tag{9-6}$$

is a measure of the thermal stability where $\theta = T(1000/p)^{R/c_p}$ is potential temperature, $R = 2.87 \times 10^6$ erg g^{-1} deg^{-1} is the gas constant for dry air, and $c_p = 1.004 \times 10^7$ erg g^{-1} deg^{-1} is the specific heat at constant pressure.

Integrating Eq. (9-2) yields

$$u = \frac{u_*}{k_o}\left[\ln \frac{z}{z_o} + \alpha \frac{z - z_o}{L}\right] \tag{9-7}$$

which is the log-linear profile proposed by Monin and Obukov (1954). Under neutral and stable conditions, this profile is valid up to heights of 100 to 200 meters. Under strongly unstable conditions it should not be considered valid much above 10 meters.

In like manner

$$e_p(z) - e_{ps} = - e_p^*\left[\ln \frac{z}{z_o} + \alpha_e \frac{z - z_o}{L}\right] \quad \text{and} \tag{9-8}$$

$$\theta(z) - \theta_s = - \theta_*\left[\ln \frac{z}{z_o} + \alpha_\theta \frac{z - z_o}{L}\right] . \tag{9-9}$$

Eqs. (9-6) and (9-7) define constants e_p^* and θ_* for potential vapor pressure and potential temperature whose role is similar to that of u_*. The constant of integration z_o is related to the surface roughness. Best estimates of z_o are given in Table 9-1. It is very small compared with those z of interest, and may for practical purposes be ignored in the second term in parentheses. The gradient Richardson number is defined as

BEST DOCUMENT AVAILABLE

Table 9-1. Roughness parameter for various typical surfaces

Surface	z_o (cm)
Sea surface	0.001
Mud flats, smooth ice	0.001
Sun-baked sandy alluvium (level desert, India)	0.03
Sand	0.04 - 0.06
Lawn (1 cm grass length)	0.10
Lawn (1.5 cm grass length)	0.20
Natural snow surface	0.20 - 0.50
Lawn (3 cm grass length)	0.60 - 0.80
Lawn (5 cm grass length)	1.0 - 2.0
Downland (winter)	1.0 - 2.0
Fallow land	2.0 - 3.0
Russian steppe	2.0 - 3.0
Downland (summer)	2.0 - 4.0
Open grass land	3.0 - 4.0
Long grass (60-70 cm length)	4.0 - 9.0
Wheat field	4.5
Turnip field	6.5
Fully grown root crops	14.0

$$Ri = \frac{g}{\theta} \frac{d\theta/dz}{(du/dz)^2} \quad . \tag{9-10}$$

It is a dimensionless number describing the balance between the stabilizing influence of thermal stratification and the destabilizing influence of wind shear. It is the ratio of the relative work being done against buoyancy to the mechanical energy production potential of the environmental shear. Substituting the derivatives of the log-linear relationships into the expression for Richardson number, and assuming $\alpha = \alpha_\theta = \alpha_e$, it follows that

$$Ri = \frac{z/L}{1 + \alpha z/L} \quad , \quad \frac{z}{L} = \frac{Ri}{1 - \alpha Ri} \quad . \tag{9-11a,b}$$

Expression (9-3) for L is only exactly equal to the classical Monin-Obukov length when $K = K_\theta$, but it is the quantity of most interest and most investigators conclude that $K \simeq K_\theta \simeq K_e$.

From Eq. (9-4) and Eq. (9-5) it follows that

BEST DOCUMENT AVAILABLE

$$K/u_* = k_o z/(1 + \alpha\, z/L) \tag{9-12}$$

or using Eq. (9-11b) an alternate expression is

$$K/u_* = k_o\, z(1 - \alpha\, Ri). \tag{9-13}$$

Estimates of α range from 0.6 to 8. Deacon (1962) recommends 4 and Businger et al. (1971) find 4.7. In this paper a value of 4.7 will be used.

The relationship between potential refractive index and height is developed in Appendix C. From Eq. 9-2,

$$\phi = e^{0.714z/H}\,[N(1 - 0.286\,\tfrac{z}{H}) + 71.95\,\tfrac{z}{H}\,e^{-z/H}] \tag{9-14}$$

$$\phi \simeq e^{0.714z/H}\,[N - 0.286\,N\,\tfrac{z}{H} + 71.95\,\tfrac{z}{H}] \quad \text{for } z << H.$$

Low in the atmosphere the last two terms in the braces cancel almost exactly, so

$$\phi \simeq N(1 + 0.714\,\tfrac{z}{H})\ . \tag{9-15}$$

Therefore, from

$$\phi = M\,(1 + 0.714\,\tfrac{z}{H}) - \tfrac{z}{a} \times 10^6 - 0.714 \times 10^6\,\tfrac{z^2}{a\,H} \quad ---$$

$$\phi \simeq M - 0.13\,z \tag{9-16}$$

for small z, if typical values of M = 300 and H = 8 km are chosen.

Therefore, in an adiabatic atmosphere in which $d\phi/dz = 0$, $dM/dz = 0.13\ (m^{-1})$ or $0.039\ (ft^{-1})$. On the other hand, ducting occurs when $dM/dz = 0$, or

$$\frac{d\phi}{dz} = -\,0.13\ (m^{-1}). \tag{9-17}$$

From Eq. (9-2)

$$\frac{\partial\phi}{\partial z} = -\,77.6\,[1000 + 9620\,\tfrac{e_p}{\theta}]\,\frac{1}{\theta^2}\,\frac{\partial\theta}{\partial z} + 4810\,\frac{1}{\theta^2}\,\frac{\partial e_p}{\partial z}\ . \tag{9-18}$$

BEST DOCUMENT AVAILABLE.

If θ and e_p have the same functional height dependence, it is clear that ϕ will closely approximate the same function because the coefficients and θ vary over only a small percent of their magnitude in the boundary layer. Then

$$\phi(z) - \phi_s = \phi_* [\ell n(z/z_o) + \alpha z/L] \tag{9-19}$$

where

$$\phi_* = \frac{(\phi_r - \phi_s)}{\ell n \frac{z_r}{z_o} + \alpha \frac{z_r}{L}} \equiv \frac{\phi_r - \phi_s}{\ell n \frac{z_r}{z_o} + \frac{\alpha \, Ri_r}{1 - \alpha \, Ri_r}}$$

where the subscript r applies to a reference level at which measurements can be made and s applies to the surface level $z = z_o$. Therefore,

$$M(z) - M_s = \frac{M_r - M_s - 0.13\, z_r}{\ell n \frac{z_r}{z_o} + \frac{z_r}{L}} \left[\ell n \frac{z}{z_o} + \frac{z}{L}\right] + 0.13\, z \tag{9-20}$$

where $M_r - M_s - 0.13\, z_r = \phi_r - \phi_s$.

Solving for the height d of the duct, at which $dM/dz = 0$, we find

$$d = - \left[\frac{0.13 \left(\ell n \frac{z_r}{z_o} + \alpha \frac{z_r}{L}\right)}{\phi_r - \phi_s} + \frac{\alpha}{L} \right]^{-1} \tag{9-21}$$

where d, z_r and L are in meters.

The first term within the braces is negative yielding typically a positive duct thickness. Note that the meaning of d is that a ray launched horizontally at that height will just follow the curvature of the earth. It does not necessarily mean that radio waves are trapped regardless of frequency. Radiation with wavelengths very short compared with d will be trapped; wavelengths comparable to d or longer will leak energy from the guide. To judge the effectiveness of the guide for trapping radar waves, wave guide theory must be employed (e.g., Budden, 1961).

Although there is more physical basis for the log-linear profiles, power law profiles can be used to describe the distribution of properties in the boundary layer with considerable accuracy. The interest in power law profiles lies in the fact that analytic solutions of the diffusion equation can

BEST DOCUMENT AVAILABLE

be found for a variety of cases of interest. The power law solutions for the steady, horizontally homogeneous case will now be compared with Eqs. (9-19), (9-20) and (9-21).

If it had been assumed that u, θ, and e_p obey power laws rather than the log-linear function, say

$$\phi - \phi_s = \frac{\phi_r - \phi_s}{z_r^m} z^m = b_2 z^m, \quad u = \frac{u_r}{z_r^m} z^m \equiv bz^m, \quad \theta - \theta_s = \frac{\theta_r - \theta_s}{z_r^m} z^m = b_1 z^m, \tag{9-22}$$

it follows that

$$\frac{d\phi}{dz} = mb_2 z^{m-1}, \quad \frac{du}{dz} = mb z^{m-1}, \quad \frac{d\theta}{cz} = mb_1 z^{m-1}, \tag{9-23}$$

and from Eqs. (9-1) and (9-23) that

$$\frac{K}{u_*} = \frac{u_*}{bm} z^{1-m}. \tag{9-24}$$

The power law profile for M is readily found from Eqs. (9-16) and (9-22) to be

$$M - M_s = (M_r - M_s - 0.131 z_r) \left(\frac{z}{z_r}\right)^m + 0.131 z. \tag{9-25}$$

Again setting dM/dz = 0 at the height d, we find

$$d = \left[- \frac{0.131 z_r^m m^{-1}}{M_r - M_s - 0.131 z_r} \right]^{\frac{1}{m-1}} \tag{9-26}$$

for a duct whose refractive index distribution can be adequately represented by a power law. The dependence of duct thickness on L and on m is shown in Fig. 9-3 for comparison. Regardless of the profile chosen, the crucial measurable is the difference in refractive index between the air and sea surface. Using ship meteorological observations in the Near East and Southeast Asia areas the refractive index differences between sea-surface and bridge height were calculated and reported by Gossard (1957). The refractive index was presented in terms of the quantity B related to ϕ as $B = \phi + .012z$ where z is in meters (see Fig. 1-17). The correction to convert from $B_s - B_b$ as given to $\phi_s - \phi_b$ is easily made if an average bridge height, indicated b

BEST DOCUMENT AVAILABLE

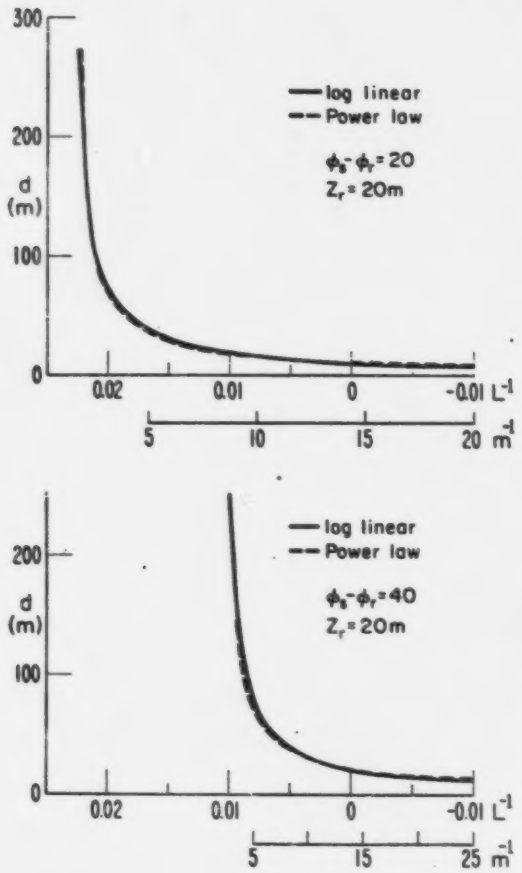

Figure 9.3--How surface evaporation duct thickness depends on atmospheric stability for a log linear model (upper frame) in which the height of measurement, z_r = 20 m, the roughness parameter z_o = 0.001 cm and β = 4.7 and for a corresponding power law model (lower frame) in which $\phi - \phi_s = (\phi_r - \phi_s)(Z/Z_r)^m$. Thermal stability enters through the Monin-Obukov length L in the log linear model and through m in the power law model (from Gossard, 1978).

subscript "b," is assumed. Under high wind conditions thermal stability is nearly neutral because wind shear appears squared in the denominator of the Richardson number. Under these conditions the profile of ϕ can be considered to be logarithmic and this was the case about 85% of the time in the areas analyzed. Then the duct height in meters is just

$$d = -7.7 \frac{\phi_s - \phi_b}{\ln \frac{z_b}{z_o}} .$$

Other climatological studies of duct height in special areas have been reported by Hitney (1973) and Jeske (1965). Generally, there is good agreement between duct thickness calculated from (9-26) and radar trapping conditions over the Carribean/Florida region, and over the North Sea. There is sometimes good agreement in the Mediterranean in some climatological regimes. It often fails badly in some coastal lang-sea flow regimes, such as southern California, because low elevated layers may completely dominate the propagation conditions.

BEST DOCUMENT AVAILABLE

9.3 Structure Parameter of Refractive Index in the Boundary Layer

In radio and bistatic radar forward scatter and in radar backscatter the important characteristic of the clear air is the spatial spectrum of turbulent fluctuations in the radio refractive index. The quantity most commonly used to describe this characteristic is the structure constant or structure parameter generally designated C_n^2. The relationships of the turbulence parameters to the atmospheric budget equations are summarized in Appendix E.

In the following an inertial subrange in the turbulence spectrum of wind will be assumed to exist, so that the energy distribution is given by (e.g., Lumley and Panofsky, 1964)

$$E(k) = a' \varepsilon^{2/3} k^{-5/3} \tag{9-27}$$

where a' is a universal constant, ε is the turbulent mechanical energy dissipation rate and is also the (constant) rate of transfer of energy downward in scale through the spectrum toward higher wavenumbers k. For any other passive additive scalar, say ϕ, the quantity corresponding to E is (Corrsin, 1951)

$$E_\phi = a\varepsilon^{-1/3} \varepsilon_\phi k^{-5/3} \tag{9-28}$$

where E_ϕ is the rate of destruction of variance of ϕ (actually $\overline{\phi^2}/2$).

Alternatively, the turbulence can be described in terms of a structure function

$$D(\ell) = C_\phi^2 \ell^{2/3} . \tag{9-29}$$

The structure parameter C_ϕ^2 is given according to Ottersten (1969), by

$$C_\phi^2 = 2.8 \varepsilon^{-1/3} \varepsilon_\phi \tag{9-30}$$

whence

$$E_\phi = (a/2.8) C_\phi^2 k^{-5/3}. \tag{9-31}$$

For the case of a one-dimensional spectrum of temperature, Wyngaard et al. (1971) find $a_1 = 0.8$. The constant appearing in the structure constant is

BEST DOCUMENT AVAILABLE

about 4 times this, so their result implies a factor of 3.2. It is important to note that their constant is based on rate-of-destruction of $\overline{\theta'^2}/2$ rather than $\overline{\theta'^2}$. Therefore, the appropriate constant to compare with Ottersten's is 1.6 vs. 2.8. Here we arbitrarily use 2.8.

Potential temperature, potential vapor pressure, and potential refractive index can all be considered passive scalars when the turbulent mixing takes place adiabatically. The quantity C_ϕ^2 can be used to describe the intensity of turbulent fluctuations in refractive index and therefore to characterize the radar backscatter to be expected from the clear air.

The turbulent energy budget equation is (e.g., Lumley and Panofsky, 1964)

$$\frac{d(\overline{u^2}/2)}{dt} = - \overline{u'w'} \frac{\partial u}{\partial z} + \frac{g}{\theta} \overline{\theta'w'} - \varepsilon + \frac{\partial}{\partial z} (\overline{w'u'^2}) \qquad (9\text{-}32)$$

and the budget equation for $\overline{\phi^2}$ is

$$\frac{d(\overline{\phi^2}/2)}{dt} = - \overline{\phi'w'} \frac{\partial \phi}{\partial z} - \varepsilon_\phi \, . \qquad (9\text{-}33)$$

When the turbulent energy is not changing with time, or is changing only very slowly, and when the gradient of the vertical transport of energy is negligible as in the regime of forced convection,

$$\varepsilon = - \overline{u'w'} \frac{\partial u}{\partial z} (1 - R_f) \qquad (9\text{-}34)$$

where R_f is the flux Richardson number defined as

$$R_f = (g/\theta) \overline{\theta'w'}/\overline{u'w'} \frac{du}{dz} = (K_h/K_m)Ri. \qquad (9\text{-}35)$$

Primes denote deviations from the ambient (unprimed) quantity. Overbars denote means. The quantities K_h and K_m are the eddy diffusion coefficients of heat and momentum, respectively, and their ratio can usually be assumed to be approximately unity. The gradient Richardson number, Ri, is the quantity most easily measured and the one to be considered here. In Eq. (9-34), terms involving flux divergence have been assumed negligible. This is justifiable in the range $0.3 > Ri > -0.1$ (Wyngaard and Coté, 1971; Fig. 2).

The corresponding steady state balance equation for rate of destruction of variance of ϕ (really $\overline{\phi^2}/2$) is

BEST_DOCUMENT AVAILABLE

$$\varepsilon_\phi = - \overline{\phi' w'} \frac{\partial \phi}{\partial z} . \qquad (9\text{-}36)$$

Recalling that, by definition,

$$u_*^2 = - \overline{u' w'} = K \frac{\partial u}{\partial z} , \qquad (9\text{-}37)$$

and

$$- \overline{\phi' w'} = K \frac{\partial \phi}{\partial z} \qquad (9\text{-}38)$$

and substituting Eqs. (9-34) and (9-36) into Eq. (9-33), we find

$$C_\phi^2 = 2.8 \, [u_*/|\partial u/\partial z|]^{4/3} \, (1\text{-}Ri)^{-1/3} \, (\partial \phi/\partial z)^2 \qquad (9\text{-}39a)$$

$$= 2.8 \, (K/u_*)^{4/3} \, (1\text{-}Ri)^{-1/3} \, (\partial \phi/\partial z)^2 . \qquad (9\text{-}39b)$$

Equation (9-10) shows that K/u_* does not depend on wind speed or shear except implicitly through Ri. If it is assumed that the height distributions of θ and e_p are log-linear in accord with Eqs. (9-5) and (9-6), ϕ is given by Eq. (9-19). If ϕ_r is the potential refractive index at some reference height z_r,

$$\phi_* = \frac{\phi_r - \phi_s}{\ell n \frac{z_r}{z_o} + \alpha \frac{z_r}{L}} \equiv \frac{\phi_r - \phi_s}{\ell n \frac{z_r}{z_o} + \frac{\alpha Ri_r}{1 - \alpha Ri_r}} .$$

From Eq. (9-21) and Eq. (9-7b)

$$\frac{\partial \phi}{\partial z} = \frac{\phi_*}{z} \left(1 + \alpha \frac{z}{L}\right) \quad \frac{\phi_*}{z(1-\alpha Ri)} \qquad (9\text{-}40)$$

so from Eqs. (9-40), (9-39b), and (9-10)

$$C_\phi^2 = 2.8 \, \phi_*^2 \, k_o^{4/3} \, (1\text{-}\alpha Ri)^{-2/3} \, (1\text{-}Ri)^{-1/3} \, z^{-2/3} . \qquad (9\text{-}41)$$

Using dimensional reasoning, Wyngaard et al. (1971) conclude that the optical refractive index structure constant is given by

$$C_n^2 = f_3(Ri) \, z^{4/3} \, (d\theta/dz)^2 \qquad (9\text{-}42)$$

where f_3 is completely determined by Ri. Combining Eq. (9-10) with Eq. (9-39)

$$C_\phi^2 = a \, k_o^{4/3} \, (1\text{-}\alpha Ri)^{4/3} \, (1\text{-}Ri)^{-1/3} \, z^{4/3} \, (d\phi/dz)^2 . \qquad (9\text{-}43)$$

BEST DOCUMENT AVAILABLE

If ϕ is determined by temperature alone, it is readily seen that

$$f_3(Ri) \equiv a\, k_o^{4/3}\, (1-\alpha Ri)^{4/3}\, (1-Ri)^{-1/3}. \qquad (9\text{-}44)$$

Businger et al. (1971) find $\alpha = 4.7$ from data collected at Liberal, Kansas and Wyngaard et al. (1971) find that $a = 3.2$. If these constants are inserted into Eq. (9-44) assuming $k_o = 0.4$, and the result compared with the plot of f_3 by Wyngaard et al., the curves are not separable on this scale of plot in the domain of $Ri > 0$. It may therefore be concluded that the function (9-44) derived from the energy and temperature balance equations, fits the empirical result of Wyngaard et al. satisfactorily under stable conditions.

Under unstable conditions Eq. (9-44) becomes invalid for $Ri < -0.1$. This is understandable, because the important terms in the balance equation are then different; the shear term becomes unimportant and is dominated by the energy flux divergence in Eq. (9-32).

In the unstable region Wyngaard et al. find, from the Kansas data, that

$$C_\phi^2 = k_o^2\, \phi_*^2\, z^{-2/3}\, g\,(z/L) \qquad (9\text{-}45)$$

where $g(z/L) = 4.9\,[1 - 7\,(z/L)]^{-2/3}$ and z/L is related to Ri through Eq. (9-8). Plots of C_ϕ vs. height are shown as the solid curves in the lower frame of Fig. 9-4 using Eqs. (9-41) and (9-45). Under unstable conditions L is negative. When $-7(z/L) \gg 1$

$$C_\phi^2 \simeq 35\, k_o^2\, \phi_*^2\, (-L)^{2/3}\, z^{-4/3}. \qquad (9\text{-}46)$$

This -4/3 power law is commonly observed under sunny conditions when mild instability exists. Tsvang (1969) reports the law to hold to heights of 100-500 m.

In the presence of a capping inversion, Frisch and Ochs (1975) suggest that Eq. (9-45) be modified by a factor G which is a function only of the dimensionless quantity z/z_i where z_i is the height of the capping inversion. They find

$$G(z/z_i) = 1.0 + 0.84\, z/z_i + 4.13\, (z/z_i)^2 \text{ for } 0 \leq z/z_i < 0.8.$$

The dashed curves in Fig. 9-4 are the modified profiles using Eq. (9-47) assuming $z_i = 500$ m.

BEST_DOCUMENT AVAILABLE

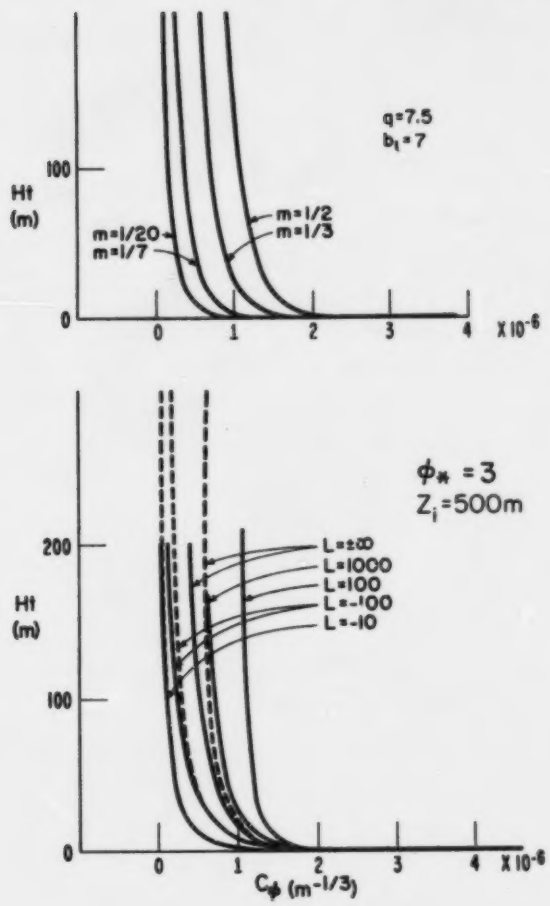

Figure 9.4--Height distribution of C_ϕ within the surface evaporation duct for the log linear model (bottom frame) assuming $\phi_* = 3$, $z_o = 0.001$ cm and $\beta = 4.7$ and for a power law profile (top frame) with the characteristics shown in the legend (from Gossard, 1978).

If it had been assumed that u, θ and e_p had obeyed power laws instead of the log-linear function the relations (9-22) and (9-24) substituted in (9-39b) would give

$$C_\phi^2 = 3.2\, m^{2/3}\, (u_*/b)^{4/3}\, (\phi_r - \phi_s)^2\, z_r^{-2m}\, (1 - Ri)^{-1/3}\, z^{(2/3)(m-1)} \quad (9\text{-}48)$$

where $Ri = (g/\theta)(b_1/b^2\, m)\, z^{1-m}$. Appropriate values of m depend on conditions of thermal stability. The coefficient b_1 in Ri has negligible influence on C_ϕ because (1-Ri) is raised to a small power. The important stability dependence enters through m. Curves of C_ϕ vs. height for several m are shown in the top frame of Fig. 9-4 for comparison with the log-linear solutions, and their similarity is clear.

BEST DOCUMENT AVAILABLE

CHAPTER 10 - BOUNDARY LAYERS UNDERGOING MODIFICATION

10.1 Introduction

With modern high speed computers, equations such as (9-32) and (9-33), along with equations relating higher order products of their variables, can be solved more or less rigorously if various closure assumptions are granted. These techniques have usually been applied to the development of the daytime convective boundary layer. For a few examples see Deardorff (1974a,b), Wyngaard and Coté (1974), Mellor and Yamada (1974), Zeman and Lumley (1976) and Burk (1977). These approaches involve minimal approximations in the solution and are particularly valuable for research in atmospheric dynamics and kinematics. However they are costly in computer time and time delays. Depending on the model chosen from the hierarchy of closure models available, the computer time can be many tens of hours for each hour of real time of the model. On the other hand, solution of the classical diffusion equation gives inexpensive and fast results that are adequate for many applications (e.g., Slade, 1968). Perhaps more important, solutions of the diffusion equation can provide guidance in determining which problems are important and worthy of more rigorous solution, as well as guidance in minimizing the cost of studies using numerical techniques by providing foreknowledge of the behavior to be expected. Therefore, the use of the classical diffusion equation in predicting some transitional effects of the atmosphere on radar and radio propagation will be briefly reviewed. In this approach it will be assumed that balance equations such as (9-34) and (9-36) apply in which the terms $d(\overline{u'^2}/2)/dt$ and $d(\overline{\theta'^2}/2)/dt$ were neglected. If these terms are compared with typical magnitudes of the rate of energy production represented by the first term on the right of Eq. (9-34), it is seen that the approximation is valid for transitional processes having a time scale longer than about a half hour (or the equivalent spatial transitional scale). The results for C_ϕ^2 should therefore not be applied to small scale or rapidly changing situations. Furthermore, it will be assumed that the atmosphere is neutral or stably stratified and that eddy transport is the dominant modification process, i.e., radiation divergence within the atmosphere is ignored.

Problems of this sort are governed by the classical "heat conduction" equation except that the eddy coefficients are functions of position. The general equation is therefore

$$\frac{d\chi}{dt} = \nabla \cdot K_\chi(x,y,z)\, \nabla\chi \qquad (10\text{-}1)$$

BEST DOCUMENT AVAILABLE

where χ may represent heat = $\rho c_p \theta$, e_p or ϕ. Expanding (10-1) in partial derivitives gives

$$\frac{\partial \chi}{\partial t} + u \frac{\partial \chi}{\partial x} + v \frac{\partial \chi}{\partial y} + w \frac{\partial \chi}{\partial z} = \frac{\partial}{\partial x}\left(K \frac{\partial \chi}{\partial x}\right) + \frac{\partial}{\partial y}\left(K \frac{\partial \chi}{\partial y}\right) + \frac{\partial}{\partial z}\left(K \frac{\partial \chi}{\partial z}\right). \qquad (10\text{-}2)$$

10.2 Spatial Transition at the Lower Boundary

Traditional Diffusion Equation Approach

If attention is confined to steady, two-dimensional horizontal flow in the x direction, w = 0 and derivitives of χ with respect to y and t are also zero. Neglecting diffusive transport in the x direction compared with advective transport Eq. (10-2) reduces to

$$u \frac{\partial \chi}{\partial x} = \frac{\partial}{\partial z}\left[K(z) \frac{\partial \chi}{\partial z}\right] . \qquad (10\text{-}3)$$

Equation (10-3) will be used to calculate the variation of radio duct thickness and refractive index structure constant with distance downwind of a transition in the lower boundary beyond which heat and/or moisture are flowing from the boundary into the air mass. Upwind of the transition the atmosphere is assumed to be homogeneous and the lower boundary has constant temperature and humidity. The situation is illustrated schematically in Fig. 10-1 where the flow is from land to water and $\chi = e_p$, θ, or ϕ. Examples of boundary layer modification of this type are shown in Fig. (10-2), taken from the Canterbury Project in New Zealand in 1947.

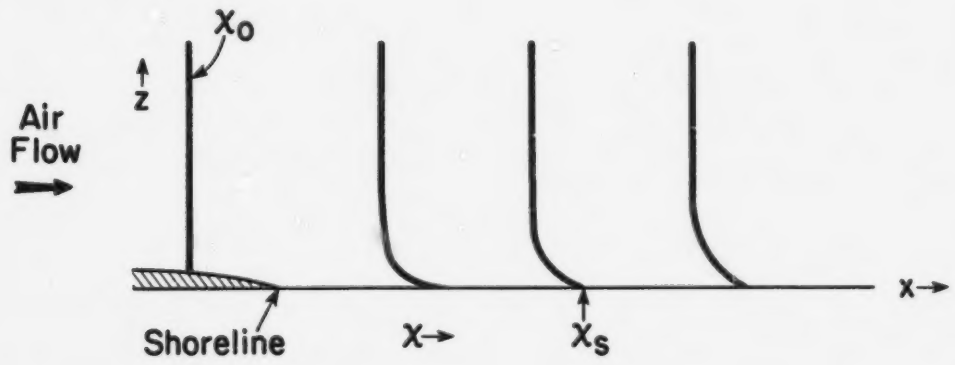

Figure 10.1--Schematic representation of modification of surface layer in neutral airmass moving offshore over cooler water surface.

BEST DOCUMENT AVAILABLE

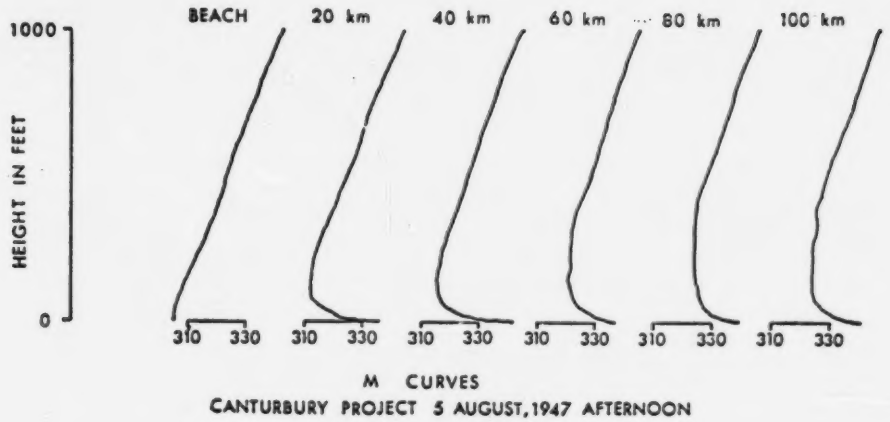

Figure 10.2--Example of modification of the surface layers of an airmass of neutral stability as it moves offshore the distances indicated. The modified refractive index M = (n-1) x 10^6 + 0.157z where n is radio refractive index and z is height in kilometers. Trapping (or ducting) of radio waves occurs where dM/dz = 0. Data from the Canterbury Project (Unwin, 1951).

The power law profile is far more tractable mathematically than the log-linear for the solution of problems of this kind. The value of χ at the lower boundary will be assumed to be a constant, χ_s, after the transition, and to be a constant χ_o prior to transition ($x < 0$).

Expressing the power law for wind in the form $u = bz^m$ and solving for K using Eq. (9-24) and inserting it into Eq. (10-3), it is found in accord with (9-22) that

$$\frac{\partial \chi}{\partial x} = az^{-m} \frac{\partial}{\partial z} \left[z^{1-m} \frac{\partial \chi}{\partial z} \right] \tag{10-4}$$

where $a = u_*^2/mb^2$ and $b = u_r z_r^{-m}$. Frost (1946) found the solution of Eq. (10-4) to be

$$\chi - \chi_o = \frac{\chi_s - \chi_o}{\Gamma\left(\frac{m}{2m+1}\right)} \int_{\zeta_o}^{\infty} \zeta^{-(m+1)/(2m+1)} \exp(-\zeta) d\zeta \tag{10-5}$$

where $\zeta = z^{2m+1}/ax\,(2m+1)^2$. This can be written in terms of the incomplete gamma function tabulated in Appendix C. Interpreting χ as ϕ and assuming $\phi_s - \phi_o = 10$, a plot of $\phi - \phi_o$ vs. $[(2m+1)^2\,\zeta]^{1/2m+1}$ is shown in Fig. 10-3. However, if the duct thickness and C_ϕ^2 distribution are of primary importance, it is not ϕ but its height gradient that is needed. From (10-5)

BEST DOCUMENT AVAILABLE

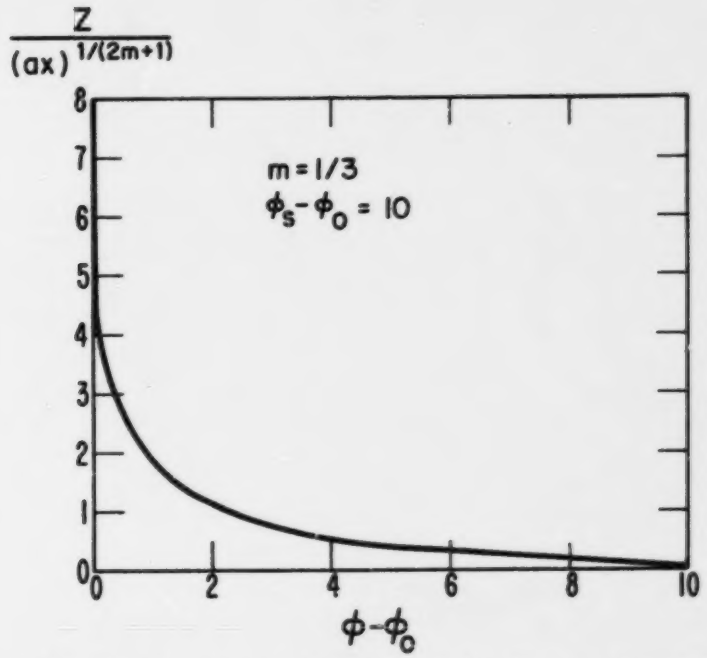

Figure 10.3--Theoretical potential refractive index distribution with height z and offshore distance x. The subscript "o" indicates the unmodified value; s indicates the (water) surface value.

$$\frac{\partial \phi}{\partial z} = (\phi_s - \phi_o) \frac{(2m+1)^{1/(2m+1)}}{\Gamma\left(\frac{m}{2m+1}\right)} \frac{z^{m-1}}{(ax)^{m/(2m+1)}} \exp[-z^{2m+1} (ax)^{-1} (2m+1)^{-2}] . \quad (10\text{-}6)$$

Substituting $\partial\phi/\partial z \approx \partial M/\partial z - 0.13$ and noting that $\partial M/\partial z = 0$ at the height at which the gradient of ϕ is just sufficient for trapping, the duct thickness $z = d$ is found. For large x, or small d^{2m+1}/ax, the exponential tends to unity, so

$$d \approx \left[\frac{0.131\ \Gamma\left(\frac{m}{2m+1}\right)(2m+1)^{-1/(2m+1)}}{(\phi_s - \phi_o)} (ax)^{m/(2m+1)} \right]^{\frac{1}{m-1}} . \quad (10\text{-}7)$$

In Fig. 10-4 the duct thickness has been plotted vs. distance assuming $u_r = 5\ m\ s^{-1}$, $z_r = 10$ m, $z_o = 0.001$ cm, $m = 1/3$ so $b = 2.32$, and $a = (u_*/b)^2/m = 0.0222$. The initial difference in refractive index between the air and the water surface was $\phi_s - \phi_o = 10$.

Examination of C_ϕ^2 reveals that the factor containing Ri in Eq. (9-39b) is near unity for a reasonable range of Ri (say $-0.5 < Ri < 0.2$) because of the small negative power (-1/3) to which the factor is raised. Therefore,

BEST DOCUMENT AVAILABLE

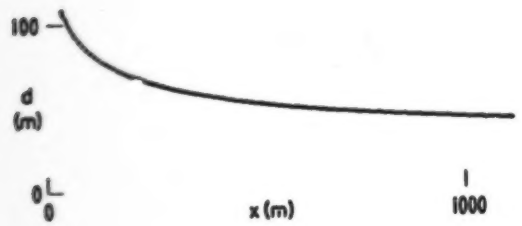

Figure 10.4--Radio duct thickness vs. distance offshore with the same assumptions as those in Fig. 10.3, i.e., $\phi_\delta - \phi_o = 10$, $m = 1/3$.

$$C_\phi^2 \simeq 3.2 \left(\frac{K}{u_*}\right)^{4/3} \left[\frac{\partial \phi}{\partial z}\right]^2 . \qquad (10\text{-}8)$$

From Eq. (10-8), using Eq. (9-24) for K/u_*, we find

$$C_\phi^2 = 3.7(\phi_s - \phi_o)^2 \left[\frac{\left(\frac{u_*}{bm}\right)^{2/3}(2m+1)^{1/(2m+1)}(ax)^{-m/(2m+1)}z^{(m-1)/3}}{\left(\frac{m}{2m+1}\right)}\right]^2 \exp\left[-\frac{z^{2m+1}}{ax(2m+1)^2}\right]. \qquad (10\text{-}9)$$

In Fig. 10-5 C_ϕ is plotted vs. height for three off-shore distances for the same conditions as those in Fig. 10-4.

Flux Integral Method

The flux integral method was first used by von Karman to obtain the velocity distribution in unstratified flow downwind of the leading edge of a flat plate in a wind tunnel. This method is valuable because it allows great flexibility in the class of physical problems that can be solved. Although well known in aerodynamics, it has received little attention in geophysics. It has been applied to radio propagation problems by Gossard (1978).

von Karman constructed the so-called momentum integral based on the Leibnitz Rule:

$$D(x) = \rho \int_0^{\delta(x)} u(u_\delta - u)dz$$

where $D(x)$ is the total drag on the plate per unit width, δ is the depth of the boundary layer above the flat plate and u_δ is the velocity of the flow outside the boundary layer (assumed to be constant both for $x < 0$ and $z > \delta$). The derivative of D with downwind distance x was then equated to the momentum flux per unit area toward the plate, assuming the flux to be independent of height for $z < \delta$ and zero above δ.

BEST DOCUMENT AVAILABLE

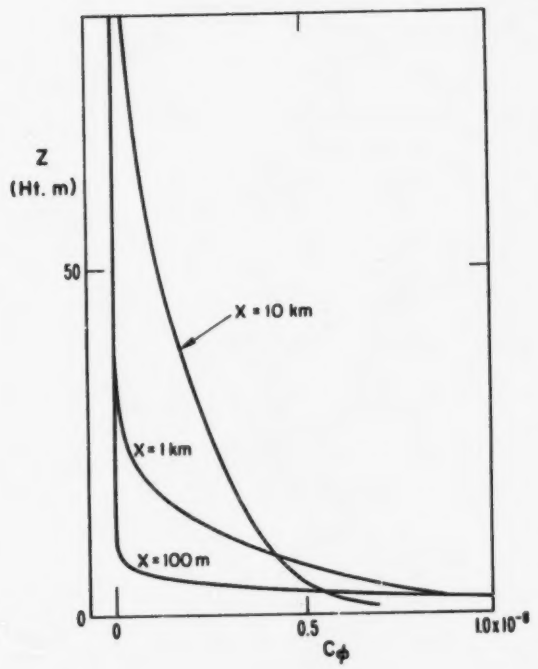

Figure 10.5--Height distribution of refractive index structure constant for three offshore distances.

The approach can be generalized for any passive quantity, i.e.,

$$M(x) = \int_0^{\delta(x)} u(\chi - \chi_o)dz \qquad (10\text{-}10)$$

where χ may be momentum density (ρu), water vapor density (ρs where s is specific humidity), heat energy density ($\rho\, c_p\, \theta$ where c_p is specific heat at constant pressure), or $\rho\phi$ where $\rho\phi$ is without physical interpretation. M(x) is the total flux from a strip of unit width, so d M(x) = F(x) dx where F is the vertical flux per unit area of momentum, water vapor, or heat respectively. For ϕ there is no comparable interpretation, but F then has dimensions of mass flux.

Analogous to (9-38),

$$F = -K(z)\partial\phi/\partial z \qquad (10\text{-}11)$$

where the sign has been chosen so that flux is upward when ϕ decreases with height. If power laws are assumed, (9-1) and (10-11) give

$$F = -(u_*/qm)z^{1-m}\partial\phi/\partial z \qquad (10\text{-}12)$$

where b in (9-22) has been written as q u_* where q is a proportionality constant. The height distribution of ϕ can be written in the form

BEST DOCUMENT AVAILABLE

$$\phi - \phi_s = (\phi_o - \phi_s)(z/\delta)^m \tag{10-13}$$

because $\phi = \phi_\delta = \phi_o$ for $x < 0$ or $z > \delta$; therefore

$$F(x) = (u_*/q)(\phi_s - \phi_o)\delta(x)^{-m} . \tag{10-14}$$

To demonstrate the method we choose the case when ϕ_s and ϕ_o are constant for comparison with the rigorous solution (10-6). Then (10-10) gives

$$F(x) = \partial M(x)/\partial x = u_* q(\partial/\partial x)(\phi_s - \phi_o) \int_o^{\delta(x)} z^m[1 - (\tfrac{z}{\delta})^m]dz$$

$$= (u_*/q)(\phi_s - \phi_o)\delta^{-m} \tag{10-15}$$

and it is readily found that

$$\delta = [(q^2 m)^{-1}(2m + 1)^2 x]^{1/(2m+1)} . \tag{10-16}$$

Substituting δ into (10-13),

$$\frac{\partial\phi}{\partial z} = (\phi_o - \phi_s)(2m + 1)^{-2m/(2m+1)} \frac{m z^{m-1}}{(ax)^{m/(2m+1)}} \tag{10-17}$$

where $a = (q^2 m)^{-1}$ as before. Ignoring the exponential factor in (10-6) (which is essentially unity for appreciable x) it is seen that (10-17) is identical to (10-6) except that the factor $(2m + 1)/\Gamma[m/(2m + 1)]$ has been replaced by m. The two factors are compared in Table 10-1 over the probable range of m. It is apparent that the approximation involved in the use of (10-10) and (10-11) is satisfactory.

Table 10-1. Comparison of $(2m + 1)/\Gamma[m/(2m + 1)]$ with m.

m	$(2m + 1)/\Gamma[m/(2m + 1)]$	m
1/7	0.15	0.147
1/5	0.20	0.200
1/2	0.55	0.500

From (10-17) and the condition $d\phi/dz = -.13(m^{-1})$ the duct thickness is readily found to be

$$d = \left[\frac{0.131}{\phi_s - \phi_o} \frac{(2m + 1)^{2m/(2m+1)}}{m} (ax)^{m/(2m+1)}\right]^{1/(m-1)} \tag{10-18}$$

BEST DOCUMENT AVAILABLE

and from (9-39b) (assuming $(1 - Ri)^{-1/6} \approx 1$ as before),

$$C_\phi^2 \approx 3.2(\phi_s - \phi_o)^2 (mq)^{-4/3} (2m + 1)^{-4m/(2m+1)} \cdot m(ax)^{-2m/(2m+1)} z^{2(m-1)/3} . \quad (10\text{-}19)$$

Equations (10-18) and (10-19) differ from (10-7) and (10-8) only in that the factor $(2m + 1)/\Gamma[m/(2m + 1)]$ has been replaced by m.

The method can be used to treat a variety of cases, and the results have been given by Gossard 1978 for:

A) Case of uniform roughness, $\phi_s - \phi_o$ = constant.
B) Case of uniform roughness, $\phi_s - \phi_o \propto x^\alpha$.
C) Abrupt transition in roughness, $\phi_s - \phi_o$ = constant.

A plot of the boundary layer thickness $\delta(x)$ is shown in Fig. 10-6, and a plot of duct thickness is shown in Fig. 10-7. The profile of C_ϕ artificially drops to zero at the height δ because in this approximation $\partial\phi/\phi z = 0$ for $z>\delta$. Of course it actually continues to decrease as $z^{(m-1)/3}$ in accord with (10-19). The Flux Integral Approximate Method can be used to solve many problems that are otherwise quite intractable (Gossard, 1978). An example is the logarithmic profile that is otherwise only solvable numerically.

Logarithmic Profiles

Suppose the profiles are assumed to obey logarithmic instead of power laws. This is the case for which (10-10) has found considerable application in aerodynamics. The fluid is then assumed to be neutral, and the distribution of momentum downwind of the leading edge of a flat plate or airfoil is typically examined. Here we use the method to examine the distribution of refractive index when the profiles of wind and refractive index follow logarithmic rather than power-law variations.

We choose ϕ_o constant and assume ϕ to be of the form

$$\phi - \phi_s = (\phi_\delta - \phi_s)[\ln(z/z_o)]/[\ln(\delta/z_o)] \quad (10\text{-}20)$$

where z_o is a small length characterizing the roughness of the surface. We further assume that

BEST_DOCUMENT AVAILABLE

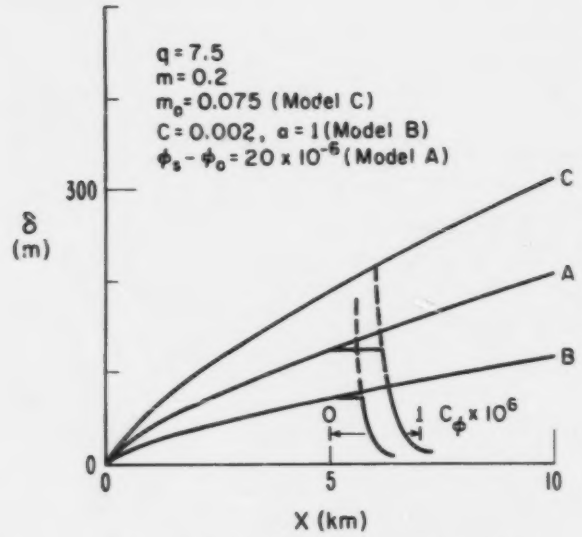

Figure 10.6--Increase in depth of boundary layer δ with distance x from transition for Models A, B, and C and the conditions indicated in legend. Profiles of C_ϕ at a distance of 5 km downwind of transition are also shown. C_ϕ artificially drops to zero above δ because of the assumption in this approximation that F = 0 above δ, i.e., $\partial\phi/\partial z = 0$ for $z > \delta$. Actually it continues to decrease as $z^{(m-1)/3}$ in accord with (10-19) shown by the dashed curves.

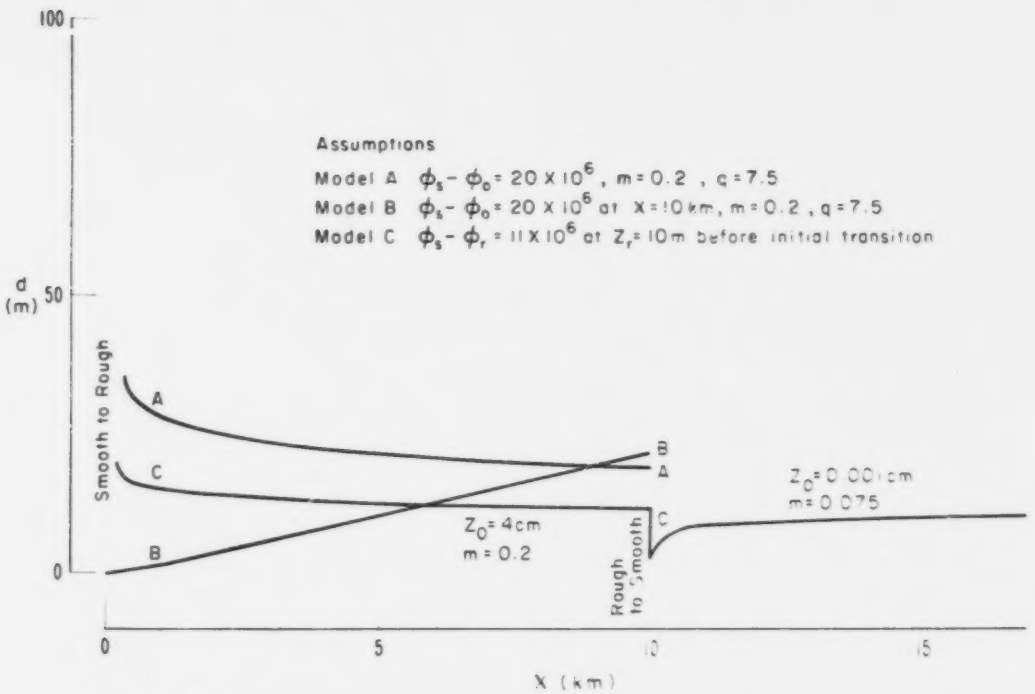

Figure 10.7--Change in radio or optical duct thickness with distance x from transition for Models A, B, and C for conditions indicated in legend. The transitions in surface roughness apply to Model C only.

BEST DOCUMENT AVAILABLE

$$u = (u_*/k_o)\ln(z/z_o)$$

where $k_o \simeq 0.4$ is von Karman's constant. Then

$$K = u_*^2/(\partial u/\partial z) = k_o u_* z \ . \qquad (10\text{-}21)$$

From (10-11),

$$F = -K\,\partial\phi/\partial z = -k_o u_*(\phi_\delta - \phi_s)/\ln(\delta/z_o) \ . \qquad (10\text{-}22)$$

Returning now to (10-10) and noting that $\phi_\delta = \phi_o$ = constant, we find

$$F = \partial M(x)/\partial x = (u_* z_o/k_o)(\phi_\delta - \phi_s)\frac{\partial}{\partial x}\int_1^{\delta/z_o} \ln(z/z_o)\ \ 1 - \frac{\ln(z/z_o)}{\ln(\delta/z_o)}\ \ d(z/z_o)$$

$$= -k_o u_*(\phi_\delta - \phi_s)/\ln(\delta/z_o).$$

Integration leads to the equality

$$(u_* z_o/k_o)(\phi_s - \phi_\delta)(\partial/\partial x)[\delta/z_o + 1 - (2\delta/z_o)/\ln(\delta/z_o) + 2/\ln(\delta/z_o)]$$

$$= k_o u_*(\phi_s - \phi_\delta)/\ln(\delta/z_o)$$

and differentiation with x gives the equality

$$\int \ln(\delta/z_o)d(\delta/z_o) - 2\int d(\delta/z_o) + 2\int d(\delta/z_o)/\ln(\delta/z_o)$$

$$- 2\int d(\delta/z_o)/(\delta/z_o)\ln(\delta/z_o) = (k_o^2/z_o)x$$

which integrates to

$$k_o^2\,\frac{x}{z_o} = \frac{\delta}{z_o}\ln\frac{\delta}{z_o} - 3\,\frac{\delta}{z_o} + 3 + 2\ln\frac{\delta}{z_o} + 2\,\frac{\ln(\delta/z_o)}{2.2!} + \frac{\ln(\delta/z_o)}{3.3!} \ \ldots \qquad (10\text{-}23)$$

so

$$k_o^2\,\frac{x}{z_o} = \frac{\delta}{z_o}\ln\frac{\delta}{z_o} - 3\,\frac{\delta}{z_o} + 3 + 2\,\mathrm{li}\,\frac{\delta}{z_o} - 2\gamma - 2\ln[\ln(\delta/z_o)] \qquad (10\text{-}24)$$

where $\gamma = 0.5772$ is Euler's constant and li is the logarithmic integral. In writing the above equality, the identity

BEST DOCUMENT AVAILABLE

$$\int \frac{dy}{\ln y} = \ln(\ln y) + \ln y + \frac{\ln y}{2 \cdot 2!} + \frac{\ln y}{3 \cdot 3!} \quad \ldots = \mathrm{li}\, y - \gamma$$

has been used.

As before, to obtain the duct height, d, we take the height derivative of (10-30) and solve for the height at which $d\phi/dz = -0.131$, we find

$$d = (1/0.131)(\phi_s - \phi_o)/\ln(\delta/z_o) \tag{10-25}$$

where δ/z_o can be found from (10-24) for a given x. Of course (10-24) cannot be solved explicitly for δ as in the earlier models, but it is explicit in x and can easily be plotted. It is shown in Fig. 10-7.

Similarly, from (9-39a) and (10-20),

$$C_\phi^2 = 3.2\, k_o^{4/3}(\phi_s - \phi_o)^2[\ln(\delta/z_o)]^{-2} z^{-2/3} \tag{10-26}$$

where δ/z_o is again found from (10-24). In this approximation $(1 - Ri)^{1/6} \approx 1.0$ for reasonably small values of Ri. The plot of duct thickness vs. distance off shore is shown as the lower curve in Fig. 10-8 assuming $z_o = 0.001$ cm — a typical value for water surfaces. Comparing Fig. 10-8 with 10-6 and 10-7 it is readily seen that the behavior of boundary layer thickness

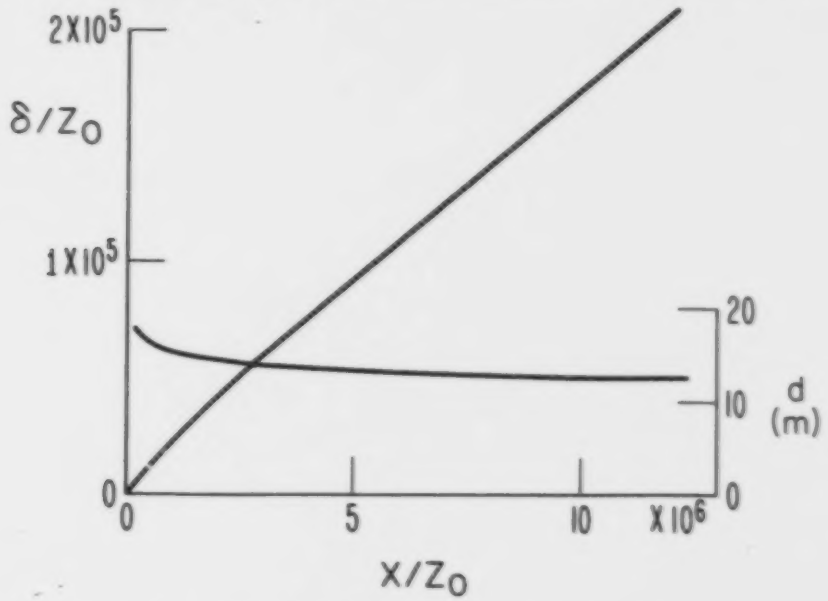

Figure 10.8--Change in depth of boundary layer δ and duct thickness d with distance x downwind of a transition in surface value of φ, assuming logarithmic profiles of properties.

BEST DOCUMENT AVAILABLE

and duct thickness is very similar for logarithmic profiles and power-law profiles if a power of 1/10 is chosen as the power-law index under neutral stability conditions. This is in agreement with the comparisons of duct thickness for power-law and log-linear profiles shown in Fig. 9-5.

10.3 Boundary Layer Modification Due to Radiational Cooling of the Ground

Constant Flux Assumption at Lower Boundary

Assume now that the ground and lower atmosphere are uniform horizontally, so that gradients in x and y can be ignored. The important term on the left-hand side of Eq. (10-2) is then the temporal variation and we have the equation

$$\frac{\partial \chi}{\partial t} = \frac{\partial}{\partial z} \left(K \frac{\partial \chi}{\partial z} \right) \tag{10-27}$$

to be solved with the constraint of a reasonable lower boundary condition. The problem to be solved is the effect on radio refractive index distribution and structure constant of the diurnal variation of temperature at the earth's surface due to radiational heating and cooling of the surface. Because we are dealing with radiational cooling, it is temperature change that causes the change in potential refractive index. We therefore interpret χ as $\rho c_p \theta$. The heat flux is then

$$F(t,z) = - K \frac{\partial \chi}{\partial z} \tag{10-28}$$

as seen by analogy with momentum flux in Eq. (9-4). If K(z) is invariant in time,

$$\frac{\partial F}{\partial t} = - K \frac{\partial}{\partial z} \left(\frac{\partial \chi}{\partial t} \right) \equiv K \frac{\partial^2}{\partial z^2} \left(K \frac{\partial \chi}{\partial z} \right)$$

so

$$\frac{\partial F}{\partial t} = K \frac{\partial^2 F}{\partial z^2} \tag{10-29}$$

is the equation to be solved. The boundary constraint at z = 0 is that

$$F(t,0) = - F_A = F_G - R$$

BEST DOCUMENT AVAILABLE

where R is the net outward radiation at night from the surface of the earth. F_A is the component supplied by conduction from the air and F_G is the component supplied by conduction within the soil. Direct radiation from the air is ignored.

We assume that $\theta(z)$ passes through a condition $\theta(z) = \theta_o$ = constant at some time near sunset so that θ_o = constant can be assumed as an initial condition. We will also at first assume that F_A changes from zero at about sunset to some value at which it remains constant throughout the rest of the night. We proceed as in the derivation of Eq. (10-6). We assume a power law wind profile of the form $u = bz^m$ and solve for K, using Eq. (9-24). Inserting into Eq. (10-29) we have

$$\frac{\partial F}{\partial t} = az^{1-m} \frac{\partial^2 F}{\partial z^2} \tag{10-30}$$

where $a = u_*^2/mb$ in contrast to our earlier definition of a. A solution, assuming the heat flux from the air into the soil at the lower boundary to remain constant after sunset, was found by Frost (1946). Frost's solution is

$$\frac{\partial \theta}{\partial z} = \frac{F_A z^{m-1}}{a\rho c_p \Gamma[1/(1+m)]} \int_{\xi_o(z,t)}^{\infty} \xi^{-m/(m+1)} e^{-\xi} d\xi \tag{10-31}$$

where $\xi = z^{m-1}/(m+1)^2$ ta and the integral divided by $\Gamma[1/(1+m)]$ is the function, $I(m, \xi_o)$ tabulated in Appendix C.

From Eq. (9-2)

$$\frac{\partial \phi}{\partial z} \simeq -\frac{77.6}{\theta^2}\left(P_o + \frac{9620\, e_p}{\theta}\right)\frac{\partial \theta}{\partial z} = -Q\frac{\partial \theta}{\partial z} \tag{10-32}$$

where $Q \simeq 1.14$ for typical values of θ and e_p (300 K and 10 mb, respectively).

Therefore, denoting the Incomplete Gamma Function by $I[1/(1+m), \xi_o]$, the radio duct thickness is given by

$$d = \left[\frac{0.131\, a\, \rho\, c_p}{Q\, F_A\, I(m,\xi_o)}\right]^{\frac{1}{m-1}} . \tag{10-33}$$

It is useful to carry the analysis a step further and calculate the fall in temperature at the ground. Returning to Eq. (10-31) and integrating by parts

BEST DOCUMENT AVAILABLE

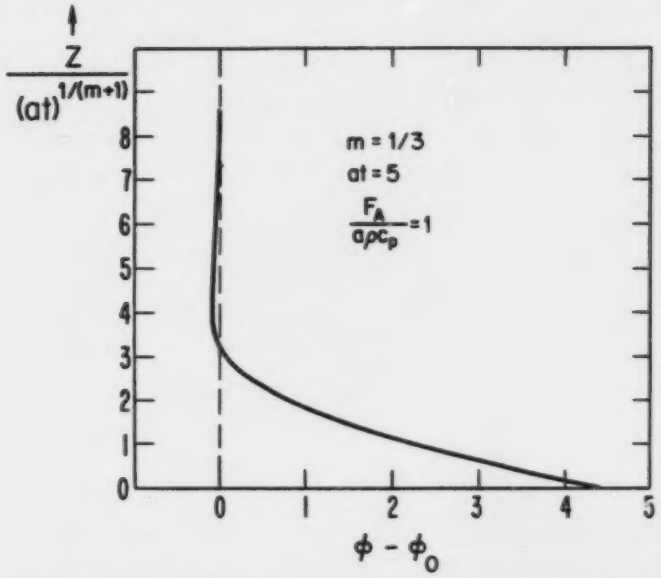

Figure 10.9--Theoretical potential refractive index distribution with height z and time t after nightfall assuming surface heat flux F_A to be constant through the night. Subscript "o" indicates initial value near sunset.

$$\theta - \theta_o = \frac{F_A}{a\rho\, c_p\, m\, \Gamma[1/(1+m)]} \left\{ z^m \int_{\xi_o}^{\infty} \xi^{-\frac{m}{m+1}} e^{-\xi}\, d\xi - \left[(m+1)^2\, at \right]^{\frac{m}{m+1}} e^{-\xi} \right\} \quad (10\text{-}34)$$

which, for z = 0, gives the temperature at the ground

$$\theta_s = \theta_o - \frac{F_A [(m+1)^2\, at]^{\frac{m}{m+1}}}{a\rho\, c_p m \Gamma[1/(1+m)]} . \quad (10\text{-}35)$$

If the refractive index ϕ depends only on temperature then ϕ will have the same form. The plot of $\phi - \phi_o$ is shown in Fig. 10-9 for the conditions given. It should be compared with the measured distributions of ϕ shown in Fig. 10-14.

When K = constant, m = 1. Then $\xi = z^2/4at$ and letting $\zeta^2 = \xi$, Eq. (10-34) can be written

$$\theta - \theta_o = \frac{F_A}{a\rho\, c_p\, \sqrt{\pi}} \left\{ 2z \int_{\zeta_o}^{\infty} e^{-\zeta^2}\, d\zeta - 2(at)^{1/2}\, e^{-\zeta^2} \right\}$$

or

BEST DOCUMENT AVAILABLE

$$\theta - \theta_o = \frac{F_A(4at)^{1/2}}{a\rho\, c_p\, \sqrt{\pi}} \left[\frac{z\sqrt{\pi}}{(4at)^{1/2}} \operatorname{erfc} \zeta_o - e^{-z^2/4at} \right] \qquad (10\text{-}36)$$

where erfc = 1 - erf and erf ζ_o is the widely tabulated error function equal to

$$(2/\sqrt{\pi}) \int_0^{\zeta_o} \exp(-\zeta^2) d\zeta \ .$$

Equation (10-36) is the classical solution to the heat conduction problem when the heat conductivity coefficient is constant.

Actually, of course, there is little physical basis for the assumption that F_A (the contribution of outgoing radiative heat flux contributed by the air) is constant throughout the night. An alternative assumption (Brunt, 1939) is that the heat flux from the soil F_G is constant. Then, assuming the soil conductivity K_1 to be constant, Brunt found from Eq. (10-29) that the temperature at the ground is

$$T_s = T_o - \frac{2F_G t^{1/2}}{\rho_1\, c_1\, (K_1\, \pi)^{1/2}} \qquad (10\text{-}37)$$

where ρ_1 and c_1 are soil density and specific heat, respectively. Actually, it is more reasonable to assume that $R = F_A + F_G$ is constant through the night rather than either F_A or F_G so equations like (10-35) and (10-37) can only provide rough estimates and qualitative guidance of what to expect from more rigorous numerical solutions.

To calculate C_ϕ, return to Eqs. (9-39b), (9-24), (10-31), (10-32), and (10-35). It is found that

$$C_\phi = 9.9\, (K/u_*)^{2/3}\, |\partial\theta/\partial z|\, (1 - Ri)^{-1/6}$$

$$= 1.9\, (1-Ri)^{-1/6}\, \Delta\theta (a/u_*)^{2/3}\, m\Gamma[1/(1+m)] z^{-(1+2m)/3}\, \xi_o^{\,m/(m+1)}\, I(\xi_o, m) \qquad (10\text{-}38)$$

where

$$\xi_o = z^{m+1}/(m+1)^2\, ta, \quad \Delta\theta = \theta_s - \theta_o \text{ [found from Eq. (10-35)]}$$

and

BEST DOCUMENT AVAILABLE

$$I = \frac{\int_{\xi_o}^{\infty} \xi^{-m/(1+m)} e^{-\xi}\, d\xi}{\Gamma[1/(1+m)]}$$

where this function (the incomplete Γ function) is tabulated in Appendix E. A plot of C_ϕ vs. time at a height of 30 m for F_A = constant (solid curve) is shown in Fig. 10-10, and a plot of the height distribution of C_ϕ one hour after sunset is shown in Fig. 10-11. It was assumed that $F_A = 10$ cal m^{-2} s^{-1} $a = 0.05$ $m^{4/3}$ s^{-1}, $u_* = 0.2$ m s^{-1}, $m = 1/3$.

There are several approximations in these approaches. It is assumed that m and K are constant during the modification process and that the important physics is in the change in $d\theta/dz$. It has been assumed that the fluxes (either F_A or F_G or both) are constant through the night when actually it is more reasonable to assume that the sum $F_A + F_G$ is constant. Therefore, equations like (10-33) and (10-38) can only provide rough estimates and qualitative guidance of what to expect from more realistic numerical solutions. However, Eq. (10-33) is capable of well representing most of the qualitative features in radar ducting observations such as those shown in Fig. 9-2.

Quasi-Sinusoidal Variation of Surface Temperature

There are other boundary value problems with analytical solutions that can be used to provide guidance in the use of more rigorous numerical methods for analysis of diurnal effects of the atmosphere on radar propagation and scatter. A sinusoid of the form $\theta_s - \theta_o = \Delta\theta \cos \sigma t$ is the simplest diurnal lower boundary condition that might be assumed. However, the earth's surface temperature diurnal variation differs significantly from a sinusoid. The temperature rises rapidly following sunrise on a clear morning and falls more slowly after sunset. Figure 10-12 shows the diurnal cycle of temperature measured at Manor, Texas (Gerhardt and Jehn, 1950), at a height of 2.5 cm (1 inch) and at 10.7 m on an almost clear night with very light winds. Figure 10-13 shows a comparable case with higher winds recorded at O'Neill, Nebraska (Lettau and Davidson, 1957). It is evident that the surface temperature variation more nearly resembles a slightly unsymmetrical trochoid than a sinusoid. In the following development a trochoidal lower boundary condition will be assumed.

BEST DOCUMENT AVAILABLE

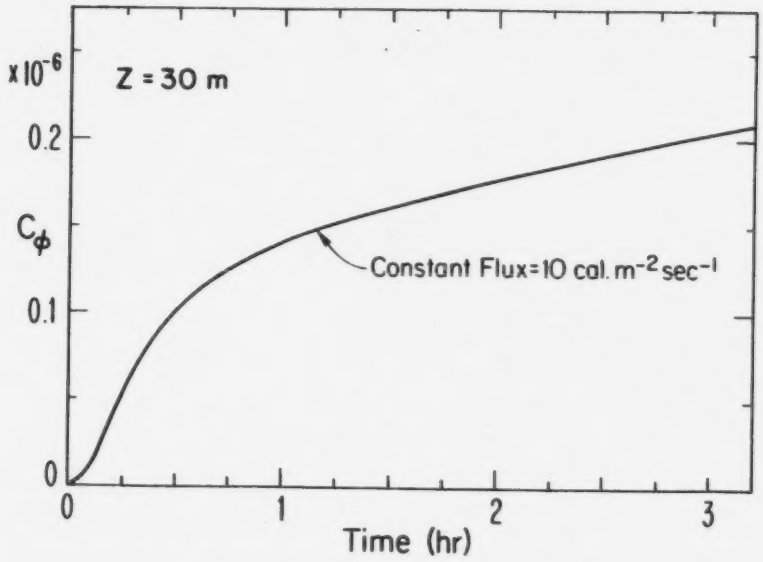

Figure 10.10--Variation of structure constant with time at a height of 30 m assuming surface heat flux F_A to be constant.

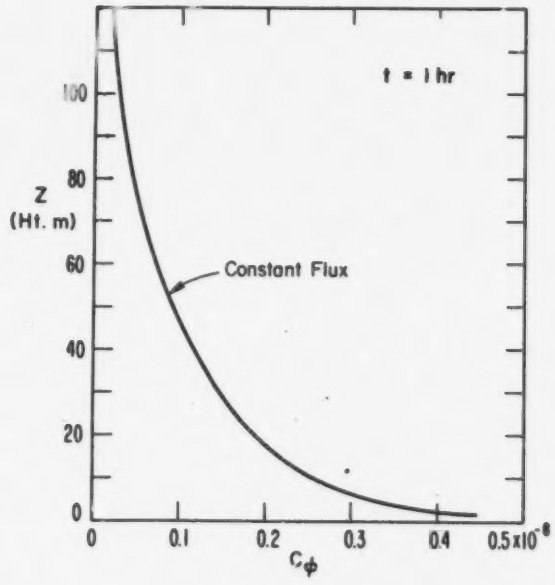

Figure 10.11--Variation of structure constant with height one hour after sunset assuming surface heat flux F_A to be constant.

BEST DOCUMENT AVAILABLE

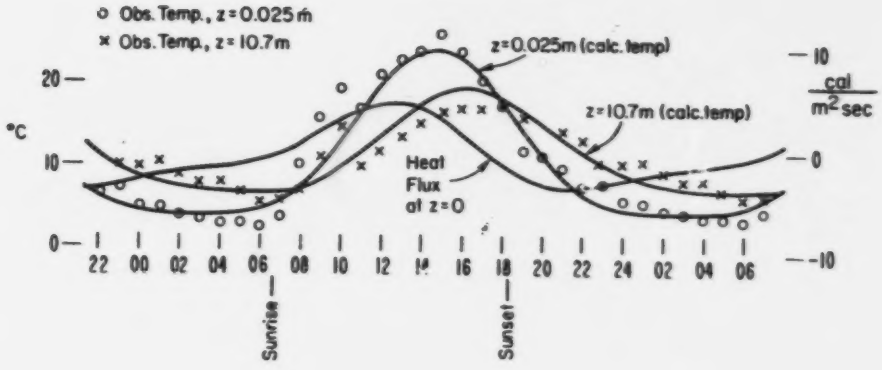

Figure 10.12--Temperatures measured at a height of 0.025 cm and 10.7 m on a tower near Manor, Texas, compared with calculations made by assuming a trochoidal distribution of surface temperature. Surface heat flux has also been calculated. Winds were very light. (Data from Gerhardt and Jehn, 1950.)

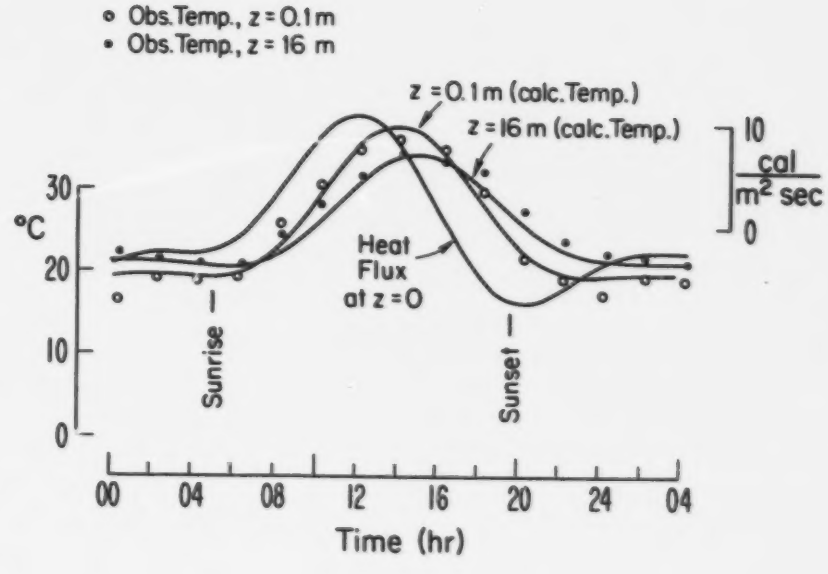

Figure 10.13--Same as Fig. 10.11 except measurements were made near O'Neill, Nebraska, under wind conditions of about 5 m sec^{-1} at a height of 16 m. Observations were at heights of 0.1 m and 16 m.

BEST DOCUMENT AVAILABLE

If K is constant (i.e., m = 1), a solution of Eq. (10-27) is

$$\theta - \theta_o = \Delta\theta\, e^{-\sqrt{\sigma/2K}\, z} \cos(\sigma t - \sqrt{\sigma/2K}\, z). \qquad (10\text{-}39)$$

When z = 0, this solution obeys the sinusoidal lower boundary condition.

However, we want a solution that becomes trochoidal at the ground, i.e.,

$$\theta - \theta_o = \Delta\theta \cos \sigma t + f\Delta\theta \cos 2\sigma t \qquad (10\text{-}40)$$

where f is some small constant. By a proper choice of f and $\Delta\theta$, Eq. (10-40) provides an adequate fit to the data as shown in Fig. 10-11. For the calculated curves $\Delta\theta$ = 10°C and f = 1/4 were chosen.

A solution to Eq. (10-27) that satisfies this boundary condition is

$$\theta - \theta_o = \Delta\theta e^{-\sqrt{\sigma/2K}\, z} \cos(\sigma t - \sqrt{\sigma/2K}\, z) + f\Delta\theta e^{-\sqrt{\sigma/K}\, z} \cos(2\sigma t - \sqrt{\sigma/K}\, z) \qquad (10\text{-}41)$$

whence

$$\frac{\partial\theta}{\partial z} = \Delta\theta \sqrt{\sigma/2K}\, e^{-\sqrt{\sigma/2K}\, z} (\sin y - \cos y) + f\Delta\theta \sqrt{\sigma/K}\, e^{-\sqrt{\sigma/K}\, z} (\sin y' - \cos y'), \qquad (10\text{-}42)$$

where $y = \sigma t - \sqrt{\sigma/2K}\, z$ and $y' = 2\sigma t - \sqrt{\sigma/K}\, z$. If variation in vapor pressure is ignored, and if it is assumed that Ri is negligible, Eq. (10-42) can be used to obtain the time and height variation of C_ϕ from Eq. (9-39b), i.e.,

$$C_\phi = 1.95\, (K/u_*)^{2/3}\, \Delta\theta \sqrt{\sigma/2K}\, e^{-\sqrt{\sigma/2K}\, z} (\sin y - \cos y) + f \sqrt{\sigma/K}\, e^{-\sqrt{\sigma/K}\, z} (\sin y' - \cos y') . \qquad (10\text{-}43)$$

In arriving at the constant 1.9 it has been assumed that $\partial\phi/\partial z \simeq -1.14\, \partial\theta/\partial z$. In order to obtain a most realistic value for the constant K from the Manor data, the measured temperature variation at a height of 10.7 m was compared with that at 2.5 cm. Using Eq. (10-41), K was varied until the amplitude and relative phase shift of the computed temperatures matched those of the observed temperatures at the two heights. A value of K = 200 cm^2/s was found. If this value is arbitrarily assumed to be applicable at a height of 1 m, Eq. (9-13) yields $u_* \simeq 5$ cm/s and $K/u_* = 40$ cm = 0.4 m under neutral conditions.

BEST DOCUMENT AVAILABLE

Plots of C_ϕ along with potential refractive index, ϕ, and modified refractive index M are shown in Fig. 10-14 for $\Delta\theta$ = 10 and f = 1/4. The height of the nose of the M curves is the thickness of the radio duct at night. The calculated curves of ϕ should be compared with profiles reported by Rocco and Smyth (1949) shown in Fig. 10-15 also measured under low wind conditions.

Features of interest in the distribution of C_ϕ include the very low values at all heights near sunrise and the double maximum that occurs for a short time after sunrise and sunset. For the assumed conditions, C_ϕ^2 gets as high as 2.5×10^{-13} ($m^{-2/3}$) at the surface. Maximum values occur 4 to 5 hours after sunrise and sunset. In accord with the assumption that K is constant in the calculation of $|d\theta/dz|$, the value of K/u_* has also been held constant in Eq. (10-43).

Ri was calculated from Eq. (9-11a) assuming a value for L. However, for the assumptions made the effect of Ri on C_ϕ is quite negligible. To see this, note that as L becomes very small Ri approaches a maximum value of + 0.21. When this is inserted into Eq. (9-39b), it has negligible effect on

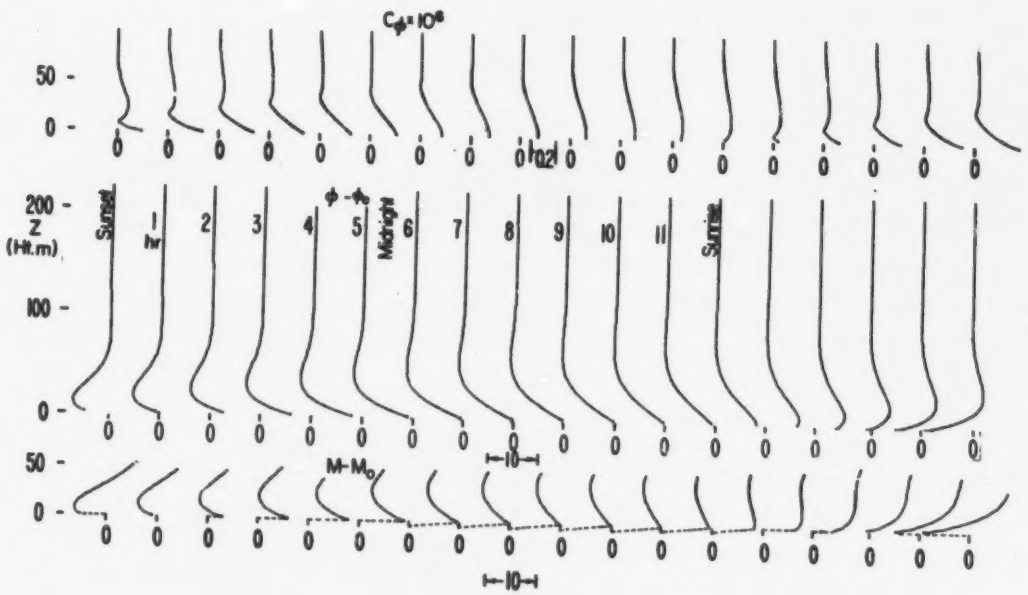

Figure 10.14--Calculations of structure constant (top frame), height distribution of potential refractive index (middle frame) and the height distribution of M (bottom frame) assuming the conditions that fit the observations of Fig. 10.11. The minima of the M curves indicate the duct thickness. The eddy diffusivity coefficient was assumed constant and the Richardson Number was ignored in the calculation of C_ϕ.

BEST DOCUMENT AVAILABLE

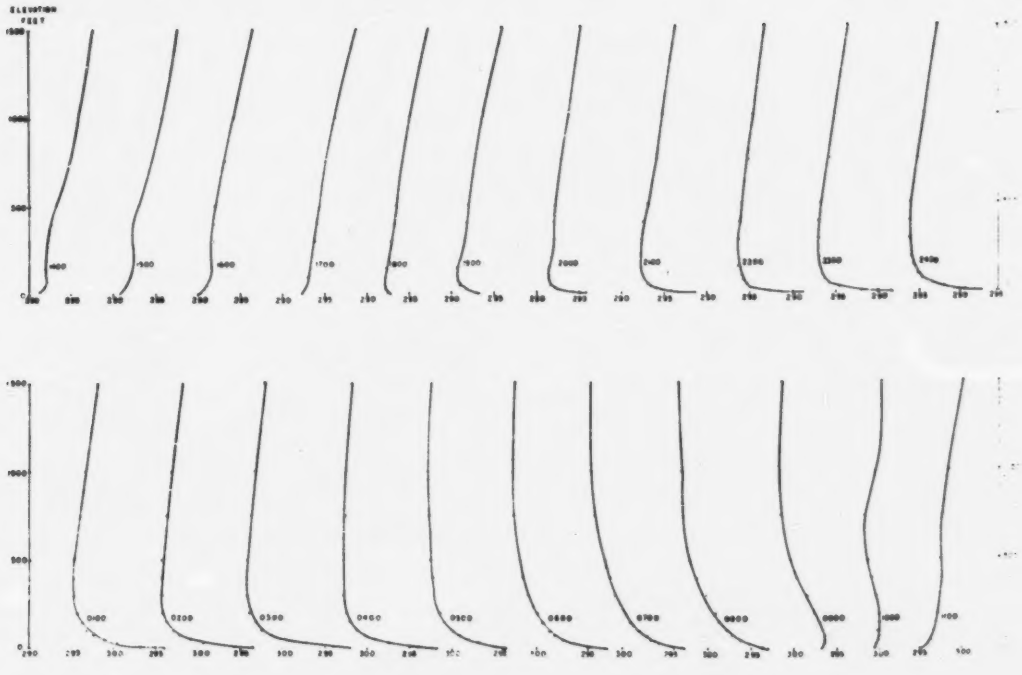

Figure 10.15--Measured height distributions of potential refractive index near Sentinel, Arizona, for each hour of most of the diurnal cycle. Measurements were made on a tower and with captive balloon (adapted from Rocco and Smyth, 1949).

C_ϕ because of the small power (-1/6) to which the (1-Ri) factor is raised. The principal effect of stability would be implicit and appear in $d\phi/dz$. However, in this problem $d\phi/dz$ has been obtained from Eq. (10-42) in which stability is not a factor except as it may affect the value of the average K deduced from the observational data.

The distributions of C_ϕ should only be considered as qualitative for several reasons:

1) K was not allowed to vary over the diurnal cycle which is equivalent to the assumption that the wind profile does not vary diurnally.

2) The structure parameter C_ϕ was calculated to a height of 200 m which is usually higher than the surface layer to which the theory applies, especially during daytime convection. Thus the basic assumptions on which the form of the profile is based are violated and the distributions should be considered qualitative at the higher altitudes.

3) The various assumptions made in the derivation of Eq. (10-43) were applicable only under conditions of forced convection. The physics is very different under free convective conditions, so the post-sunrise patterns may be substantially in error.

The diurnal variation of the temperature at 16 m and at 0.1 m gave K - 2000 cm^2 s^{-1} for the O'Neill, Nebraska data. The patterns of C_ϕ, ϕ, and M were similar to those of the Manor, Texas data except that the layers were thicker because of the larger K. For this reason, significant gradients of θ existed to higher altitudes.

REFERENCES

Abramowitz, M., and I.A. Stegun (1964): Handbook of mathematical functions. NBS (Formula 15.3.1, p 558) U.S. Govt. Printing Office, 1043 p.

Agee, E.M. (1971): An artificially induced snowfall. Bull. Amer. Meteorol. Soc., 52, 557-560.

Anderson, L.J., and E.E. Gossard (1953:. The effect of the oceanic duct on microwave propagation, Transactions, Amer. Geophys. Union, 34, 695-700.

Arnold, A., J.R. Rowland, T.C. Konrad, J.H. Richter, D.R. Jensen, and V.P. Noonkester (1975): Simultaneous observations of clear air convection by a pulsed radar, an FM-CW radar, an acoustic sounder and an instrumented aircraft, in Proceedings of the 16th Radar Meteorological Conference, pp. 290-295, American Meteorological Society, Boston, Mass.

Atlas, D. (1959): Meteorological angel echoes. J. Meteorol., 16, 6-11.

Atlas, D. (1964): Advances in radar meteorology. Adv. in Geophysics, 10, 478 p.

Atlas, D. (1954): The estimation of cloud parameters by radar. J. Meteorol., 11, 309-317.

Atlas, D., and S. Bartnoff (1953): Cloud visibility, radar reflectivity, and drop-size distribution. J. of Meteorol., 10, 143-148.

Atlas, D., K.R. Hardy, and T.G. Konrad (1966a): Radar detection of the tropopause and clear air turbulence, in Proceedings of the 12th Weather Radar Conference, pp 279-284, American Meteorological Conference, Boston, Mass.

Atlas, D., M. Kerker, and W. Hitschfeld (1953): Scattering and attenuation by non-spherical atmospheric particles. J. Atmos. and Terrestrial Physics, 3, 108-119.

Atlas, D., K.R. Hardy, and K. Naito (1966b): Optimizing the radar detection of clear air turbulence, J. Appl. Meteorol., 5, 450-460.

Atlas, D., J.I. Metcalf, J.H. Richter, and E.E. Gossard (1970): The birth of "CAT" and microscale turbulence, J. Atmos. Sci., 27, 903-913.

Atlas, D., and C.W. Ulbrich (1974): The physical basis for attenuation rainfall relationships and the measurement of rainfall parameters by combining attenuation and radar methods. J. de Recherches Atmos., 3, 275-298.

Auer, A.H., Jr. (1975): Metropolitan land use in the metropolitan St. Louis area. Report No. A5116, Department of Atmospheric Science, College of Engineering, University of Wyoming, Laramie, Wyo. 30 pp.

Auer, A.H., and J.D. Marwitz (1968): Estimates of air and moisture flux into hailstorms on the high plains. J. Appl. Meteorol., 7, 196-198.

Austin, P.M., and A.C. Bemis (1950): A quantitative study of the "bright band" in radar precipitation echoes. J. Meteorol., 7, 145-51.

Balsley, B.B., and V.L. Peterson (1981): Doppler radar measurements of clear air atmospheric turbulence structure at 1290 MHz. J. Appl. Meteorol., 20, 266-274.

Bartnoff, S., and D. Atlas (1951): Microwave determination of particle-size distribution. J. Meteorol., 8, 130-131.

Battan, L.J. (1973): Radar Observation of the Atmosphere, The Univ. of Chicago Press, 324 p.

Batchelor, G.K. (1953): Homogeneous Turbulence, Cambridge Univ. Press, 195 p.

Bean, B.R., and E.J. Dutton (1966): Radio Meteorology. U.S. Government Printing Office, Washington, DC, 431 p.

Bean, B.R., B.A. Cahoon, C.A Samson, and G.D. Thayer (1966): A World Atlas of Atmospheric Radio Refractivity. U.S. DoC, ESSA Monograph 1, U.S. Govt. Printing Off. 130 pp.

Bean, B.R. (1972): Application of FM-CW radar and acoustic echo-sounder techniques to boundary layer and CAT studies in Remote Sensing of the Troposphere (Ed. V.E. Derr) Superintendent of Documents, U.S. Govt. Printing Off. 20-1 to 20-18.

Bergeron, T. (1933): On the physics of clouds. Memo. Met. Assoc., Intern. Union for Geodesy and Geophysics, Lisbon, 43 p.

Best, A.C. (1951): Drop size distribution in cloud and fog. Quart. J. Roy. Meteorol. Soc., 77, 418-426.

Bolgiano, R. (1958): The role of turbulent mixing in scatter propagation. IRE Trans. on Antennas and Propagation AP-6, 161-168.

Booker, H.G., and W.E. Gordon (1950): A theory of radio scattering in the troposphere. Proc. of the IRE pp. 401-412.

Booker, H.G., and J.T. DeBettencourt (1955): Theory of radio transmission by tropospheric scattering using very narrow beams. Proc. IRE, 43, 281-290.

Borovikov, A.M., V.V. Kostarev, I.P. Mazin, V.I. Smirnov and A.A. Chernikov (1967): Radar measurement of precipitation rate. Keter Press Israel, Envlish Translation available from U.S. Dept. of Commerce FSTI, Springfield, Va., 112 p.

Boucher, R.J. (1952): Empirical relationship between radar reflectivity drop size distribution and liquid water content in clouds. Mount Washington Observatory, Contract AF 19(122)-399, 14 p.

Braham, R.R., and P. Squires (1974): Cloud Physics - 1974. Bull. Amer. Meteorol. Soc., 55, 6, 543-556.

Breed, D.W., L.O. Grant, and J. Dye (1976): Cloud droplet distribution in high elevation continental cumulis. Proc. Intern. Conf. on Cloud Physics, Boulder, CO, 658-664.

Bringi, V.N., and Seliga, T.A. (1977): Scattering from non-spherical hydrometeters. Proc. Open Symposium, Commission F, URSI, La Baule, France, 199-204.

Brown, H.A. (1960): Report on radar thin lines, in Proceedings of the 8th Weather Radar Conference, pp. 65-72, American Meteorological Society, Boston, Mass.

Browning, K.A., and T.W. Harrold (1969): Air motion and precipitation growth in a wave depression. Quart. J. Roy. Meteorol. Soc., 95, 288, 302-306.

Browning, K.A., and D. Atlas (1966): Velocity characteristics of some clear air dot angels. J. Atmos. Sci., 23, 592-604.

Browning, K.A., and H. Wexler (1966): The determination of kinematic properties of a wind field using a single Doppler radar. Proc. 12th Radar Conf., Boston, 125-127.

Browning, K.A., and F.H. Ludlam (1962): Airflow in convective storms. Quart. J. Roy. Meteorol. Soc., 88, 117, 287, 359-361, 474, 475-476.

Browning, K.A., J.R. Starr, and A.J. Whyman (1972): Measurements of air motions in regions of clear air turbulence using high power Doppler radar, Nature, 239, 267-269.

Browning, K.A., J.R. Starr, and A.J. Whyman (1973a): The structure of an inversion above a convective boundary layer as observed using high power pulsed Doppler radar, Boundary Layer Meteorol., 4, 91-111.

Chadwick, R.B., K.P. Moran, R.G. Strauch, G.E. Morrison, and W.C. Campbell (1976a): A new radar for measuring winds. Bull. Amer. Meteorol. Soc., 57, 1120-1125.

Chadwick, R.B., K.P. Moran, R.G. Strauch, G.E. Morrison, and W.C. Campbell (1976b): Microwave radar wind measurements in the clear air. Radio Sci., 11, 795-802.

Chadwick, R.B., and C.G. Little (1973): The comparison of sensitivities of atmospheric echo-sounders. Remote Sensing Environ., 2, 223-234.

Chadwick, R.B., and R.G. Strauch (1979): Processing of FM-CW Doppler radar signals from distributed targets. IEEE Transactions on Aerospace and Electronic Systems, AES-15, 1.

Chadwick, R.B., and K.P. Moran (1980): Long term measurements of C_n^2 in the boundary layer. Radio Sci., 15, 355-361.

Chernikov, A.A. (1968): Radio-wave scattering in clouds and the radar equation. Proc. 3rd All-Union Conf., Radar Meteorology, Moscow, 68-73.

Clark, T.L., and W.D. Hall (1979): A numerical experiment on stochastic condensation theory. J. Atmos. Sci., 35.

Corrsin, S. (1951): On the spectrum of isotropic temperature fluctuations in an isotropic turbulence. J. Appl. Phys., 22, 417-423.

Cox, D.C., H.W. Arnold, and A.J. Rustako (1977): Some observations of anomalous depolarization on 19 and 12 GHz earth-space propagation paths. Radio Sci., 12, 435-440.

Craig, R.A. (1946): Measurements of temperature and humidity in the lowest 1000 feet of the atmosphere over Massachusetts Bay. Papers in Physical Oceanography and Meteorology, Massachusetts Inst. of Technology and Woods Hole Oceanographic Institution, Vol. X, No. 1, 47 pp.

Cunningham, R.M. (1952): Distribution and growth of hydrometeors around a deep cyclone. MIT Weather Radar Res. Rep., No. 18, 297-302.

Cunningham, R.M., V.G. Plank, and C.M. Campen (1956): Cloud refractive index studies. AFCRC-TR-56-210, Air Force Cambridge Research Center.

Day, J.P., and L.G. Trolese (1950): Propagation of short radio waves over desert terrain. Proc. IRE, 38, 2, 165-175.

Deacon, E.L., (1962): Aerodynamic roughness of the sea. J. Geophys. Res., 67, 3167-3172.

Deirmendjian, D. (1969): Electromagnetic Scattering on Spherical Polydispersions. Amer. Elsevier Publishing Co., Inc., New York, 290 p.

Deley, G.W. (1970): Waveform design. Radar Handbook, Chapter 3, M.I. Skolnik, Editor, McGraw-Hill, New York.

Diem, M. (1948): Messung der Grösse von Wolkenelementen, II. Meteor. Rundschau, 1, 261-273.

Donaldson, R.J., Jr. (1955): Drop-size distribution, liquid water content, optical transmission, and radar reflectivity in fog and drizzle. Proc. 5th Weather Radar Conf., Asbury Park, New Jersey, 275-280.

Doviak, R.J., P.S. Ray, R.G. Strauch, and L.J. Miller (1976): Error estimation in wind fields derived from dual-Doppler radar measurements, J. Appl. Meteorol., 15, 868-878.

Doviak, R.J., and C.T. Jobson (1979): Dual-Doppler radar observations of clear air wind perturbations in the planetary boundary layer, J. Geophys. Res., 84, 697-702.

Doviak, R.J., and M. Berger (1980): Waves in the optically clear planetary boundary layer resolved by dual-Doppler radars. Radio Sci., 15, 297-317.

Dye, J.E. (1976): Comparisons of the electrostatic disdrometer with impactor slides. J. Appl. Meteorol., 15, 783-789.

Dye, J.E. (1974): Observations of precipitation development in cumulus congestus clouds on July 9, 1973. Proc. Conf. on Cloud Physics, Boston, Mass., 148-151.

Eastwood, E. (1967): Radar Orinthology. 278 pp., Methuen, London.

Findeisen, W. (1938): Die kolloid meteorologische vorgange bei der neiderschlagsbeldung. Meteor. Zeitschr., 55, 121-133.

Foote, G.B., and P.S. du Toit (1969): Terminal velocity of raindrops aloft. J. Appl. Meteorol., 8, 249-253.

Friend, A.W. (1939): Continuous determination of air-mass boundaries by radio. Bull. Amer. Meteorol. Soc., 20, 202-205.

Friend, A.W. (1949): Theory and practice of tropospheric sounding by radar. Proc. IRE., 37, 116-138.

Frisch, A.S., and S.F. Clifford (1974): A study of convection capped by a stable layer using Doppler radar and acoustic echo sounders. J. Atmos. Sci., 31, 1622-1628.

Frisch, A.S., R.B. Chadwick, W.R. Moninger, and J.M. Young (1976): Observations of boundary layer convection cells measured by dual-Doppler radar and echosonde and by microbarograph array. Boundary Layer Meteorol., 10, 55-68.

Frisch, A.S., and G.R. Ochs (1975): A note on the behavior of the temperature structure parameter in a convective layer capped by a marine inversion. J. Appl. Meteorol., 14, 415-419.

Frisch, A.S., and R.G. Strauch (1976): Doppler radar measurements of turbulent kinetic energy dissipation rates in a northeastern Colorado convective storm. J. Appl. Meteorol., 15, 1012-1017.

Frost, R. (1946): Turbulence and diffusion in the lower atmosphere. Proc. Roy. Soc. London, 186, 20-35.

Frost, R. (1948): Calculation of night minimum temperatures. Prof. Notes, Meteor. Off., London, #95, 2-6.

Gage, K.S., and B.B. Balsley (1978): Doppler radar probing of the clear atmosphere. Bull. Amer. Meteorol. Soc., 59, 1074-1093.

Gage, K.S., and J.L. Green (1979): Tropopause detection by partial specular reflection using VHF radar. Science, 203, 1238-1240.

Gans, R. (1912): Uber die from ultramiskroskopischer goldteilchen. Annalen der Physik, 37, 881-900.

Geotis, S.G. (1964): On sea breeze angels, in Proceedings of the 11th Weather Radar Conference, pp. 6-9, American Meteorological Society, Boston, Mass.

Glover, K.M., and K.R. Hardy (1966): Dot angels: Insects and birds, in Proceedings of the 12th Weather Radar Conference, pp. 264-268, American Meteorological Society, Boston, Mass.

Goldhirsh, J., and I. Katz (1974): Estimation of raindrop size distribution using multiple wavelength radar systems. Radio Sci., 9, 439-446.

Gorelick, A.G., and Yu. V. Mel'nichuk (1963): Radar study of dynamic process in the atmosphere. Tr. Vses. Nav. Meteor. Souesh., No. 5.

Gossard, E.E. (1960): Power spectra of temperature, humidity, and refractive index from aircraft and tethered balloon measurements. IRE Trans. Antennas Propagat., AP-8, 186-201.

Gossard, E.E. (1977): Refractive index variance and its height distribution in different air masses. Radio Sci., 12, 89-105.

Gossard, E.E. (1978a): The distribution of radio refractive index structure parameter in boundary layers undergoing spatial or temporal transition. Radio Sci., 13, 255-259.

Gossard, E.E., (1978b): The height distribution of refractive index structure parameter in an atmosphere being modified by spatial transition at its lower boundary. Radio Sci., 13, 489-500.

Gossard, E.E. (1979): A fresh look at the radar reflectivity of clouds. Radio Sci., 14, 1089-1097.

Gossard, E.E., and A.S. Frisch (1976): Kinematic models of a dry convective boundary layer compared with dual-Doppler radar observations of wind fields. Boundary Layer Meteorol., 10, 311-330.

Gossard, E.E., and W.H. Hooke (1975): Waves in the Atmosphere; Atmospheric Infrasound and Gravity Waves - Their Generation and Propagation. Elsevier, 532 p.

Gossard, E.E., and J.H. Richter (1970): The shape of internal waves of finite amplitude from high resolution radar sounding of the lower atmosphere. J. Atmos. Sci., 27, 971-973.

Gossard, E.E., J.H. Richter, and D. Atlas (1970): Internal waves in the atmosphere from high-resolution radar measurements. J. Geophys. Res., 75, 3523-3536.

Gossard, E.E., D.R. Jensen, and J.H. Richter (1971): Analytical study of tropospheric structure as seen by high-resolution radar. J. Atmos. Sci., 28, 794-807.

Gossard, E.E., R.B. Chadwick, K.P. Moran, R.G. Strauch, G.E. Morrison, and W.C. Campbell (1978): Observations of winds in the clear air using FM-CW radar. Radio Sci., 13, 285-289.

Gossard, E.E., and R.B. Chadwick (1979): Studies of insects by high resolution radar. Proc. 14th Conf. and Agric. and Forest Meteorol., Minneapolis, Minn; American Meteorological Society, Boston, Mass., 268-271.

Gossard, E.E., and R.G. Strauch (1981): The refractive index spectra within clouds from forward-scatter radar observations. J. Appl. Meteorol., 20, 170-183.

Gradshteyn, J.S., and I.M. Ryzhik (1965): Tables of integrals series and products. (Formula 3.478), Academic Press, N.Y., 342 p.

Green, J.L., J.M. Warnock, R.H. Winkler, and T.E. VanZandt (1975b:. Studies of winds in the upper troposphere with a sensitive VHF radar. Geophys. Res. Lett., 2, 19-21.

Green, J.L., R.H. Winkler, J.M. Warnock, W.L. Clark, K.S. Gage, and T.E. VanZandt (1978): Observations of enhanced clear air reflectivity associated with convective clouds. Proc. 18th Conf. on Radar Meteorology, Amer. Meteor. Soc., Atlanta, GA, March 28-31, 1978, 88-93.

Gunn, K.L.S., and J.S. Marshall (1958): The distribution with size of aggregate snowflakes. J. Meteorol., 15, 452-466.

Gunn, R., and G.D. Kinzer (1949): The terminal velocity of fall for water droplets in stagnant air. J. Meteorol., 6, 243-48.

Gurvich, A.S., B.M. Koprov, L.R. Tsvang, and A.M. Yaglom (1967): Empirical data on the small-scale structure of atmospheric turbulence, in Atmospheric Turbulence and Radio Wave Propagation, Proc. Int. Colloq., Moscow, June 15-22, 1965, Nauka, Moscow, p 30-52.

Hanna, S.R., and F.A. Gifford (1975): Meteorological effects of energy dissipation at large power parks. Bull. Amer., 56, 1069-1076.

Hardy, K.R., and H. Ottersten (1969): Radar investigations of convective patterns in the clear atmosphere. J. Atmos. Sci., 26, 666-672.

Hardy, K.R. (1972): Studies of the clear atmosphere using high power radar, in Remote Sensing of the Troposphere, Chap. 14, edited by V.E. Derr, NOAA, Washington, DC.

Hardy, K.R., and I. Katz (1969): Probing the clear atmosphere with high power high resolution radars. Proc. IEEE, 57, 468-480.

Hardy, K.R., and H. Ottersten (1969): Radar investigations of convective patterns in the clear atmosphere. J. Atmos. Sci., 26, 666-672.

Hardy, K.R., D. Atlas, and K.M. Glover (1966): Multiwavelength backscatter from the clear atmosphere. J. Geophys. Res., 71, 1537-1552.

Harper, W.G., F.H. Ludlam, and P.M. Saunders (1957): Radar echoes from cumulus clouds, in Proceedings of the 6th Weather Radar Conference, pp 267-273, American Meteorological Society, Boston, Mass.

Harper, W.G. (1958): Detection of bird migration by centimetric radar: A cause of radar angels, Proc. Roy. Soc. London, B149, 484-502.

Harper, W.G. (1964): Cloud detection with 8-6 millimetre wavelength radar. Met. Mag., Lond., 93, 337-345.

Hill, R.J. (1978): Models of the scalar spectrum for turbulent advection, J. Fluid Mech., 88, 541-562.

Hodkinson, J.R. (1966): The optical measurement of aerosols. Aerosol Sci., C.N. Davies, Ed., Academic Press, New York, 287-357.

Hooke, W. (ed.) (1978): Project PHOENIX, Available from ERL/NOAA Boulder, CO 80302, 280 p.

Huff, F.A. (1972): Potential augmentation of precipitation from cooling tower effluents. Bull. AMS., 53, 639-644.

Imai, I. (1950): On the velocity of falling raindrops. Geophys. Mag., (Tokyo) 31, 244-249.

James, P.K. (1980): A review of radar observations of the troposphere in clear air conditions. Radio Sci., 15, 151-175.

Jensen, N.O., and D.H. Lenshow (1978): An observational investigation of penetrative convection. J. Atmos. Sci., 35, 1924-1933.

Jeske, H. (1965): Die ausbreitung elektroagnetischer Wellen im cm-bis m-Band über dem Meer unter besonderer Berücksichtigung der meteorologischen Bedingungen in der maritimen Grenzschich, Hamburger Geophysikalische Einzelschriften, De Gruyter and Co., Hamburg.

Jiusto, J.E. (1974): Remarks on visibility in fog. J. Appl. Meteorol., 13, 608-610.

Joss, J., and A. Waldvogel (1970): Raindrop size distributions and Doppler velocities. Preprints 14th Radar Meteorol. Conf., Boston, Am. Meteorol. Soc., 153-156.

Junge, C. (1952b): Gesetzmässigkeiten in der grössenverteilung atmosphärischu aerosole über dem Koninent. Ber. dt. Wetterd. U.S. Zone, 35, 264, 51, 62.

Katzin, M., R.W. Bauchman, and W. Binnian (1947): 3- and 9-centimeter propagation in low ocean ducts. Proc. IRE, 35, 891-905.

Kerr, D.E. (1951): Propagation of Short Radio Waves. Office of Scientific Research and Development, National Defense Research Committee, 728 p.

Kerker, M., M.P. Langleben, and K.L.S. Gunn (1951): Scattering of microwaves by a melting spherical ice-particle. J. Meteorol., 8, 424.

Knollenberg, R.G. (1976): Three new instruments for cloud physics measurements: the 2-D spectrometer, the Axially Scattering spectrometer, and the Active Scattering spectrometer. Proc. Intern. Cloud Physica Conf., Boulder, CO, U.S.A. 554-561.

Kohn, N., A. Johnson, and C. Mohr (1978): MUDRAS multiple Doppler radar analysis system. NOAA Tech. Memo. ERL WPL-35, 70 p.

Konrad, T.G. (1970): The dynamics of the convective process in clear air as seen by radar. J. Atmos. Sci., 27, 1138-1147.

Konrad, T.G., and F.L. Robison (1972): Simultaneous measurements of radar reflectivity and refractive index spectra in clear air convection. J. Appl. Meteorol., 11, 1114-1119.

Konrad, T.G., and F.L. Robison (1973): Development and characteristics of free convection in the clear air as seen by radar and aircraft. J. Appl. Meteorol., 12, 1284-1294.

Kovasnay, L.S.G., M.S. Uberoi, and S. Corrsin (1949): The transformation between one- and three-dimensional power spectra for an isotropic scalar field. Phys. Rev., 76, 1263-1264.

Kropfli, R. (1977): A dual Doppler radar study of the urban boundary layer: A summary of METROMEX results. NOAA Tech. Memo. ERL WPL-26, 110 p.

Kropfli, R.A., I. Katz, T.G. Konrad, and E.B. Dobson (1968): Simultaneous radar reflectivity measurements and refractive index spectra in the clear atmosphere. Radio Sci., 3, 991-994.

Kropfli, R.A., and N.M. Kohn (1976): Dual Doppler observations of the convective mixing layer at St. Louis, in Proceedings of the 17th Conference on Radar Meteorology, pp 321-325, American Meteorological Society, Boston, Mass.

Kropfli, R.A., and L.J. Miller (1976): Kinematic structure and flux quantities in a convective storm from dual-Doppler radar observations. J. Atmos. Sci., 33, 3, 520-529.

Kropfli, R.A., and P.H. Hildebrand (1980): Three-dimensional wind measurements in the optically clear planetary boundary layer with dual-Doppler radar. Radio Sci., 15, 2, 283-296.

Labitt, M. (1981): Coordinated radar and aircraft observations of turbulence. Project Report ATC 108, MIT Lincoln Laboratory, 39 p.

Lane, J.A., and R.W. Meadows (1963): Simultaneous radar and refractometer soundings of the troposphere, Nature, 197, 35-36.

Lettau, H.H., and B. Davidson (Eds.) (1957): Exploring the Atmosphere's First Mile. Pergamon, London, 575 p.

Lhermitte, R.M. (1970): Dual-Doppler radar observation of convective storm circulation. Preprints 14th Radar Meteorol. Conf., Boston, Am. Meteorol. Soc., 139-144.

Lhermitte, R.M. (1966): Probing air motion by Doppler analysis of radar clear air returns. J. Atmos. Sci., 23, 575-591.

Lhermitte, R.M., and D. Atlas (1963): Doppler fall speed and particle growth in stratiform precipitation. Proc. Tenth Wea. Radar Conf., 297-302.

Lhermitte, R.M., and L.J. Miller (1970): Doppler radar methodology for the observation of convective storms. Prep. 14th Radar Meteor. Conf., Tucson, Ariz., 133-138.

Little, C.G. (1969): Acoustic methods for the remote probing of the lower atmosphere. Proc. IEEE, 57, 4, 571-578.

Little, C.G. (1972): Status of remote sensing of the troposphere. Bull. Am. Meteorol. Soc., 53, 10, 936-949.

Little, C., and E.E. Gossard (1975): The 1972 Haswell, Colorado, atmospheric boundary layer experiment (1975). Proc. of 3rd Symposium on Meteorological Observations of the American Meteorological Society, Boston, MA, 6 p.

Luck, D. (1949): Frequency Modulated Radar. McGraw-Hill, New York.

Lumley, J.L., and H.A. Panofsky (1964): The Structure of Atmospheric Turbulence, Monographs and Texts in Physics and Astronomy XII. Interscience Publishers, a Division of John Wiley and Sons, New York.

Marshall, J.S., and W.M.K. Palmer (1948): The distribution of raindrops with size. J. Meteorol., 5, 165-166.

Mason, B.J. (1971): The Physics of Clouds. Oxford Univ. Press, London and New York, 671 p.

McCormick, K.S., and A.J. Tangerud (1974): A lower power high resolution radar for tropospheric studies. Norwegian Defence Research Establishment, FFIE, Teknisk Notat E-652.

McAllister, L.G. (1968): Acoustic sounding of the lower troposphere. J. Atmos. Terr. Phys., 30, 1439-1440.

Metcalf, J. (1975): Microstructure of radar echo layers in the clear atmosphere. J. Atmos. Sci., 32, 362-370.

Monin, A.S., and A.M. Obukhov (1954): Basic regularity in turbulent mixing in the surface layer of the atmosphere. Trudy Geophys. Inst. ANSSSR, No. 24, p 163.

Moninger, W.R. (1980): Triple Doppler radar study of winter storms in the Sierra Nevada foothills Proc. 19th Conf. on Radar Meteor., Miami, Fla., American Meteorological Society, Boston, Mass. 17-21.

Moninger, W.R., A.S. Frisch, W.C. Campbell, and R.G. Strauch (1978): Doppler radar measurements of plume dispersal and dissipation rates in the boundary layer. Proc. 18th Conf. on Radar Meteorology, Atlanta, GA., American Meteorological Society, Boston, Mass., 49-53.

Moninger, W.R., and M. Sanders (1980): The MASTER system--an interactive Doppler radar data-processing system. NOAA Tech. Memo. ERL WPL-55, 55 p.

Miller, K.S., and M.M. Rochwarger (1972): A covariance approach to spectral moment estimation. IEEE Trans. Inf. Theory IT-18, 588-596.

Miller, L.J. (1975): Internal airflow of a convective storm from dual-Doppler radar measurements. Pageoph., 113, 715-785.

Miller, L.J. (1978): Horizontal airflow and precipitation fallspeed in a convective storm from triple Doppler radar measurements. Proc. 18th Weather Radar Conference, Atlanta, GA., Americal Meteorological Society, Boston, Mass., 207-211.

Miller, L.J., and R.G. Strauch (1974): A dual Doppler radar method for the determination of wind velocities within precipitating weather systems. Remote Sensing of Environ., 3, 219-235.

Naito, K., and D. Atlas (1966): On microwave scatter by partially coherent clouds. Proc. 12th Weather Radar Conference (Boston) pp 7-12.

Nathanson, F.E. (1969): Radar Design Principles. McGraw-Hill, New York.

Noonkester, V.R. (1976): The evolution of the clear air convective layer revealed by surface-based sensors. J. Appl. Meteorol., 15, 594-606.

Noonkester, V.R. (1978): Multisensor measurements of ocean based convective activity, in Proceedings of the 18th Conference on Radar Meteorology, pp 55-64, American Meteorological Society, Boston, Mass.

Noonkester, V.R., J.H. Richter, and D.R. Jensen (1976a): Meteorological interpretation of FM-CW radar and acoustic sounder echoes in a coastal environment, in Conference on Coastal Meteorology, Sept. 21-23, 1976, Virginia Beach, VA., preprint vol, pp 20-27, American Meteorological Society, Boston, Mass.

Noonkester, V.R., J.H. Richter, and D.R. Jensen (1976b): Marine fog investigations in San Diego, in Proceedings of the 17th Conference on Radar Meteorology, pp 282-289, American Meteorological Society, Boston, Mass.

Ottersten, H. (1969): Atmospheric structure and radar backscattering in clear air. Radio Sci., 4, 1179-1193.

Panchev, S. (1971): Random Functions and Turbulence. Pergamon Press, 444 p.

Pearson, K. (Ed.) (1951): Tables of the Incomplete Γ-Function. Cambridge Univ. Press, 164 pp.

Pena, J.A. (1977): Personal communication, Dept. of Meteorology, the Pennsylvania State University, Univ. Park, PA, 16802.

Petrocchi, P.J., and W.H. Paulsen (1966): Meteorological significance of vertical density profiles of clouds and precipitation obtained with the AN/TPQ-11 radar. Proc. 12th Radar Meteor. Conf., Norman, OK 467-472.

Plank, V.G. (1952): Refractive properties of air masses. Rep. No. 243, 28 pp, U.S. Naval Electronics Laboratory, San Diego, California.

Plank, V.G., D. Atlas, and W.H. Paulsen (1954): The nature and detectability of clouds and precipitation as determined by 1.25 centimeter radar. J. Meteorol., 12, 358-378.

Plank, V. (1956): A meteorological study of radar angles. Pap. 52, 117 pp., Geophys. Res. Dir., Air Force Cambridge Res. Lab., Hanscom Field, Bedford, Mass.

Probert-Jones, J.R. (1962): The radar equation in meteorology. Quart. J. Roy. Meteorol. Soc., 88, 485-495.

Pruppacher, H.R., and K.V. Beard (1970): A wind tunnel investigation of the internal circulation and shape of water drops falling at terminal velocity in air. Quart. J. Roy. Meteorol. Soc., 96, 247-256.

Pruppacher, H.R., and R.L. Pitter (1971): A semi-empirical determination of the shape of cloud and rain drops. J. Atmos. Sci., 28, 86-94.

Rastogi, P.K., and J. Röttger (1980): Radar detection of the tropopause by coherent reflections at very high frequencies. Proc. 19th Conf. on Radar Meteorol., Miami, Fla, USA, American Meteorological Society, Boston, Mass., 616-623.

Rayleigh, L. (1881): Scientific Paper 76, Phil. Mag., 12, 81.

Readings, C.J., E. Golton, and K.A. Browning (1973): Fine scale structure and mixing within an inversion. Boundary Layer Meteorol., 4, 275-287.

Richter, J.H. (1969): High resolution tropospheric radar sounding. Radio Sci., 4, 1261-1268.

Richter, J.H., and D.R. Jensen (1973): Radar cross-section measurements of insects. Proc. IEEE, 61, 143-144.

Richter, J.H., D.R. Jensen, V.R. Noonkester, J.B. Kreasky, M.W. Stillmann, and W.N. Wolf (1973b): Remote radar sensing, atmospheric structure and insects. Science, 180, 1176-1178.

Richter, J.H., D.R. Jensen, V.R. Noonkester, T.G. Konrad, A. Arnold, and J.R. Rowland (1974): Clear air convection: A close look at its evolution and structure. Geophys. Res. Lett., 1, 173-176.

Richter, J.H., and H.V. Hitney (1975): The effect of the evaporation duct on microwave propagation. U.S. Naval Electronics Laboratory, San Diego, Calif. Tech. Rept. TR 1949, 31 pp.

Riley, J.R. (1979): Radar as an aid to the study of insect flight, in A Handbook on Biotelemetry and Radio Tracking, edited by C.J. Amlaner, Jr., and D.W. Macdonald, pp. 131-141, Pergamon, New York.

Ricks, N.R. (1977): A feasibility study for the application of K-band radar in the investigation of cooling tower plumes. NOAA Tech. Memo., ERL-ARL-66, 39 p.

Rocco, M.D., and J.B. Smyth (1949): Diffraction of high-frequency radio waves around the earth. Proc. IRE, 37, 10, 1195-1203.

Röttger, J. (1978): Evidence for partial reflection of VHF radar signals from the troposphere. J. Geophys., 44, 393-394.

Rumler, W.D. (1968): Two-pulse spectral measurements. Tech. Memo. MM-68-4121-15, Bell Telephone Laboratories, Whippany, NJ.

Rüster, R., J. Röttger, and R.F. Woodman (1978): Radar measurements of waves in the lower stratosphere. Geophys. Res. Lett., 5, 555-558.

Sal'man, Ye. M. (Ed.) (1973): Radiolokatsionnaya Meteorologiya. Leningrad Gidrometeoizdat Press. (For English Translation see N75-16904 08-42) CSCL 04B, 210 p.

Schaefer, G.W. (1976): Radar observations of insect flight, from Insect Flight (R.C. Rainey, ed.), Proc. Symposium of Roy. Entom. Soc. of Lond., 157-197.

Seliga, T.A., and V.N. Bringi (1976): Potential use of radar differential reflectivity measurements at orthogonal polarizations for measuring precipitation. J. Appl. Meteorol., 15, 69-76.

Sellers, W.D. (1972): Physical Climatology. The University of Chicago Press, p 13.

Showalter, A.K. (1939): Further studies of American air mass properties. Mon. Weather Rev., 67, 204-218.

Sirmans, D., and B. Bumgarner (1975): Numerical comparison of five mean frequency estimators. J. Appl. Meteorol., 14, 991-1003.

Sloss, P.W., and D. Atlas (1968): Wind shear and reflectivity gradient effects on Doppler radar spectra. Preprints 13th Radar Meteor. Conf., Montreal, Amer. Meteor. Soc., 44-49.

Smith, R.L. (1964): Scattering of microwaves by cloud droplets. Proc. 11th Weather Radar Conference (Boulder, CO) pp. 202-207.

Srivastava, R.C., and S.D. Atlas (1972): The effects of a finite radar pulse volume on turbulence measurements. Preprints 15th Radar Meteor. Conf., Urbana, Ill., Amer. Meteor. Soc., 297-302.

Squires, P. (1958): The microstructure and colloidal stability of warm clouds. Pt. I, The relationship between structure and stability. Tellus, 10, 256-261.

Strauch, R.G. (1976): Theory of Application of the FM-CW Doppler Radar, Ph.D. Thesis, University of Colorado.

Strauch, R.G., and F.H. Merrem (1976): Structure of an evolving hailstorm, Part III: Internal structure from Doppler radar. Mon. Wea. Rev., 104, 588-595.

Strauch, R.B., W.C. Campbell, R.B. Chadwick, and K.P. Moran (1976): Microwave FM-CW Doppler radar for boundary layer probing. Geophys. Res. Lett., 3, pp 193-196.

Strauch, R.G., R.A. Kropfli, W.B. Sweezy, W.R. Moninger, and R.W. Lee (1978): Improved Doppler velocity estimates by the poly-pulse-pair method. Proc. 18th Conf. on Radar Meteor., Atlanta, GA, American Meteorological Soc., Boston, Mass.

Tatarski, V.I. (1961): Wave Propagation in a Turbulent Medium, translated by R.A. Silverman, McGraw-Hill, New York, 285 p.

VanZandt, T.E., J.L. Green, K.S. Gage, and W.L. Clark (1978): Vertical profiles of refractivity turbulence structure constant: comparison of observations by the Sunset radar with a new theoretical model. Radio Sci., 13, 819-829.

Villars, F., and V.F. Weisskopf (1955): On the scattering of radio waves by turbulent fluctuations in the atmosphere. Proc. IRE, 43, pp. 1232-1239.

Warner, C. (1977): Calculations of backscattering and depolarization by wet hailstones at 2.88 GHz. Scientific Rept. 17w-90, McGill Univ., 57 p.

Waterman, P.C. (1965): Matrix formulation of electromagnetic scattering. Proc. IEEE, 53, 805-812.

Weickmann, H.K., and H.J. aufm Kampe (1953): Physical properties of cumulus clouds. J. Meteorol., 10, 204-211.

Wexler, R. (1955): An evaluation of the physical effects in the melting layer. Proc. Fifth Wea. Radar Conf., Fort Monmouth, NJ, 329-34.

Woodman, R.F., and A. Guillen (1974): Radio observations of winds and turbulence in the stratosphere and mesosphere. J. Atmos. Sci., 31, 493-505.

Woodman, R.F. (1980): High-altitude-resolution stratospheric measurements with the Arecibo 430-MHz radar. Radio Sci., 15, this issue.

Woodman, R.T., R.P. Kugel, and J. Röttger (1980): A coherent integrator-decoder preprocessor for the 50MHz SOUSY radar. Radio Sci., 15, this issue.

Woodward, P.M. (1967): Radar ambiguity analysis. RRE Tech Note 731 (AD-653404), Royal Radar Establishment, England.

Wyngaard, J.C., Y. Izumi, and S.A. Collins, Jr. (1971): Behavior of the refractive-index-structure parameter near the ground. J. Optical Soc. of Amer., 61, 12, 1646-1650.

Wyngaard, J.C., and O.R. Coté (1971): The budgets of turbulent kinetic energy and temperature variance in the atmospheric surface layer. J. Atmos. Sci., 28, 190-201.

Wyngaard, J.C., W.T. Pennell, D.H. Lenshaw, and M.A. LeMone (1978): The temperature-humidity covariance budget in the convective boundary layer. J. Atmos. Sci., 35, 48-58.

Wyngaard, J.C., and M.A. LeMone (1980): Behavior of the refractive index structure parameter in the entraining convective boundary layer. J. Atmos. Sci., 37, 1573-1585.

BEST DOCUMENT AVAILABLE

APPENDIX A - SOME FUNDAMENTAL RADAR RELATIONSHIPS

The Radar Equation

The power intercepted and reradiated by a target in the center of a radar beam is

$$\frac{P_t G_T A_T}{4\pi r^2} \tag{1A}$$

where P_t is transmitted power, G_T is gain of the transmitting antenna, and A_T is the target cross-sectional area. If the target scatters isotropically, the power intercepted by the receiving antenna is

$$P_r = \frac{P_t G_T A_T}{4\pi r^2} \frac{A_e}{4\pi r^2} . \tag{2A}$$

The effective area A_e of the receiving antenna is related to its gain by

$$A_e = G_R \frac{\lambda^2}{4\pi} . \tag{3A}$$

For a parabola whose aperture is A_p

$$G_R \simeq A_p \frac{8\pi}{3\lambda^2} \text{ so } A_e \simeq \frac{2}{3} A_p . \tag{4A}$$

Early derivations of the radar equation assumed the power to be constant between half-power points of the beam and zero elsewhere. For such a "top hat" beam

$$G_R = 16/\theta\phi \tag{4Aa}$$

or just $G_R = 16/\theta^2$ if the beam is conical with beamwidth θ (rad). However, Probert-Jones (1962) studied the more realistic case of a Gaussian beam. The gain of such an antenna is related to its beamwidths θ,ϕ in radians, as

$$G_R = k^2 \pi^2/\theta\phi \tag{4Ab}$$

where k^2 is a dimensionless constant near unity depending on how much of the power from a particular antenna feed is intercepted by the dish. If we consider a parabolic dish of diameter D,

BEST DOCUMENT AVAILABLE

$$\theta = \phi = 1.56\ \lambda/D \tag{5A}$$

for a top hat beam, and from Eq. (4A) and Eq. (4Ab)

$$\theta = \phi = 1.22\ \lambda/D \tag{5Aa}$$

for a Gaussian beam; thus $G_R = k^2\pi^2\ D^2/(1.22\ \lambda)^2$ for $\phi = \theta$.

If we replace the geometrical target cross-sectional area with the backscattering cross-section σ (which is the ratio of the actual backradiated power by the target to the power that would have been backscattered by an isotropic scatter) and replace A_e in Eq. (2A) using Eq. (3A), we find

$$P_r = P_t \frac{G^2\ \sigma\ \lambda^2}{64\pi^3\ r^4} \quad . \tag{6a}$$

Radar Reflectivity and Backscatter

Separating the system parameters from target parameters and range, we can write

$$P_r = \frac{P_t\ G^2\ \lambda^2}{64\pi^3}\ \frac{\sigma}{r^4} = K\ \frac{\sigma}{r^4} \quad . \tag{7A}$$

If N is the total number of scatterers in a volume V, the total received power is

$$P_r = \frac{K}{r^4} \sum_{i=1}^{N} \sigma_i \ . \tag{8A}$$

If we choose to express the summation in terms of an <u>average</u> reflectivity per unit volume, it can be written

$$P_r = \frac{K}{r^4}\ \eta V \tag{9A}$$

where V is volume and the quantity

$$\eta = \frac{1}{V} \sum_{i=1}^{N} \sigma_i \tag{10A}$$

is the so-called radar reflectivity.

If τ is the pulse length, the effective pulse volume for distances much greater than a pulse length is approximately

BEST DOCUMENT AVAILABLE

$$V = \frac{\pi r^2 \theta\phi c}{8} \tag{11A}$$

where θ and ϕ are the radar beamwidths of a top hat beam. Insertion into Eq. (9A) yields, for the top hat beam,

$$P_r = \frac{P_t G^2 \lambda^2}{64\pi^2} \frac{\eta}{r^2} \frac{\theta\phi c\tau}{8} \quad . \tag{12A}$$

For a Gaussian beam the integration over the intercepted volume should include the gain function, so

$$P_r = \frac{P_t \lambda^2}{\ell 4\pi^3} \int_V \frac{G^2 \theta\phi\eta}{r^4} \, dV \tag{13A}$$

which may be integrated to yield (Probert-Jones, 1962)

$$P_r = \overbrace{\frac{c}{1024\pi^2 \ell n 2}}^{\text{constant}} \quad \overbrace{(P_t \tau \lambda^2 G_o^2 \theta\phi)}^{\text{radar parameters}} \quad \overbrace{\frac{\eta}{r^2}}^{\text{target parameters}} \tag{14A}$$

where G_o is defined by the following expression for gain with a Gaussian beam:

$$G(\theta,\phi) = G_o \exp - \left[\left(\frac{\theta^2}{2\sigma_\theta^2} + \frac{\phi^2}{2\sigma_\phi^2}\right)\right] .$$

Probert-Jones took account of the fact that when the entire transmitted beam is filled with targets the two-way beam pattern must be used to find the received power and the equivalent cone for two way transmission reduces the received power by the factor 2 ℓn 2) which appears in the constant factor of Eq. (14A).

After eliminating G using (3A) and (4Aa), Eq. (12A) gives for a "top hat" beam:

$$P_r = 0.0795 \, P_t A_e \frac{\Delta}{r^2} \eta \tag{15A}$$

where $\Delta = c\tau/2$ is the range cell depth. From Eqs. (14A), (3A) and (4Ab) we find a Gaussian beam:

$$P_r = 0.0354 \, P_t A_e \frac{\Delta}{r^2} \eta \quad . \tag{15Aa}$$

We see that calculated received power will be overestimated by 3.5 dB if a "top hat" beam is assumed as was done prior to 1962; 1.4 dB results from the 2 ℓn 2 factor and 2.1 dB from the $16/\pi^2$ factor relating beamwidth and gain.

BEST DOCUMENT AVAILABLE

Backscatter from Spherical Drops

For spherical targets σ and η can be related to the refractive index of the particulate (say ice or water). From Mie theory for backscattering from a spherical drop

$$\sigma = \frac{\pi a^2}{\alpha^2} \left| \sum_{j=1}^{\infty} (-1)^j (2j+1) (a_j - b_j) \right|^2 \qquad (16A)$$

where

a is drop radius

$\alpha = 2\pi a/\lambda$

a_j are the coefficients of terms arising from induced magnetic dipoles, quadrapoles, etc.

b_j are the coefficients of terms arising from induced electric dipoles, quadrapoles, etc.

j number of the term in the expansion.

The coefficients a_j, b_j can be expressed in terms of Bessel and Hankel functions of the 2nd kind with arguments α and refractive index

$$m = n - ik$$

where n is refractive index and k is the absorption coefficient. In the Rayleigh approximation of $a \ll \lambda$

$$\sigma_i = \frac{\lambda^2}{\pi} \alpha^6 \left| \frac{m^2 - 1}{m^2 + 2} \right|^2 = \frac{(2\pi)^6 a^6}{\lambda^6} \frac{\lambda^2}{\pi} |K|^2 = \frac{2^6 \pi^5 a^6}{\lambda^4} |K|^2 \qquad (17A)$$

so

$$\sigma \equiv \sum_i \sigma_i = \frac{\pi^5}{\lambda^4} |K^2| \sum_i N_i D_i^6 \qquad \text{in the Rayleigh limit} \qquad (18A)$$

or

$$\sigma = \frac{36\pi^3}{\lambda^4} \frac{|K|^2}{\rho^2} \frac{M^2}{\Sigma N_i} \qquad (19A)$$

where $K = |(m^2 - 1)/(m^2 + 2)|$. $|K|^2 \approx 0.93$ for water, D is drop diameter, ρ is density $= 1.0$ gm cm^{-3} and $M = (\pi/6) \rho \Sigma N_i D_i^3$ is the mass of liquid water per unit volume.

Radar reflectivity (Eq. 10A) is thus related to the radar reflectivity factor,

BEST DOCUMENT AVAILABLE

$$Z = \sum_i N_i D_i^6 \quad \text{(where the summation is over all size increments in a unit volume)} \tag{20A}$$

as

$$\eta = \frac{\pi^5 |K|^2 Z}{\lambda^4} \tag{21A}$$

so

$$Z = \frac{\lambda^4 \eta}{\pi^5 |K|^2} \quad . \tag{22A}$$

Since the total mass of water in the unit volume is $M = (\pi/6)\rho\Sigma N_i D_i^3$ we have from (20A)

$$Z = \frac{36M^2}{\rho^2 \pi^2 N} \tag{23A}$$

if the volume is assumed to contain N drops of uniform size $\bar{D}$ so that $Z = N\bar{D}^6$. The reflectivity factor Z is usually expressed in units of (mm^6/m^3) introducing a factor of 10^{18}; thus from Eqs. (15A) and (21A)

$$Pr = 2.26 \times 10^{-17} \frac{P_t A_e}{\lambda^4} \frac{\Delta}{r^2} Z \qquad \text{(top hat beam)}$$

and from Eqs. (15Aa) and (21A)

$$Pr = 1.01 \times 10^{-17} \frac{P_t A_e}{\lambda^4} \frac{\Delta}{r^2} Z \qquad \text{(Gaussian beam)} \ .$$

Doppler Radars

Pulse Radars

The basic relation between radial velocity of a target and Doppler frequency shift is

$$V = (\lambda/2)\ \Delta\phi/T = (\lambda/2)\ f_D \tag{24A}$$

where T is the pulse repetition period, $\Delta\phi$ is pulse to pulse change in path length to the target (measured in wavelengths) and f_D is the corresponding Doppler frequency shift. Because the sampling period is T the maximum frequency that can be sensed unambiguously (the Nyquist frequency), is

$$f_{D(Max)} = (2T)^{-1} \ . \tag{25A}$$

Whence

$$\Delta f_D = (2T)^{-1}/N/2 = (NT)^{-1} \ . \tag{26A}$$

BEST DOCUMENT AVAILABLE

Therefore, the maximum radial velocity that can be sensed without "folding" is

$$V_M = \frac{\lambda}{4T} \quad ; \tag{27A}$$

so the total unambiguous range is $\pm \lambda/4T$. From (26A), the velocity resolution ΔV is

$$\Delta V = \frac{\lambda}{2NT} \ . \tag{28A}$$

FM-CW Radars

For a linearly frequency modulated, continuous wave (CW) system, the important parameters are defined in Fig. 1A. The basic sampling interval during a sweep is Δt, but T is the effective sampling interval in the Doppler velocity computation because target range changes from sweep-to-sweep are used to determine velocity. N is the number of sweeps, and the number of samples per sweep is M.

From Fig. 1A, target range is

$$R \doteq \frac{cTf}{2B} \tag{29A}$$

where f, the signal frequency which determines target range is much greater than the Doppler frequency. Since the maximum frequency sampled by a digital system (the Nyquist frequency) is $(2\Delta t)^{-1}$, the maximum range without "folding" is given by

$$R_M = \frac{cT}{4B\Delta t} \tag{30A}$$

and, since the maximum resolution in the frequency spectrum is therefore $(2\Delta t)^{-1}/1/2\ M = (M\Delta t)^{-1} = T^{-1}$, the range resolution is

$$\Delta R = \frac{cT}{2M\Delta tB} = \frac{c}{2B} \ . \tag{31A}$$

Therefore, the Doppler velocity is given by (24A), i.e.,

$$V = (\lambda/2)\ \Delta\phi/T \equiv (\lambda/2)\ f_D \tag{32A}$$

where $\Delta\phi$ corresponds to the change in path length from sweep to sweep and is also the change in phase from sweep to sweep of the signal; f_D is the corresponding Doppler frequency shift. Therefore the maximum velocity without

BEST DOCUMENT AVAILABLE

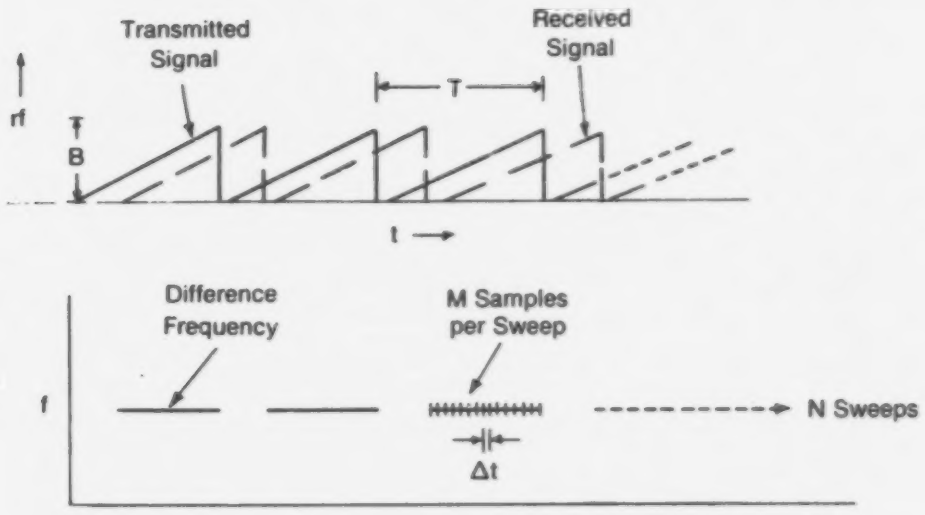

Figure 1A.--Schematic picture of the modulation of digital FM-CW radar.

folding (see Fig. 7-1) is $(\lambda/2)\ f_{D(max)}$ where $f_{D(max)}$ is, again, the Nyquist frequency; i.e., $f_{D(max)} = (2T)^{-1}$ whence the maximum frequency resolution is

$$\Delta f_D = (2T)^{-1}/(N/2) = (NT)^{-1} . \qquad (33A)$$

Therefore, from (32A), the maximum radial velocity without folding is

$$V_M = \pm \frac{\lambda}{4T} \qquad (34A)$$

and, from (33A), the velocity resolution is

$$\Delta V = \frac{\lambda}{2NT} . \qquad (35A)$$

Equations (34A) and (35A) are identical to (27A) and 28A) except for the different definitions of T.

BEST_DOCUMENT AVAILABLE

APPENDIX B - RELATIONSHIPS BETWEEN N AND ϕ

Dividing (1-13) by (1-12),

$$\phi = N\left(\frac{1000}{p}\right)^{.714} (1 + 4810\ e/p\theta)/(1 + 4810\ e/pT). \quad (1B)$$

Eq. (1A) can easily be rewritten in terms of $q = 0.622\ \rho e/p$ (gr m^{-3}) where ρ is air density. Writing θ in terms of p and T, ϕ can be expressed in terms of pressure, temperature and N. However, we are often given temperature and humidity as functions of height rather than pressure, so it is useful to express ϕ in terms of N and height.

Writing the denominator of (1B) as TN/77.6p it is evident that

$$\phi = \left(\frac{1000}{p}\right)^{.714} \frac{77.6}{T}\left[p + \frac{4810e}{T}\left(\frac{1000}{p}\right)^{-.286}\right]. \quad (2B)$$

Combining the hydrostatic equation,

$$dp = -\rho g\, dz \quad (3B)$$

with the equation of state,

$$\rho = \frac{p}{RT} \quad (4B)$$

where ρ is density, $g = 9.8$ m s^{-2} is gravitational acceleration and $R = 2.87 \times 10^{-3}$ mb m^3 gr^{-1} deg^{-1} is the (dry) gas constant, we readily find that

$$d(\ln p) = -\frac{g}{RT}\, dz\ .$$

Therefore

$$\frac{1000}{p} = e^{(g/R\bar{T})(z-z_o)} \quad (5B)$$

where $\bar{T}$ is the value of T logarithmically averaged over the interval $z-z_o$ and z_o is the height at the 1000 mb level. Thus we define a function f(z) such that

$$\left(\frac{1000}{p}\right)^{-.286} \approx 1 - 0.286\ (g/R\bar{T}\ (z-z_o) + \frac{1}{2}\ [0.286\ (g/R\bar{T})\ (z-a_o)^2 \ldots \equiv f(z)$$

which converges quickly because $0.286\ \frac{g}{RT}\ (z-z_o)$ is fairly small (i.e., <0.29) for heights less than about 9 km. The next term in the expansion would contribute less than 0.4 percent at a height of 7.5 km.

BEST DOCUMENT AVAILABLE

Finally, assuming an exponential density distribution of scale height H, equation (5B) gives

$$\rho_o \, e^{-z/H} = (p/R\bar{T})$$

so

$$\frac{\partial p}{\partial z} = - \rho_o e^{-z/H} \, g \, dz = - (R\bar{T}/H) \, \rho_o e^{-z/H}$$

or

$$H = \frac{R\bar{T}}{g} \qquad (6B)$$

is the scale height for the height interval $z-z_o$. Therefore, eliminating e from Eq. (2B) using (1-12), ϕ can be expressed in terms of N, H(T) and z as

$$\phi = e^{0.714z/H} \, [N \, f(z) + (77.6)(0.286)(p/T)z/H] \, . \qquad (7B)$$

However from (4A) $p/T = \rho_o \, R \, e^{-z/H} \simeq 3.47 \, e^{-z/H}$ assuming the 1000 mb density $\rho_o \simeq 1.21 \times 10^3$ gr m^{-3}. For soundings at Denver, p ≃ 850 mb where one millibar i one dyne $cm^{-2} = 10^4$ dynes m^{-2}). From (7A)

$$\phi = e^{0.714z/H} \, [N \, f(z) + 77.0 \, (z/H)e^{-z/H}] \, . \qquad (8B)$$

The magnitudes of terms can be estimated by noting that N closely follows an exponential height distribution such that $N = N_s \, e^{-z/H}$ where, according to Bean and Dutton (1966), H ≃ 7 km when N_s is the sea level value of N. (H ≃ 8 km for the density distribution). For the profile in Fig. 5, we estimate $N_s \simeq 330$; so, ignoring the small differences in H, Eq. (8B) can be written

$$\phi \simeq e^{.714z/H} \, [330 \, e^{-z/H} - (0.286)(330)(z/H)e^{-z/H} + 77.0 \, (z/H)e^{-z/H}$$

$$+ 13.5 \, (z/H)^2 \, e^{-z/H}] \, .$$

The last three terms in braces approximately cancel for $z/H \simeq 1.0$ and become small for $z/H \ll 1.0$. Therefore, to a good approximation

$$\phi \simeq N \, e^{.714 \, z/H}$$

and, at constant height,

$$d\phi = \frac{\partial \phi}{\partial N} \, dN$$

whence

$$C_\phi^{\,2} = e^{1.428 \, z/H} \, C_N^{\,2} \qquad (9B)$$

where $C_N^{\,2} = C_n^{\,2} \times 10^{12}$ from the definition, $N = (n-1) \times 10^6$.

BEST DOCUMENT AVAILABLE

APPENDIX C

TABLE I--(Adapted from Pearson, 1951 Ed.)

TABLES OF THE INCOMPLETE GAMMA FUNCTION

m = 1/7			m = 1/4			m = 1/3		
ax/z^{2m+1}	$z/(ax)^{1/(2m+1)}$	$I(\zeta,m)^*$	ax/z^{2m+1}	$z/(ax)^{1/(2m+1)}$	$I(\zeta,m)^*$	ax/z^{2m+1}	$z/(ax)^{1/(2m+1)}$	$I(\zeta,m)^*$
∞	0	1.0000	∞	0	1.0000	∞	0	1.0000
8.3129	0.1926	0.2777	6.0178	0.3022	0.6054	4.8299	0.3887	0.4193
4.1564	0.3302	0.2252	3.0089	0.4798	0.5182	4.4149	0.5891	0.3378
2.7709	0.4526	0.1895	2.0059	0.6287	0.7303	1.6099	0.7514	0.2869
2.0782	0.5661	0.1660	1.5044	0.7616	0.7649	1.2074	0.2930	0.2500
1.6625	0.6734	0.1478	1.2035	0.8838	0.7918	0.9659	1.0209	0.2212
1.3854	0.7760	0.1331	1.0029	0.9980	0.8137	0.8049	1.1390	0.1977
1.1875	0.8748	0.1209	0.8596	1.1060	0.8320	0.6899	1.2493	0.1781
1.0891	1.9706	0.1104	0.7522	1.2090	0.8476	0.6037	1.3535	0.1614
0.9236	1.0637	0.1014	0.6686	1.3077	0.8611	0.5366	1.4527	0.1469
0.8312	1.1545	0.0935	0.6017	1.4029	0.8729	0.4829	1.5475	0.1343
0.4156	1.9793	0.0473	0.3008	2.2270	0.9407	0.2414	2.3456	0.0617
0.2770	2.7131	0.0269	0.2005	2.9182	0.9705	0.1609	2.9916	0.0317
0.2078	3.3934	0.0162	0.1504	3.5352	0.9830	0.1207	3.5552	0.0172
0.1662	4.0366	0.0101	0.1203	4.1022	0.9903	0.0965	4.0646	0.0096
0.1385	4.6515	0.0064	0.1002	4.6324	0.9944	0.0804	4.5344	0.0055
0.1187	5.2440	0.0042	0.0859	5.1337	0.9967	0.0689	4.9739	0.0032
0.1039	4.8179	0.0027	0.0752	5.6117	0.9980	0.0603	5.3888	0.0019
0.0923	6.3759	0.0018	0.0668	6.0701	0.9988	0.0536	5.7834	0.0011
0.0831	6.9204	0.0012	0.0601	6.5119	0.9954	0.0482	6.1608	0.0007

* $$I(\zeta,m) = \frac{\int_{\zeta}^{\infty} \zeta^{-(m+1)(2m+1)} e^{-\zeta}\, d\zeta}{\int_{0}^{\infty} \zeta^{-(m+1)/(2m+1)} e^{-\zeta}\, d\zeta}, \quad \zeta = x^{2m+1}/(2x+1)^2\, ax$$

TABLE II--(Adapted from Pearson, 1951 Ed.)

TABLES OF THE INCOMPLETE GAMMA FUNCTION

m = 1/7			m = 1/4			m = 1/3		
$at/z^{(m+1)}$	$z/(at)^{1/(m+1)}$	$I(\xi,m)^*$	$at/z^{(m+1)}$	$z/(at)^{1/(m+1)}$	$I(\xi,m)^*$	$at/z^{(m+1)}$	$z/(at)^{1/(m+1)}$	$I(\xi,m)^*$
∞	0	1.0000	∞	0	1.0000	∞	0	1.0000
7.1595	0.1786	0.8734	5.7243	0.2476	0.8504	6.2921	0.2516	0.8326
3.5797	0.3276	0.7777	2.8622	0.4312	0.7494	3.1460	0.4232	0.7284
2.3865	0.4671	0.6961	1.9081	0.5964	0.6663	2.0974	0.5737	0.6447
1.7898	0.6009	0.6249	1.4310	0.7507	0.5953	1.5730	0.7119	0.5742
1.4319	0.7304	0.5621	1.1449	0.8974	0.5336	1.2584	0.8416	0.5136
1.1932	0.8567	0.5063	0.9541	1.0383	0.4794	1.0487	0.9650	0.4607
1.0227	0.9804	0.4565	0.8178	1.1746	0.4315	0.8989	1.0833	0.4142
0.8949	1.1019	0.4120	0.7155	1.3070	0.3889	0.7865	1.1974	0.3730
0.7955	1.2215	0.3721	0.6360	1.4362	0.3510	0.6991	1.3080	0.3365
0.7159	1.3395	0.3363	0.5724	1.5625	0.3170	0.6292	1.4156	0.3038
0.3579	2.4565	0.1246	0.2862	2.7205	0.1184	0.3146	2.3811	0.1141
0.2386	3.5025	0.0471	0.1908	3.7629	0.0455	0.2097	3.2275	0.0445
0.1789	4.5050	0.0179	0.1431	4.7366	0.0178	0.1573	4.0050	0.0177
0.1431	5.4762	0.0068	0.1145	5.6623	0.0070	0.1258	4.7348	0.0071
0.1193	6.4232	0.0026	0.0954	6.5515	0.0028	0.1049	5.4288	0.0029
0.1022	7.3506	0.0010	0.0818	7.4114	0.0011	0.0899	6.0943	0.0012
0.0894	8.2616	0.0003	0.0716	8.2469	0.0004	0.0787	6.7364	0.0005
0.0795	9.1584	0.0008	0.0636	9.0618	0.0002	0.0699	7.3587	0.0002
0.0715	10.0427	0.0000	0.0572	9.8588	0.0000	0.0629	7.9640	0.0000

* $$I(\xi_o,m) = \frac{\int_{\xi_o}^{\infty} \xi^{-m/(1+m)} e^{-\xi}\, d\xi}{\int_{0}^{\infty} \xi^{-m/(1+m)} e^{-\xi}\, d\xi}, \quad \xi = x^{m+1}/(m+1)^2\, at$$

BEST DOCUMENT AVAILABLE

APPENDIX D - RELATIONSHIP BETWEEN DOPPLER SPECTRAL WIDTH AND TURBULENCE

One of the functions that contribute to Doppler spectral width is turbulence because turbulence causes different scatterers in the resolution volume to move with different radial velocity. In the discussion of velocity variance and spectrum broadening, the fundamental concepts and definitions are important. A covariance will be used which is defined as

$$C_{\underset{\sim}{\ell}}(\underset{\sim}{\ell}) = \langle u_{\ell}(\underset{\sim}{r}_1)\, u_{\ell}(\underset{\sim}{r}_1 + \underset{\sim}{\ell})\rangle \tag{1D}$$

where $\underset{\sim}{\ell}$ is the separation of two positions, $\underset{\sim}{r}_1 - \underset{\sim}{r}_2$, and $\langle\ \rangle$ signifies an average over ensembles. By such an average, it is meant that cross-covariances are computed for time series from sensors separated by a distance $\underset{\sim}{\ell}$, resulting in the function $C(\underset{\sim}{\ell})$. Clearly, if $\underset{\sim}{\ell}$ is small compared with scale sizes in u, the covariance is large; if $\underset{\sim}{\ell}$ is large, the covariance will tend toward zero for noisy processes. When $\underset{\sim}{\ell} = 0$, Eqn. (1D) defines the variance

$$\sigma_{\ell}^2 = \langle u_{\ell}^2 \rangle \ . \tag{2D}$$

It should be noted that the Ergodic Hypothesis states that this kind of ensemble average is the same as the time average of the spatial autocorrelation functions for infinite space and time samples in temporally and spatially homogeneous media.

The covariance function bears the well-known Fourier Transform relation to the velocity spectral density tensor, so

$$C_{ij}(\underset{\sim}{r}_1 - \underset{\sim}{r}_2) = \int \phi_{ij}(\underset{\sim}{\kappa}) e^{i\underset{\sim}{\kappa}\cdot(\underset{\sim}{r}_1 - \underset{\sim}{r}_2)}\, d\underset{\sim}{\kappa} \tag{3D}$$

and

$$\phi_{ij}(\underset{\sim}{\kappa}) = \frac{1}{(2\pi)^3} \int C_{ij}(\underset{\sim}{\ell}) e^{-i\underset{\sim}{\kappa}\cdot\underset{\sim}{\ell}}\, d\underset{\sim}{\ell} \ . \tag{4D}$$

Therefore, the temporal variance of velocity at a point (or the temporal average of the squared differences over an infinite ensemble of spatial points) is

$$\sigma^2 = C_{ii}(0) = \int \phi_{ii}(\underset{\sim}{\kappa})\, d\underset{\sim}{\kappa} \ . \tag{5D}$$

If both velocity components are along the x direction; the longitudinal velocity correlation function

$$C_{\ell\ell}(\underset{\sim}{r}_1 - \underset{\sim}{r}_2) = \int \phi_{\ell\ell}(\underset{\sim}{\kappa})\, d\underset{\sim}{\kappa} \ . \tag{6D}$$

BEST DOCUMENT AVAILABLE

The turbulence broadening of the spectrum results from the variance of radial velocity within the pulse volume. This variance is the difference between the total variance σ^2 containing contributions from all scales, and the variance of the radial velocity averaged over the pulse volume $\sigma_{\bar{u}}^2$. Thus the broadening that results from the variance in radial velocity is (Frisch and Clifford, 1974):

$$\sigma_{\ell\ell} = \sigma^2 - \sigma_{\bar{u}}^2 \ . \tag{7D}$$

The spatial average $\bar{u}$ is by definition

$$\bar{u} = \frac{1}{V} \iiint_{-\infty}^{\infty} A(x,y,z)\ u\ dx\ dx\ dz \equiv \frac{1}{V} \int A(\underset{\sim}{r})\ u(\underset{\sim}{r})\ d\underset{\sim}{r} \tag{8D}$$

where A is the antenna illumination function. Therefore,

$$\bar{u}\ \bar{u} = \frac{1}{V^2} \int A(\underset{\sim}{r}_1)\ u(\underset{\sim}{r}_1)\ d\underset{\sim}{r}_1 \int A(\underset{\sim}{r}_2)\ u(\underset{\sim}{r}_2)\ d\underset{\sim}{r}_2$$

and

$$\sigma_{\bar{u}}^2 = \langle \bar{u}\ \bar{u} \rangle = \frac{1}{V^2} \iint A(\underset{\sim}{r}_1)\ A(\underset{\sim}{r}_2)\ \langle u(r_1)\ u(r_2) \rangle\ d\underset{\sim}{r}_1\ d\underset{\sim}{r}_2 \ .$$

So, using Eq. (1D)

$$\sigma_{\bar{u}}^2 = \frac{1}{V^2} \iint A(\underset{\sim}{r}_1)\ A(\underset{\sim}{r}_2)\ C_{\ell\ell}(r_1 - r_2)\ d\underset{\sim}{r}_1\ d\underset{\sim}{r}_2 \ . \tag{9D}$$

Then Eqs. (6D), (7D), (8D), (9D) give

$$\sigma_{\ell\ell}^2 = \int \phi_{\ell\ell}(\underset{\sim}{\kappa})\ \ 1 - \frac{1}{V^2} \int A(\underset{\sim}{r}_1) e^{i\underset{\sim}{\kappa}\cdot\underset{\sim}{r}_1}\ d\underset{\sim}{r}_1 \int A(r_2) e^{i\underset{\sim}{\kappa}\cdot\underset{\sim}{r}_2}\ dr_2\ \ d\underset{\sim}{\kappa} \ . \tag{10D}$$

If Eq. (6D) is used in Eq. (9D), we obtain the basic result of Srivastava and Atlas (1972) for the filtering effect of volume averaging by the radar pulse, i.e.,

$$\phi_{\bar{u}}(\underset{\sim}{\kappa}) = \phi_{\ell\ell}(\underset{\sim}{\kappa})(2\pi)^6 |F_I(\underset{\sim}{\kappa})|^2 \tag{11D}$$

where we have defined $\phi_{\bar{u}}(\underset{\sim}{\kappa})$ by the relationship $\sigma_{\bar{u}}^2 = \int \phi_{\bar{u}}(\underset{\sim}{\kappa})\ d\underset{\sim}{\kappa}$ and the notation $|F_I(\underset{\sim}{\kappa})|^2$ has been chosen for convenient cross reference with

BEST_DOCUMENT AVAILABLE

rivastava and Atlas. Thus, in our notation their $|F_I(\underset{\sim}{\kappa})|^2$ is

$$|F_I(\underset{\sim}{\kappa})|^2 = \frac{1}{(2\pi)^6 V^2} \int A(\underset{\sim}{r}_1) e^{i\underset{\sim}{\kappa}\cdot\underset{\sim}{r}_1} d\underset{\sim}{r}_1 \int A(\underset{\sim}{r}_2) e^{i\underset{\sim}{\kappa}\cdot\underset{\sim}{r}_2} d\underset{\sim}{r}_2 \qquad (12D)$$

so that

$$\sigma_{\ell\ell}^2 = \int \phi_{\ell\ell}(\underset{\sim}{\kappa}) \left[1 - (2\pi)^6 |F_I(\underset{\sim}{\kappa})|^2\right] . \qquad (13D)$$

A convenient (and fairly realistic) function to choose for $A(\underset{\sim}{r})$ (the two-way illumination function) is a Gaussian beam cross section and a Gaussian shaped pulse; thus, following Frisch and Clifford (1974), we choose

$$A(\underset{\sim}{r}) = e^{-\frac{x^2}{2b^2} - \frac{y^2 + z^2}{2a^2}} \qquad (14D)$$

where a and b are the standard deviations of the linear beamwidth and pulse length. The linear beamwidth is related to the angular beamwidth by $a = \frac{B}{\sqrt{8\ell n 4}}$ where B is the 1-way half power angular beamwidth. The pulse volume is therefore

$$V = \int A(\underset{\sim}{r})\, d\underset{\sim}{r} = (2\pi)^{3/2}\, b\, a^2 . \qquad (15D)$$

Then, letting $\kappa^2 = \kappa_x^2 + \kappa_y^2 + \kappa_z^2$ and $r^2 = x^2 + y^2 + z^2$, we find

$$\frac{1}{V} \int A(\underset{\sim}{r}) e^{i\underset{\sim}{\kappa}\cdot\underset{\sim}{r}}\, d\underset{\sim}{r} = \frac{1}{V} \iiint e^{-x^2/2b^2 - y^2/2a^2 - z^2/2a^2}\, e^{i(\kappa_x x + \kappa_y y + \kappa_z z)}$$

$$= e^{-(1/2)(\kappa_x^2 b^2 + \kappa_y^2 a^2 + \kappa_z^2 a^2)}$$

whence

$$|F_I|^2 = \frac{1}{(2\pi)^6} e^{-(\kappa_x^2 b^2 + \kappa_y^2 a^2 + \kappa_z^2 a^2)} . \qquad (16D)$$

The following solution is from Labbitt (1980). Let

$$\kappa_x^2 = \kappa^2 \cos^2\phi$$

$$d\underset{\sim}{\kappa} = \kappa^2 \sin\phi\, d\phi\, d\theta\, d\kappa$$

BEST DOCUMENT AVAILABLE

and convert to polar coordinates (see Fig. 2-3 for reference). Using Eq. (13E) in (9E) for $\phi(\underset{\sim}{\kappa})$ and using Eqs. (12D) and (9E) in (13D), we find, noting that the integral over θ is just 2π, that

$$\sigma_{\ell\ell}^2 = \frac{\alpha\varepsilon^{2/3}}{2} \int_0^{\pi} \sin^3\phi \int_0^{\infty} \kappa^{-5/3} \left[1 - e^{-\kappa^2(a^2\sin^2\phi + b^2\cos^2\phi)}\right] d\kappa \, d\phi \, .$$

Labbitt (1980) points out that a solution for the inner integral has the form (e.g., Gradshteyn and Ryzhik [1965])

$$\int_0^{\infty} x^{\nu-1} \left(1 - e^{-\mu x^p}\right) dx = \frac{1}{|p|} \mu^{-\frac{\nu}{p}} \Gamma\left(\frac{\nu}{p}\right)$$

so that

$$\sigma_{\ell\ell}^2 = \frac{9}{8} \alpha\varepsilon^{2/3} \Gamma(5/3) \int_0^{\pi} \sin^3\phi (a^2 \sin^2\phi + b^2\cos^2\phi)^{1/3} \, d\phi \, .$$

Substituting $t = \cos^2\phi$

$$\sigma_{\ell\ell}^2 = \frac{9}{4} \alpha\varepsilon^{2/3} \Gamma(5/3) \, a^{2/3} \int_0^1 (1 - t)\left(1 - \left[1 - \frac{b^2}{a^2}\right]t\right)^{1/3} t^{-1/2} \, dt \, .$$

The integral representation of the Gaussian hypergeometric function is given by (e.g., Abramowitz and Stegan [1964])

$$F(a,b;\, c;\, z) = \frac{\Gamma(c)}{\Gamma(b)\,\Gamma(c-b)} \int_0^1 t^{b-1} (1 - t)^{c-b-1} (1 - tz)^{-a} \, dt$$

where $\mathrm{Re}(c) > \mathrm{Re}(b) > 0$. Therefore,

$$\sigma_{\ell\ell}^2 = \Gamma(2/3) \, \alpha(\varepsilon\, a)^{2/3} F\left(-\,1/3,\, 1/2;\, 5/2;\, 1 - \frac{b^2}{a^2}\right) . \qquad (17D)$$

For $b^2 \leq a^2$ (i.e., pulse length smaller than beamwidth), the hypergeometric series is: (e.g., Abramowitz and Stegan, p. 558)

$$F(-\,1/3,\, 1/2;\, 5/2;\, h) = 1 - h/15 - h^2/105 - (5/1701)h^3 \ldots$$

where $h = 1 - b^2/a^2$. The series converges for $h^2 \leq 1$.

For $a^2 \leq b^2$ (beamwidth smaller than pulse length),

$$F(-\,1/3,\, 2;\, 5/2;\, g) = 1 - (4/15)g - (8/105)g^2 - (32/1701)g^3 \ldots$$

where $g = 1 - a^2/b^2$. The series converges for $0 \leq g \leq 1$. It is monotonic and bounded by $0.491 \leq F \leq 1$.

BEST DOCUMENT AVAILABLE

APPENDIX E - VARIOUS SPECTRAL FORMS AND CONSTANTS; THE ENERGY BALANCE EQUATIONS

Some Spectral Relationships

The relationship between the spatial covariance function $C(\ell)$ along a line and the power spectrum $\phi(\kappa)$ of some quantity (n for example) is

$$\phi(\kappa) = \frac{2}{\pi} \int_0^\infty C(\ell) \cos\kappa\ell \, d\ell \, . \tag{1E}$$

The corresponding 3 dimensional spectrum in vector $\underset{\sim}{\kappa}$ is

$$\phi(\underset{\sim}{\kappa}) = \frac{1}{(2\pi)^3} \int_{\infty}^{\infty} C(\ell) \varepsilon^{-i\underset{\sim}{\kappa}\cdot\underset{\sim}{\ell}} d\underset{\sim}{\ell} \, . \tag{2E}$$

From Fig. 2-4 we see that

$$d\underset{\sim}{\ell} = \ell^2 \, d\ell \, \sin\theta \, d\theta \, d\phi \quad \ell^2 \, d\ell \, d\beta \, d\phi \tag{3E}$$

where $\beta = -\cos\theta$. Therefore:

$$\phi(\underset{\sim}{\kappa}) = \frac{1}{(2\pi)^3} \int_0^\infty C(\ell)\ell^2 d\ell \int_{-1}^{1} e^{-i\kappa\ell\beta} \, d\beta \int_0^2 d\ell \, .$$

Noting that

$$\int_{-1}^{1} e^{i\kappa\ell\beta} \, d\beta = \frac{e^{i\kappa\ell\beta}}{i\kappa\ell}\Bigg|_{-1}^{1} = \frac{2 \sin \kappa\ell}{\kappa\ell}$$

it follows that

$$\phi(\underset{\sim}{\kappa}) = \frac{2}{(2\pi)^2} \int_0^\infty C(\ell) \, \frac{\sin \kappa\ell}{\kappa} \, d\ell \, .$$

Put $\ell \sin \kappa\ell = -\frac{d}{d\kappa} (\cos\kappa\ell)$, so

$$\phi(\underset{\sim}{\kappa}) = \frac{2}{(2\pi)^2} \, \frac{1}{\kappa} \, \frac{d}{d\kappa} \int_0^\infty C(\ell) \cos\kappa\ell d\ell \, .$$

Comparison with Eq. (1E) then shows how $\phi(\underset{\sim}{\kappa})$ is related to the spectrum along a line in the direction $\underset{\sim}{\ell}$; that is

BEST DOCUMENT AVAILABLE

$$\phi(\kappa) = -\frac{1}{4\pi}\frac{1}{\kappa}\frac{\partial \phi_1}{\partial \kappa} \quad . \tag{4E}$$

Similarly, if the medium is isotropic, the three dimensional spectrum in vector κ [i.e., $\phi(\kappa)$] can be related to the power spectrum $E(\kappa)$ of the single quantity κ by integrating over all directions in κ space. In what follows, the subscript n will signify refractive index, rather than ϕ because of possible confusion with the spectral function. Analogous to Eq. (3E), let

$$d\kappa = \kappa^2 \, d\kappa \, \sin\theta \, d\theta \, d\phi$$

and define

$$E_n(\kappa) \, d\kappa = \phi_n(\kappa) \, \kappa^2 \, d\kappa \int_{-1}^{1} d\beta \int_{0}^{2\pi} d\phi \quad .$$

Then

$$\phi_n(\kappa) = \frac{E_n(\kappa)}{4\pi\kappa^2} \quad . \tag{5E}$$

Eliminating $\phi(\kappa)$ using Eq. (4E), we find (Kovasnay, Uberoi, Corrsin, 1949; Bolgiano, 1958)

$$E_n(\kappa) = -\kappa \frac{\partial \phi_1}{\partial \kappa} \tag{6E}$$

as the relation between the power spectrum of a passive scalar in an isotropic medium and the spatial spectrum measured by a sensor moving along a line in a fluid.

Similar reasoning leads to the relation between the energy spectrum of the velocity field and the components along a line in isotropic turbulence, but the situation is more complicated because of the vector nature of velocity. If we define the energy spectrum $E(\kappa)$ such that

$$\overline{u_{11}^2}/2 = \int_0^\infty E(\kappa) \, d\kappa \quad , \tag{7E}$$

the equation in tensor notation analogous to (5E) is (e.g., Batchelor, 1951 [3.4.12]; Lumley and Panofsky, 1964 [Eq. 1.78])

$$\phi_{ij}(\kappa) = \frac{E(\kappa)}{4\pi\kappa^2}\left(\delta_{ij} - \frac{\kappa_i \kappa_j}{\kappa^2}\right) \tag{8E}$$

BEST DOCUMENT AVAILABLE

where $\phi_{ij}(\underset{\sim}{\kappa})$ is the spectral density tensor, δ_{ij} is the Kroeneker delta and $\kappa_{ii}^2 = \kappa_{11}^2 + \kappa_{22}^2 + \kappa_{33}^2$. For example, choosing the velocity component along a line in the x direction,

$$\phi_{xx}(\underset{\sim}{\kappa}) = \frac{E(\kappa)}{4\pi\kappa^2} \left(1 - \frac{\kappa_x^2}{\kappa^2}\right) . \qquad (9E)$$

Similarly, the equation for isotropic turbulence analogous to (6E) is found to be (e.g., Lumley and Panofsky, 1964; Eq. 1.84)

$$E(\kappa) = \frac{1}{2} \kappa^3 \frac{\partial}{\partial\kappa} \left(\frac{1}{\kappa} \frac{\partial S(\kappa_1)}{\partial\kappa}\right) \qquad (10E)$$

where $S(\kappa_1) = \int_0^\infty \int_0^\infty \phi_{11} \, d\kappa_2 \, d\kappa_3$ is the one-dimensional spectrum that would be measured by a sensor traveling along a line and is defined to be non zero only for positive values of κ.

The Balance Equations for Kinetic Energy and Temperature

Under neutral or somewhat stable conditions, the equation relating kinetic energy production, dissipation, and transport is

$$\frac{de}{dt} = - \overline{u'w'} \frac{d\bar{u}}{dz} + \frac{g}{T_o} \overline{\theta'w'} - \frac{d(\overline{ew'})}{dz} - \varepsilon \qquad (11E)$$

where $e = \overline{u'^2}/2$, $\varepsilon = \nu \overline{\left(\frac{\partial u_i}{\partial x_j}\right)^2}$ and ν is kinematic viscosity.

Similarly, for potential temperature variance,

$$\frac{d(\overline{\theta'^2}/2)}{dt} = - \overline{\theta'w'} \frac{d\theta}{dz} - \frac{d}{dz} (\overline{w'\theta'^2}) - \varepsilon_\theta \; ; \qquad (12E)$$

so it is clear that the dissipation rate ε_θ applies to one-half the variance rather than variance. It is common to make the left-hand sides of Eqs. (11E) and (12E) zero by assuming steady-state conditions and to assume the (higher order) transport terms (2nd from the right) to be zero. Equation (12E) has the same form for any passive scaler.

BEST DOCUMENT AVAILABLE

The Spectral Forms and Constants

We will need to define some quantities and use some relationships based on the theory of homogeneous, isotropic turbulence found in a variety of textbooks [e.g., Lumley and Panofsky (1964); Batchelor (1953); Panchev (1971)]. We repeat them here in summary for convenience.

Velocity Field

$$E(k) = \alpha \varepsilon^{2/3} k^{-5/3} \quad \text{where} \quad \alpha = 1.53\text{-}1.68$$

$$S(k_1) = A \varepsilon^{2/3} k_1^{-5/3} \quad \text{where} \quad A = 0.50\text{-}0.55 \qquad (13E)$$

$$D_u(\ell) = \overline{[u(x+\ell) - u(x)]^2} = \underbrace{B \varepsilon^{2/3}}_{C_u^2} \ell^{2/3} \quad \text{where} \quad B = 2.0\text{-}2.2 \ .$$

Refractive Index Field

$$E_\phi(k) = \alpha_\phi \varepsilon^{-1/3} \varepsilon_\phi k^{-5/3} \quad \text{where} \quad \alpha_\phi = 1.33\text{-}1.67$$

$$S_\phi(k_1) = A_\phi \varepsilon^{-1/3} \varepsilon_\phi k_1^{-5/3} \quad \text{where} \quad A_\phi = 0.8\text{-}1.0 \qquad (14E)$$

$$D_\phi(\ell) = \underbrace{B_\phi \varepsilon^{-1/3} \varepsilon_\phi}_{C_\phi^2} \ell^{2/3} \quad \text{where} \quad B_\phi = 3.2\text{-}4.0 \ .$$

The quantities E, S and L are the spectral density, one-dimensional spectrum and structure function respectively; k is wavenumber, ϕ is potential refractive index, u is velocity, ℓ is sensor separation length, ε and ε_ϕ are the dissipation rates of kinetic energy and refractive index half variance respectively. These relationships are valid over the inertial subrange. In applying them to radar data care must be exercised because the outer scale may be smaller than the radar resolution. The values chosen for the various constants are from Wyngaard (private communication) and from papers by Wyngaard et al. (1971) and Hill (1978).

Unfortunately, there has been much confusion in the values of the constants because of different definitions of the spectral quantities by different authors. The relationships between the various constants are (e.g., Panchev, 1971; Tatarski, 1971)

$$\alpha = \frac{55}{36} \frac{\sqrt{3}}{\pi} \Gamma(5/3) \ B = 0.76B \qquad (15E)$$

BEST DOCUMENT AVAILABLE

$$A = \frac{18}{55}\,\alpha = \frac{2}{3\Gamma(1/3)}\,B \qquad (16E)$$

i.e.,

$$A \simeq 0.327\alpha \simeq 0.248B \quad . \qquad (17E)$$

Most experimenters try to measure α_1 which from (13E) is equal to $A = 0.525 \pm .025$.

Confusion by a factor of two is common because of different ways the velocity spectrum can be normalized and the definition of $E(\kappa)$; i.e., $\overline{u'^2} = 2\int_0^\infty E(\kappa)\,d\kappa$. Similar confusion is common in the constants related to the temperature because the dissipation of variance that arises naturally in the balance equations is $\theta'^2/2$. The corresponding confusion carries over into considerations of refractive index.

The Refractive Index Field

Although most readers are more familiar with C_n^2, the potential quantites such as potential temperature θ or potential refractive index ϕ (see Appendix B) are more legitimately considered to be "passive" and are therefore more useful for the application of turbulence theory. That is, they are conserved in parcels transported across isobaric surfaces.

Clearly, if we are to use the relationships (11E) and (12E) to relate spectral quantities to meteorological parameters, it is simplest to define ε_θ in terms of one-half the variance, where θ is potential temperature. Measurements by Wyngaard and Coté (1971) then give $A_\theta = 0.8$. Surveying the literature on experiments in a variety of fluids, Hill (1978) finds $A_\theta/2 = 0.41$-0.5. A value commonly quoted is $A_\theta/2 = 0.7$ from Ottersten (1969), based on early measurements by Gurvich et al. (1967). However, this value ($A_\theta = 1.4$) now seems too large. We have usually assumed $A_n = 0.8$. As pointed out by Ottersten (1969), the relation (14E) applies here, so

$$B_n = 3/2\ \Gamma(1/3)\ A_\theta \simeq 4A_\theta \qquad (18E)$$

or

$$B_n \simeq 3.2 \quad . \qquad (19E)$$

BEST DOCUMENT AVAILABLE

Therefore:

$$C_n^2 = 4A_n \varepsilon^{-1/3} \epsilon_n = 3.2 \varepsilon^{-1/3} \epsilon_n \cdot \tag{20E}$$

Thus expressing (18E) in terms of C_n^2, the one-dimensional spectrum is very simply related to C_n^2 (Ottersten, 1969) by

$$\Phi_{\ell n}(\kappa) = 1/4 \, C_n^2 \, \kappa^{-5/3} \, . \tag{21E}$$

as stated in (2-44). Using (14E) with $A_n = 0.8$, we find

$$\alpha_n = 1.33 \, . \tag{22E}$$